High-Efficiency Photon Sieves and Applications

A Ph.D. dissertation

Presented to

the Faculty of the School of Engineering and Applied Science

University of Virginia

In partial fulfillment

of the requirements for the degree

Doctor of Philosophy (Electrical and Computer Engineering)

by

Matthew N. Julian

B.S. Physics, Stevens Institute of Technology, 2015

M.E. Engineering Physics, Stevens Institute of Technology, 2015

August 2019

Approval Sheet

This Ph.D dissertation is submitted in partial fulfillment of the requirements for the degree

of

Doctor of Philosophy (Electrical and Computer Engineering)

Matthew Julian

This Ph.D. dissertation has been read and approved by the Examining Committee:

Professor Mool Gupta, Advisor

Professor Andreas Beling, Committee Chair

Professor Kyusang Lee

Professor Patrick Hopkins

Dr. Hyun Jung Kim, NASA Langley Research Center

Accepted for the School of Engineering and Applied Science:

Dr. Craig H. Benson, Dean, School of Engineering and Applied Science

August 2019

To my grandfather, Joseph Julian,

and

To Ari Eisner and Harry Lenzing,
for inspiring a younger me and instilling him with a love of the Natural Philosophy and its infinite beauty.

Acknowledgements

There are a number of people to whom I owe thanks for supporting me throughout the process of my doctoral study. Although I can only mention a few names here, I would like to extend a thank you to everybody who helped me along the way. I would also like to extend my thanks to my committee for agreeing to hear this defense.

First, I must thank my advisor, Dr. Mool Gupta, for providing me with the opportunity to pursue research avenues that piqued my interest, and for his guidance along the way to keep me on track towards my defense.

Secondly, I would like to acknowledge the people at NASA LaRC who made this dissertation possible through IRAD funding and graduate student support, and who provided the opening for me to pursue a Ph. D. at NASA. In particular, I would like to thank Dave MacDonnell and Tom Jones for providing the opportunity.

I would also be remiss if I did not mention Dr. Hyun Jung Kim, who not only assisted with experiments and serves on my committee, but who acted as both a colleague and a mentor to me during my years here. She afforded me the opportunity to co-author proposals and explore my own intellectual curiosity, the results of which are partly included in this dissertation. Working with Dr. Kim has certainly allowed me to grow as a scientist and a person, and for that I am eternally grateful to her.

My friends and colleagues at UVA, especially George, Harold, Raj, Zeming, and Elisa, with whom I collaborated with heavily and bounced ideas off of when projects were stuck, were incredibly important to me during my time here. I certainly would not have completed my Ph. D. without them.

I would also like to thank Phillip and Doris Snow for letting me stay with them during my first summer here on my frequent trips to UVA; their kindness and support was crucial to my initial research successes here in graduate school.

To my friends in New Jersey and Virginia, I thank you all for your support, for helping me enjoy life outside of the lab, and for keeping me sane over the course of my studies. In no particular order, thank you to Jay, John, Jess, Connor, Brian, Lindsey, Jon, Emma, Mike, Amanda, Tressa, Mondo, Annmarie, and everybody at Almighty – I love you all; you make my life so much brighter.

Of course, I must thank my family for their immeasurable support and countless phone calls. My parents, Maria and Jeff, my brother Alexander, Aunt Lala, Grandma, Nanny, and Poppy: whether guidance or reassurance, they were never short in their support when I needed it.

Lastly, I have to thank Hannah. She has stuck with me through four years of difficulty, stress, and distance, all the while offering me her unwavering support through all of my ups and downs; I know that she is indescribably proud of what I have done here. These four years have been long and hard at times, but they finally come to a close with the completion of this page. I love you, Bee; we finally made it.

Abstract

Flexible, planar diffractive optical focusing elements are of interest due to their relative design simplicity, large-area scalability, and low cost of manufacturing compared to refractive optics, metamaterial lenses, and microlens arrays. Fresnel zone plates have been considered for this application. However, the relatively large side-bands produced in the zone plate focal plane result in a reduced signal contrast, which is not ideal for many applications. In order to eliminate this issue, photon sieves have been investigated. Developed in 2001, photon sieves are essentially zone plates with the Fresnel rings segmented into a large number of circular pinholes. Replacing the continuous zones with pinholes allows one to modulate the number and position of pinholes in a photon sieve, which allows for relatively simple manipulation of the incident wavefront, tighter focusing, and near-zero focal plane side-lobes. These properties have led to photon sieves being evaluated for applications in remote sensing, beam shaping, optical multiplexing, photolithography, lenses in telescopes and imaging, among other things. However, the reported focusing efficiency of photon sieves has been significantly lower (<7%) than their corresponding zone plate (>70%), which provides the motivation for this work.

In this work, photon sieves were fabricated on lightweight, flexible polyimide substrates via a novel pulsed laser ablation method in order to demonstrate a low-cost large area fabrication process for their feasibility in space-based and other applications. Flexible, single-step phase-type devices with efficiencies of ~11% were demonstrated and performance agreed well with finite-difference time domain (FDTD) simulations. In order to further increase efficiencies, a multi-step photon sieve concept was investigated, modeled, fabricated, and tested. Testing of a fabricated four-step photon sieve showed

efficiencies of ~50%, nearly five times the highest reported value for a photon sieve in the scientific literature. Higher step numbers were simulated via FDTD, and a fundamental efficiency limit was found to approach 70%. We envision that these drastically increased efficiencies will allow photon sieves to be adopted for widespread applications, where previously low efficiency hindered their use.

Additionally, several fundamental limitations of photon sieves were investigated as they related to the current state of the art. Key metrics such as operating bandwidth, focusing efficiency, and fabrication tolerances were analyzed both numerically and experimentally, and new limitations on photon sieve performance were demonstrated. For example, it was found that an inherent trade-off exists between photon sieve bandwidth and focusing efficiency in the current design paradigm, and that in order to improve this metric, a new paradigm must be adopted.

Lastly, as a result of the increased efficiencies developed in this work, photon sieves were demonstrated as focusing- optics in a laser ablation system. The fundamental differences in ablation processes and focused beam characteristics between photon sieve and traditional lens were investigated. It was found that photon sieve beams have a less intense heat affected zone (HAZ) compared to traditional lenses, which results in more consistent marking at various laser beam energy densities. This reduced HAZ and consistency has important implications in many laser-processing applications, especially semiconductor processing and optical surgery, where high precision and localization is required.

Table of Contents

Table of Figures

Chapter 1: Introduction and Motivation

1.1 Introduction

Refractive optics have long been used in various applications in which the phase of wavefront of light needs to be manipulated. However, at short wavelengths, the absorption coefficient of refractive optical materials becomes very high, and refractive optics become unviable. In order to overcome this issue, diffractive optics have been investigated for focusing applications. Diffractive optical elements (DOEs) such as the Fresnel zone plate have long been used for focusing x-ray wavelength [1-3]. In addition to their robustness of operating wavelength, DOEs also offer the benefits of reduced weight and volume, as they are inherently planar structures. Furthermore, because they are planar, they can often be made flexible, making them suitable for active tuning and space applications [4-6]. However, DOEs generate undesirable side lobes at the focal plane.

For applications such as cubeSAT and low Earth orbit (LEO) imaging and communication satellites, lightweight focusing optics are necessary as the price to send objects into LEO can be as high as $13,000/kg [7]. For this reason, photon sieve DOEs have been investigated by NASA and the U.S. Air Force [6, 8-12]. Photon sieves have also been evaluated for applications in axicon lens systems, optical communication, optical multiplexing of vortex beams, multi-on-axis foci, fiber to on-chip-waveguide coupling, and nanolithography [13-20]. However, photon sieve focusing efficiency, defined as the ratio of power contained within the primary focal point to the total incident light power, has historically been very low (~1-11% maximum), which has limited their use in widespread applications and is the primary motivation for this work.

In order to address the current gaps in photon sieve technology, three main topics have been explored: demonstration of a pulsed laser ablation method for the fabrication of photon sieves, the achievement of high-efficiency photon sieves, and demonstration of a novel application of photon sieves for laser-based processing of materials

1.2 Photon Sieve Fundamentals

Photon sieves (PSs) are diffractive optical elements based on the geometry of Fresnel zone plates (FZPs). Essentially, a Fresnel zone plate is a DOE consisting of a series of concentric rings of decreasing width. These rings are positioned such that the phase of light from each ring will cause constructive interference at a designated focal point. Fig. 1 shows the design principle of a FZP [27].

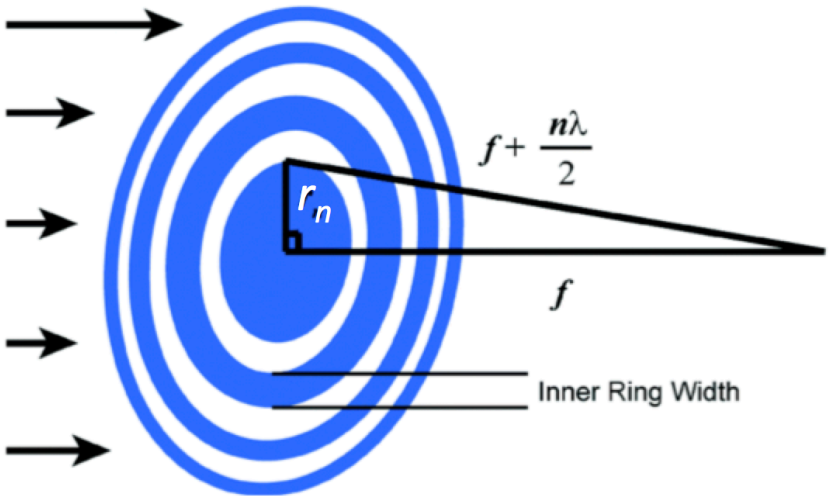

Figure 1: Design principle of a Fresnel zone plate. Each zone is positioned such that the spacing between each zone is an integer multiple of λ/2.

As can be seen in Fig. 1, adjacent zones are λ/2 out of phase with one another and will therefore destructively interfere. In order to account for this, every second zone (i.e. all odd number zones or all even number zones) is either blocked by an opaque material

(amplitude type), or phase shifted (phase type) to produce constructive interference. The choice of blocking even or odd numbered zones is arbitrary and has no effect on performance. From this, we can see that the radius of the nth zone of a zone plate is given by

$$r_n = \sqrt{n\lambda f + \frac{n^2\lambda^2}{4}}, \tag{1}$$

where r_n is measured from the center of the zone plate to the outer edge of the nth zone. The resolution of a zone plate is determined by the width of the outermost zone (the smallest feature size of the zone plate). For a typical lens, the resolution (minimum focal spot size) is given by

$$resolution = \frac{\lambda}{2NA} = \frac{\lambda}{2\,sin(\theta)}. \tag{2}$$

As we examine the outer edge of the zone plate, it resembles a diffraction grating of grating pitch $2w$, where w is the width of the outermost zone. Based on the diffraction grating equation

$$sin(\theta) = \frac{\lambda}{2w}. \tag{3}$$

By combining equations (2) and (3), we see that the resolution of the zone plate is equal to the width of its outermost zone, w.

A photon sieve, as seen in Fig. 2 [12], is simply a FZP with the zones split into a large number of circular pinholes [26]. The design equations are largely the same, with one caveat: because the centers of the sieve pinholes are positioned on the edge of the corresponding Fresnel zones, only every other ring is counted. So, the factor n in equation (1) is replaced by $2n$, resulting in

$$r_n = \sqrt{2n\lambda f + n^2\lambda^2}. \tag{4}$$

Although replacing the rings with pinholes may seem straightforward, there are a few key differences. The primary difference is that the photon sieve pinholes can be made larger than the underlying Fresnel zone widths. This is because the contribution of each pinhole to the focal point intensity is given as a Bessel function, as shown by Cao and Jahns [27]. Specifically, the contribution from each pinhole F is given as

$$F \, \alpha \frac{d}{w} J_1 \left(\frac{\pi d}{2w} \right), \tag{5}$$

where J_1 is the first-order Bessel function of the first kind, and *d* is the pinhole diameter. By plotting (5), it can be seen that for various *d/w* values, the contribution is maximized. Specifically, the function is maximized at *d/w = 1.53, 3.53, 5.53*, and so on. This leads to the relaxed fabrication constraints in photon sieves compared to Fresnel zone plates. Furthermore, the resolution of a photon sieve is still governed by the outermost zone width of the underlying zone plate. Therefore, whereas zone plate resolution is limited by the minimum feature size, photon sieve resolution is not. Hence, for a photon sieve and zone plate with the same focal length, ring number, and diameter, both should focus on the same size point, but the photon sieve will have larger features. Furthermore, for a photon sieve and zone plate with equal minimum feature sizes, the photon sieve will have a tighter focus. Lastly, because the photon sieve is broken up into circular apertures, the apertures can be arranged easily to generate specific wavefront properties which would be difficult to achieve with zone plates. By doing this, photon sieves have been used to generate beams with orbital angular momentum [19], as well as generalized, customized wavefronts [28]. Additionally, the spatial density of pinholes can be modulated ring by ring, which leads to suppression of higher diffracted orders and thus suppressed side-lobes in the focal plane. This provides photon sieves with inherently greater contrast than zone plates. This

improved contrast, combined with the superior resolution for a given feature size, should make photon sieves attractive for imaging and focusing applications. However, the main drawback of photon sieves is their low efficiencies.

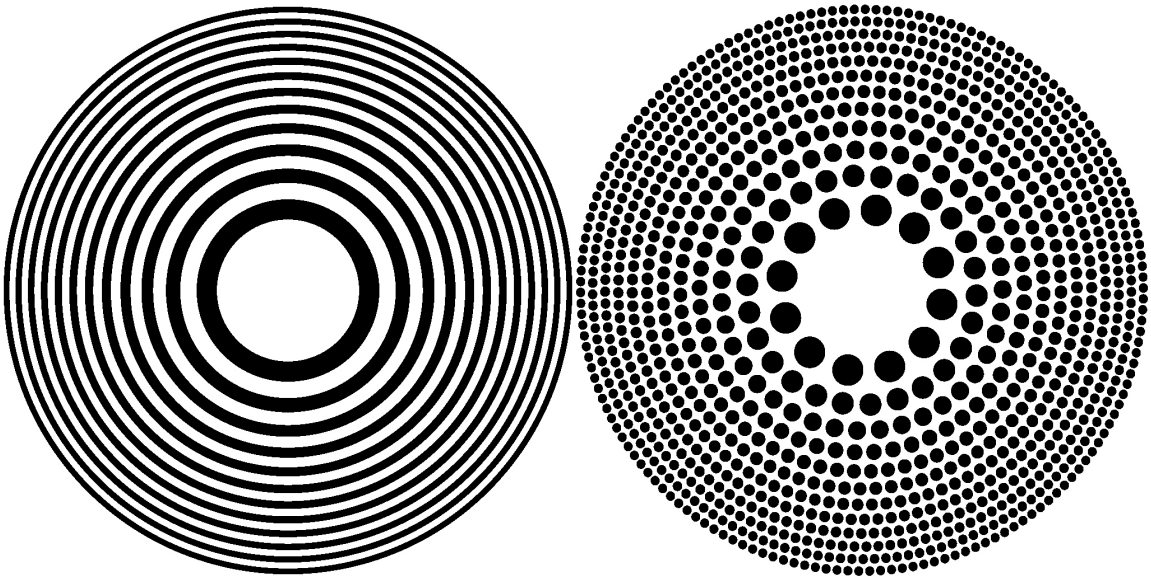

Figure 2: Image showing a Fresnel zone plate and corresponding photon sieve.

Photon sieves suffer from inherently lower focusing efficiency compared to zone plates. Whereas a typical amplitude zone plate has an efficiency of 10%, the corresponding photon sieve will be limited to a little over 1% efficiency. This issue has been addressed via overlapping pinholes [29] and binary phase photon sieves [30, 31], but the former resulted in efficiencies of only a few percent, and efficiencies of ~11% for binary devices are still greatly overshadowed by the 40.5% efficiency of binary phase zone plates. This efficiency difference has largely limited photon sieve usefulness up to the point of this present work, despite the superior imaging properties of the photon sieve.

1.3 Problem Statement

There is a need to develop high-efficiency, broadband, planar optics that are readily scalable to large or small areas. From applications such as space-based telescopes and LIDAR receivers to near-eye displays and integrated optics, planar optics are becoming increasingly attractive and important in various fields of research and commercial product development. Photon sieves offer a unique capability over other planar lenses in that they can achieve high-contract focal points with resolutions below the Airy disk that limits typical lens systems. However, the low focusing efficiencies and large chromatic aberrations present in photon sieves limit their applicability to many applications that require high-quality focal planes over a large operational bandwidth.

To address these issues, the basic design of the photon sieve needs to be generalized and adjusted, or a new operational paradigm must be presented, as the photon sieve design itself is the limiting factor of both efficiency and bandwidth. However, this is not a straightforward task, as the design geometry is also the exact criteria that allows the sieve to act as a lens at all. Therefore, emphasis must be placed on studying the effects of these design alterations on the lensing properties of the sieves.

Additionally, in order to address the various physical dimensions that planar optics applications may require (meter-square to micron-square areas), a novel laser ablation fabrication technique was examined that is easily scalable to large or small areas. This technique allows for the writing of large or small features over large or small areas so long as the proper system is used for a given application. Laser ablation also allows for the precise depth-milling of phase grating structures. However, because the laser process is

ablative, care must be taken to study the interaction of laser and material, and to ensure that surface morphology is optimized for a given application, as the surface will affect the optical performance of the sieve through increased scattering, phasefront error, and stray light.

1.4 Objective

This dissertation examines a novel method of low-cost large area photon sieve fabrication using laser ablation process and achievement of very high-efficiency along with investigations on improvements on the bandwidth to allow for improved focusing performance and increased applicability of photon sieves in various fields. Through the use of computational modeling, various photon sieve design alterations were conceived and tested, and their performance and effect on focusing efficiency, and bandwidth were studied. Appropriately designed sieves were then fabricated and tested to compare with numerical results. The optical properties and surface morphology of these sieves were characterized, and the effect of various laser processing parameters on sieve performance was examined. By optimizing design and fabrication, improvements in photon sieve efficiency and bandwidth have been demonstrated and limits can be placed on the upper bound of photon sieve performance, and design tradeoffs can be understood.

Chapter 2: Literature Review

Here, a review of the current photon sieve state of the art will be presented in order to lay out the framework for the work presented in this thesis. The Literature review will be broken into two parts, each designed to reflect one of the primary goals of this thesis.

2.1 Photon Sieve Efficiency

Photon sieves possess several advantages over other diffractive focusing elements such as Fresnel zone plates. Their low side bands and design flexibility allow for increased imaging contrast, resolution, and easy integration into various beam-shaping applications [25, 26]. However, currently photon sieve efficiency has been limited to ~1-11%, which has limited its use in several applications. In order to increase photon sieve efficiency, substrates with very low optical absorption can be combined with anti-reflective coatings, however the efficiency increase would only be on the order of a few percent. Alternative amplitude-modulation based designs have been investigated in order to increase photon sieve efficiency as well, such as “Fibonacci sieves”, where photon sieve rings are opened or closed according to the Fibonacci sequence [20], and hybrid zone plate/sieve designs [29], where the inner rings of the photon sieve (which contribute the largest amount of optical throughput) are fully opened into Fresnel rings as opposed to pinholes. However, the efficiency increases from both of these designs were minimal (~50% increase from 1-2% efficiency) and resulted in higher side lobes (and thus reduced contrast). Binary phase photon sieves have been demonstrated in the form of membrane-based space telescopes [6]. However, the efficiency of this design reached only 11%, and no concrete methods of further enhancing the efficiency were presented. Additionally, the work presented in [6] does not provide any potential upper limit for photon sieve efficiency, and thus leaves

significant room for improvement in the state of the art. It is well known that blazed grating zone plates (so-called "Fresnel lenses") can achieve significantly higher efficiencies than their traditional binary counterparts by up to an order of magnitude [2]. Surprisingly, though, such a concept has not been mentioned or explored for photon sieves.

2.2 Enhancement of Photon Sieve Bandwidth

Photon sieves suffer from sever chromatic aberration due to their geometry being based on a single design wavelength, as is shown in equation (4). This limits photon sieve use in broadband, or "white light" applications, as the focal plane will be blurred due to the different wavelength focusing in different positions along the optical axis. In order to address this, the photon sieve design itself must be generalized. In 2007, it was shown that so-called "fractal photon sieves", photon sieves with rings opened/closed according to a particular mathematical pattern may provide higher bandwidth [32]. This fractal photon sieve is able to produce multiple foci along the optical axis for a given wavelength. Therefore, as multiple wavelengths pass through the sieve, the various foci produced by each color can potentially overlap with different order foci of another color, thus artificially increasing the bandwidth of the device. However, these fractal-type photon sieves still suffer from low efficiencies, and the efficiency of each color in a given focal plane varies greatly depending on which order foci are overlapped.

A different, more promising method of increasing photon sieve bandwidth has been presented over the course of several works from the same group. This method is based on a known technique called "wavefront coding," in which a phase mask is used in the pupil of an optical system in order to generate a wavelength-invariant point spread function at the focal plane [33, 34**]**. This phase mask technique was first demonstrated as a two-

component optical system [33, 34], and later as a directly encoded single photon sieve. By altering the strength of the phase mask, the spectral width of the photon sieve usable bandwidth is increased by nearly two orders of magnitude [35, 36]. However, given that a typical photon sieve bandwidth, depending on the numerical aperture of the sieve itself, for a sieve operating in the visible spectrum, can be anywhere from a few picometers to a few nanometers, this is not a large improvement. In the demonstrated work, the usable bandwidth of a photon sieve was increased to 28 nm from 0.32 nm, which is a large improvement but still leaves the device with a very narrow bandwidth [36]. This same work combined this so-called "wavefront coded" photon sieve with a traditional refractive lens to achieve full-visible-spectrum achromatic focusing. However, by combining the planar photon sieve with a thick optical lens, one of the key advantages of the planar optic (its planarity) is lost. Additionally, the wavefront coding alters the point spread function of the focusing optic such that it becomes asymmetric, and not directly applicable for imaging. However, simple post-processing can be performed to produce a perfectly clear white light image [33-36].

Lastly, this wavefront coded photon sieve was further improved by taking advantage of the harmonic property of diffractive optics [37]. This states that by adjusting the geometry such that every P^{th} zone of the zone plate or photon sieve is exposed, there will now be P wavelengths that will focus to the same design focal plane. The design equation for a harmonic photon sieve is given in equation (6), and a wavefront coded harmonic photon sieve in equation (7) [37]:

$$\sqrt{(x_m^2 + y_m^2) + f^2} - f = nP\lambda \tag{6}$$

$$\sqrt{(x_m^2 + y_m^2) + f^2} - f = nP\lambda + \frac{\alpha}{kR^3}(x_m^2 + y_m^2) \qquad (7)$$

In equation (6), if P = 1, the equation reduces to the same form of (4) and we have the geometry of a typical photon sieve. As P increases, the number of rings in the sieve decreases by 1/P. Equation (7) is identical to (6) except for the extra term on the right-hand side. Here, α is the strength of the wavefront coding mask. If α=0, equation (7) is equivalent to (6). *R* is the radius of the entire aperture of the photon sieve.

By combining these two techniques, a harmonic diffractive photon sieve was demonstrated to have multispectral properties, with each spectral peak being additional broadened by the wavefront coding. Specifically, peaks at 437.5, 500, 583.3, and 700 nm were shown, with each peak having a spectral bandwidth of 16, 18, 22, and 28 nm, respectively. Although this demonstrated great improvement in the current state of the art, the possibility for harmonic diffractive photon sieve geometry *is* chosen such that fully achromatic focusing across the visible spectrum can be achieved. The presence of any limitation to this technique has also not been studied. By examining equation (7), one can see that the strength of the wavefront coding, and thus the achromatic quality of the photon sieve, depends both on the magnitude of α and the radius of the sieve aperture. Therefore, it is possible that a limitation exists such that only certain combinations of radii and α values will properly focus the incident light. Additionally, these studies were performed exclusively with low photon sieve efficiency, amplitude-type photon sieves, and therefore it is not known if these techniques are compatible with high-efficiency designs. The three

open-ended areas of the state of the art will be addressed in the work presented in this dissertation in Chapter 8 and appendix A.

2.3 Laser Ablation for Fabrication of Diffractive Optics

Laser ablation has been demonstrated previously for the fabrication of various types of diffractive optics [38-41]. Parameters such as *the* number of pulses and laser pulse energy must be optimized in order *to* control etch depth and surface morphology. However, despite these past efforts related primarily to gratings and zone plates, there has not been any demonstration of photon sieve fabrication using laser ablation. Additionally, the effect of etch depth error and surface roughness on focusing characteristics of the ablated lenses are not presented in the previous works, thus leaving a lapse in the collective knowledge base.

Chapter 3: Light-Matter Interactions – Laser Ablation and Plasmonics

This chapter will serve as a brief review of the fundamental processes that govern light-matter interactions as they relate to the topics contained in this dissertation. Specifically, laser ablation and plasmonics will be discusses, and these two topics will appear in chapters 5, 6, 7, and 9 (laser ablation) as well as in chapters 8 and appendices A and B (plasmonics). Both of these sub-fields of optical physics deal with the electronic and optical response of materials in the presence of incident radiation and will therefore be covered in a single chapter.

When light is incident on a material, the primary material property that governs the initial interaction is the dielectric function, or complex refractive index, of the material. This complex refractive index, written as $\tilde{n} = n - j\kappa$, describes the reflection and absorption of light incident at an interface (such as a material surface and air, for example) and bulk. Therefore, this physical quantity governs the amount of light that is transmitted through a material, how deeply the light will penetrate, how the energy will be absorbed, and so forth. As these processes are typically related to the electronic structure of a material, the refractive index (in the form of the dielectric function) therefore partially describes the electronic response of a material to an optical stimulus. In the case of metals, electronic conductivity must also be considered. From this starting point, we will explain briefly the physics of laser ablation and plasmonics as they relate to the presented work.

3.1 Laser Ablation

Laser ablation is the removal of material from a substrate by direct absorption of incident laser energy. When laser energy impinges a material, one of three regimes will be present in the interaction: slight heating, surface melting, and ablation. Ablation can occur as a result of continuous wave (CW) or pulsed laser illumination and occurs when the incident optical energy is above the so-called "threshold fluence" or "threshold energy density" of a material. The specific ablation threshold for a given material will depend intimately on the material absorption behavior and thermal conductivity (as well as the presence of any defect, microstructures, etc.) as well as the incident laser processing parameters (such as pulse width and wavelength).

In this thesis, laser ablation is achieved through nanosecond pulsed laser irradiation of the material surface. As a result, the discussion below will be focused on the photothermal response of materials, as is typically present in nanosecond ablation processes. In the case of an ultrafast (picosecond or femtosecond) ablation process, the ablation mechanism is less understood, but is generally agreed upon to depend minimally on material thermal properties and primarily on the effect of the extremely strong electric field on the material. The intense field regime causes things like direct material ionization, plasma generation, and the so-called "Coulomb explosion", which occurs as a result of repulsive Coulomb forces between ionized atoms in a small volume of a material [42]. In nanosecond material ablation, the primary mechanism for material removal is evaporation or sublimation as a result of localized heating due to optical absorption. Therefore, in the nanosecond regime, the material thermal conductivity is also an important parameter in the ablation process.

When nanosecond laser pulses are incident on a material, the initial response is a reflection and absorption of the incident laser energy. The specific absorption mechanism depends on the material itself. For insulators and semiconductors, absorption generally results from transitions of electrons from the valence to conduction band energy states. In metals, the absorption can occur through various processes resulting from the presence of free electrons in the material. The electrons of the material will oscillate as a result of the incident electric field, and will subsequently collide with atoms, defects, and ions in the material. These are known as phononic collisions, and they transfer the kinetic energy of the electron into thermal energy that is dissipated into the lattice. This transfers the incident radiative energy from optical (energy of the electric field), to kinetic energy of the electrons, to thermal energy in the lattice.

Once the energy has been absorbed by the material, it will begin to dissipate into the lattice at a rate dictated primarily by the material thermal conductivity. The more conductive a material is, the further and faster the heat will dissipate. This heating occurs on a nanosecond or microsecond timescale, as a result of the short optical pulse, and therefore causes a rapid increase in the local temperature of a material. If the incident energy density is high enough, this temperature will exceed the vaporization temperature of the material, and ablation will occur. The area over which ablation and/or melting of the material will occur depends on the electronic and thermal properties of the material. For materials such as metals, which have fast thermalization times (that is to say, electron kinetic energy is rapidly transferred to the lattice, typically on the order of a few ps in metals), thermal energy is spread across a greater area, which results in a larger heat affected zone (HAZ) in the material. Physically, the manifests itself as clear evidence of

thermal disruption to the material across an area (in this case) larger than the area exposed to the incident radiation. In other materials, such as semiconductors, insulators, or polymers, the HAZ is much smaller than for a metal, as the electron thermalization time is generally much longer. Specifically, in the case of polymers, thermalization times can be on the order of microseconds, which results in a very small HAZ and minimal presence of thermal processes (depending on the laser wavelength) even in the nanosecond pulse regime [42]

The phenomenon of ablation can be used to precisely machine material micro- or nano-structures to engineer various optical, thermal, and mechanical properties [42]. By carefully designing the experimental setup and optimizing the choice of materials, clean features can be made that enable various functionalities in a given application.

3.2 Plasmonics

Plasmonics is the study of the interaction between light and metals. Due to their free electrons, metals interact much differently with light than other materials. At low frequencies, such as visible wavelengths and longer, electrons on the metal surface can easily oscillate at a sufficiently rapid rate so as to effectively filter the incident radiation, as described in the previous section. The vast majority of light in this regime is reflected at the metal surface, and the remainder is absorbed by the first few nanometers of electrons in the metal. At higher frequencies, however, the surface electrons can no longer oscillate to follow the incident electric field. This allows for deeper penetration of the incident light into the metal, and the metal behaves similarly to a dielectric. However, at a specific frequency, the plasma frequency, the oscillation of surface electrons will be exactly resonant with the incident electric field, leading to the formation of standing waves on the

metal surface. For most metals, this frequency occurs in the ultraviolet spectrum. These standing waves are known as surface plasmons. Surface plasmons can be exploited for various functionalities in a wide range of fields such as alternative energy, thermal management, optical filtering, nano-optics, and so forth [43-46]. Surface plasmons can also be scattered by material nanostructures, material interfaces, or boundaries into which they propagate, and thus be re-radiated into free space; this allows for phenomenon such as optical filtering and extraordinary optical transmission [47, 48]. In the context of this thesis, plasmonics were studied as color filters and diffractive scatterers in order to explore a potential method of minimizing chromatic aberrations in photon sieves as additional research in appendix A.

The location of the plasmon resonance of a particular structure depends strongly on the geometry of that structure and can be engineered by structuring the metal surface. Typical methods of structuring include the fabrication of nano-antennae, metal-insulator-metal geometries, nano-slits, nano-particles of various shapes, and so forth [43-52]. So, there is no single equation to describe the location of the plasmon resonance of a nanostructured material. However, in any case, the location will have a dependence on the geometry of the structure, and the refractive indices (permittivity) of the metal and the surrounding dielectric. As such, the location can easily be tailored to produce a response at a given frequency depending on the intended application.

Chapter 4: Modeling of Photon Sieves

In order to predict the behavior of both amplitude and phase type photon sieves in this work, MATLAB and finite-difference time domain (FDTD) simulations were performed in order to simulate focal point size and focusing efficiency. Here, focusing efficiency is defined as the ratio of power contained within the primary focal point (defined as the area inside the first null of the focal plane) to the total incident light power. The input source is made to be the same diameter as the photon sieve. Photon sieve spot sized is defined by the full-width at half-maximum (FWHM) of the focal point.

Initially, MATLAB code was used based on a vector diffraction theory treatment of photon sieves described by Tang et. al. [53]. This approach was chosen for its robustness in describing photon sieve geometry, as scalar theory breaks down as the feature sizes approach the dimensions of the wavelength. In order to find the focal point FWHM and diffraction efficiencies, these integrals are computed, a focal point intensity distribution was plotted, and focusing efficiency was computed.

Subsequently, for phase-type and plasmonically-enhanced photon sieves, FDTD simulations were employed, as they proved less time consuming and a bit more robust and straightforward. In the FDTD case, an incident optical field was propagated through the photon sieve, and the transmitted optical power located in the focused beam was recorded.

4.1 Vector Diffraction Theory of Photon Sieves

In order to understand the intensity distribution of light after being diffracted by a photon sieve, we employed vector diffraction, specifically the angular spectrum representation of Fourier optics [54] in order to model the optical field propagation at all points along the optical axis. Here we will follow the convention outlined by [55], but in

deeper, step-by-step detail. The angular spectrum representation of an arbitrary light field understands the field as a superposition of plane and evanescent waves propagating in all directions with all amplitudes. The interference of all of these waves produces our observed evolution of the optical field. In order to understand the total diffracted field of the photon sieve, we must consider the interference of the field of each pinhole with every other pinhole. The total diffracted field is therefore the sum of the individual diffracted fields from each pinhole.

As a starting statement, as expressed in [54], the angular spectrum representation of an electromagnetic field can be shown as:

$$E(x,y,z) = \iint_{-\infty}^{\infty} A(k_x,k_y;z)e^{i(k_x x+k_y y+k_z z)}dk_x dk_y \tag{8}$$

This is obtained by taking first the Fourier transform of the object plane geometry, which will give us the form of the aperture function (or Fourier spectrum of E) $A(k_x,k_y)$. Then, in accordance with the Helmholtz equation

$$(\nabla^2 + k^2)E(r) = 0 \tag{9}$$

which all time-harmonic optical fields must satisfy, we see that the form of the optical field must be

$$A(k_x,k_y;z) = A(k_x,k_y,0)e^{\pm ik_z z} \tag{10}$$

Thus, if we then take the inverse Fourier transform of this equation, we will get back the form of E(x,y,z) as shown in equation (8). This is the basis of the angular spectrum representation. We find the aperture function of our object plane, which decomposes our field into an angular spectrum of optical waves. Then, by taking the inverse transform of this aperture function multiplied by the propagator factor given by the solution to the Helmholtz equation, we obtain a very accurate expression for the field at a point (x,y,z) that is valid for all object plane geometries and feature sizes (e.g. sizes smaller than the optical wavelength, which render typical Fourier optics and scalar diffractive theory invalid). Now, we will look at how to apply this method to analyze a photon sieve and its diffractive properties.

Consider a photon sieve lying in the x-y plane at z=0, and having a focal plane at (x,y,z=f). The sieve can be centered at (0,0,0) with a focal point at (0,0,f), but such strict constraints are not necessary for our analysis. What is important is that the sieve in positioned at z=0 in the x-y plane, and its focus lies at z=f in the x-y plane.

Consider an incident field propagating along the z-axis and having components $E_i(x, y, 0) = E_x(x, y, 0)\hat{x} + E_y(x, y, 0)\hat{y}$. This light will encounter both pinholes of the sieve and opaque regions. We will consider the field inside of an individual pinhole to be of constant amplitude within the pinhole, as the amplitude changes very little as we move outward from the hole center. As is convention in Fourier optics, and is necessary for our angular spectrum method, we will start by mathematically defining the amplitude or aperture function of the photon sieve. The basis of this aperture function will be the following:

$$E_n \begin{cases} = E_i, inside\ of\ pinhole \\ = 0, else \end{cases} \tag{11}$$

where E_n is the field inside of the nth pinhole. Let the center of the nth pinhole be (x_n,y_n), and the radius of the nth pinhole to be r_n. We can then derive the following condition to define the aperture function, or field incident on the nth pinhole:

$$\begin{cases} E_{nx}(x,y,0) = \begin{cases} E_x(x_n,y_n), & (x-x_n)^2+(y-y_n)^2 \le r_n^2 \\ 0, & else \end{cases} \\ E_{ny}(x,y,0) = \begin{cases} E_y(x_n,y_n), & (x-x_n)^2+(y-y_n)^2 \le r_n^2 \\ 0, & else \end{cases} \end{cases} \tag{12}$$

According to the angular spectrum method, we can represent the field at some point (x,y,z) as the inverse Fourier transform of the Fourier transform of the aperture function, multiplied by a propagation factor. In order to arrive at this conclusion, let us take a step-by-step formalism of the method. We have already defined the aperture function. According to Fourier optics, taking the two-dimensional Fourier transform of this function will allow us to decompose the incident field defined by the aperture into a superposition of plane and evanescent waves, each traveling in a unique angular direction. This is the so-called "angular representation" of the incident field. Mathematically, this appears as:

$$A(k_x,k_y) = \frac{1}{4\pi^2}\iint_{-\infty}^{\infty} E_i(x,y,z)e^{-i(k_x x+k_y y)}dxdy \tag{13}$$

where k_x and k_y are the x and y components of the wave vector k. In the context of the photon sieve, this integral takes the form:

$$A_x = \frac{1}{4\pi^2} \iint_{(x-x_n)^2+(y-y_n)^2 \le r_n^2} E_x(x_n, y_n) e^{-i(k_x x + k_y y)}\, dxdy$$

$$A_y = \frac{1}{4\pi^2} \iint_{(x-x_n)^2+(y-y_n)^2 \le r_n^2} E_y(x_n, y_n) e^{-i(k_x x + k_y y)} dxdy \tag{14}$$

where we write $k^2 = k_x^2 + k_y^2 + k_z^2,\ |k| = 2\pi/\lambda$.

Let us deviate from our present discussion briefly in order to resolve the above $A_{x,y}$ integrals. It is important now to note that our apertures are circular, as described by our integration boundaries via our aperture function. In order to understand the result of the above integrals, it is important to understand the behavior of an oscillating field inside an aperture of circular geometry.

Consider the wave equation

$$\frac{\delta^2 E}{\delta t^2} = c^2 \nabla^2 E \tag{15}$$

For a circular oscillating field, solutions of the wave equation take the form of Bessel functions.

Now, as we evaluate the above integrals, we see that the solutions take the form

$$A_x(k_x, k_y) = \frac{1}{4\pi^2} E_x(x_n, y_n) e^{-i(px_n + qy_n)} r_n J_1(r_n k_r)/k_r$$

(15)

$$A_y(k_x, k_y) = \frac{1}{4\pi^2} E_y(x_n, y_n) e^{-i(\quad px_n + qy_n)} r_n J_1(r_n k_r)/k_r$$

where we have employed the following coordinate transforms:

$$p = \frac{k_r}{k} cos(\beta)$$

$$q = \frac{k_r}{k} sin(\beta)$$

$$m = \begin{cases} \sqrt{1 - p^2 - q^2}, & p^2 + q^2 \leq 1, plane\ wave\ condition \\ i\sqrt{p^2 + q^2 - 1}, & p^2 + q^2 \geq 1, evanescent\ wave\ condition \end{cases}$$

Where p, q, and m are used in place of the form of the wavenumber equation

$$k^2 = k_x^2 + k_y^2 + k_z^2$$

and k_r is the "radial wavenumber", or the projection of k onto the x-y plane. Beta is the polarization angle of the hole in the coordinate system and must be simulated from 0 to 2π in order to account for waves exiting the pinhole is all directions. Combining k_r and β allow us to account for all of the possible magnitudes and directions of the plane and evanescent waves arising from the angular spectrum representation of each pinhole. It should be noted that evanescent waves are not able to propagate into the far field due to their exponential decay with distance and will not be present in our future calculations.

We must also define vectors from the center of the nth pinhole to each point within the focal plane. Let (x,y, f) be a point inside the focal plane at z = f, while the pinhole is centered at (x_n,y_n,0) as always. We then make the coordinate transforms:

$$x' = x - x_n, \qquad y' = y - y_n, \qquad r' = \sqrt{x'^2 + y'^2}$$

$$x' = r'\cos(\alpha), \qquad y' = r'\sin(\alpha)$$

Next, we use the angular spectrum representation given by (8) to express the vector diffraction field at z > 0 as:

$$E_{nx} = \iint_{-\infty}^{\infty} A_x(p,q) e^{ik(px+qy+mz)} dpdq$$

$$E_{ny} = \iint_{-\infty}^{\infty} A_y(p,q) e^{ik(px+qy+mz)} dpdq \tag{16}$$

$$E_{nz} = \iint_{-\infty}^{\infty} \left[\frac{p}{mA_x(p,q)} + \frac{q}{mA_y(p,q)}\right] e^{ik(px+qy+mz)} dpdq$$

Finally, in order to solve for the field from the nth pinhole at a given point (x,y,z) away from the photon sieve, we substitute equation (15) into equation (16). This gives us:

$$E_{nx} = r_n E_x(x_n, y_n) \int_0^{\infty} exp(ikmz)\, J_1(r_n k_r) J_0(r' k_r) dk_r$$

$$E_{ny} = r_n E_y(x_n, y_n) \int_0^{\infty} exp(ikmz)\, J_1(r_n k_r) J_0(r' k_r) dk_r \tag{17}$$

$$E_{nz} = -ir_n [E_x(x_n, y_n)\cos(\alpha)$$

$$+ E_y(x_n, y_n)\sin(\alpha)] \int_0^{\infty} \frac{k_r J_0(k_r r') J_1(r_n k_r)\, exp(ikmz)}{kmz} dk_r$$

The total field at the point (x,y,z) is then given as the sum of the individual contributions:

$$E_x(x,y,z) = \sum_{n=1}^{total\ \#\ holes} E_{nx}(x,y,z)$$

$$E_y(x,y,z) = \sum_{n=1}^{total\ \#\ holes} E_{ny}(x,y,z) \tag{18}$$

$$E_z(x,y,z) = \sum_{0}^{total\ \#\ holes} E_{nz}(x,y,z)$$

The total intensity is then simply:

$$I = |E_x(x,y,z)|^2 + \left|E_y(x,y,z)\right|^2 + |E_z(x,y,z)|^2 \quad (19)$$

From a numerical simulation standpoint, this full calculation can be carried out by defining x', y', r', and alpha values from each pinhole to a point on the focal plane. We then take these values and use them for the field equations $E_{nx,y,z}$, which are computed in a loop that iterates the value of beta from 0 to 2π. Once this is finished, we take a running total of the field (the summations expressed above) and move on to the next point (x,y) on the focal plane, where the same calculations are carried out. This is done for each point (x,y) within the focal plane. Thus, the field at each point (x,y) within the focal plane is calculated for each value of beta, for each pinhole of the sieve.

4.2 Finite-difference Time Domain (FDTD) Method

Finite-difference time domain simulations involve making iterative solutions to Maxwell's equations at a number of "mesh cells" (typically with dimensions of a few cubic nanometers, but larger dimensions can be used if needed) which are iteratively stepped forward in time. This type of simulation gives a very exact solution to the behavior of the electric and magnetic fields of an optical source as it propagates through space and time and interacts with different materials, interfaces, and structures.

Here, FDTD methods were used to simulate the phase-type devices, as a theoretical description of phase type photon sieves does not exist as it does for zone plates. In order to model photon sieves in an FDTD environment, a commercial solver (Lumerical FDTD) was employed. The photon sieves were defined by a dielectric substrate with refractive

index of 1.7 (based on the index of the polyimide used in experiments), and the sieve pattern was represented by an etch layer or index 1.0 spanning from the surface of the substrate to a specified depth into the dielectric. In order to compensate for the computational time required by FDTD simulations as dimensions grow large, photon sieves with smaller diameters were used. This has no effect on the efficiency, as the incident light was made to be the same diameter as the photon sieve in the simulation. The dimensions of the photon sieve used were: focal length 10 microns, wavelength 633 nm, ring number 2, and total diameter ~10 microns. An example of the FDTD environment used for the binary phase photon sieves is shown in the Lumerical screenshot in Fig. 3.

In the case of photon sieves with plasmonic-correction of chromatic aberrations, a similar overall lens size and focal length were used. However, in this case, two simulations were performed. The first simulation was used to generate the broadband optical field transmitted through a finite array of nanostructures (as will be explained in a later chapter), and the second was to import that field as a unique, finite-dimensioned source positioned at the center of each photon sieve "pinhole" position. This allowed for reduced simulation time and complexity, as the initial simulation can be constrained to the optical near field, while the second involves only a simple far-field projection of the emitted signals from the nanostructure, which serves to compute the interference and focusing behavior of the photon sieve.

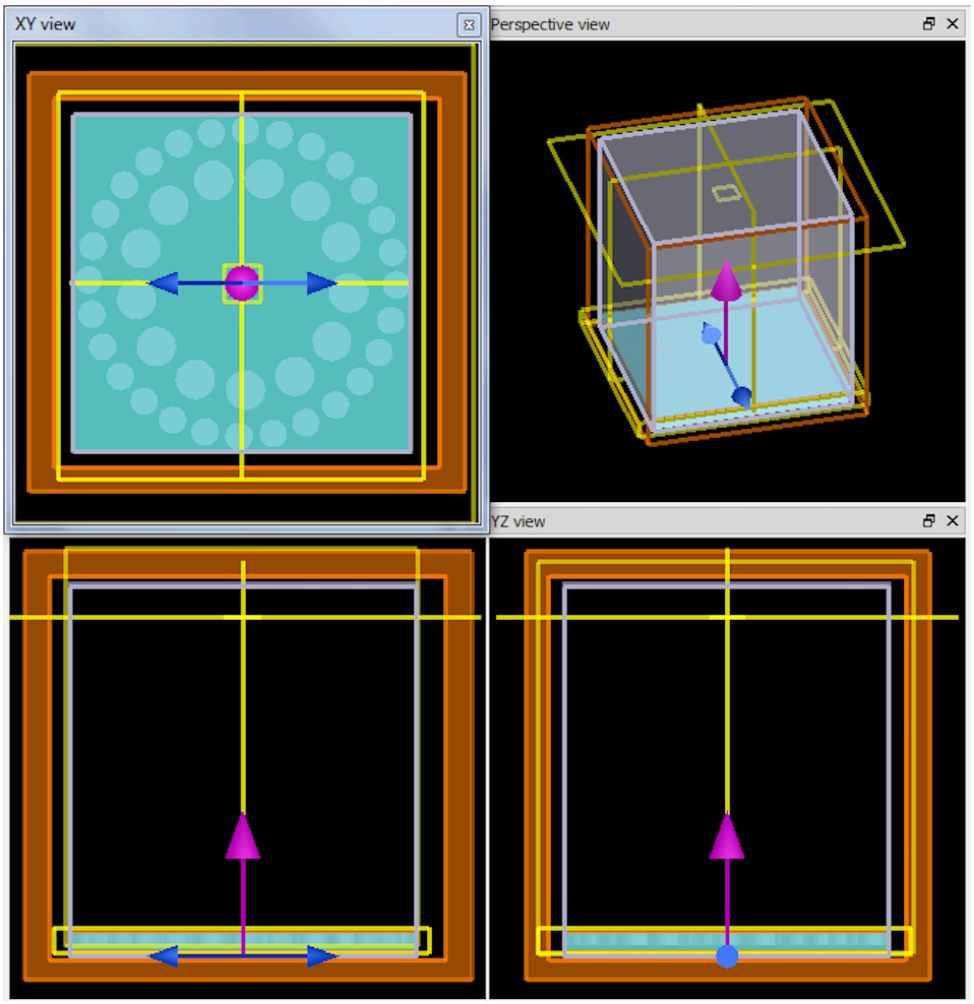

Figure 3: Lumerical FDTD environment showing binary phase photon sieve simulation setup.

Chapter 5: Laser Fabrication and Characterization of Amplitude Photon Sieves

Here we will examine the efficacy of using a pulsed laser ablation technique for fabricating amplitude-type photon sieves. The experiments carried out in this chapter serve as the basis for the fabrication technique that is to be used in the remainder of this thesis, and thus provides the backbone of the presented work. Laser-based fabrication is chosen for several reasons. It is a low-cost, high-throughput, highly customizable and robust option compared to typical lithography and etching processes, which makes it suitable for large-area fabrication of patterns written into various substrates. In order to determine if laser ablation is useful for fabricating photon sieves, photon sieve surface morphology must be characterized, and optical performance must be measured and compared to idealized simulations in order to understand any deviations from expected behavior that arise from the fabrication process. In this chapter, the choice of opaque metal materials, surface morphology, and photon sieve optical performance are analyzed and discussed, and the laser fabrication technique is evaluated for its appropriateness moving forward.

5.1 Choice of Material

In this section, amplitude type photon sieves, which consist of transparent holes in an otherwise opaque metal film, were demonstrated. The initial research for this endeavor aimed to optimize the choice of material to be used as the metal film. At the time of this research, two experimental options were available: chromium (Cr) and silver (Ag). Chromium is commonly used in lithographic masks; however, it also has a relatively high vaporization temperature (2944 K), which necessitates a high incident laser fluence. On

the other hand, Ag films are slightly more prone to oxidation and are less stable than Cr, which make them less attractive for photon sieve applications, however they also have a much lower vaporization temperature (2435 K) which makes them more suitable for the laser process parameters. Here, both materials were tested, and the effects of the laser process on pattern quality and surface morphology were studied.

Initially, Cr films were tested. Cr was deposited on soda lime glass substrates via electron beam physical vapor deposition at a rate of 1 angstrom per second. Prior to deposition, substrates were cleaned via subsequent rinsing with acetone, isopropyl alcohol, and deionized water, and were then exposed to an O_2 plasma etch for ten minutes. Once the Cr films were deposited, the photon sieve pattern was written into the film via a laser-galvo system controlled by a PC. A schematic of the experimental setup is shown in Fig. 4. Initially, the laser wavelength chosen was 532 nm due to availability in the laboratory and is well suited for ablation processing. However, in subsequent experiments (section 5.2), a 1064 nm laser was used, as it has a much higher output pulse energy, which allowed for easier ablation and faster throughput.

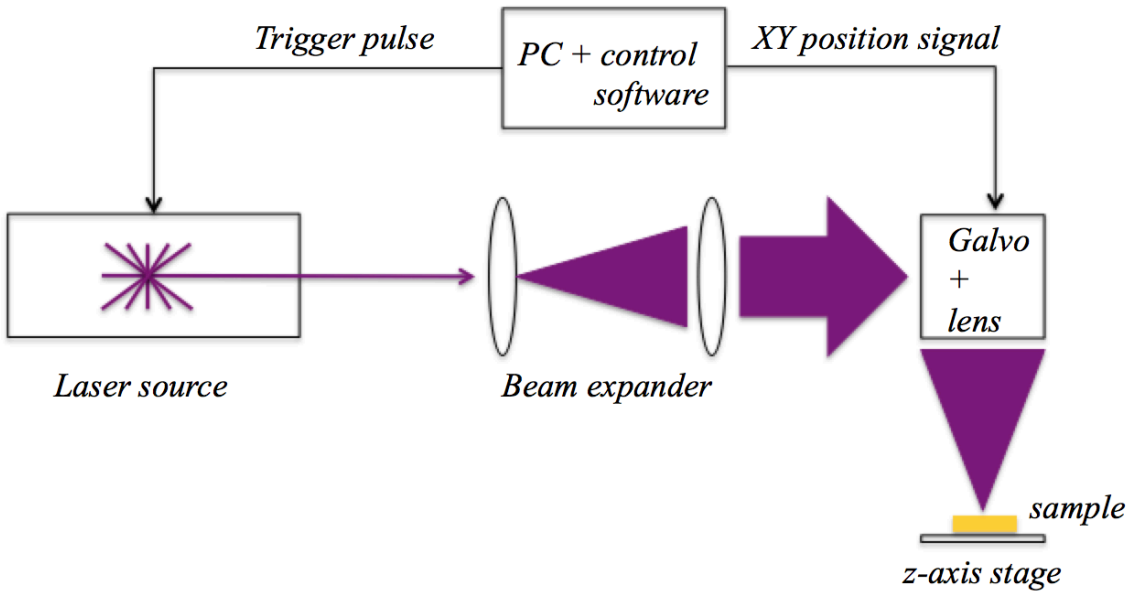

Figure 4: Schematic of the laser ablation setup used to fabricate photon sieves.

To understand the behavior of Cr in the laser ablation process for the fabrication of photon sieves, patterns were written at various laser fluences at 532 nm wavelength. Based on the installed focal length of the lens, the maximum achievable fluence from the 532 nm laser system is 10.19 J/cm^2. The pulse repetition rate can be tuned from 10 kHz to 600 kHz, the pulse width is 1.5 ns, the maximum pulse energy is 16 µJ, and the spot size is ~ 20 µm at the sample surface. For these experiments, the pulse rate was kept at 600 kHz, as lower rep rates failed to adequately produce ablated marks in the metal films, likely due to the low pulse energy of the 532 nm laser and high reflection from metal films. The scanning speed was held at 50 mm/s.

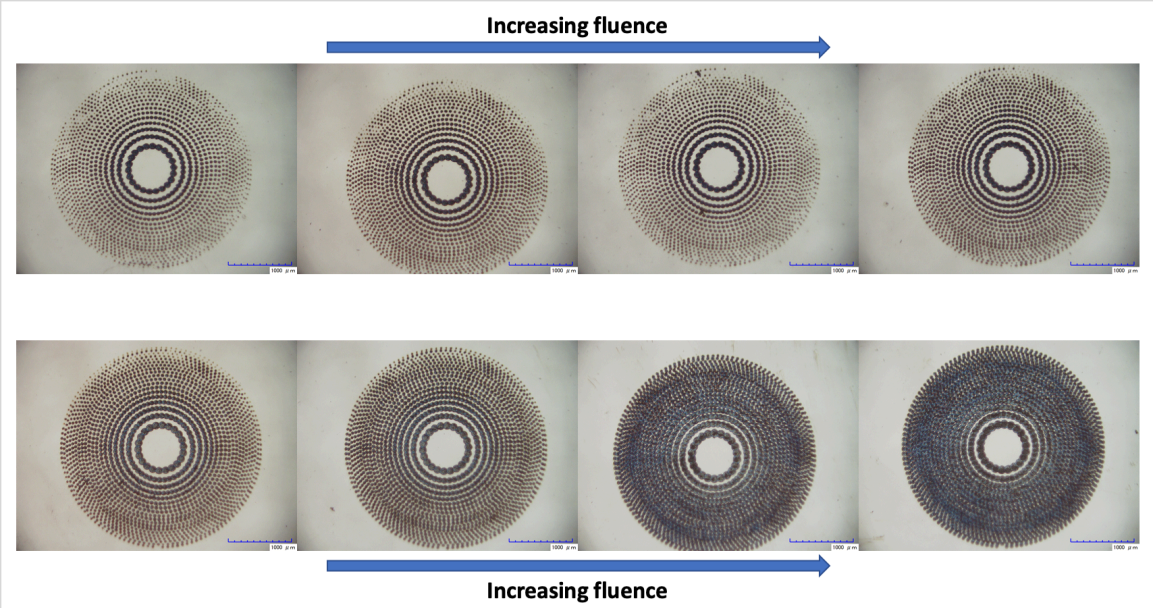

Figure 5: Effect of laser fluence on photon sieve pattern quality in Cr films. Fluence was varied from 1.53 to 3.06 J/cm2.

Fig. 5 shows photon sieve patterns written in 150 nm Cr films on soda lime glass substrates at various incident fluences. As can be seen in the figure, at lower fluences the inner photon sieve pinholes appear to be relatively clean marks, but outer pinholes are underdeveloped, and features are not fully ablated. As the fluence is increased, out features become fully present, but the increased HAZ associated with increased fluence caused negative effects on inner pinholes. Features overlapping, film cracking, and substrate damage were observed in inner pinholes, as is shown in Fig. 6. To alleviate these issues, thinner Cr films were tested in order to reduce the amount of material being ablated, and thus lowering the necessary laser fluence to achieve clean features. However, 50 nm and 100 nm of Cr were shown to have fairly high transmission at 633 nm, making them inappropriate for amplitude-modulation-based lensing applications. An example of a clean marked Cr photon sieve is shown in Fig. 7. This sieve showed fair surface quality, although several cracks in the Cr

film were present as shown in the figure. However, the increased optical throughput of the Cr film diminished the focusing properties of the photon sieve. From this point, Ag films were investigated.

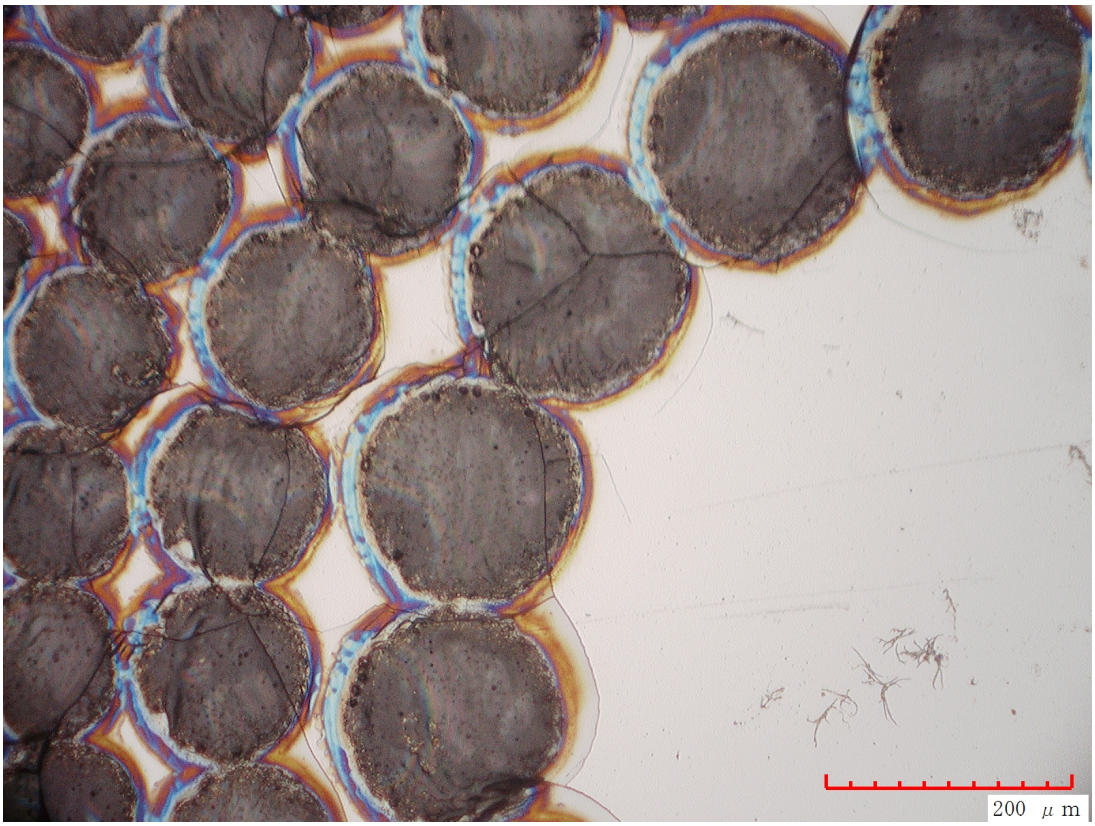

Figure 6: Inner rings of the Cr photon sieve at high laser fluences, showing overlapping features and cracking as a result of the increased thermal stress and HAZ associated with higher fluences.

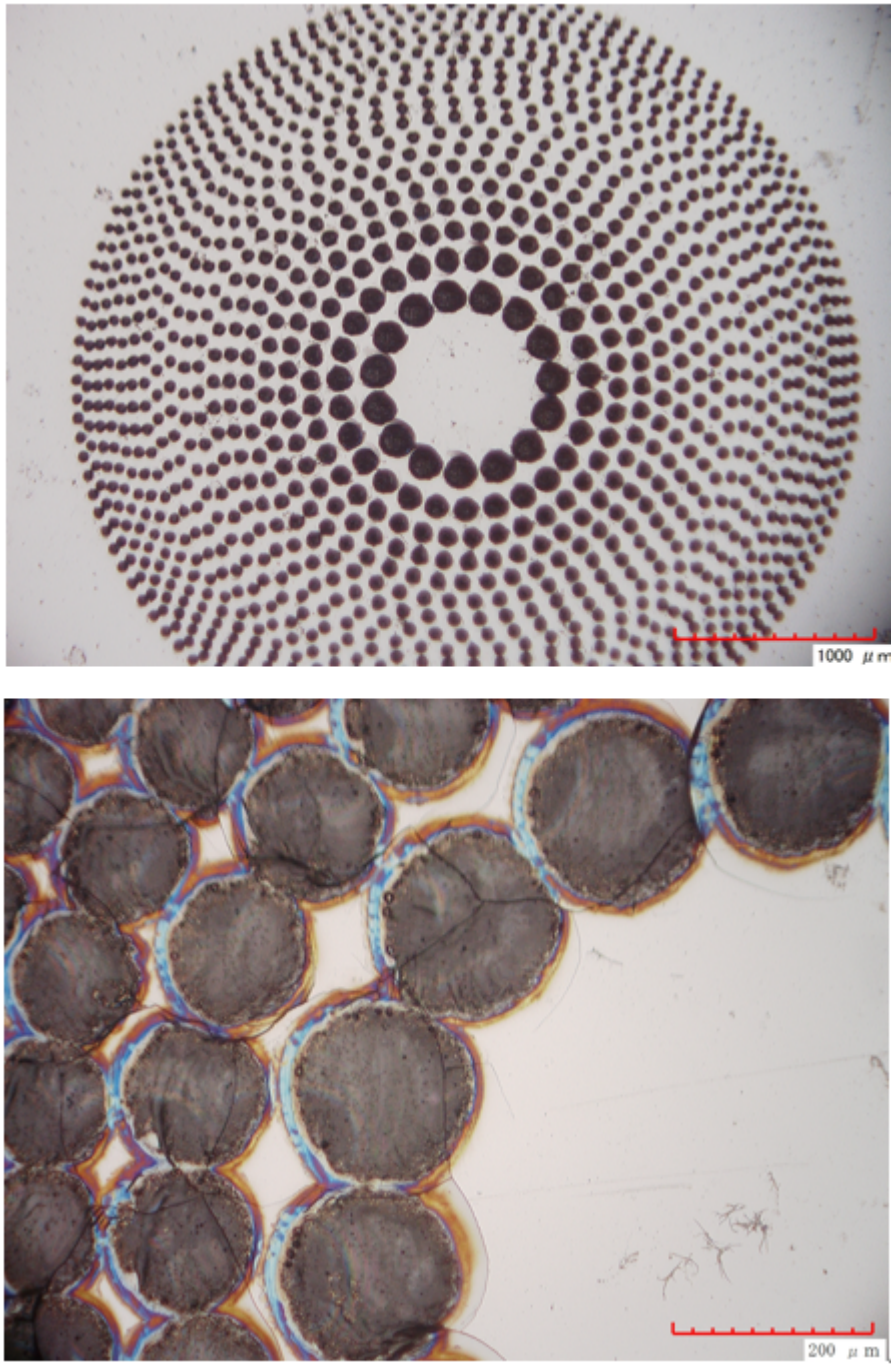

Figure 7: Photon sieve written in 50 nm thick Cr film. Overview of the full device (top), and inner rings showing film cracking and damage (bottom).

For Ag experiments, 50 nm of Ag was deposited onto soda lime glass, which was cleaned using the same procedure are described for Cr samples. Laser scanning speed and rep rate were fixed at 50 mm/s and 600 kHz, respectively, using the 532 nm laser system.

The fluence was increased to a range from 5.09 to 7.62 J/cm^2, as Ag exhibits higher reflectivity than Cr at 532 nm, and thus requires a higher laser fluence to achieve ablation. A photon sieve written at 5.09 J/cm^2 is shown in Fig. 8. As is seen in the figure, the film is much cleaner and pattern of a much higher quality when compared to the Cr photon sieves. Additionally, 50 nm of Ag was measured to have only ~2% optical transmission at 633 nm, making it sufficiently opaque for amplitude-based lensing applications such as photon sieves.

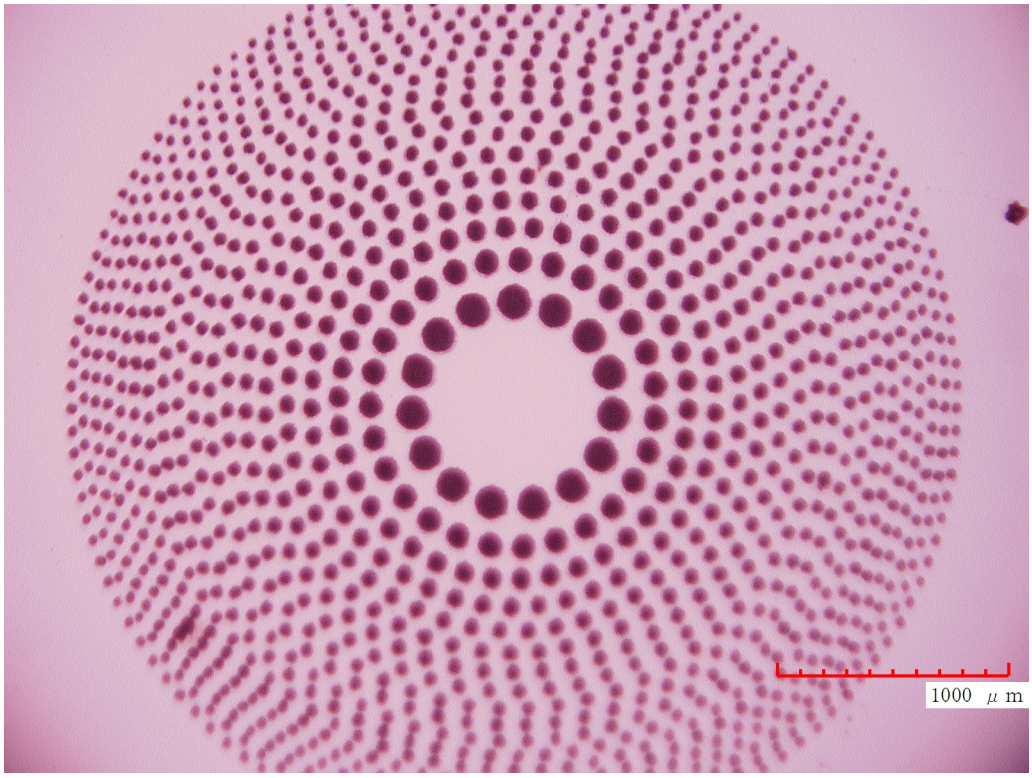

Figure 8: Photon sieve written at 5.09 J/cm^2 in 50 nm thick Ag film. The film is fully intact and sufficiently opaque, unlike the Cr counterparts shown previously.

The difference in mark quality can be attributed to the lower vaporization temperature of the Ag, as well as the presence of a melting phase. In Cr, the material sublimates, which could cause increased mechanical stress to the surrounding areas. It is also a brittle material and can oxidize at high temperatures. Additionally, the higher vaporization temperature

requires a higher laser pulse energy, which generates a larger HAZ, which has negative effects on the quality of the mark.

As a result of the research discussed in this section, Ag was found to be superior to Cr for the purposes of laser ablation processing of photon sieves, due to its high opacity in thin layers (i.e. shallow skin depth at optical frequencies) and relatively lower vaporization temperature. As a result, Ag was chosen as the material to use moving forward in the following section. However, the following section will use a 1064 nm laser as opposed to 532 nm. This change occurred as a matter of convenience. The 532 nm laser used in section 5.1 is located at UVA, whereas the 1064 nm laser was built shortly after the presented research was concluded, and is located at NIA, where the researcher is located. As a result, the 1064 nm laser was utilized for the following section. A similar fluence optimization was carried out for 50 nm of Ag as was presented in section 5.1. Optical microscope results of said fluence test are shown in Fig. 9.

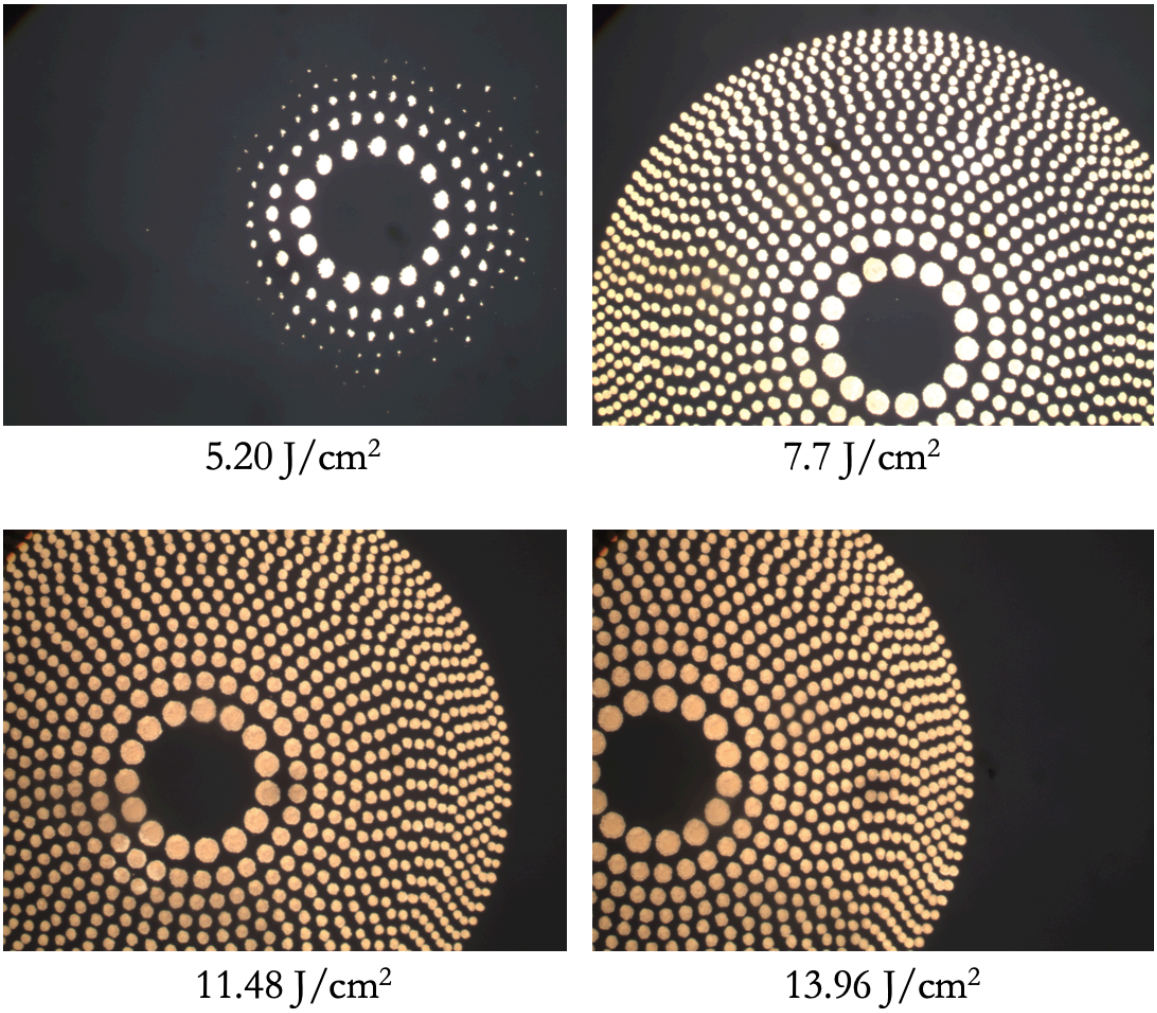

Figure 9: Photon sieves written in 50 nm of Ag on soda lime glass using a 50 ns, 1064 nm pulsed laser at 30 kHz rep rate. The laser beam was scanned at 100 mm/s. Incident fluences are listed below each pattern.

5.2 Experimental setup and fabrication

In order to demonstrate the efficacy of the laser ablation method for fabricating photon sieves, experiments began with simple amplitude type devices. The setup consisted of a 1064 nm wavelength ytterbium fiber laser (IPG Photonics YLP-RA-1-50-30-30), with a pulse width of 50 ns, pulse repetition rate of 30 kHz, and an average output power of 9W. The beam was then expanded before entering a galvanometric scan head (Sino-Galvo JD2206) fitted with an f-theta lens of 100 mm focal length. The beam was scanned at 100

mm/s. The focal spot diameter was approximately 35 μm. Therefore, the laser delivered 1 pulse/μm on the sample surface, and the laser fluence was 62.36 J/cm^2 at the surface (2.02 J/cm^2 absorbed by 96.5% reflectivity Ag at 1064 nm wavelength). The laser and scan head were controlled simultaneously via a commercial control board and software (Lanmark Controls Maestro3000). The total time to produce a 30.22 mm^2 sieve was tens of seconds.

In order to produce filled circles, the software raster scans the beam with a given line-line spacing distance. For this experiment, the raster line-line spacing distance was set to 10 μm in order to produce sufficient overlap between the scan lines and ensure that the full pinhole area is ablated.

Amplitude photon sieves were fabricated in a 50 nm thick Ag film on a soda lime glass substrate. Ag/glass samples were fabricated in the optical cleanroom at NASA LaRC. Prior to deposition, the glass slides were cleaned via subsequent sonication in acetone, IPA, and DI water for 10 minutes each. The slides were then blown dry with compressed air. Ag films were then deposited via DC magnetron sputtering, and thickness was monitored via the sputtering system thickness monitor. The optical transmission of the films at 633 nm wavelength was found to be ~2%. In order to reduce this transmission to near zero, metal films with higher reflectivity and or shallower penetration depth could be used. However, no such materials were available in our sputtering system. Furthermore, a thicker Ag film could be used. This was tested, and 100 nm thick films were used as well. However, the increased film thickness required a significantly higher laser power to fully ablate, which in turn increased the size of the in-plane heat affected zone, which caused adjacent features to blend together instead of forming distinct pinhole structures. This issue could be

mitigated by the use of a shorter pulse laser system, which will be able to ablate thicker films while maintaining a minimized HAZ.

5.3 Photon Sieve Tolerance to Angle of Incidence, Temperature, and Illumination Light Bandwidth

An SEM image of the fabricated photon sieve is shown in Fig. 10, along with and SEM image showing the pinhole edge morphology. As can be seen in the figure, the edge of the pinhole is not smooth. This is attributed to the tails of the Gaussian laser beam having energy near the Ag film ablation threshold, which results in a partial ablation and melting of the film in that region. As will be seen in the results of this section, this morphological imperfection seems to have to ill effect on the photon sieve performance, thus giving some idea of fabrication tolerances for future devices. This partial ablation effect can be mitigated in several ways. Most practically, using a smaller diameter laser focus will increase the edge resolution of the features, and beam-shaping optics can be used to convert the Gaussian beam shape into a flat top intensity distribution. A shorter laser pulse width can also be used, as the shorter pulse width can help prevent melting at the edge of a mark [57, 58].

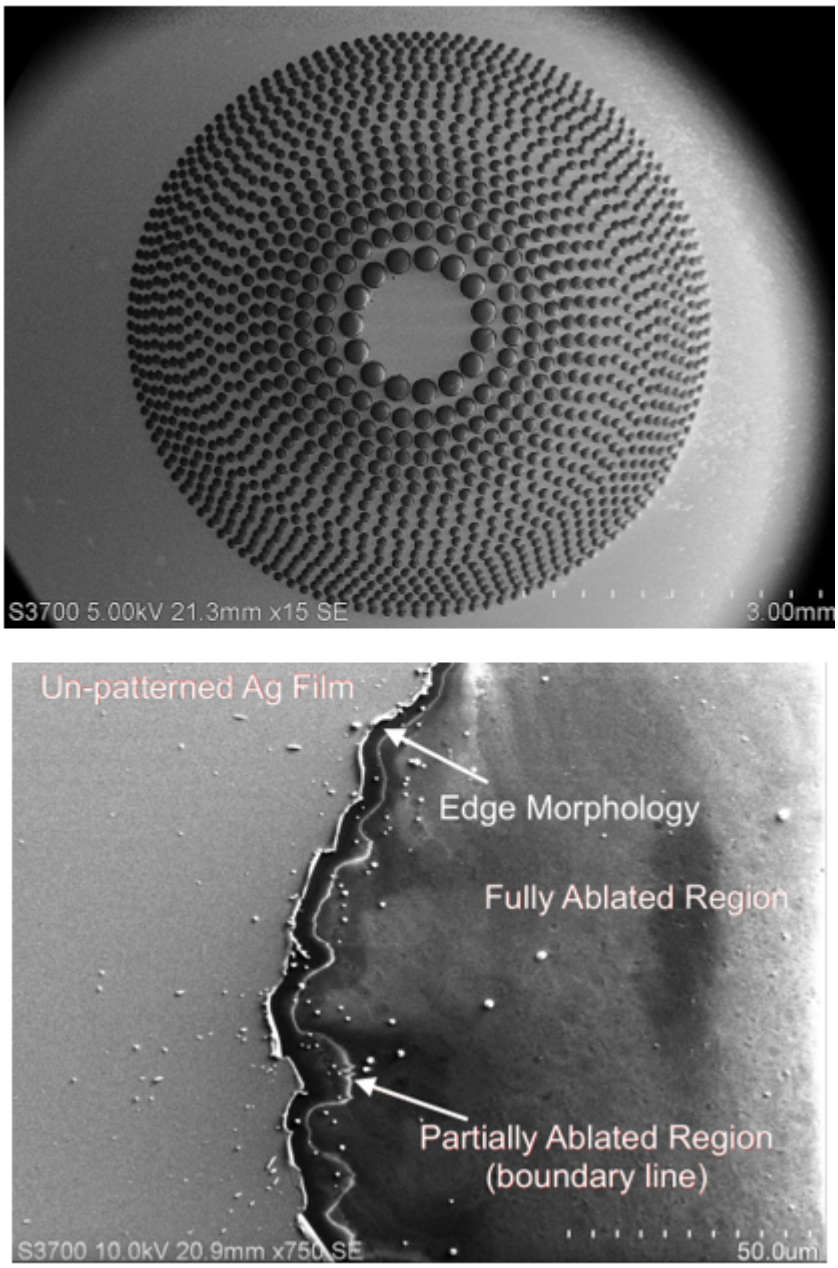

Figure 10: SEM image of the fabricated amplitude photon sieve (top) and the partial ablation region of the photon sieve pinhole edge [56].

Furthermore, ablated Ag particles ranging in size from a few microns to sub-micron were spattered about the photon sieve surface. However, the pinholes themselves stayed

fairly clear. Additionally, a vacuum nozzle was used to blow the ablation plume away from the sample surface in order to minimize re-deposition of ablated particles.

Photon sieves were characterized optically in terms of their focusing efficiency, focal point FWHM, angle of incidence tolerance, temperature, and illumination wavelength. Modeled results were also obtained for all parameters but temperature and angle of incidence, due to limitations in the MATLAB code.

Under design illumination and normal incidence, the photon sieve focal point was measured as 45.12 ± 0.74 μm, which is very close to the simulated value of 44.59 μm. The measured focusing efficiency was measured as 1.1995% ± 0.0025%, which is also in strong agreement with the simulated value of 1.275%. In order to ensure the accuracy of the efficiency measurement, a background signal was taken to account for the light directly transmitting through the Ag film. This background signal was then subtracted from measured data before efficiency was calculated. A line plot of the measured and simulated intensity distributions, along with background signal, are shown in Fig. 11.

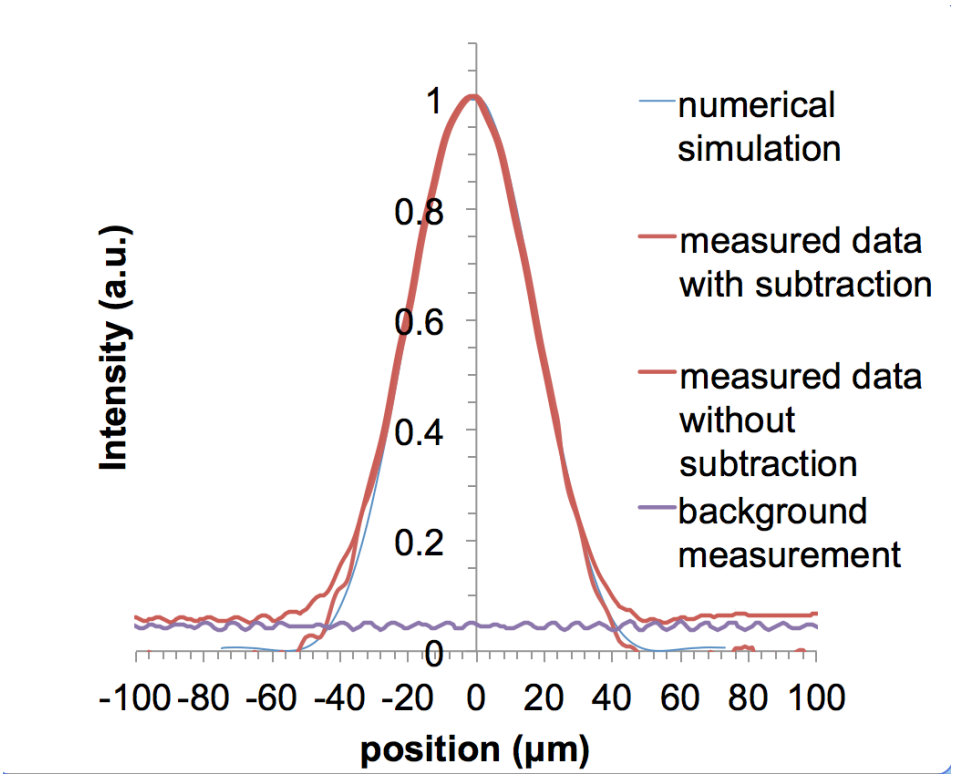

Figure 11: Plot of measured and simulated photon sieve x-axis intensity profile, along with background signal and pre-subtracted focal point data. All values are normalized to 1 [56].

Photon sieve angle of incidence (AOI) tolerance tests were also performed. AOI data was taken at various increments between 0° and 30°, with data being taken every degree from 0°- 6°, and every 2 degrees thereafter. FWHM and focal point intensity data at various AOI are summarized in Fig. 12. As can be seen, the sieves are fairly robust between angles of 0° and 5°, but performance rapidly degrades at AOI greater than 5°.

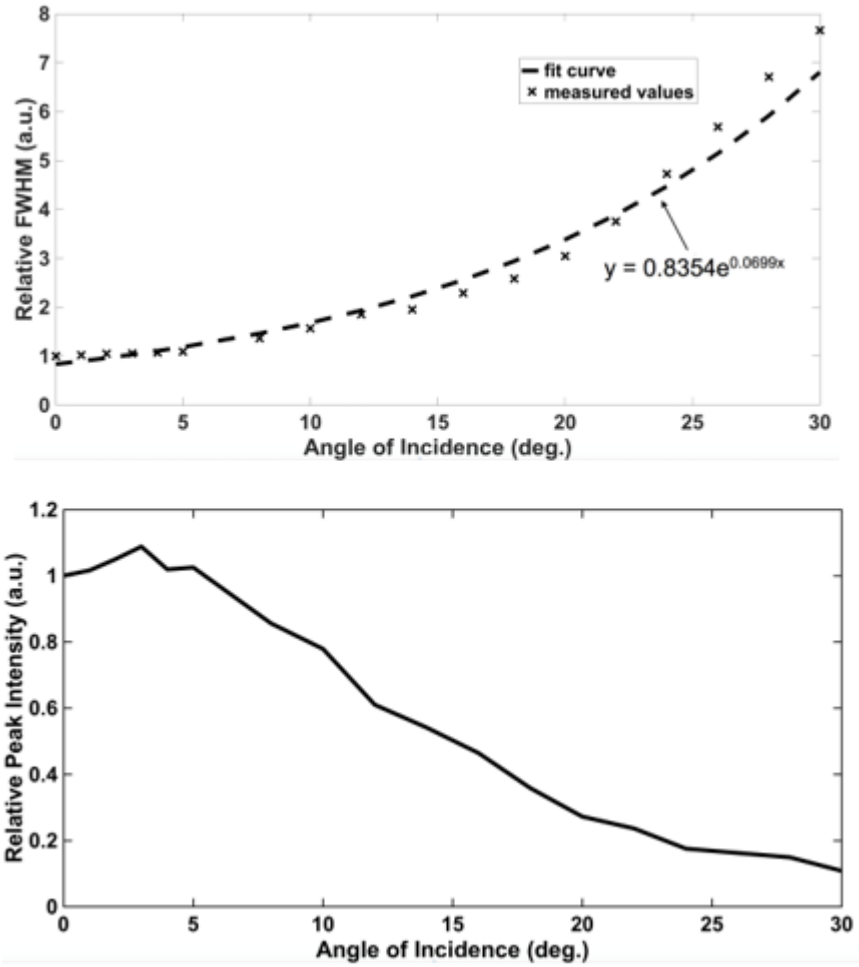

Figure 12: Plots of relative change in photon sieve FWHM (top) and relative peak intensity as a function of incidence angle. It can be seen that photon sieve performance does not change significantly angles below 5° [56].

Illumination bandwidth tests were carried out in order to understand the effects of chromatic aberration on the photon sieves, as DOEs are inherently susceptible to such chromatic effects. Some efforts prior to this work had been made to compensate for these issues in the form of photon sieves divided up into zones designed to focus different wavelengths to the same focal plane [59, 60]. However, these photon sieves are only achromatic at their design wavelength, and focusing efficiency is reduced by a factor of the number of zones (i.e. a three-wavelength sieve will see 1/3 the efficiency of each

wavelength compared to a single sieve operating at one wavelength). Additionally, other groups have carried out studies related to the development of partially achromatic photon sieves by generalizing the design and employing novel parameter optimization techniques to perfect achromatic design [35-37]. However, these designs are only broadband over a range of tens of nanometers unless integrated with a refractive optic.

Laser diodes operating from 633 nm to 638 nm were used to quantify the effects of off-design illumination on photon sieve focal point properties. The results are summarized in Fig. 13 and are compared with simulated values. As it can be seen, traditional photon sieves are very intolerant to illumination bandwidth both in terms of efficiency and focal point size.

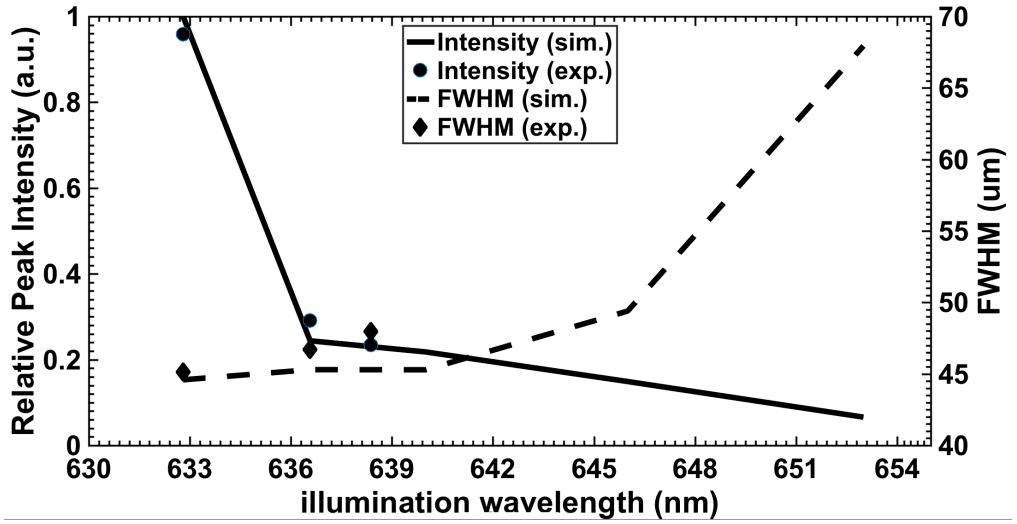

Figure 13: Plot of illumination wavelength vs. focal point FWHM and intensity. At $\Delta\lambda > 7$ nm, optical performance degrades rapidly [56].

Lastly, the effect of substrate temperature on photon sieve performance was studied. It is known that photon sieve performance is less dependent on the size of the pinholes, and strongly dependent on the ability to exactly center each pinhole at the edge of the corresponding Fresnel zone [25]. Therefore, care should be taken to fabricate photon

sieves on substrates with low thermal expansion coefficients. In our tests of Ag/glass photon sieves, temperatures from room temperature to 100°C showed no effect on photon sieve performance. This is due to the low CTE of glass. However, if temperatures were made sufficiently high, then the relative CTEs of glass and the film need to be considered, as delamination could become an issue. This is especially important for space-based applications, where temperatures can swing from -120°C to 120°C for normal materials, and higher temperatures can be seen by materials with high absorptivity and low infrared emissivity values [61].

5.4 Conclusion

Based on the work presented in this section, new insight has been gained into the fabrication and optical tolerances of photon sieves. A material study was performed, and it was found that Ag is preferable to Cr for laser ablation fabrication of photon sieves in terms of both morphology and optical performance. Photon sieves were shown to be robust in terms of low AOI deviations, but intolerant to variations in illumination wavelength. All photon sieve measured values agreed well with simulations. Furthermore, the efficacy of laser ablation fabrication of photon sieves was demonstrated, and this method was used throughout the remainder of this work.

Chapter 6: Laser Fabrication and Characterization of Binary Phase Photon Sieves on Flexible Polyimide Substrates

In order to demonstrate the feasibility of the laser ablation fabrication technique on lightweight, space qualified materials for cubeSat applications, while simultaneously improving the efficiency over amplitude type devices, binary phase photon sieves were investigated on transparent polyimide substrates. A similar approach was taken in this chapter as chapter 5. Initial studies were carried out to determine the appropriate material to use for final devices based on their compatibility with the laser process and optical performance, and tradeoffs were identified. As polymers are less absorptive in the visible spectrum, if they absorb at all, an ultraviolet source was used for photon sieve fabrication. Polymer chains typically are strongly absorbing at wavelengths below 400 nm, as the organic bonds tend to have bonding energies similar to the ultraviolet photon energy given by $E = hf$. Then, modeling was performed to predict the focusing behavior of the photon sieves. Fabricated photon sieves were then characterized and compared to numerical results.

6.1 Choice of Material

Initial studies were carried out on a NASA polyimide substrate known as Colorless Polyimide v2, or CP2. CP2 is an attractive material candidate due to its extremely high optical transmission across the visible spectrum (CP2 is clear and colorless with virtually no haze), and its space-qualified material status at NASA. CP2 samples were mounted on soda lime glass substrates and were held flat by their own static attraction to the glass substrate. The edges were secured and pulled taught using tape in order to attempt to avoid

potential shifting or wrinkling of the polymer film during the laser process. Because polymers absorb very strongly in the ultraviolet, as well as have long electron thermalization times, only a very low laser fluence is required to achieve ablation. For these experiments, fluence values began at ~0.3 J/cm^2 and were stepped up in 1% increments as necessary by controlling the average output power through the laser software.

An image showing a fabricated photon sieve on CP2 is presented in Fig. 14. As can be seen in the figure, significant wrinkling occurs during the laser process. This is attributed to an apparent thermal instability of the polyimide at high temperatures, such as those created during laser ablation. Additionally, it was also observed that CP2 is easily carbonized at these temperatures, which is also shown in Fig. 14. The CP2 marked areas appear black, and the material is badly damaged even at very low fluences. Optical profilometry was used to answer whether lower fluences are capable of producing clean marks. However, as shown in Fig. 15, it was seen that at fluences low enough to not carbonize the CP2 film, etched areas were very rough, and overall mark quality was poor. At low fluences, nearly no etching was present. As fluence was slightly increased, intense wrinkling and even the presence of through-holes can be seen.

From CP2, the material choice was shifted to DuPont Kapton™ (hereafter referred to as simple "Kapton"). From an optical standpoint, Kapton is inferior to CP2, as it has a slight haze and a yellow tint, which is indicative of optical absorption at wavelengths above ~500 nm [62]. However, Kapton exhibits no known melting temperature and extreme thermal stability [63], making it an attractive option for laser ablation processing.

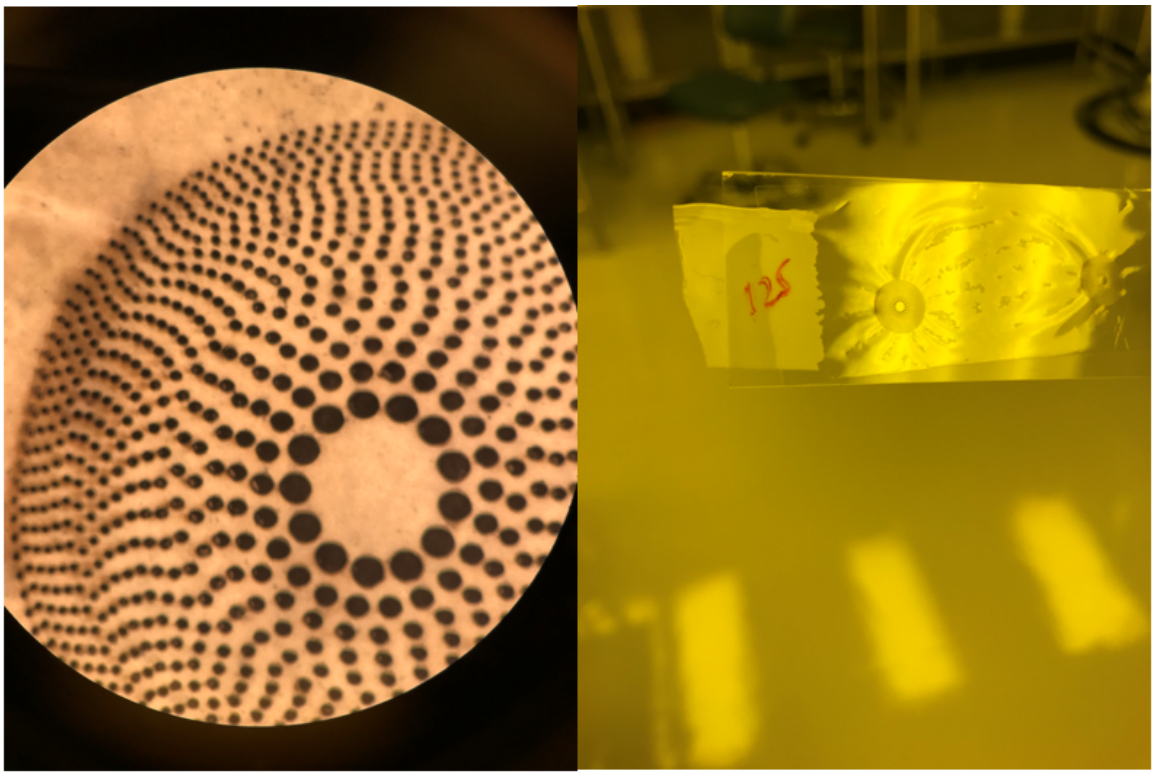

Figure 14: Optical microscope image (left) and cell phone camera image (right) of the CP2 sample showing carbonization and wrinkling at low laser fluences.

Laser ablation of Kapton was studied in the same systematic way as CP2, where a low fluence was used to begin and laser energy was increased by 1% increments. Optical profilometer and microscope data were taken at each power to see the effect of the laser energy on the mark quality. Once Kapton was proven robust to the laser processing, the effect of the number of pulses (scanning speed) was investigated, as it was found to be a bit more consistent and easier to control than sweeping laser power. A representative image and profilometer scan are shown in Fig. 16. Despite the decreased optical transmission and clarity of Kapton compared to CP2, experiments were moved forward using Kapton as it is far more compatible with the laser ablation process. Additionally, despite slight haze

and yellow tint, Kapton is still sufficiently transmissive at 633 nm, which is the design wavelength used for the photon sieves in this work.

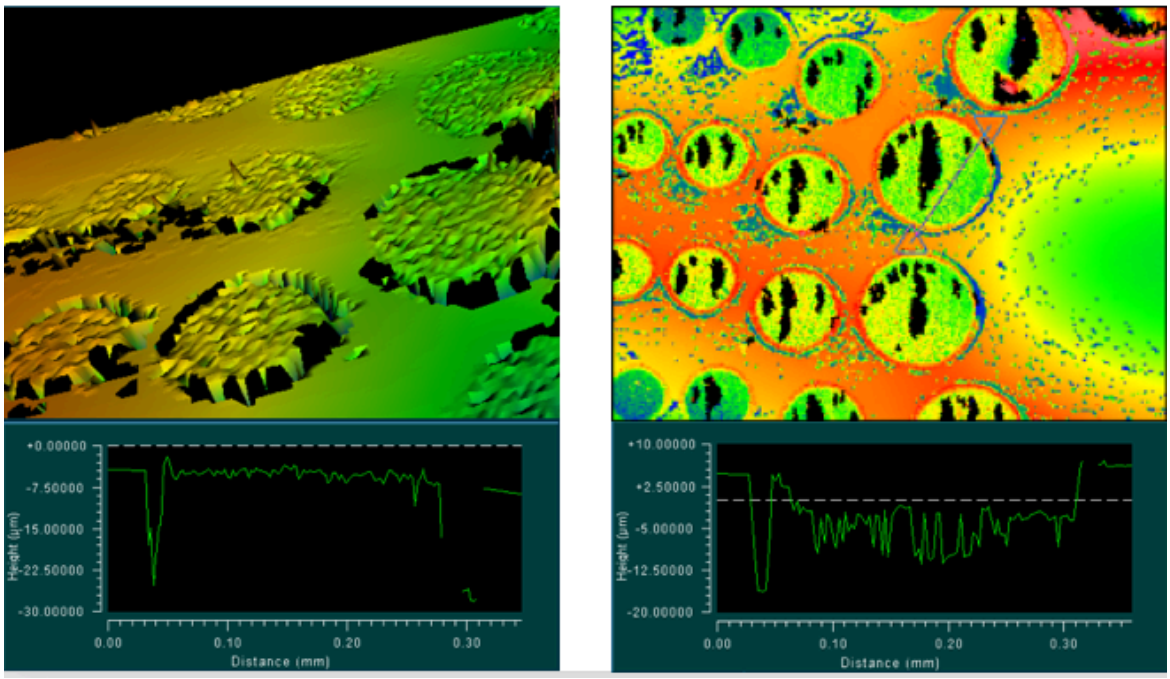

Figure 15: Optical profilometer images are shown for CP2 marked surfaces at fluences just above the ablation threshold (left), and slightly increased (right). Marks show high surface roughness, through-holes, and a heavily wrinkled substrate. All of these are evidence of CP2 being incompatible with the laser process used in this work.

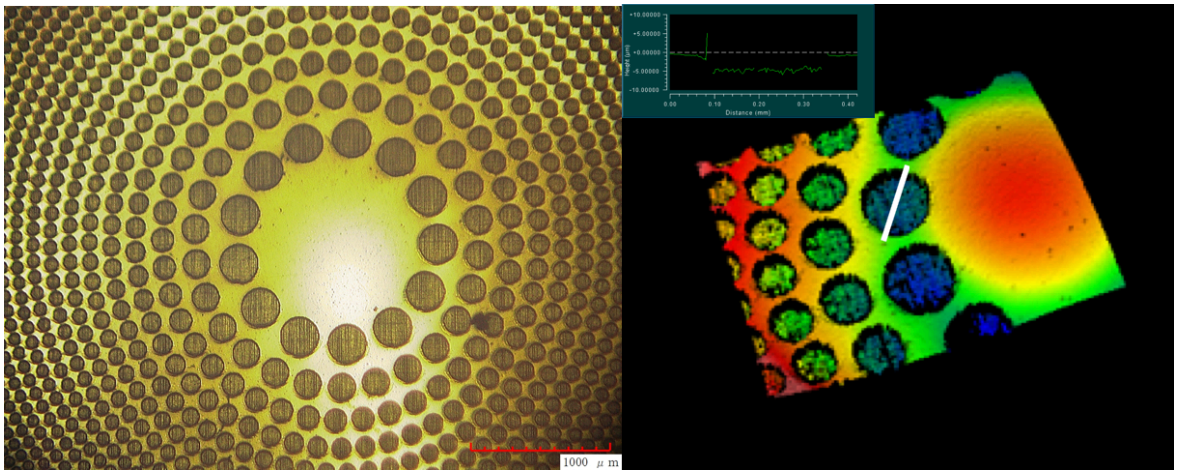

Figure 16: Optical microscope and profilometer images showing a representative Kapton photon sieve. Surface morphology and flatness is significantly improved over CP2 samples.

6.2 FDTD Modeling Results

In binary phase devices, the entire device area is transparent, and the "destructive" zones are patterned such that a half-wavelength phase shift is introduced. In general, for an N-level diffractive optic, the etch depth required for each step is given as

$$d_{etch} = \frac{(2m+1)\lambda}{N(n_{sub}-n_{env})}, \tag{20}$$

where n_{sub} and n_{env} are the refractive indices of the substrate and surrounding environment, respectively, and m is an integer. In the case of a binary phase device (N = 2) operating at 633 nm wavelength in air, etched into a substrate of n = 1.7 [63], this gives an etch depth of 0.452 μm.

Before binary phase photon sieves were fabricated, the scaled-down dimensions were simulated using FDTD methods. A photon sieve composed of two rings, a 10-μm focal length, a total diameter of 11.4 μm, and an operating wavelength of 633 nm was used for the simulations. The photon sieve patterned region was represented by an etch depth of 0.452 μm in a dielectric substrate of n = 1.7 [63]. Electric field distribution in the focal plane and along the optical axis of the simulated photon sieve is shown in Fig. 17. For the purposes of these experiments, only focusing efficiency was calculated (since FWHM will be drastically different for a device with such small dimensions). A theoretical efficiency of 11.4% was obtained for the optimally patterned binary phase device. Other devices were simulated in order to model the effect of fabrication errors (etch depth error) on focusing efficiency. These results will be summarized and compared to experiment in section 6.3.

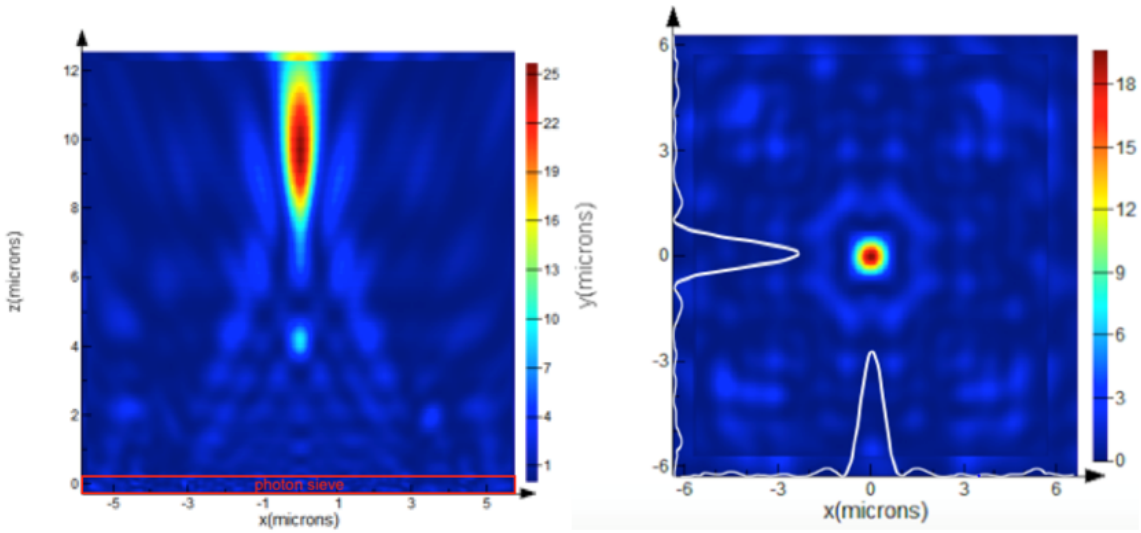

Figure 17: E-field intensity distribution along the optical axis (left) and in the focal plane (right) of the simulated photon sieve [16].

6.3 Experiment and Results

The experimental setup used is largely the same as that described in chapter 5. The main difference is the laser used and the size of the focused laser beam. In this chapter and the next, a laser of wavelength 355 nm, pulse width 25 ns, pulse repetition rate of 20 kHz, and focused spot size of ~ 15 μm is used. In addition, due to the large UV absorption of polyimide materials, a neutral density filter of OD 0.3 was placed into the laser beam path in order to prevent destruction of the substrate. The final laser fluence value at the substrate was 0.64 J/cm^2. In this experiment, commercially available Kapton polyimide substrates were used. Substrates were cleaned with acetone and DI water prior to processing. Furthermore, photon sieves were designed such that the rings were maximally filled with pinholes. This resulted in ~48% of the total device area being patterned to the proper phase, which in return leads to an enhanced focusing efficiency [63]. The total fabrication time for a 30.22 mm^2 photon sieve was tens of seconds.

Laser scanning speed at a fixed fluence (0.64 J/cm^2) was varied, and a plot was generated to understand the effect of the number of pulses per area on etching depth and surface roughness of the ablated regions. Plots of these quantities are shown in Fig. 18. The laser processing parameters were optimized to obtain a circa-wavelength surface roughness of the processed area at around 50% overlap between adjacent pulses. Minimal surface roughness is required for ideal optical performance and can be further reduced by altering laser pulse width and wavelength [64-66]. As previously mentioned, reducing the laser pulse width will reduce the thermal effect of the light-matter interaction and reduce the HAZ seen on the sample. Additionally, in the case of polymers, the laser wavelength is the key parameter governing the surface roughness of the ablated area [64]. Whereas most insulating materials have a single bandgap associated with their optical absorption, the multitude of different chemical bonds present in polymers all have different bond energies, and thus absorb light differently. When using a near-UV laser (such as 355 nm), only some of the polymer bonds are directly vaporized via photolytic processes, and ablation of the surrounding bonds is achieved as a result of heat diffusion and photothermal processes. These thermal processes can lead to surface roughness, as one would expect [64, 66]. If the laser wavelength is reduced, the incident photons will have a higher energy, and thus more or all of the different chemical bonds can be directly ablated via optical processes, resulting in a lower surface roughness.

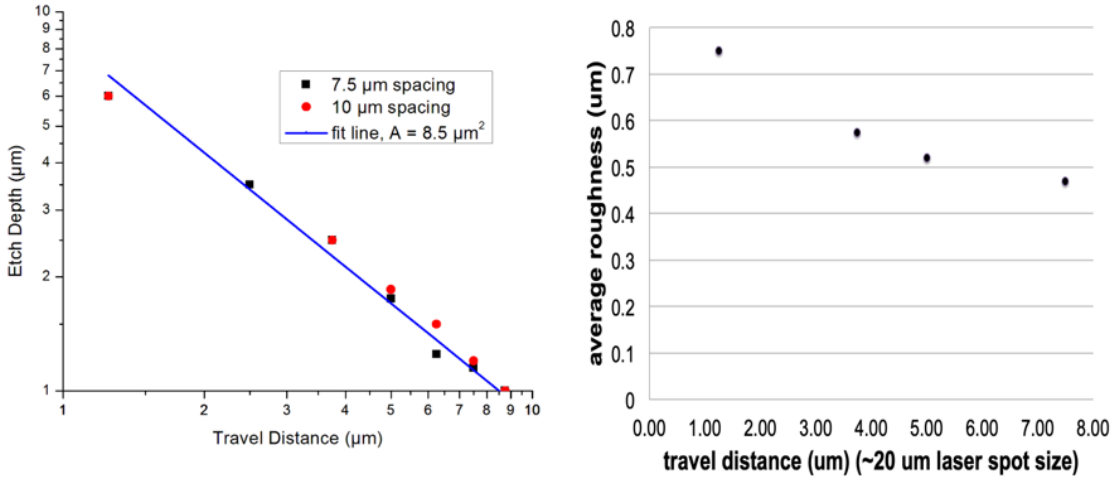

Figure 18: Plots showing the effect of distance between laser shots (scanning speed) on etch depth (top) and surface roughness (bottom). The line spacings shown in the plots refer to the center-center distance between adjacent raster scan lines. Surface roughness begins to level off at roughly 50% shot overlap for the laser system used in this study [16].

SEM images of the entire laser-fabricated device and an individual pinhole are shown in Fig. 19. An optical profilometer image of the laser-processed surface can be seen in Fig. 20.

Fabricated photon sieves were characterized in terms of their focusing efficiency and focal point FWHM. The focal point of the device can be seen in Fig. 21. The FWHM and focusing efficiency of this photon sieve were 65.9 μm and 9.5%, respectively. This focusing efficiency is in good agreement with the simulated value of 11.4%. Additionally, focusing efficiency was measured at various etch depth errors and compared with simulations. This gives an understanding of the effect of fabrication error on optical performance. As expected, focusing efficiency decreases linearly with error in etch depth. This is an intuitive result, since a linear error in etch depth is synonymous with a linear error in optical path length, and an error in optical path length is linear with the focusing efficiency of a diffractive phase grating. A plot of these results in given in Fig. 22.

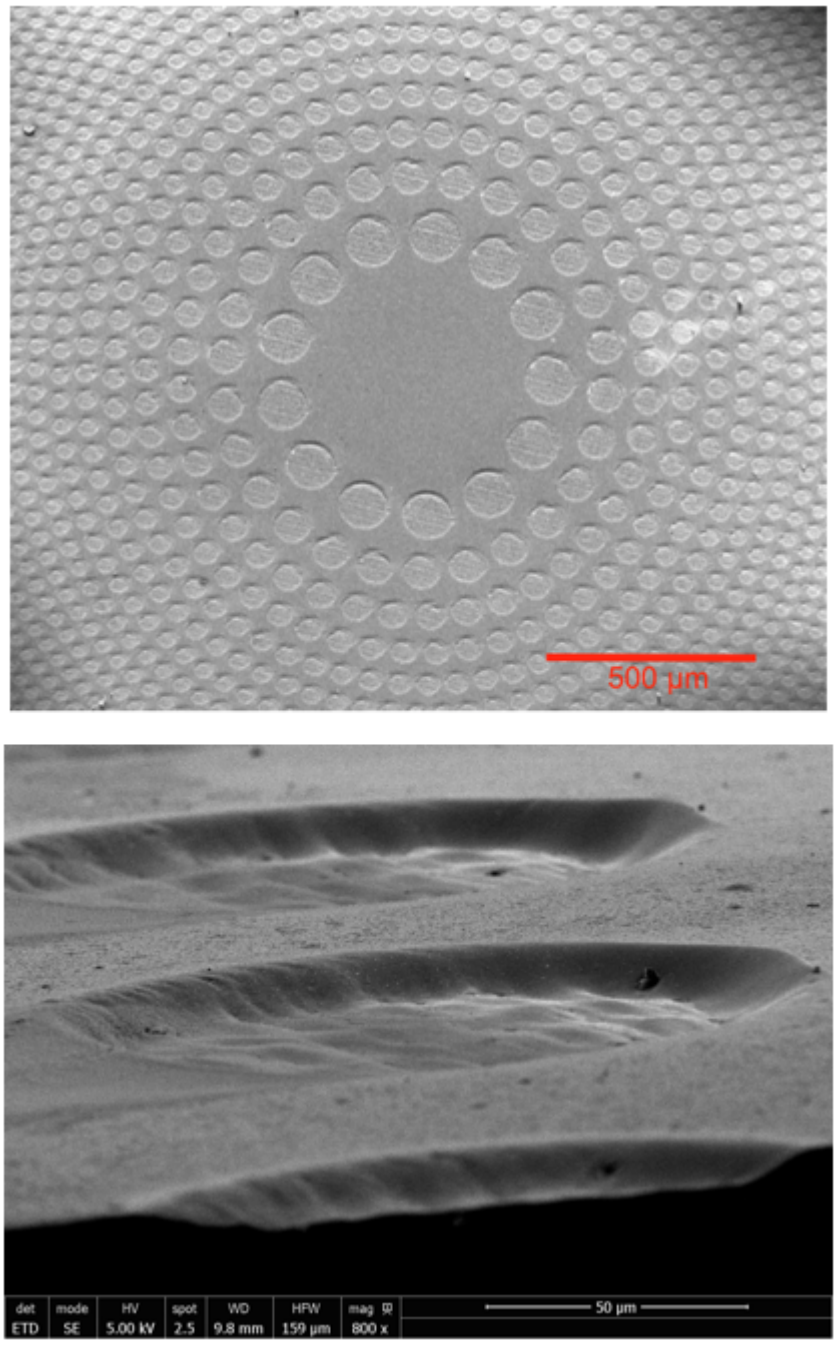

Figure 19: SEM image of the full binary phase photon sieve fabricated via UV laser ablation of polyimide substrate (top). Cross sectional and high angle view of a laser ablated pinholes in Kapton (bottom) [16].

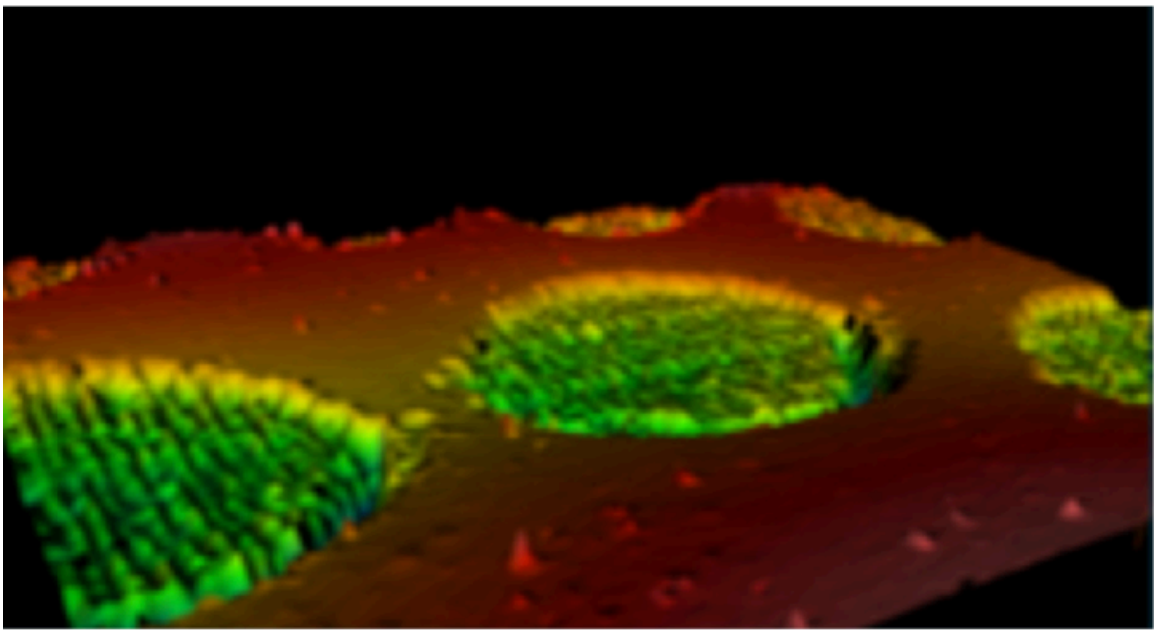

Figure 20: Optical profilometer scan of the innermost ring of the patterned polyimide surface. RMS surface roughness was measured as 469 nm [16].

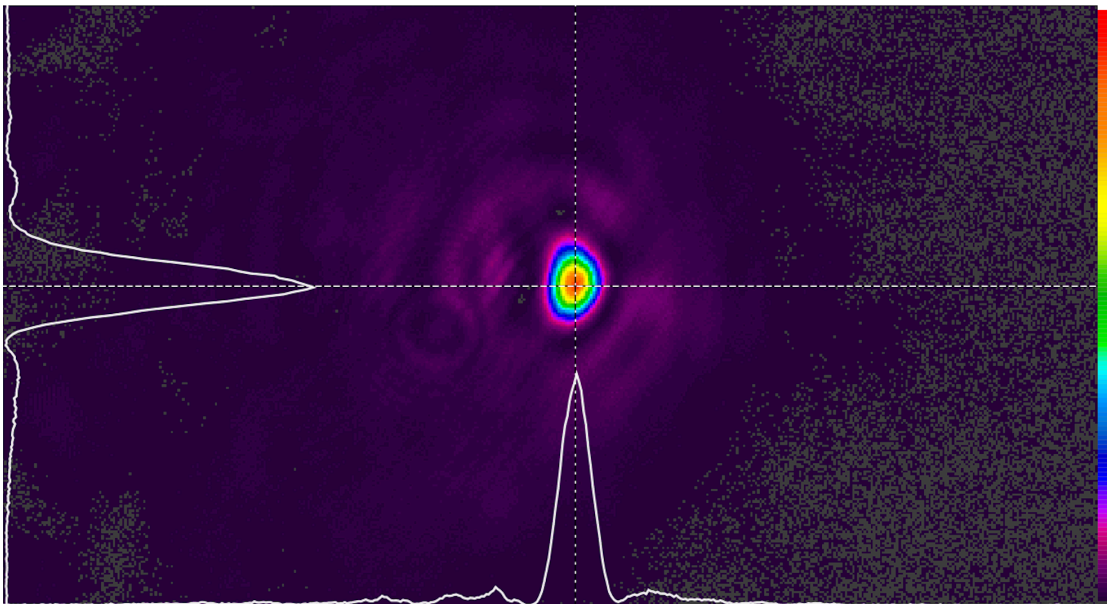

Figure 21: CCD detector image of the focal point of the optimally patterned photon sieve (FWHM = 65.9 μm) [16].

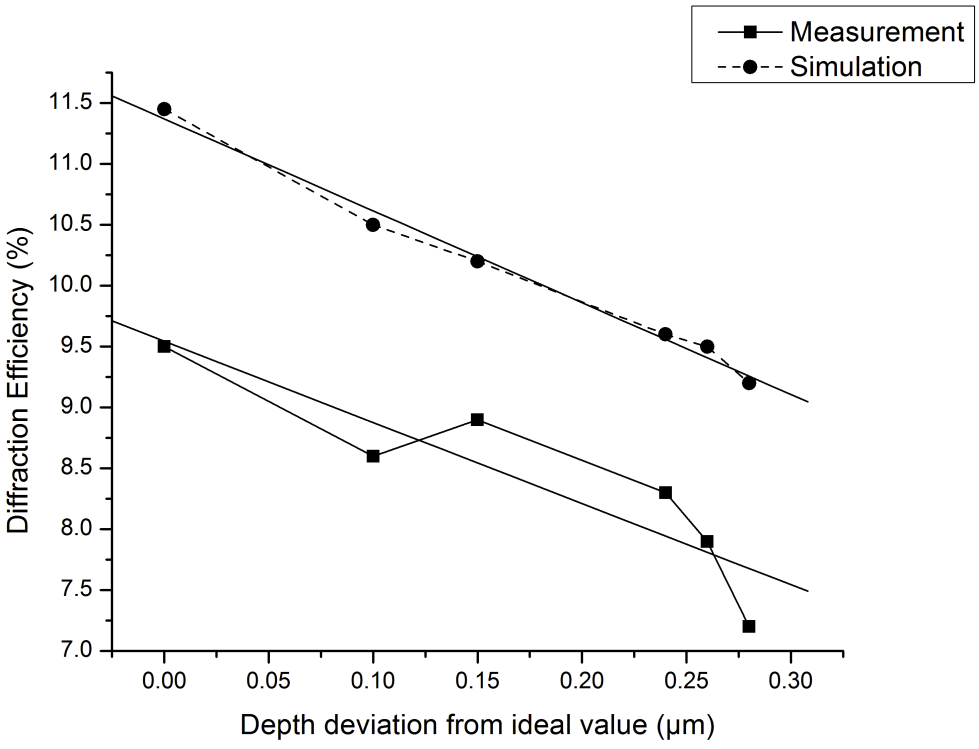

Figure 22: Plot of etch depth error showing the effect on measured and simulated focusing efficiency. Note the scale along the y-axis is altered to allow for better use of space [16].

Imaging capability of a binary phase photon sieve was demonstrated using the same setup as previous measurements, but with a scattering object (a 3x3 array of holes in a thin, nearly opaque, silver film) placed in the path of the incident laser beam. The captured image as seen by the CCD beam profiler is shown in Fig. 23 along with an optical microscope image of the object. The object and image distances were 368 mm and 330 mm, respectively, which corresponds to a theoretical magnification of 0.897, which agrees well with the observed magnification of 0.891.

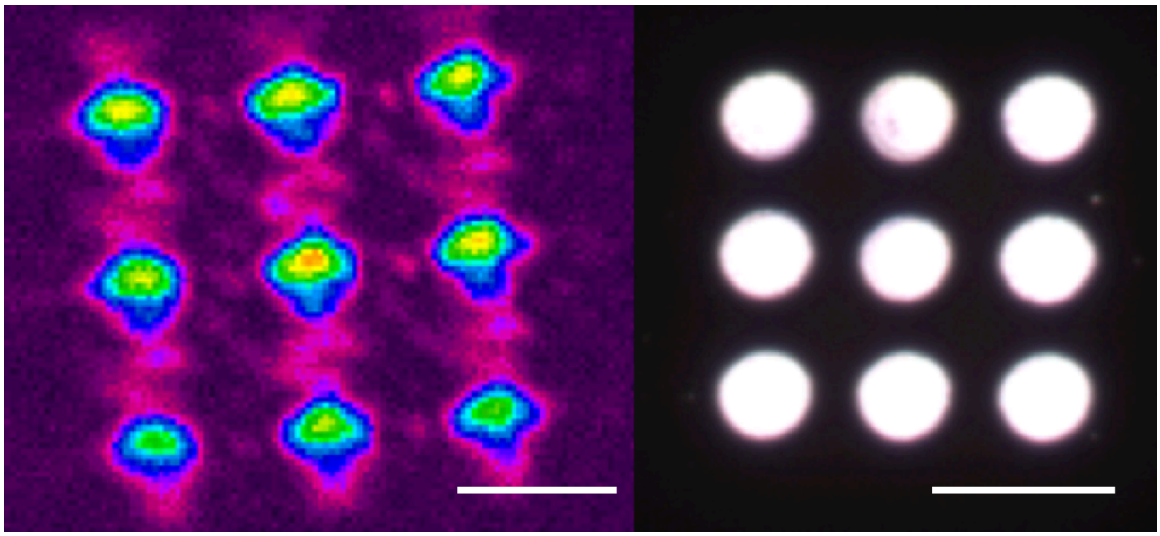

Figure 23: Image of pinhole array in Ag thin film captured using the photon sieve (left) and optical microscope (right). The measured and theoretical magnification values are 0.891 and 0.897, respectively. Each pinhole in the 3x3 array is 87 μm with a center-to-center distance of 115μm. The size of the photon sieve and microscope images are 287 μm and 322 μm, respectively. The scale bars in each image are 100 μm.

6.4 Conclusion

In this chapter, the efficacy of pulsed laser ablation fabrication of photon sieves on space-qualified polymer substrates was investigated. A systematic comparison between CP2 and Kapton polyimide substrates was performed, and Kapton was found to be more suitable for the laser ablation experiments going forward. A dependence between laser shot-shot distance and etch depth was determined and was in excellent agreement with theoretical predictions. It was also demonstrated that circa-wavelength surface roughness is attainable with nanosecond pulse widths, and it is postulated that shorter pulse widths could reduce roughness even further. Photon sieve optical properties were also measured and were in good agreement with FDTD simulations. The champion focusing efficiency of 9.5% matches the highest reported value for a photon sieve in the literature at this time, thus demonstrating that this fabrication technique is capable of generating devices that perform on par with standard lithography-fabricated optics, but with a much shorter, less

expensive, and more robust fabrication method. Additionally, the effect of fabrication error on focusing efficiency was simulated and measured.

Chapter 7: Laser Fabrication and Characterization of High-Efficiency Multilevel Phase Photon Sieves

In order for photon sieves to be more useful in various applications, the efficiency of photon sieves needs to be further increased. With the highest reported efficiency of a photon sieve being ~11% [30, 31], Fresnel zone plates are still more attractive for most applications, despite their reduced contrast. In order to address this, the concept of a multilevel phase device was explored, simulated, and experimentally validated. Although multilevel zone plates have existed for a number of years [67], the concept had not yet been extended to photon sieves prior to this work. Furthermore, the limit of photon sieve efficiency was previously unknown, and no way of predicting the efficiency existed outside of numerical simulations. In this section, in addition to developing the multilevel photon sieve concept, we address the issue of photon sieve efficiency, and analytically show that the efficiency asymptotically approaches an upper bound for high step number devices.

7.1 Design of Multilevel Photon Sieves

Like traditional photon sieves, multilevel sieves are based on the concept of the Fresnel zone plate. To briefly explain the concept of a multilevel phase photon sieve or zone plate, consider the way the Fresnel zones were initially defined. The zone radius r_n is positioned such that the edge of the n^{th} zone has a half-wavelength phase shift from the optical axis. Then, the entire zone is considered to be at the proper phase. However, this is fundamentally false, as the zone has a non-zero width, and therefore as we move from the inner zone edge to the outer zone edge, each point that we pass by has a different path length to the focal point, and therefore a different phase. In a multilevel phase device, rather

than shifting the phase of an entire zone by a constant value, we divide the bright-dark zone pairs into N sub-zones and shift each sub-zone by an amount λ/N given in equation (9). As N grows large, this results in each point in each bright and dark zone being shifted by exactly the right amount to constructively interfere at the focal point, which results in a drastically increased efficiency. In the case of a reflectionless zone plate, this efficiency approaches 100% [67]. And image describing the multilevel phase device structure is shown in Fig. 16 [68].

In order to design a multilevel zone plate (MLFZP) or multilevel photon sieve (MLPS), the following equation is used to calculate the radius of each N subzones [66]:

$$r_{n,N} = \sqrt{\lambda f(2(\frac{l}{N} + n - 2),} \tag{21}$$

where l is the index of each sub-zone and has values of $1 \leq l \leq N$. The diameters of the pinholes in each sub-zone are made to be as large as possible while avoiding overlap between subsequent sub-zones, and each zone is maximally filled with pinholes.

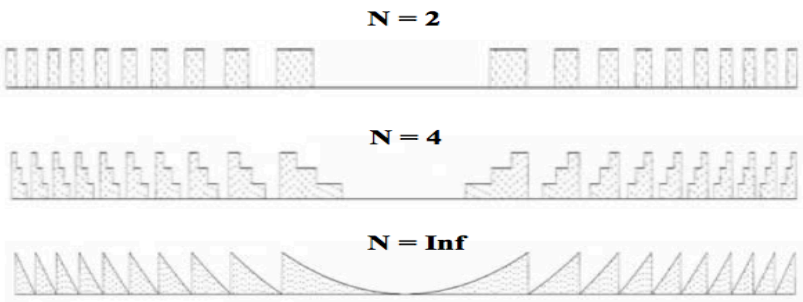

Figure 24: Comparison of various N values for a multilevel zone plate structure. Smaller N values approximate the continuous phase profile of a blazed grating, or kinoform, zone plate.

7.2 FDTD Modeling Results and Fundamental Efficiency Limit

Similar to the binary phase sieve described in the previous chapter, MLPSs were defined in the software by an etched area of index 1.0 in a dielectric substrate of n = 1.7, with etch depth for each N^{th} sub-zone given by equation (21). Step numbers of 2, 4, 8, 16, and 32 were simulated, along with the corresponding MLFZPs for comparison. An image of the simulated N = 4 MLPS focal plane and yz plane are shown in Fig. 24, along with an image of the FDTD simulation environment for the N = 4 MLPS. As anticipated, the proper phase shifting of the incident light results in a suppression of higher order maxima, and therefore side-lobes in the focal plane. The efficiency of this N = 4 device was calculated to be 28%, which is already nearly triple the highest reported efficiency for a photon sieve.

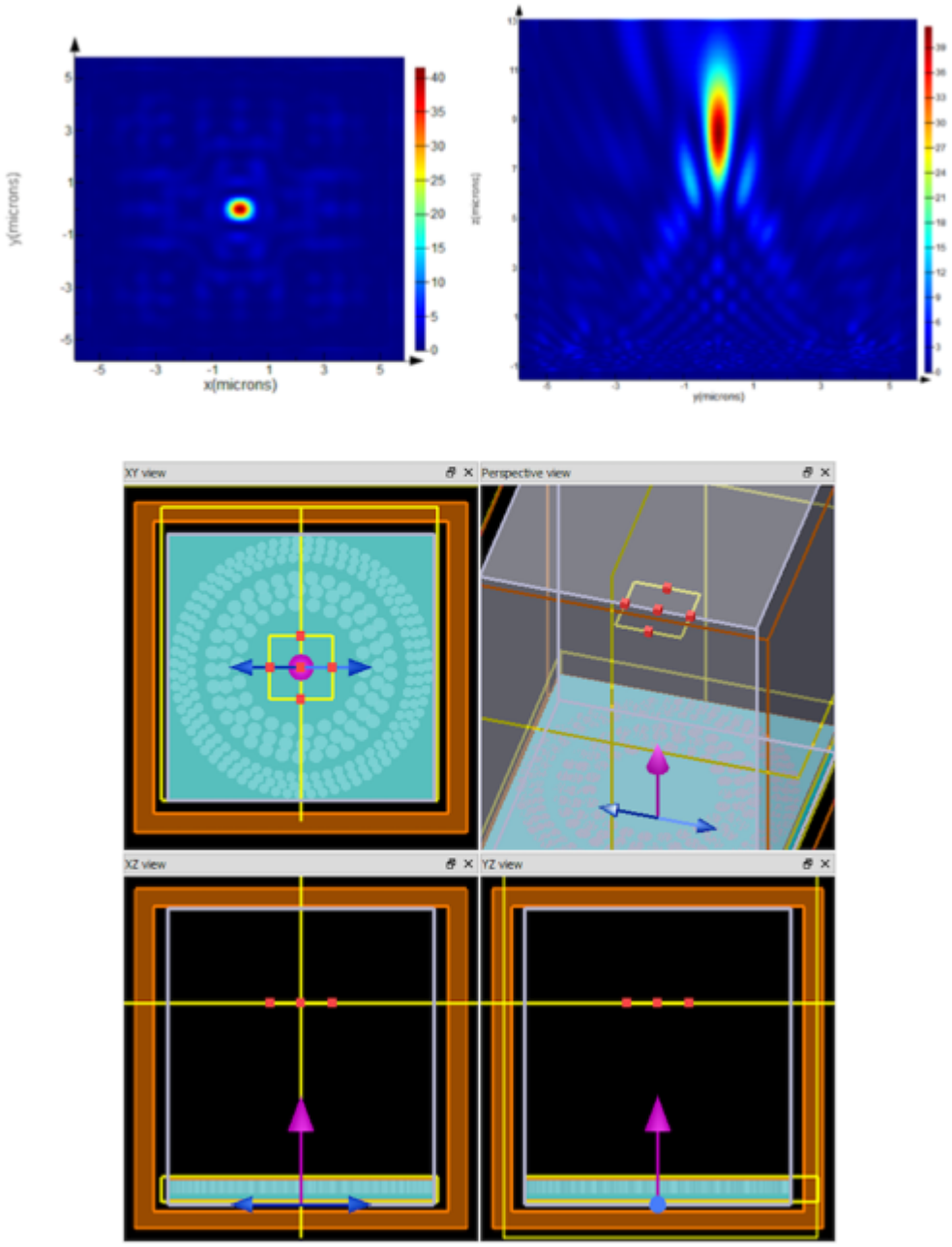

Figure 25: Focal plane intensity profile (left) and yz intensity profile (right) of the N = 4 MLPS obtained via FDTD simulations (top). Near-zero side lobes are seen in the E-field distributions, as well as reduced-intensity higher order foci, which results in a greater amount of light in the desired focal point. FDTD software environment for the presented results showing various views of the simulated region (bottom). The substrate is represented by a solid rectangle of refractive index 1.7, and pinholes are represented by an etched area inside of the substrate with an index of 1.0.

A plot of MLPS and MLFZP efficiencies obtained via FDTD simulations is given in Fig. 25. It can be seen that MLFZP efficiency follows the expected trend for efficiencies at various step numbers [67]. It should be noted that the efficiencies obtained via FDTD differ from the mathematically expected values given in [67] due to the use of a substrate with reflection loss, and our restriction of efficiency calculations to only include light contained within the first null of the focal plane. As more nulls are counted, efficiency matches the mathematical values, but these values give a skewed picture of the actual focal point intensity. From Fig. 26, we can see that the photon sieve efficiency, like the zone plate, approaches a maximum value. This can be considered in two ways: comparatively (to the zone plate) or absolutely. Comparatively, the photon sieve approaches an efficiency proportional to the square ratio of patterned areas between the MLPS and MLFZP. This actually matches the behavior for amplitude type devices first proposed by Kipp [25]. However, since as N approaches infinity, the MLFZP patterned area is 100%, as seen in the kinoform shape in Fig. 24. However, this is impossible for a photon sieve due to the geometric limitations of filling an annular ring with circles. In this work, the total patterned area of the photon sieve was calculated to be 95.6%. Therefore, the square area ratio is $(0.956)^2 = 0.914$, or 91.4%. Based on the efficiencies in Fig. 26, it can be seen that the MLPS efficiency asymptotically approaches 91% of the MLFZP efficiency. However, this is less useful than the absolute efficiency limit of the MLPS. Based on the 13.44% reflection expected from a two-surfaced substrate of n = 1.7, we can calculate that the MLPS efficiency in Fig. 26 approaches 70% for a reflectionless substrate. Therefore, the maximum theoretical efficiency of a photon sieve is 70%.

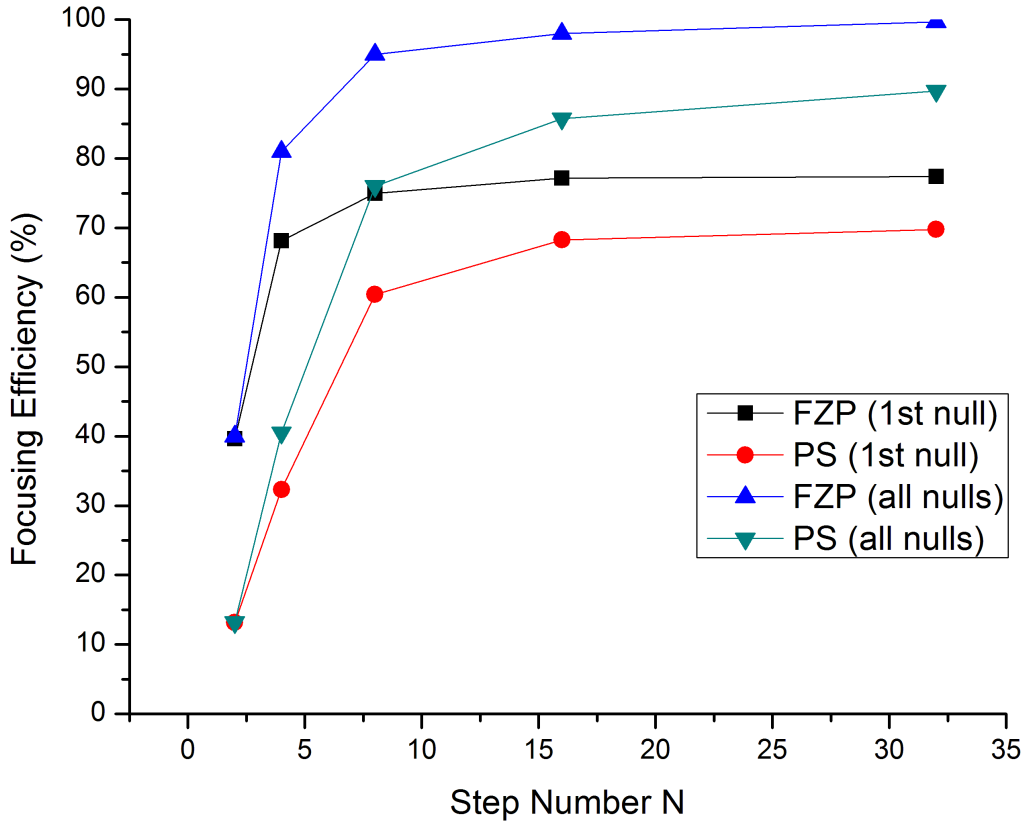

Figure 26: Plot of MLPS and MLFZP efficiencies at various step numbers. The MLPS efficiency approaches 70% after reflection is accounted for. For comparison to experimental devices, efficiency contained within the first focal plane null is recorded. In order to confirm that the simulation is working properly, efficiency values across all nulls were also recorded, as these values are already well known for MLFZPs (efficiency should approach 100%) [68].

7.3 Experiment and Characterization

N = 4 and N = 8 MLPSs were fabricated using the same system described in the previous chapter. The focal lengths (numerical apertures) of the N = 4 and N = 8 devices were 1 m (NA = 0.005) and 2 m (NA = 0.0025). The sieves had diameters of ~10 mm. An SEM image of the fabricated N = 4 MLPS and profilometer scan are shown in Fig. 27. In order to achieve the proper depths at each phase level, laser scanning speed was adjusted across each zone based on the data presented in Fig. 18. By using the trend in Fig. 18 as an

initial starting point, the scanning speed can then be quickly fine-tuned to achieve a very specific etch depth into the substrate, which allows for easy fabrication of multiple phase steps.

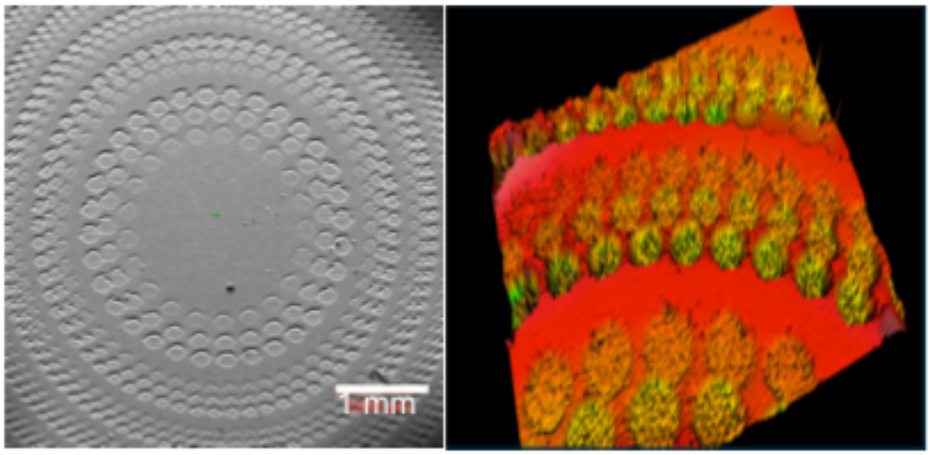

Figure 27: SEM image and optical profilometer scan of the fabricated N = 4 device [68].

The photon sieves were then characterized in terms of focusing efficiency, focal point FWHM, ellipticity, and M^2 value. The latter two measurements were added in order to demonstrate the high-efficiency photon sieves as suitable for high-quality beam focusing applications. CCD images of the focus spots are shown in Fig. 28. The measured FWHM and focusing efficiency of the N = 4 sieve were 102 μm and 25.7%, respectively, which is in good agreement with simulations. The N = 8 sieve also agreed well with simulations, showing FWHM and focusing efficiency values of 295 μm and 49.7%, respectively. Experimental comparison of focusing efficiency with simulated values is summarized in the plot in Fig. 29. The FWHM of the focal points correspond well to the size predicted for a binary phase or amplitude-type photon sieve (91.3 μm and 283 μm for the two sieve diameters and focal length shown here). Based on this, we can deduce that the overall resolution of the multilevel phase photon sieves is still governed by the width of the outermost Fresnel zone, which is the case in single-level devices. The beam ellipticity was

measured directly by the CCD detector, and was measured to be 0.96 for the 4-level device and 0.93 for the 8-level device, which correspond to a highly symmetric focal spot (where 1.0 is a perfect circle). M^2 measurements were made manually via the "four cuts" method [70]. The M^2 value was measured as ~1.38 for both samples, showing for the first time that a diffraction limited focus beam can be achieved with photon sieves.

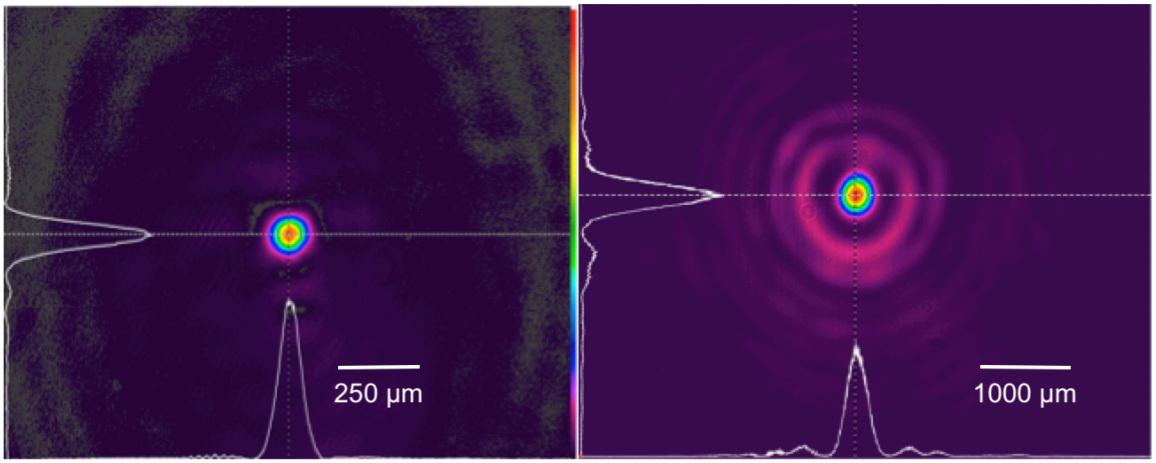

Figure 28: Focal spot of the N = 4 (left) and N = 8 (right) MLPSs). Measured FWHM (focusing efficiency) for each device is 102 µm (25.7%) and 295 µm (49.7%).

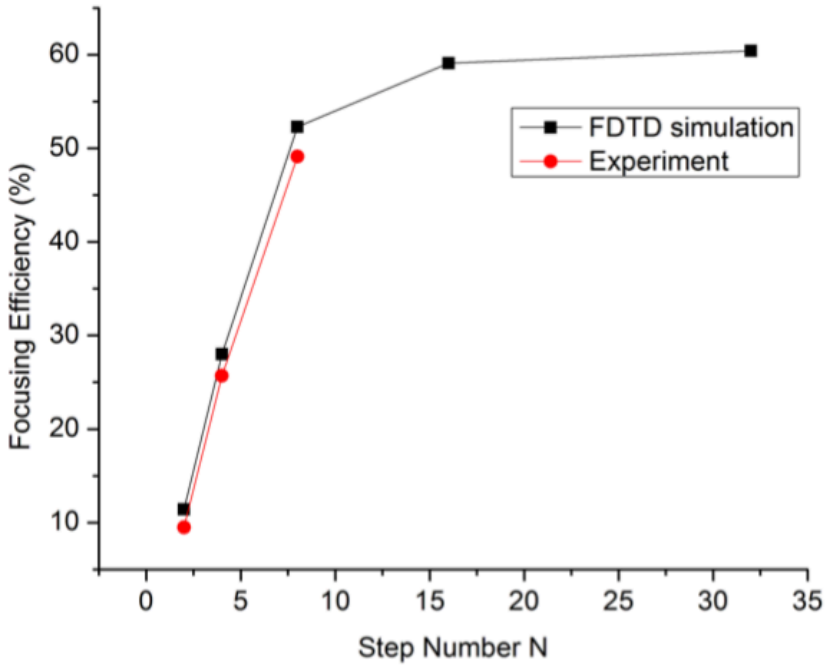

Figure 29: MLPS efficiency values for measured and simulated samples.

7.4 High-Efficiency Long-wave Infrared Multilevel Photon Sieves

Kapton is also relatively transparent at the 10.6 μm wavelength. As such, the experiments discussed thus far in this chapter are easily extended to that wavelength range in order to show photon sieve performance at infrared wavelengths. This brief experiment may be of some interest to the scientific community, as infrared lenses are typically heavy refractive lenses made of single crystal materials such as Ge, ZnSe, and ZnS. Therefore, a planar, high-efficiency optic in the infrared may be of interest for applications such as thermal imaging, spectroscopy, astronomical imaging, etc.

To demonstrate a photon sieve in this wavelength range, a Kapton substrate was etched with an 8-level photon sieve pattern using the laser ablation technique. The focal length of the designed sieve was 400 mm, and the total diameter was 8.25 mm. Then, a CO_2 laser was used to illuminate the photon sieve, and the focal point/focusing efficiency

was measured using a thermal power meter. In order to see the photon sieve focal point intensity distribution, the knife-edge scanning method was used. An image of the N = 8 photon sieve designed at 10.6 μm wavelength is shown in Fig. 30, and intensity distributions of the focused CO_2 laser beam is shown in Fig. 31. The measured FWHM of the N = 8 photon sieve was 580 μm, and the efficiency was 44%.

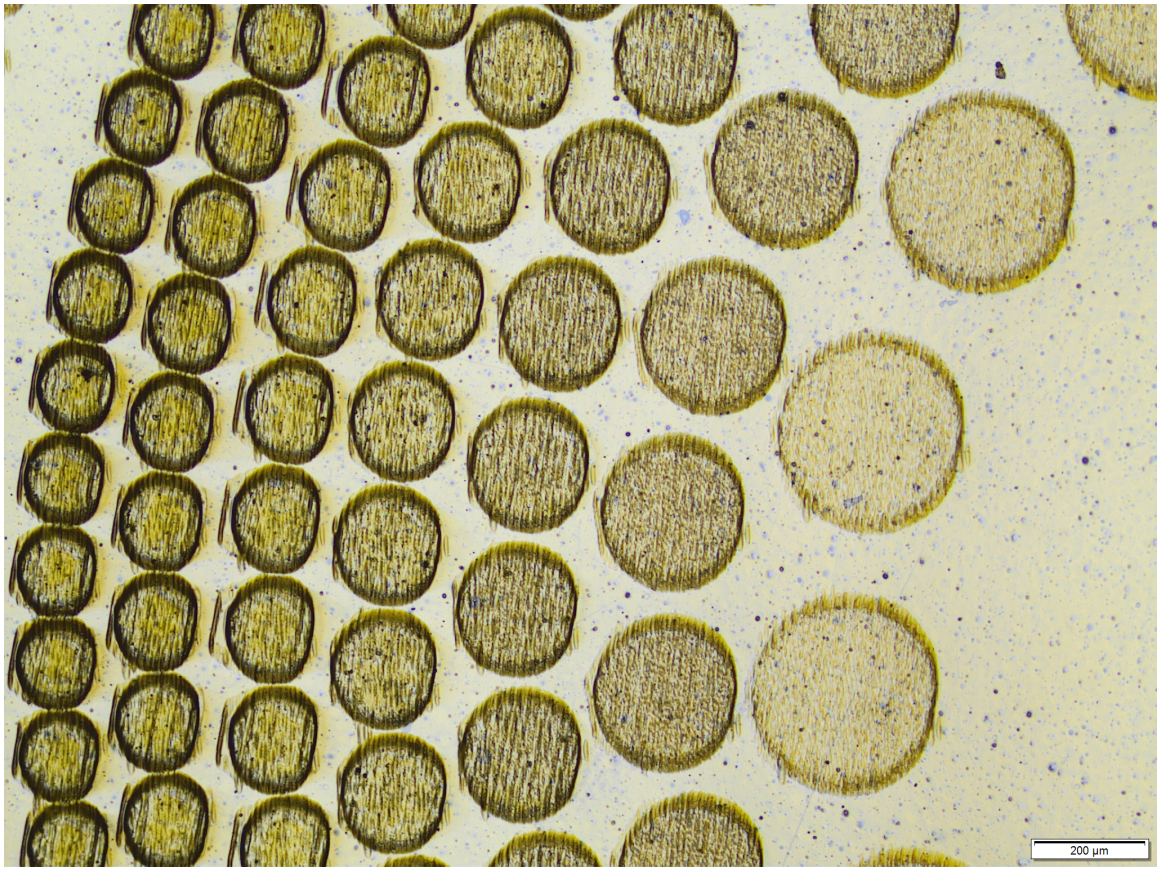

Figure 30: Innermost ring of the N = 8 MLPS designed for 10.6 μm wavelength.

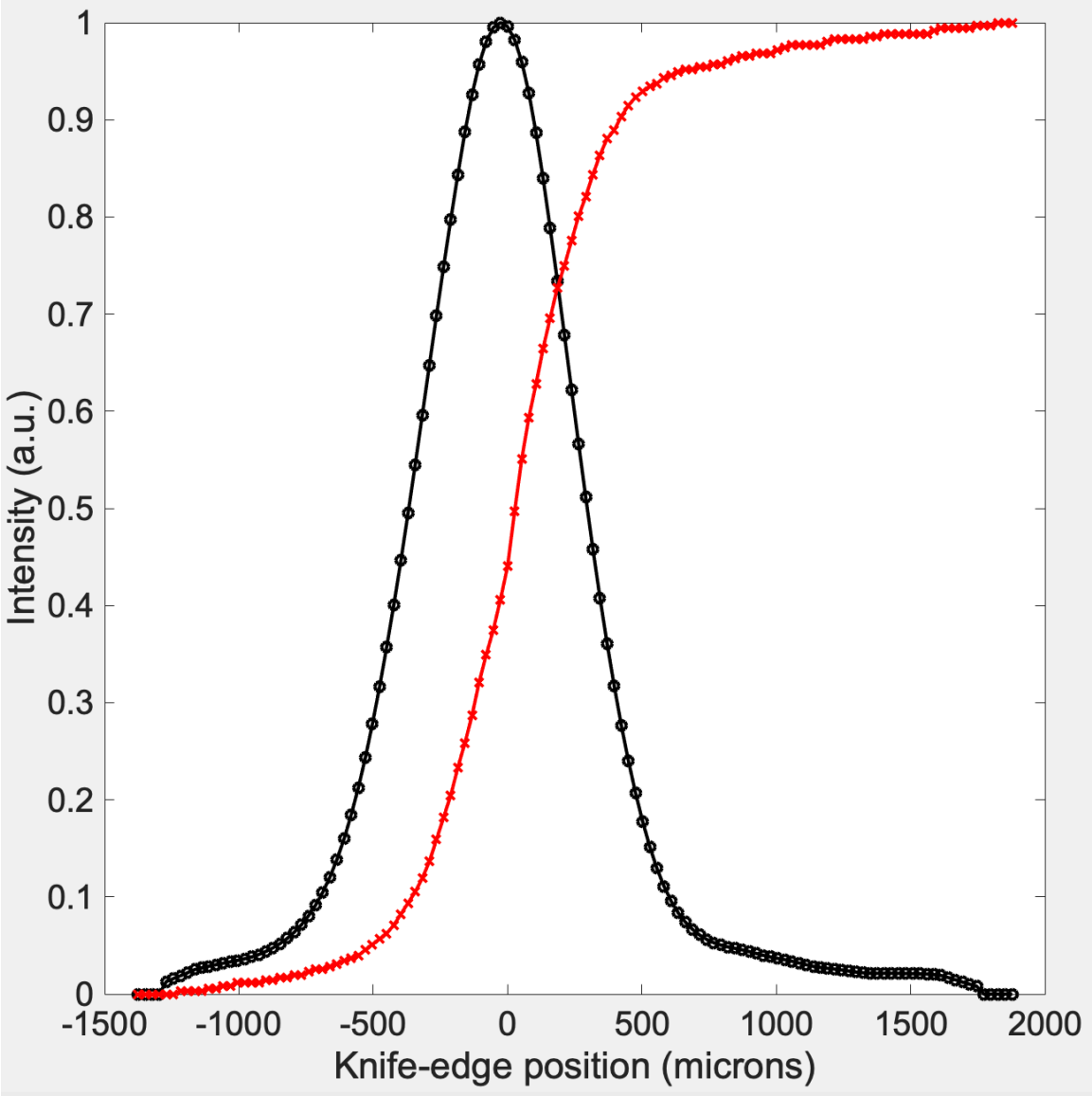

Figure 31: Beam profile intensity distribution for the focused 10.6 μm wavelength beam. Red lines correspond to measured power values at the detector, and black lines correspond to the derivative of measured values based on the knife-edge scanning method. The measured FWHM of the focused beam was 580 μm, and the efficiency was 44%.

7.5 Conclusions

We have successfully demonstrated for the first time a multilevel phase photon sieve diffractive optical element with the highest reported efficiency of 49.7%, which is

five times higher than any previously reported value. The photon sieve was fabricated on a flexible polyimide substrate by pulsed laser ablation, and its optical performance agreed well with FDTD simulations. In addition, a maximum theoretical limit of 70% for a multilevel photon sieve as the step number N approaches infinity was determined. Furthermore, the maximum possible efficiency of the photon sieve is limited by the square of the ratio of the phase shifted photon sieve area to the phase shifted area of a kinoform zone plate. The results presented in this chapter suggest that photon sieves are appropriate for various imaging and sensing applications, where previously sieve efficiency hindered their applicability. We have also demonstrated high-efficiency photon sieves at the infrared wavelength of 10.6 microns, which have potential use in various scientific imaging and sensing applications.

Chapter 8: Photon Sieve Design, Tolerances, and Fundamental Limitations

Thus far, we have discussed improvements that were made in the photon sieve state of the art in terms of efficiency and fabrication technology. Here, we will examine the fundamental limitations of photon sieve technology in terms of efficiency, fabrication speed and tolerance, bandwidth, and the effect of photon sieve design. Results from this dissertation, as well as some presented elsewhere in the scientific literature, will be discussed such that various fundamental limitation can be presented for the first time, as this is not discussed in other publications. It is important to understand these limitations so that we can properly assess the applicability of photon sieves for various applications.

8.1 Fundamental Limits of Photon Sieve Efficiency

In the previous chapter, simulation and experimental results were presented on multilevel photon sieves. A new record efficiency of nearly 50% was demonstrated, and an analytically-derived upper bound on photon sieve efficiency was shown. In this section, we will compare photon sieve efficiency to FZP efficiency in order to understand the fundamental limit of photon sieve efficiency.

A plot of photon sieve and FZP efficiencies obtained through FDTD simulations was shown in Fig. 26. As can be seen in the figure, photon sieve efficiency is always lower than the FZP efficiency, and each level off to their respective maximum efficiency values as the number of phase steps is increased. In order to better understand the photon sieve efficiency, Fig. 32 shows the ratio of FZP to photon sieve efficiency as a function of phase steps. As is seen in the figure, the ratio of sieve to FZP efficiencies approaches 91% asymptotically, and the entire curve follows a sinc^2 shape, just as the curves for photon

sieve and FZP efficiencies. As explained in the previous chapter, this 91% limit is controlled by the amount of patterned area of the photon sieve and is the maximum upper limit for a fully patterned photon sieve design. The ratio between the two efficiencies is a $sinc^2$ function scaled by a constant that varies for each phase step number. By examining the efficiency ratios at 2, 4, 8, 16, and 32 phase steps, we can see that these constants come to quite clean numbers, as shown in Table 1 below. Based on these constants and the efficiency equation for a multilevel FZP, a model can be developed to predict photon sieve efficiencies at various numbers of phase steps:

$$\eta = c_N * sinc^2\left(\frac{\pi}{N}\right) \tag{10}$$

where N is the number of phase steps, and c_N is the scaling constant for the N^{th} phase step. C_N values for 2, 4, 8, 16, and 32 phase steps are summarized in Table 1.

Step number N	**c_N**
2	1/3
4	1/2
8	4/5
16	7/8
32	9/10

Table 1. Summary of scaling constant values for modeling photon sieve efficiency.

A plot of the simulated efficiency ratios along with the model-predicted values is shown in Fig. 33.

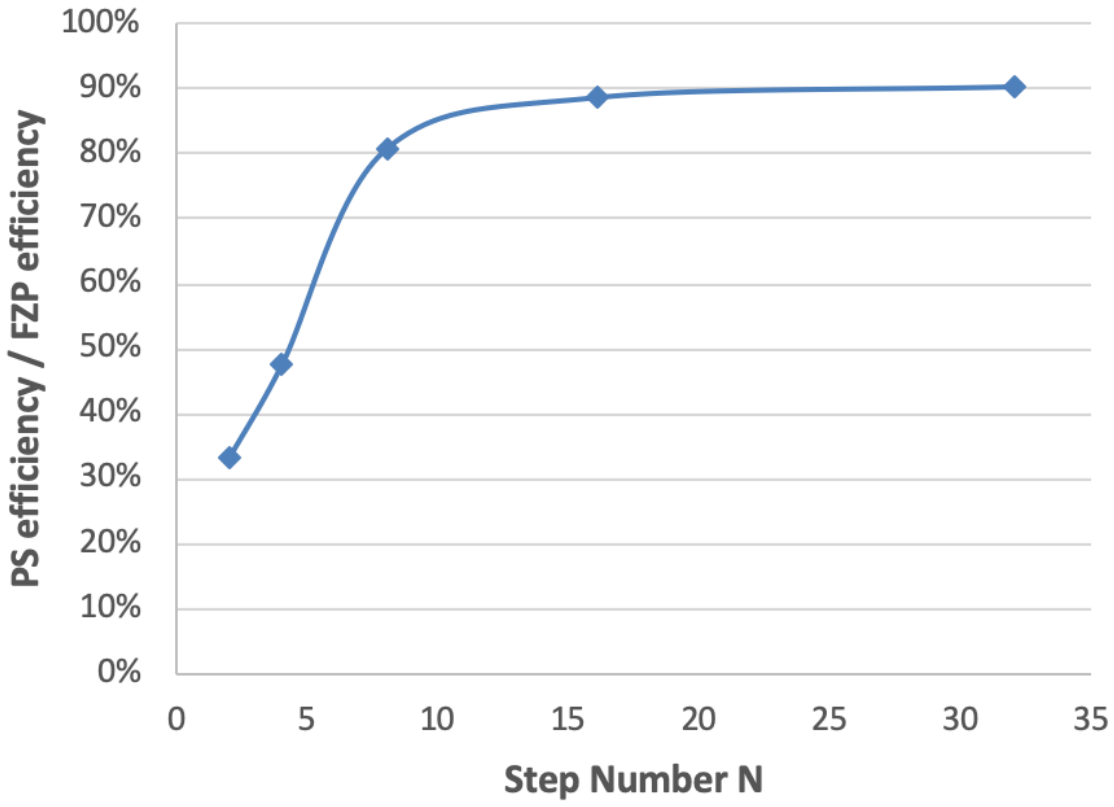

Figure 32: Plot of the ratio between photon sieve efficiency and FZP efficiency as a function of phase steps. The ratio asymptotically approaches 91%.

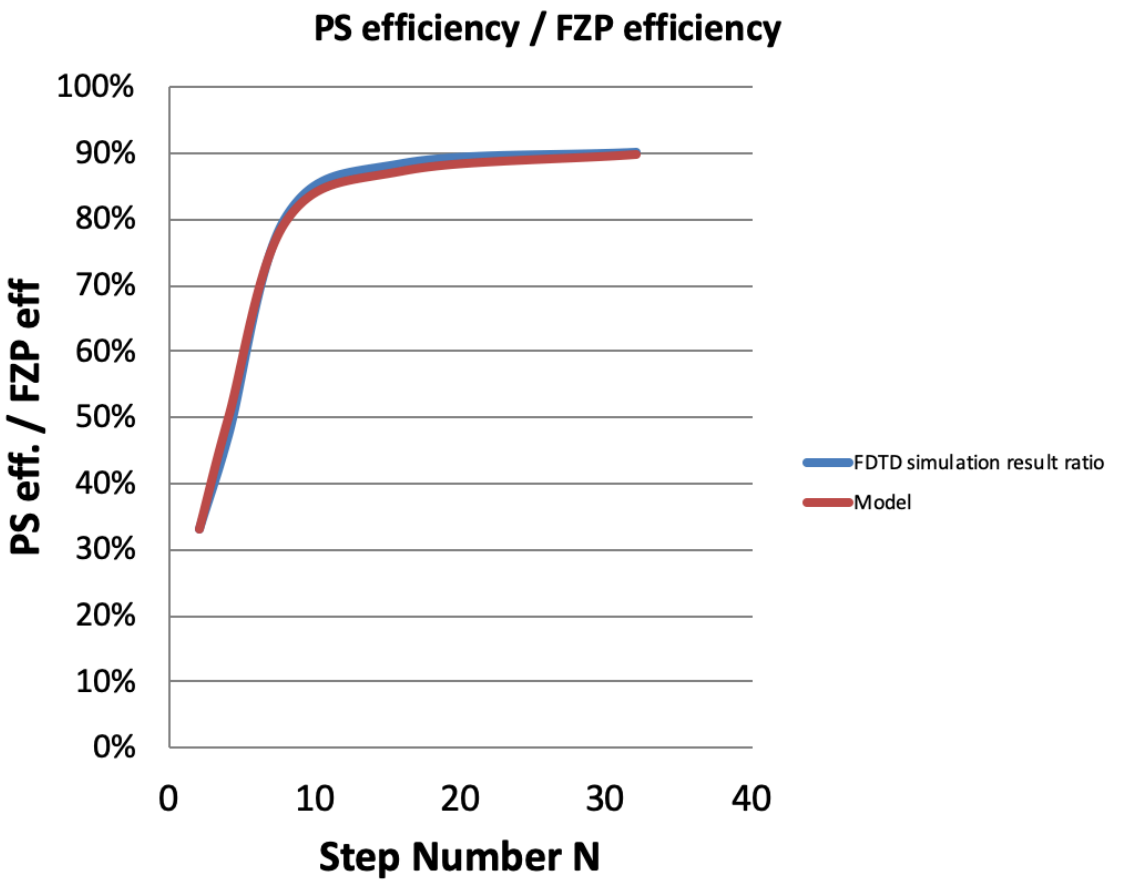

Figure 33: Plot of photon sieve and FZP efficiency ratios as predicted by the model in equation (10) and FDTD simulations.

The effect of the patterned area was described above mathematically. However, this effect can also be seen experimentally by comparing binary phase photon sieves with 23% and ~50% filling factors. Binary phase photon sieves with the same specifications as those described in chapter six were tested at both 23% and 48% fill factor, and their efficiencies were measured. As shown in chapter six, the 48% fill factor device showed ~11% efficiency, while the 23% fill factor device showed 7.9%. This reduction in efficiency resulted in an increase in stray light, which manifests itself as a higher zero-order diffracted spot in the focal plane.

The effect of temperature and angle of incidence on efficiency was also shown in a previous chapter. To briefly summarize, photon sieve efficiency remains stable until ~5 degrees angle of incidence, at which point the focal point intensity rapidly degrades. This is only the case for amplitude photon sieves, as binary phase devices will be much more sensitive to angle. This is because of the lack of true Huygens apertures in the binary phase configuration. Instead of generating new wavefronts from the aperture, the phase grating directly modifies the incident wavefront. Therefore, the flatness, angle, etch depth, and roughness of the phase grating is paramount, and deviations from ideal conditions will immediately affect device performance. The effect of temperature is fundamentally a material issue, specifically the thermal expansion coefficient of the material. So long as the pinholes remain centered on the underlying Fresnel zones, the efficiency will not be affected. However, the focal plane will shift if the rings of the photon sieve expand or contract, purely as a result of geometry. Illumination wavelength will be discussed in section 8.3. However, as discussed in chapter 5, photon sieve efficiency diminishes rapidly in the design focal plane for any wavelength off of the design wavelength, even at low numerical apertures. Shifts in illumination wavelength as small at 5 nm result in an efficiency reduction of 80% at a numerical aperture of 0.008, which would generally have a fairly large depth of focus (as will be explained in great detail in section 8.3).

8.2 Effect of Fabrication Technique on Photon Sieve Performance

Key to this dissertation is the laser ablation fabrication method used for generating photon sieve patterns on various substrates. As shown in previous chapters, the photon sieves are quite tolerant to slight surface imperfections imparted by the laser process, as experimental values agreed well with numerical simulations. However, it is worth directly

comparing standard lithographically-fabricated photon sieves with laser-ablated ones in order to understand any fundamental difference or limitations in performance, fabrication time, and pattern morphology.

As mentioned in the previous chapters, the laser ablation technique is very fast – it takes only a few seconds to generate a 1 cm^2 pattern, and only a few minutes for several square-centimeters. This is very fast compared to e-beam techniques and laser direct write techniques, but similar to mask-aligner fabrication. However, the lack of necessity for chemical post-processing further reduces the laser ablation fabrication time, making is comparable or faster than the mask aligner at small device areas. For large areas, the mask aligner will of course be faster, as there is no scanning across the substrate. The drawback to large area mask aligners is that they are not practical or commonly available and would typically need to be custom built to handle larger than wafer-sized substrates. This custom system would necessarily be very expensive. Additionally, challenges such as photoresist thickness consistency over a large area, as well as large area development are non-trivial. Lastly, for a large area mask aligner system, a large area mask still needs to be fabricated by another method. Based on this overview examination, we can see that there is some fundamental tradeoff when using the laser ablation technique in terms of fabrication times at larger areas. However, this tradeoff is skewed in favor of laser ablation due to the impractical nature of large area mask aligner systems.

In terms of surface morphology, the photon sieve is fairly robust to circa-wavelength roughness as described in chapter six. In order to further confirm this, the efficiencies and focal point profiles of laser ablated and direct-write lithography-fabricated N = 4 photon sieves were measured and compared. Optical profilometry measurements of

the surfaces were also made in order to show the difference in roughness in the marked regions. The lithographically-fabricated photon sieves were written in AZ1518 photoresist and developed in 1:6 AZ400K, and the full fabrication procedure is described in detail in chapter nine. Profilometer images of the two photon sieves are shown in Fig. 34. As is clear in the images, the lithography photon sieve is much smoother, with surface roughness nearly two orders of magnitude lower than the laser-ablated photon sieve, and with near vertical sidewalls. However, this increase in surface quality does not contribute to an increased optical performance, as the measured efficiencies were essentially identical (~25%) and matched well with the expected value. Furthermore, the laser ablated surface morphology can be improved via a shorter laser wavelength (as mentioned in Chapter 6) or by introducing an airflow to remove redeposited particles on the surface. Additionally, each focused light to a tight point with no side lobes, and a spot size near what is predicted from the diffraction integral [25]. Images of the focal points are shown in Fig. 35. Note that the focal points are different sizes, as the two sieves were made for different purposes and have different numerical apertures. Based on this, we can see that the laser ablation process does not suffer from any fundamental limitation in terms of photon sieve performance when compared to more traditionally-fabricated devices (as long as the laser parameters are optimized, as explained in chapter six). As shown in Fig. 22, the etch depth must be carefully optimized, as errors of even 100 nm result in decreases in efficiency.

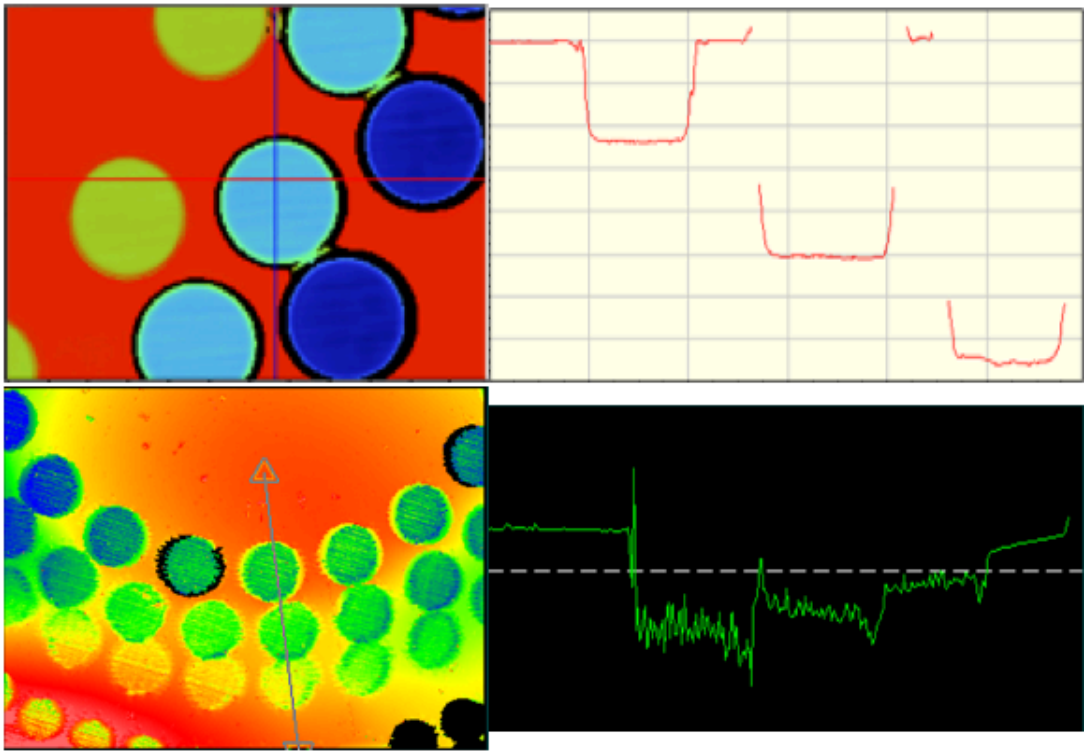

Figure 34: Optical profilometer scans of the N = 4 photon sieves fabricated via direct-write lithography (top) and laser ablation (bottom). The difference in surface roughness is nearly two orders of magnitude, but optical performance is consistent across each device. Each method is similarly capable of achieving proper patterning depth by controlling laser fluence and/or development time.

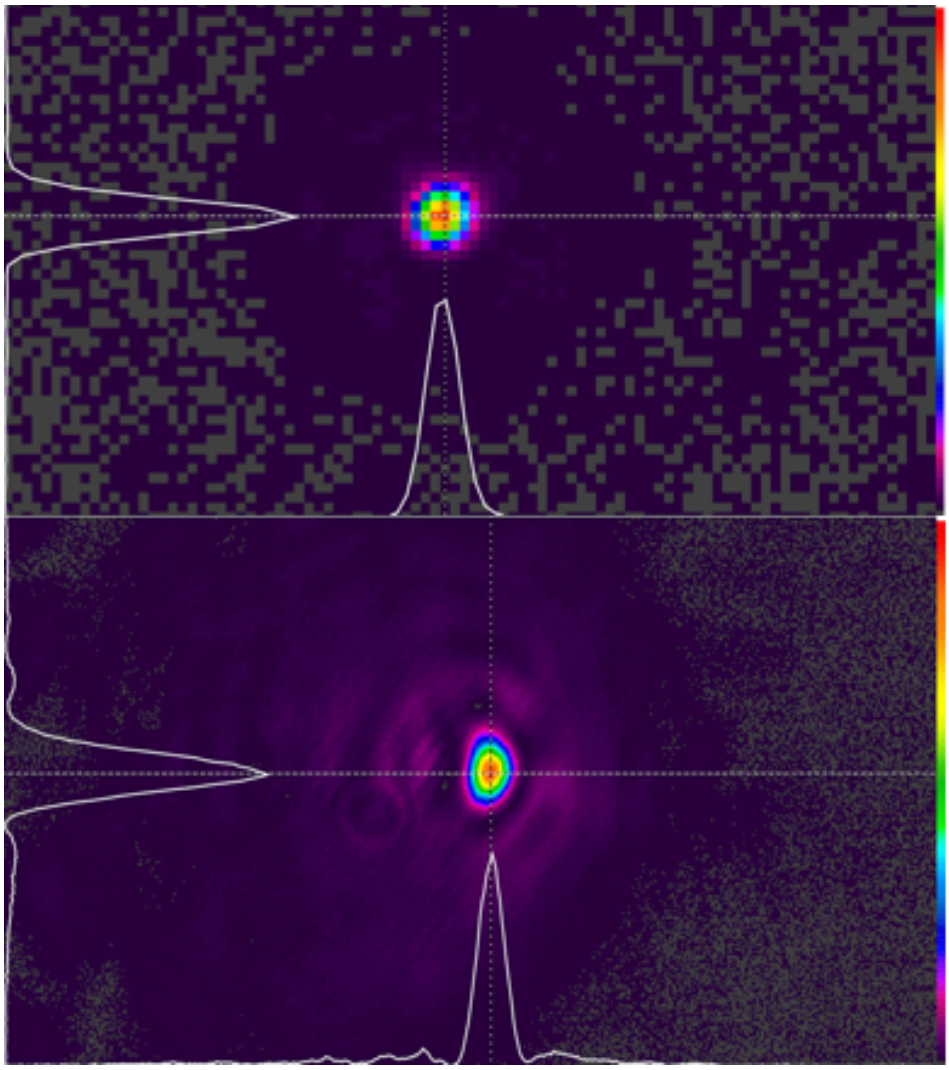

Figure 35: Focal points of the direct write lithography-fabricated photon sieve (top) and laser ablated photon sieve (bottom). Each show diffraction-limited focusing and near-theoretical efficiency values.

8.3 Limitations of Achromatic Photon Sieves

Diffractive optics inherently suffer from chromatic aberrations – shifts in focal length with wavelength. This is because the design geometry of diffractive lenses is based off a particular design wavelength in order to produce the proper phase profile across the aperture of the lens. This is akin to refractive lenses, which base their curvature off of a specific design wavelength and refractive index. As a result, other wavelengths will focus slightly differently, due to the chromatic dispersion in the material refractive index. It is

advantageous to reduce or eliminate these chromatic aberrations, as they result in blurred images under broadband illumination, which is typically the circumstance for most imaging applications.

In this section, the limitations on aberration correction of photon sieves will be discussed in the context of the state of the art. Geometric methods of controlling chromatic focal shifting were investigated both numerically and experimentally. Based on the results presented in other works on so-called "harmonic diffractive wavefront coded photon sieves" (HDWFCPSs) [37], the research presented in this chapter serves to push the limits of the previously described technique, as this technique constitutes the best attempt to date at demonstrating truly achromatic photon sieves. Specifically, while the reported work shows good results for low efficiency designs, this dissertation studies limitations of the technique as they relate to full-visible bandwidth performance and phase-type photon sieves. Through numerical and experimental studies, limitations were discovered in the HDWFCPS technology – specifically limitations related to device numerical aperture and focusing efficiency.

As described in chapter 2, one method of increasing the bandwidth of photon sieves is a combination of harmonic diffraction and wavefront coding. As a brief refresher, this technique relies on harmonic diffraction to increase the number of wavelengths that satisfy the design equation, and wavefront coding to increase the spectral bandwidth of each of those peaks. Recently, multispectral photon sieves were demonstrated using this technique (henceforth referred to as WFCPS and HDWFCPS) with a discontinuous operating bandwidth across various wavelengths in the visible spectrum [37]. This multispectral achromatic focusing certainly proved to be a large step forward in photon sieve technology,

however several limitations still remained, as mentioned in chapter 2. Specifically, no mention of design limitations (in terms of device radius, numerical aperture, etc.) was made in the previous work, nor was the ability to extend this technique to full bandwidth operation. Additionally, the issue of efficiency was not discussed, and the efficiency of the demonstrated devices was at best 1%. Here, we have studied each of these key points in an attempt to understand the fundamental limitations in this technique as it applies to photon sieve performance. In order to do this, both numerical and lab-based experiments were carried out and will be discussed below.

For wavefront coded (WFC) optical devices, the phasefront symmetry of the transmitted wave is altered. For a typical plane wave (or Gaussian beam) passing through a focusing optic, the phasefront imparted by the optic is rotationally symmetric about the center (like a typical refractive lens). The focal point generated as a result has the same symmetry as the incident light (i.e. a Gaussian beam will focus to a Gaussian beam). In the case of wavefront coding, this rotational symmetry is broken, which allows for the increased operational bandwidth. However, this asymmetry results in an asymmetric focal point, which is not directly useful for imaging. An example of this focal point is shown in Fig. 36. Although this point spread function (PSF) is not directly useful for imaging, it can easily be reconstructed to form a perfect image due to the fact that the optical transfer function (OTF) of the PSF has no zeroes, and thus this information is retrievable at all frequency points in the spectrum [33, 34, 76].

In the case of harmonic diffractive lenses, the focal point for each harmonic wavelength is identical. For a typical harmonic diffractive lens, this means that each design wavelength will focus to an identical Gaussian focal point (with size varying

slightly due to the diffraction limit of each wavelength). In the case of a HDWFC lens, each design focal point, along with some spectral bandwidth around said wavelength, will focus to a PSF like the one shown in Fig. 36.

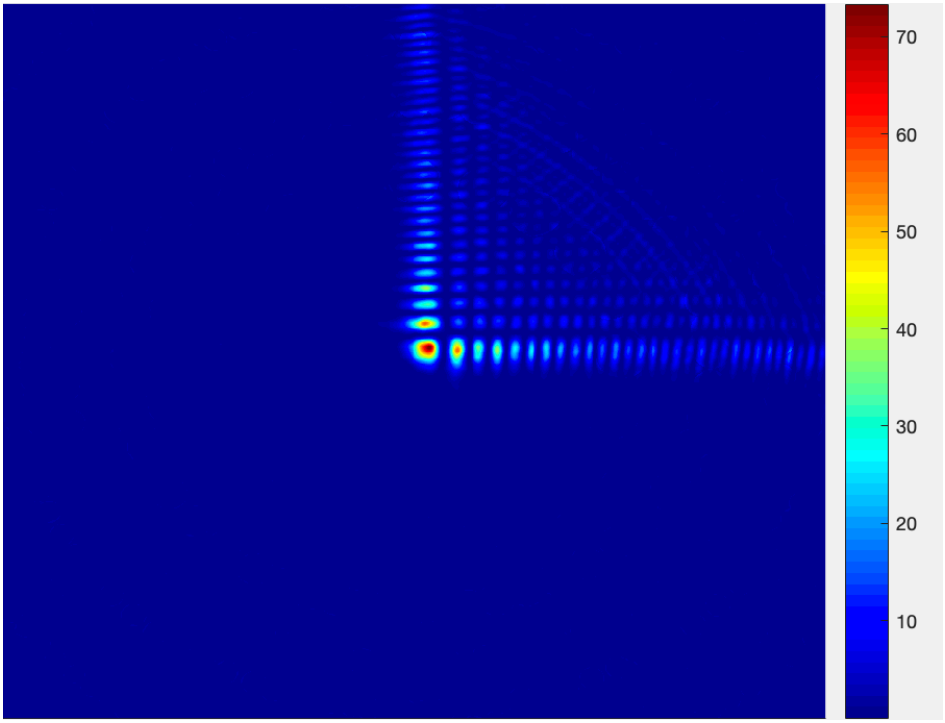

Figure 36: Example PSF in the focal plane of a wavefront coded or HDWFC photon sieve. Asymmetry in the intensity distribution is a result of the WFC technique, which generates an asymmetric phase shift across the transmitted optical phasefront. This asymmetry creates a greatly extended depth of focus, which allows for achromatic imaging over a large bandwidth.

In the context of a photon sieve, the WFC phasefront is directly encoded into the pinhole distribution of the sieve. This is also true for the harmonic diffractive photon sieve (HDPS) geometry as well. As was explained in chapter 2, for P wavelengths to satisfy the photon sieve design equation, the number of rings is reduced by 1/P such that only every P^{th} ring is present. Examples of a WFCPS, harmonic diffractive photon sieve, and HDWFCPS are shown in Fig. 37. Note the lack of symmetry about the origin in the WFC

sieve designs. The axis of symmetry is now about the line $y = -x$ for the cubic wavefront coded lenses.

Initial studies were carried out to understand the effect of ring number (and thus overall sieve diameter) on the PSF of the focal point. As seen in equation (7) in chapter 2, the photon sieve radius is a key geometric parameter in the WFC term of the photon sieve design equation. Equation (7) implies that for larger device radii, the wavefront coding term is weaker (as the term dependence on radius is $1/R^3$). Thus, for small radii, the term is much stronger. This has an important implication on the transmitted phasefront of the light passing through the sieve. In the WFCPS (and HDWFCPS), a balance is being struck between the Fresnel phasefront imparted to focus the light, and the WFC phasefront imparted to generate an achromatic PSF. If one of these phases greatly outweighs the other, the performance of the lesser-weighted phasefront will be diminished. In short, equation (7) implies that for too small an R-value, the lens will simply not focus. In order to understand the effect of this parameter, PSFs were simulated via graphical Fourier transform of the photon sieve amplitude masks (such as those shown in Fig. 37) at various P values and ring numbers. For all cases, the strength of the WFC term, governed by the variable α, is taken to be 10π [35-37].

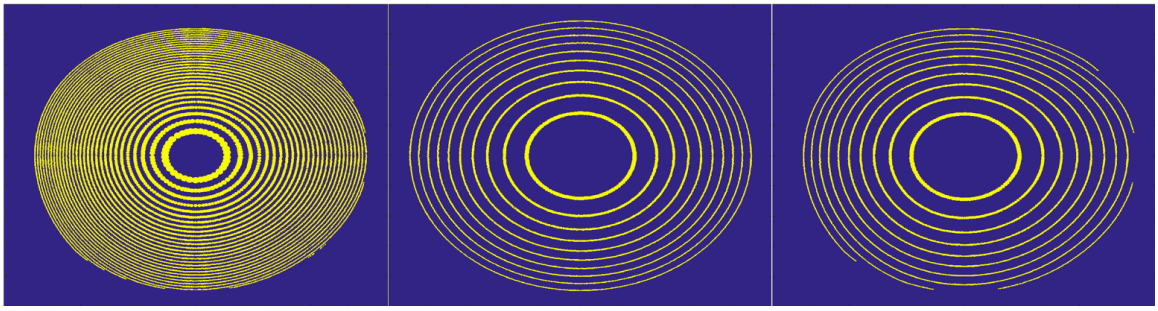

Figure 37: CAD images of a WFCPS (left), HDPS (middle), and HDWFCPS (right). The effect of the cubic phase mask is exaggerated here due to the low number of rings in the photon sieve. Pinholes that appear to be overlapping are a function of the pixel density of the MATLAB rendering of the images, as the images are meant only to demonstrate the general idea of the design.

Results of these simulations are shown in Fig. 38 for P = 1 and P = 5. As is seen in the figure, when P = 1, the PSF of each case is identical to the idea cubic PSF shown in Fig. 36. As the ring number is increased, the PSF is focused to a smaller size. In the case of P = 5, the PSF looks less like an ideal cubic PSF as low ring numbers, in addition to not being focused. We postulate this to be an effect of the reduced number of pinholes in the P = 5 sieve (since the number of rings is 1/5 the number of the P = 1 case). Because fewer rings are present, the strength of the cubic phase mask is reduced slightly, even at small radii. This is due to a decrease in overall transmission of the photon sieve. Essentially, less of the total aperture is encoded with a cubic phasefront, so the PSF is less perfect. In order to test this, simulations at P = 10 were also performed, and it was observed that the ring number needed to be even further increased in order to see an ideal cubic PSF. From these simulations, we can clearly see two design limitations in the HDWFCPS technology: the limitation of focusing ability at low radii (low numerical aperture/ring number), and the limitation of reduced PSF quality at a given ring number as P is increased. Based on the results obtained for P = 5 and P = 10 designs, it appears that if P is doubled, the number of rings required to obtain the ideal cubic PSF is also doubled. It is unclear what the exact

cutoff ring number is for high vs. low-quality PSF at a given P value, however our simulations suggest that it may be around ring number $N = 15P$, as the P = 5 sieve required ~75 rings to reach a clean PSF, while the P = 10 sieve required ~150 rings. For P = 1, this issue does not exist, only the focusing behavior is altered by ring number, which is expected based on equation (7).

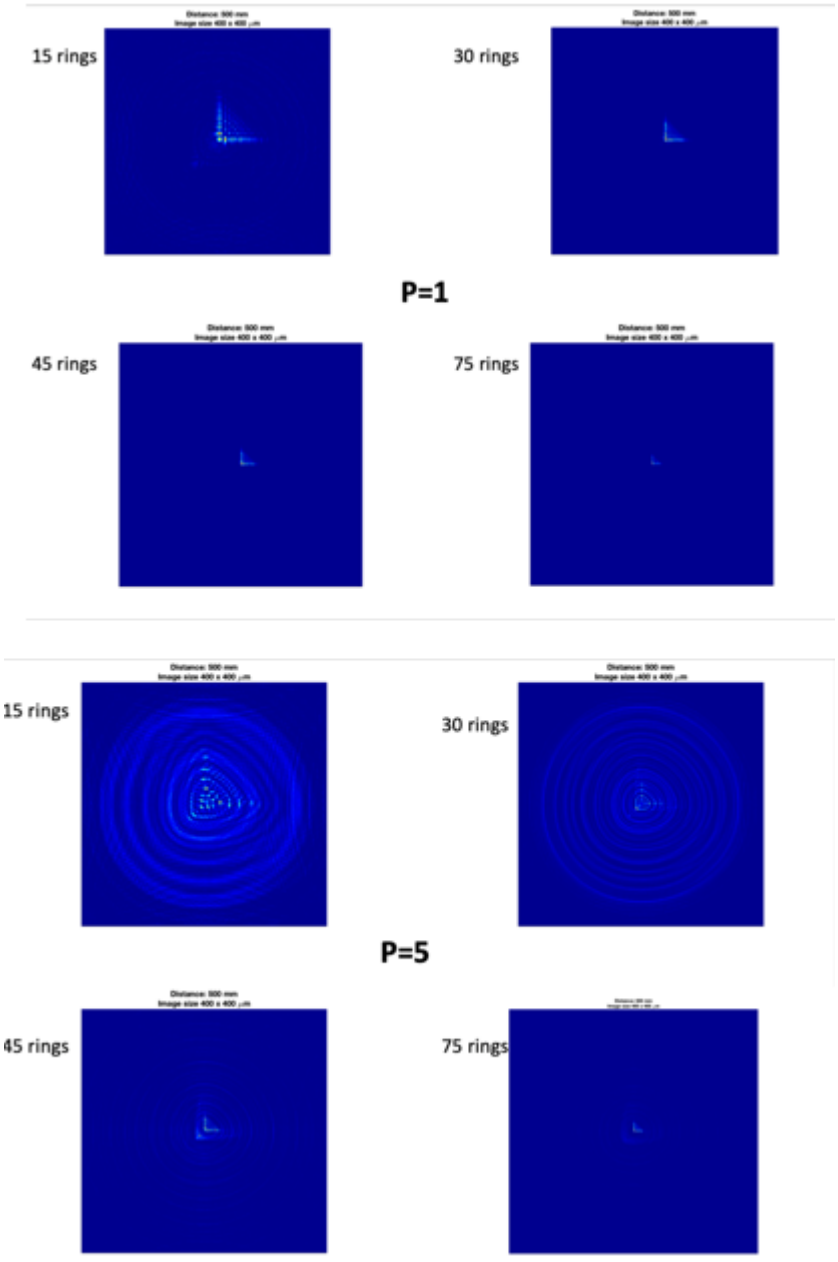

Figure 38: Simulated PSFs in the focal plane of various HDWFCPSs with $\alpha = 10\pi$. Effect of P and ring number on the focusing ability of the photon sieve is readily apparent. The window size in each PSF image is 0.4 x 0.4 mm.

Next, the potential for full spectrum focusing is studied. The effect of device design parameters (α, focal length, diameter) on the overall continuous bandwidth of the photon sieve is studied numerically through simulations, as well as through traditional depth of

focus equations. In order to verify the simulations, a sample was fabricated and tested at multiple visible wavelengths and compared with simulated results.

The diffraction-limited operational bandwidth of a typical optical system, based on the geometric depth of focus considerations, is given by [9]

$$\Delta\lambda = \frac{2\lambda^2 f}{D^2} \tag{22}$$

When placed in the context of a WFC optical system, such as a HDWFCPS, the usable operational bandwidth gains a wavefront coding term, and is given by [75]

$$\Delta\lambda = \left(\frac{3\alpha}{\pi}\right)\left(\frac{2\lambda^2 f}{D^2}\right) \tag{23}$$

Thus, the operational bandwidth of a WFC optic is easily calculable based on the design geometry and strength of the cubic phase mask. As expected, a stronger phase mask will result in a wider bandwidth. However, as shown in the previous section, we cannot arbitrarily increase the value of α due to its effect on focusing behavior shown by equation (7).

Based on equation (23), we can see that the spectral width of each harmonic wavelength is different, and that each of them is governed by the numerical aperture (*NA = D/2f*) of the photon sieve. Therefore, it can easily be deduced that for high NA photon sieves, full spectrum focusing over a continuous bandwidth is not feasible, unless very high P values are used. However, when using high P values, the overall transmission is reduced by 1/P, as discussed previously, and so practicality of such a photon sieve is severely

reduced as well. However, for lower NA photon sieves, focusing over a continuous bandwidth is certainly possible, although it had not been demonstrated previously to this dissertation. Here, a HDWFCPS with 500 mm focal length, P = 8, 150/8 = 19 total rings, design wavelength of 700 nm, and $\alpha = 25\pi$ was simulated at 50 nm increments across the visible spectrum (400 – 700 nm). A summary of the obtained PSFs is shown in Fig 39. As is seen in the figure, full spectrum imaging is achievable with HDWFCPS devices, despite having not been demonstrated previously, albeit with a low NA device (NA = 0.02).

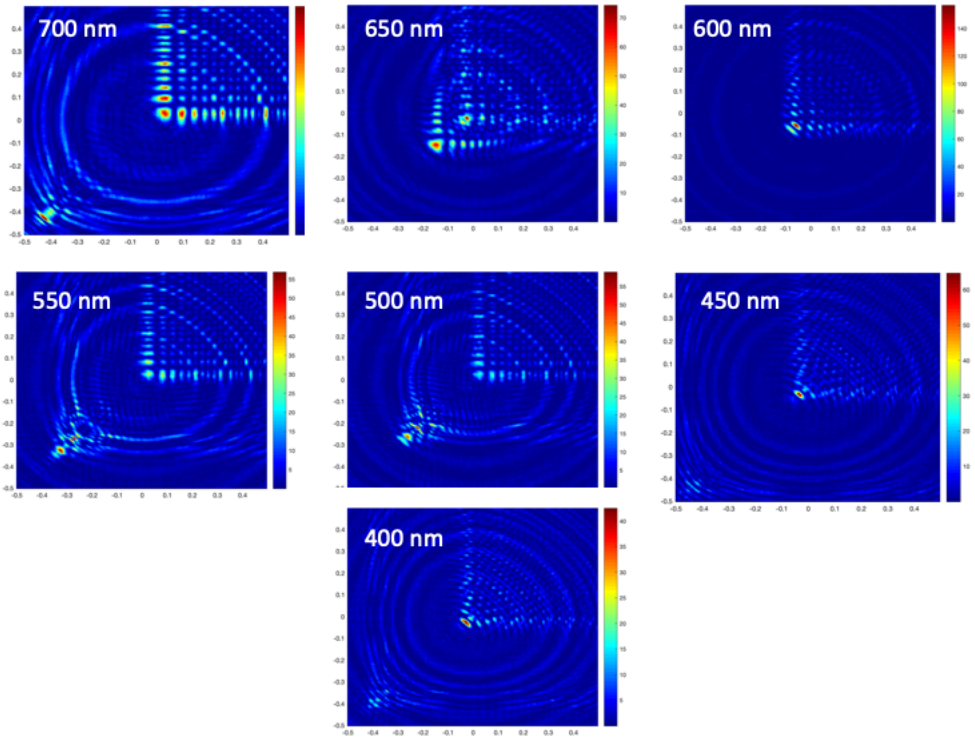

Figure 39: Simulated focal plane PSFs of a HDWFCPS showing full visible spectrum performance across a continuous bandwidth. The PSF at each wavelength is nearly invariant and agrees reasonably well with the ideal cubic PSF in Fig. 36.

In order to experimentally validate this finding, the same photon sieve was fabricated using the laser ablation process. The photon sieve was written into an optically thick Ag film on soda lime glass substrate, and the focal point PSF was measured at various wavelengths

across the visible spectrum using a tunable, multichannel laser source with wavelengths of 405, 488, 561, and 637 nm. The sieve was also tested using separate 532 nm and 633 nm lasers. A summary of the simulated and experimental PSFs are shown in Fig. 40, along with an overview image of the fabricated HDWFCPS in Fig. 40. Because this was an amplitude type device, the efficiencies of each wavelength were below 1%, as expected. Exact efficiency is difficult to calculate, as the energy is not located entirely in a single, central lobe.

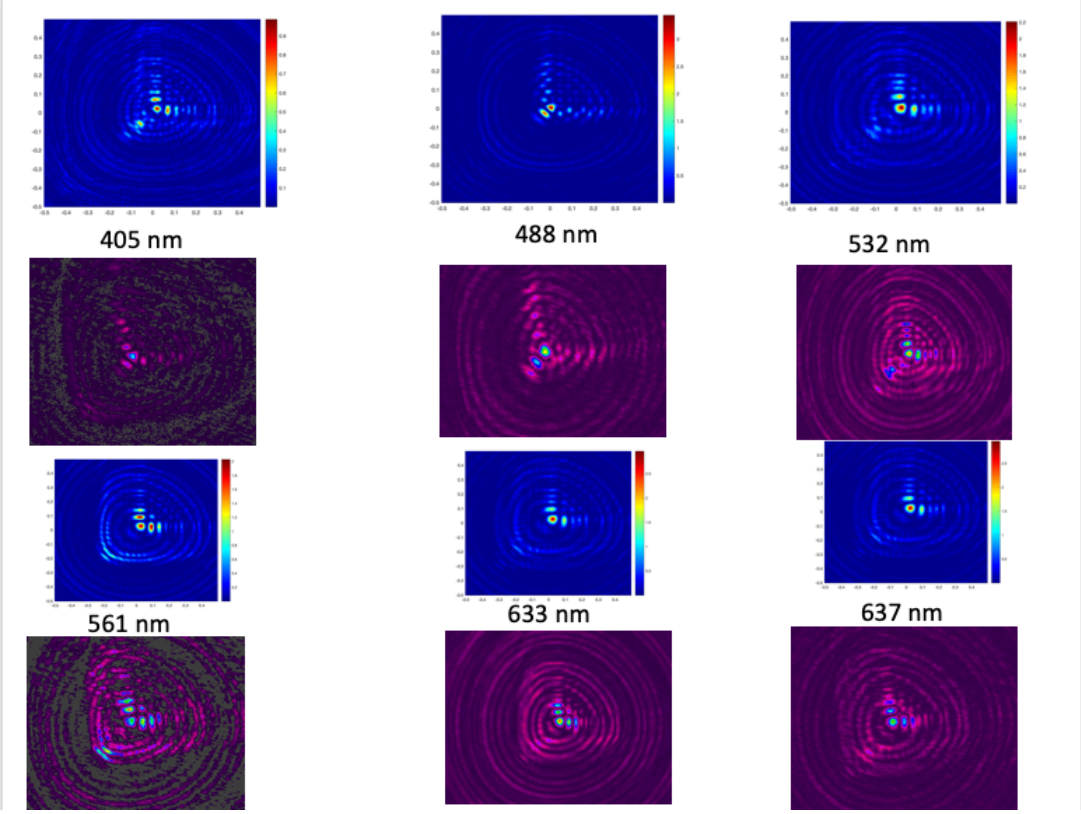

Figure 40: (top) Simulated and measured PSFs from the fabricated HDWFCPS across the visible spectrum.

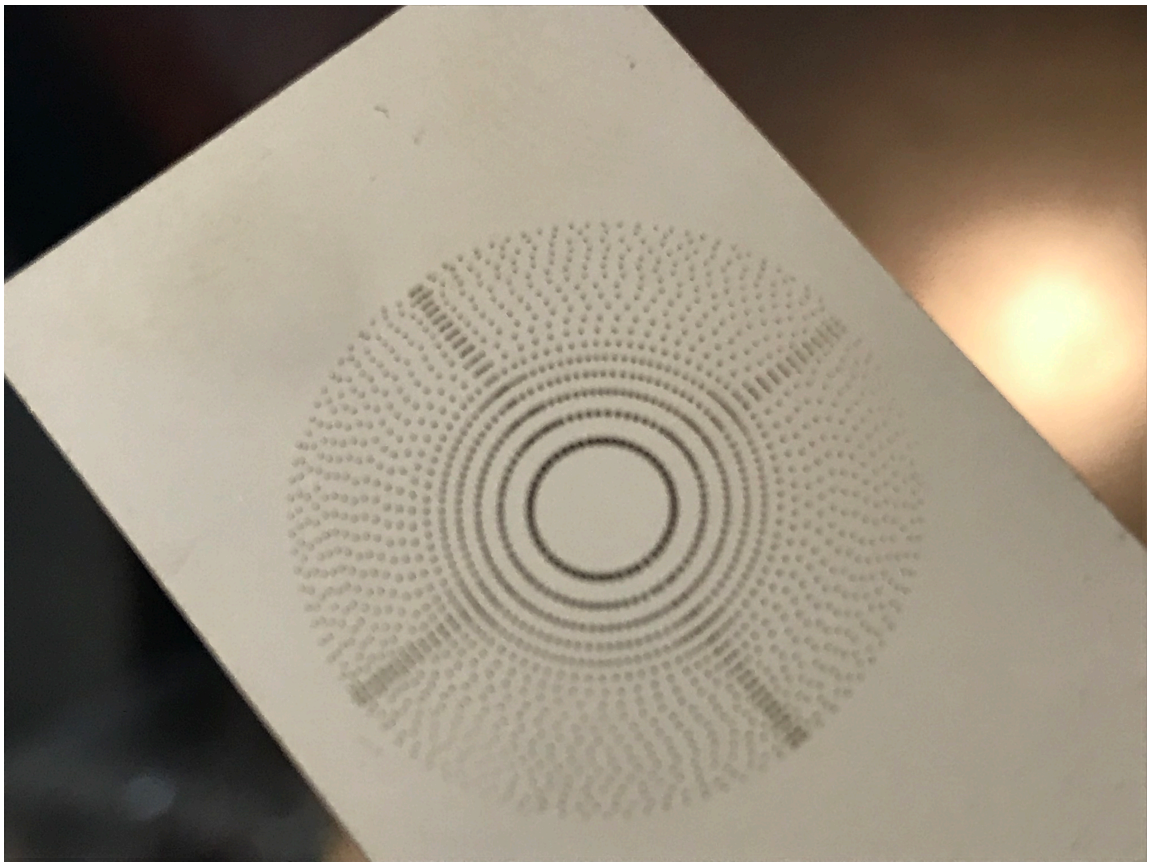

Figure 41: Camera image of the HDWFCPS fabricated in Ag used to generate the PSFs shown in Fig. 39.

As the efficiency achieved with the above photon sieve was expected to be very low, attempts were made to increase the photon sieve efficiency via a binary phase approach using a Kapton substrate, just as was described in chapter 6. The same photon sieve shown in Fig. 41 was written into a Kapton substrate and patterned to the ideal depth given by equation (20), multiplied by P in order to account for the harmonic properties of the sieve [78, 79]. An image of the obtained PSF is shown in Fig. 42. As seen in the figure, no cubic PSF is present, however a typical Gaussian focal point is clearly visible at the focus of the sieve. In order to investigate the origin of this phenomenon, the same photon sieve was written onto semi-transparent Ag and tested. This PSF is also shown in Fig. 42,

and it can clearly be seen that a cubic PSF is beginning to form. Based on this, we postulated that the increased transmission from the phase-type photon sieve, which is fully transparent, was playing a role. Specifically, it was believed that the increased stray light (light not diffracted by the photon sieve) in the HDWFCPS was "washing out" the cubic phase mask and producing a simple, Gaussian focal point. Higher P values have a lower fraction of patterned area compared to P = 1, for example, in which nearly the entire aperture is covered in "pinholes". As a result, as P is increased, less and less of the light is seeing the appropriate asymmetry (the cubic phase mask), and thus the cubic PSF may be suppressed. In order to test this, photon sieves were fabricated in Kapton at P = 8 and α = 0. This would test whether the Kapton itself was an issue (perhaps due to the index dispersion of the material), or if the issue lied within the HDWFCPS pattern. The P = 8, α = 0 photon sieve focused to a clean Gaussian focal point as expected. In order to further investigate, photon sieves with a constant $\alpha = 25\pi$ and varying P values (P = 1, 3, 5, 8) were fabricated and tested. A summary of the obtained PSFs is shown in Fig. 43. It can be seen that for P = 1, the cubic PSF is clean and clearly visible. However, at P = 3, the quality of the cubic PSF is reduced, and at P = 5 and P = 8, the focus is entirely Gaussian and lacks any cubic asymmetry. As the only difference between these patterns was the amount of patterned area of the photon sieve, it was concluded that the strength of the cubic phase mask was being diminished by the lack of diffracted light (or, said differently, the increase in stray light). From here, we were able to determine that HDWFCPS designs are not able to simultaneously show a continuous bandwidth and high efficiency, phase-type designs. However, for narrow bandwidths such as the P = 1, $\alpha = 25\pi$ case, these designs are appropriate.

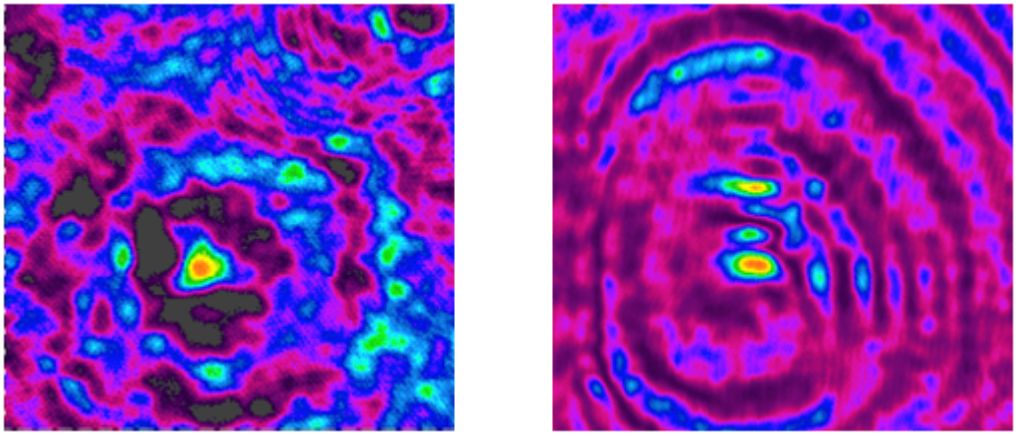

Figure 42: PSFs of the initial binary phase HDWFCPS on Kapton (left) and the same photon sieve written into semitransparent Ag (right). The difference in PSF is attributed to the decreased optical transmission, and thus increased WFC phase mask strength, in the Ag sample.

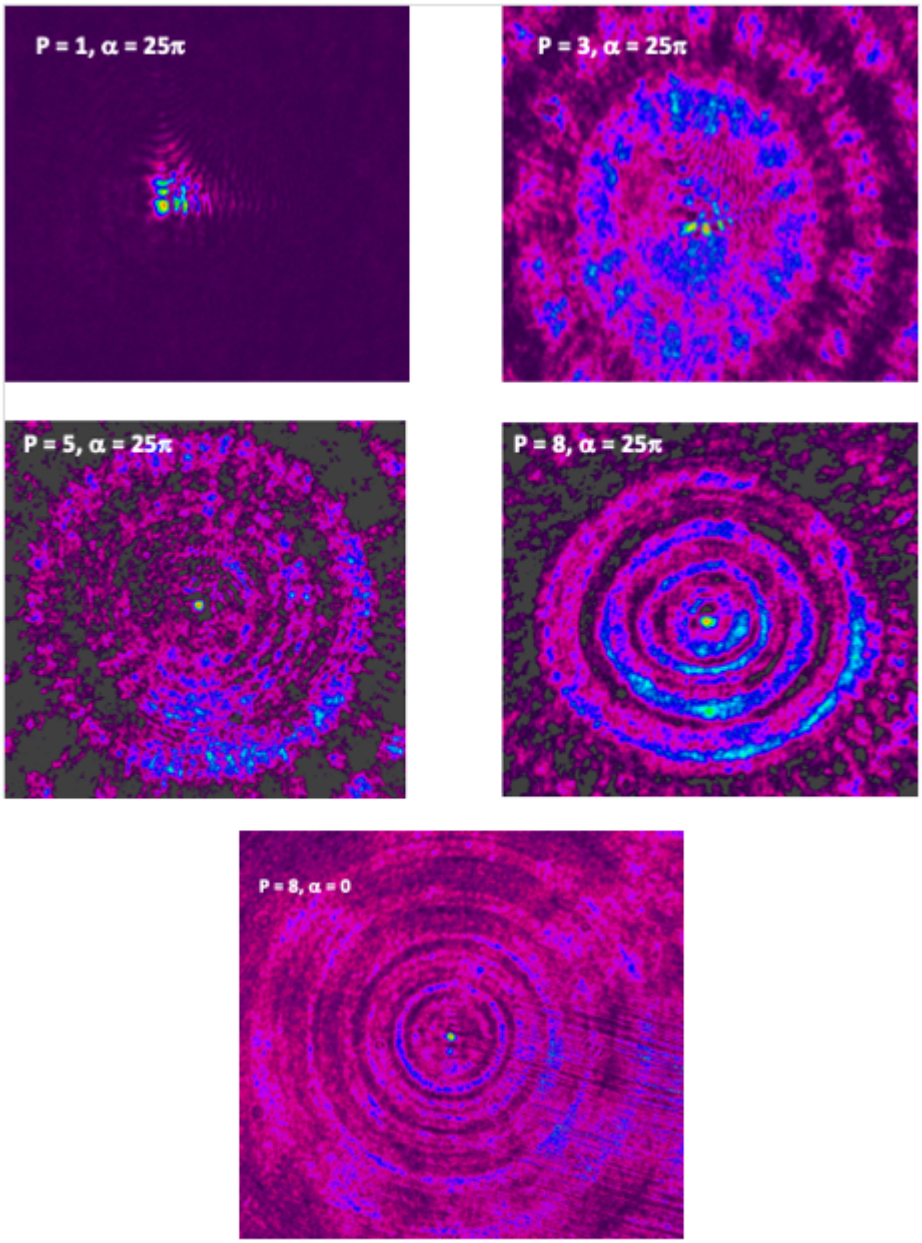

Figure 43: PSFs of the HDWFCPSs with P = 1, 3, 5 and 8. It is clearly shown that the PSF, and thus the transmitted phasefront, transitions from cubic to Gaussian as P is increased above 1. Also shown if the PSF for P = 8, α = 0. The PSF for this design is nearly identical to P = 8 and α = 25π, further supporting our hypothesis.

Based on the results of these experiments, both numerical and lab-based, we are able to conclude that several limitations exist for wide-bandwidth HDWFCPSs that were

previously unknown and/or unreported. Specifically, the limitations of this design method are as follows:

1. HDWFCPS have a focusing behavior dependency at smaller radii/ring numbers. It appears that for good focusing and ideal cubic PSF to be simultaneously attained, the photon sieve should have a number of rings approximately given by $N = 15P$.
2. The magnitude of the WFC parameter α cannot be arbitrarily increased, as it will diminish the strength of the Fresnel phase mask required for focusing as shown in equation (7).
3. Based on the diffraction-limited bandwidth given by equation (23), high NA photon sieves are not practically capable of achieving full-spectrum focusing over a continuous bandwidth. This is a result of the depth of focus of a WFC optical system, and the high P values needed to achieve overlap between spectral peaks of the harmonic wavelengths of the photon sieve.
4. HDWFCPSs are not compatible with $P > 1$ in a binary phase design. Thus, the efficiency of HDWFCPS is inherently low for wide bandwidth applications, as they are limited to amplitude-type devices for the purposes of adequate phasefront

8.4 Conclusions

We have successfully demonstrated and defined several fundamental limitations of photon sieves in terms of their design, efficiency, fabrication tolerances, and bandwidth. It was found that photon sieve efficiencies can be as high as 70% in the case of infinitely small phase steps, and that photon sieve efficiency can be modeled by scaling the equation for a multilevel FZP by simple fractions, the magnitude of which follow a sinc^2 curve. The effect of photon sieve design (etch depth, patterned area, fabrication error) was also

examined earlier in this dissertation, and it was found that the performance of the photon sieve is fundamentally limited by the ability to pattern the sieve as maximally as possible, and with minimal error. It was shown that the laser ablation technique is comparable to traditional lithography techniques so long as the process is optimized, and thus suffers from no fundamental limitations in terms of fabricated photon sieve performance. Traditionally-fabricated sieves performed identically to laser-ablated sieves despite the difference in surface morphology. Lastly, the achromaticity of photon sieves was investigated in the context of the state of the art, and several fundamental limitations of the so-called HDWFCPS were discovered, presented, and are summarized succinctly at the end of section 8.3. Based on the discussion put forth in this chapter, we now have, for the first time, a relatively clear understanding of the limitations of photon sieve technology and state of the art and have contributed significant knowledge to the field.

Chapter 9: High-Efficiency Photon Sieves for Reduced Heat Affected Zones and Recast Layers in Laser Materials Processing

In this chapter, the use of photon sieves as a focusing optic in laser materials processing is investigated. Photon sieves have some unique advantages over conventional lenses in terms of their focusing properties. For example, photon sieves are able to focus to spots narrower than the Airy disk of a refractive lens with the same numerical aperture [25]. Additionally, because they are a planar optic, they do not show signs of any significant spherical aberration, which is inherent to any curved lens [31], and they are also capable of simultaneously focusing and shaping light, which would eliminate the need for a spatial light modulator or other beam shaping optics in a laser ablation system [19, 81]. Despite these unique advantages, previous to the work presented in this dissertation the low efficiencies of photon sieves would have resulted in insufficient fluences to successfully ablate material. However, with the advent of multilevel phase photon sieves presented in chapter 7, much higher fluences are now achievable, and thus laser ablation is possible.

Here, an N = 4 photon sieve is directly compared to refractive f-theta lenses typically used in Galvo systems for laser ablation. Lines were written in stainless-steel, silicon, and germanium, at various fluences above and below the material ablation thresholds, and key ablation metrics (HAZ, recast layer, oxidized surface, spattered particles, linewidth consistency, etc.) were analyzed via optical and electron microscopy. It was found that at equal fluence values, ablated lines made by the photon sieve showed a reduced HAZ in the immediate vicinity of the mark when compared to typical Galvo lenses. This was found to be the case across all three substrates. This reduced HAZ makes it

possible for the sieve to write features very close together, such as high duty cycle gratings, an example of which is shown in stainless-steel. Additionally, it was found that the photon sieve produces a reduced recast layer width, which directly corresponds to a reduced oxide layer on the substrate surface. By examining the differences in ablated marks, surface oxides, as well as the focused beam profiles from the Galvo lens and photon sieve, it was found that these advantages are a result of the photon sieve focal spot profile. Despite the focal points of the lens and sieve having nearly identical FWHM values, the sieve intensity drops off more rapidly, resulting in a narrower $1/e^2$ diameter, and thus a reduced HAZ and a reduced amount of material removed near the edge of the mark. This narrower diameter is attributed to the inherent focusing behavior of the photon sieve, first pointed out by Kipp et. al in 2001 [25].

For these experiments, an N = 4 photon sieve with 20 mm focal length and ~4 mm diameter (NA ~ 0.1) was fabricated in AZ1518 photoresist using direct-write laser lithography. Prior to film deposition, the substrate (soda lime glass) was cleaned via subsequent ultrasonic baths in acetone, isopropanol, and DI water for ten minutes each. The sample was then dried, and 4 layers of AZ1518 were spin-coated sequentially. Each layer is 2.5 μm thick, and the total final (aggregate) film thickness is 10 μm. After each spin coating, the sample was baked on a hot plate at 100°C for 2.5 minutes, and then allowed to cool to room temperature before the next film was deposited. The finished film was allowed to dehydrate for 24 hours prior to exposure. Once exposed, the pattern was developed for 3 minutes using a 1:6 concentration of AZ400K developer, and was then hard-baked for 10 minutes at 100°C. An image of the final device is shown in Fig. 44.

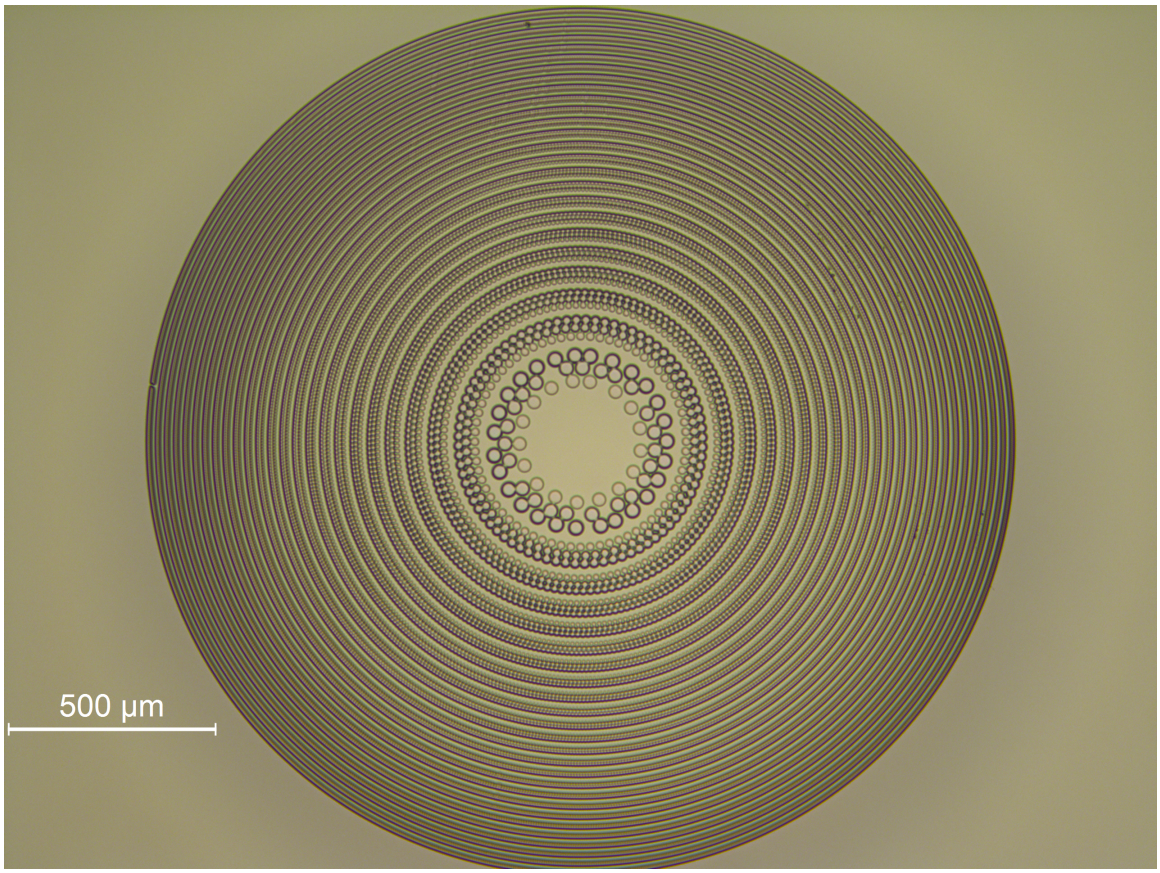

Figure 44: Optical microscope image of the photon sieve used in the laser ablation studies.

To begin, laser generated lines were drawn in Ge, Si, and stainless-steel using the photon sieve and Galvo. Prior to ablation, each sample surface was cleaned with isopropanol to remove organic residue. Fig. 45 shows an overview of sieve- and lens-written lines in stainless-steel.

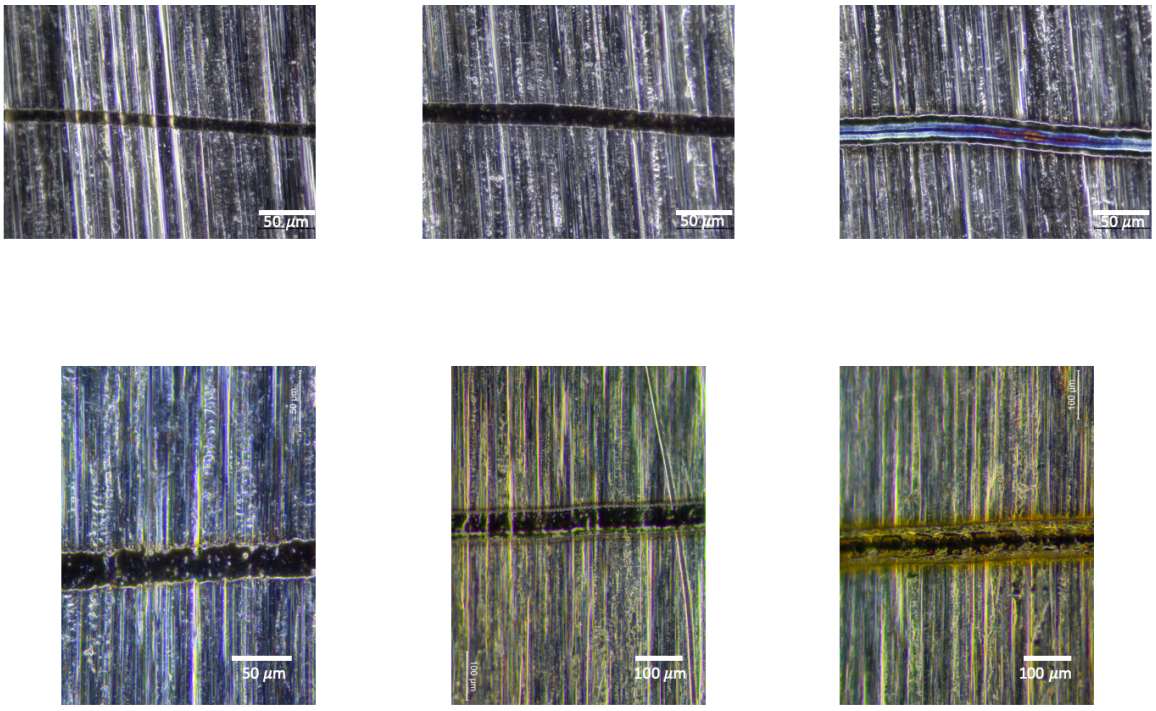

Figure 45: Lines ablated into stainless-steel using the photon sieve (top images) and lens (bottom images). Fluences were varied linearly from 3.19 J/cm^2 to 6.92 J/cm^2.

In order to evaluate the differences between corresponding lines written by the two types of lenses (photon sieve and galvo), the HAZ (as evidenced by the surface oxide layer) was analyzed. Because stainless-steel will oxidize at temperatures reached by the HAZ, the yellow/brown coloration seen in the images is indicative of surface heating of the steel, and thus the HAZ. The brightness, or intensity, of the coloration is indicative of higher temperatures. In both cases, a clear HAZ is present. However, in the case of the photon sieve, the HAZ appears to have a reduced magnitude when compared to the lens, despite the overall HAZ spreading laterally to a similar extent. Near the ablation mark of the lens, the coloration appears more intense when compared to the photon sieve, despite both HAZs reaching the same apparent magnitude at their edge. From this, we can garner than the HAZ from the lens is more intense in the immediate vicinity of the mark ("near field") compared

to the photon sieve, despite the HAZ further away ("far field") being of similar magnitude. In order to demonstrate some potential usefulness of this fact, adjacent lines were ablated into stainless-steel in a grating configuration using the photon sieve, and a duty cycle of 0.94 was achieved (< 2 μm spacing between 30 μm wide lines). An image of this is shown in Fig. 46.

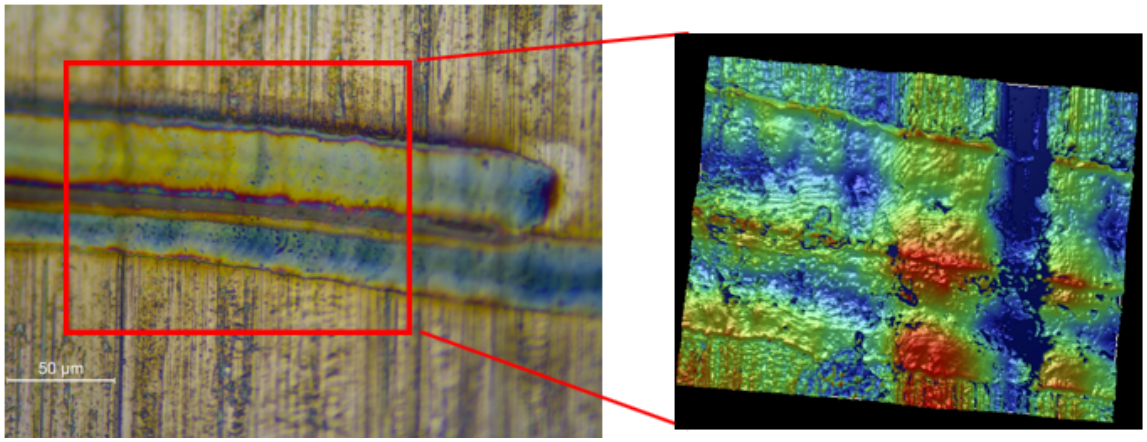

Figure 46: Lines ablated into stainless-steel using the photon sieve. Optical profilometry confirms the presence of two distinct lines with extremely fine separation. Ridges present in the profilometry are the brush-polish line of the steel. In the profilometer scan, two distinct trenches can be seen despite the brush-polish of the steel. The separation between the two lines is < 2 μm, resulting in a duty cycle of 0.94.

To further confirm the extent of the HAZ, SEM images were taken of the stainless-steel marks at 5.02 J/cm^2 for both the lens and photon sieve. When comparing the width of the HAZ zone to the overall width of the mark, the HAZ in the lens mark is clearly wider, thus confirming the optical microscope data. SEM images are shown in Fig. 47. The relative width of the HAZ in the lens case is measured as 37.3%, compared to 33% in the case of the photon sieve. Relative width, here, is defined as the fractional width of the HAZ compared to the total mark:

relative width = HAZ width / (HAZ width + melt width)

This is a relative reduction in HAZ width of 11.75% in the melting regime in the case of the sieve.

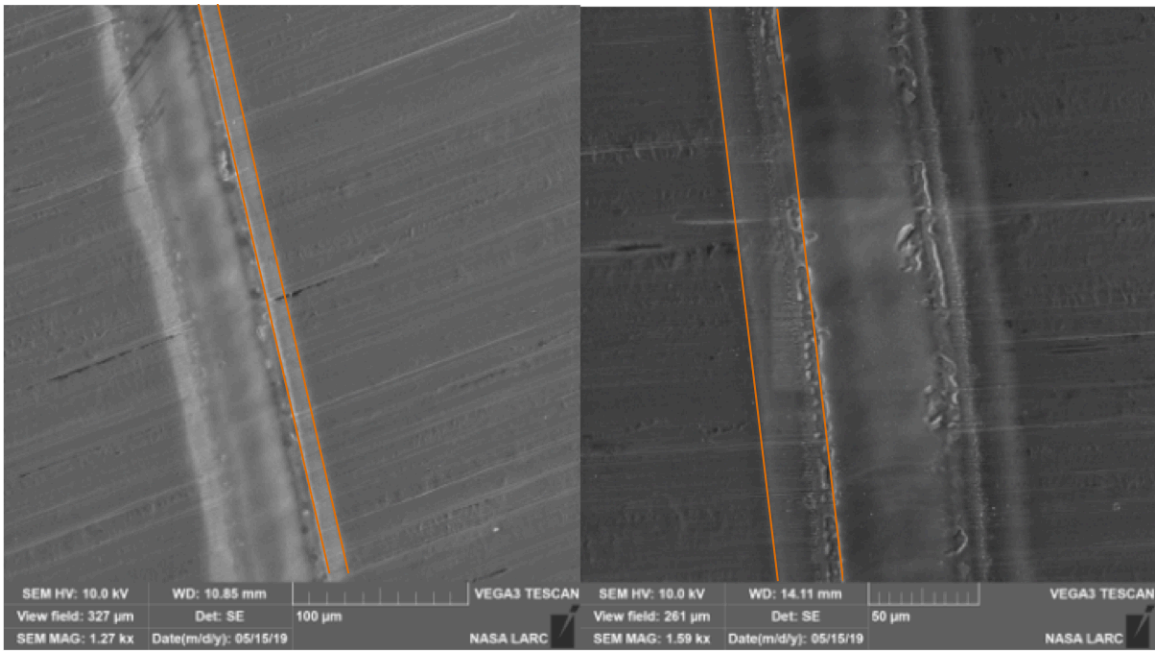

Figure 47: SEM image of the stainless-steel marks written at 5.05 J/cm^2 using the photon sieve (left) and lens (right). In each image, a melted trench is surrounded by a HAZ evidenced by the lighter coloration close to the edge of the mark. The photon sieve shows an 11.75% reduction in HAZ width in the melting regime.

Similar results were seen in Ge substrates, as can be seen in Fig. 48. In the figure, the fluences in each top/bottom pair of images are essentially the same. The photon sieve marks all have roughly the same mark width (between 21 and 22 µm), whereas the lens marks increase in width from 20 to 26 µm. Additionally, the HAZ in the near field of the mark (as seen in the brown coloration adjacent to the ablated lines) is clearly more intense in the lens case compared to the photon sieve, especially at lower fluences (far left images). The overall oxide/recast layer is less easily visible in Ge due to the instability of the oxide

layer compared to other materials, and so it is not as easily visible and thus not considered in this study). The overall result is consistent with those seen in stainless-steel.

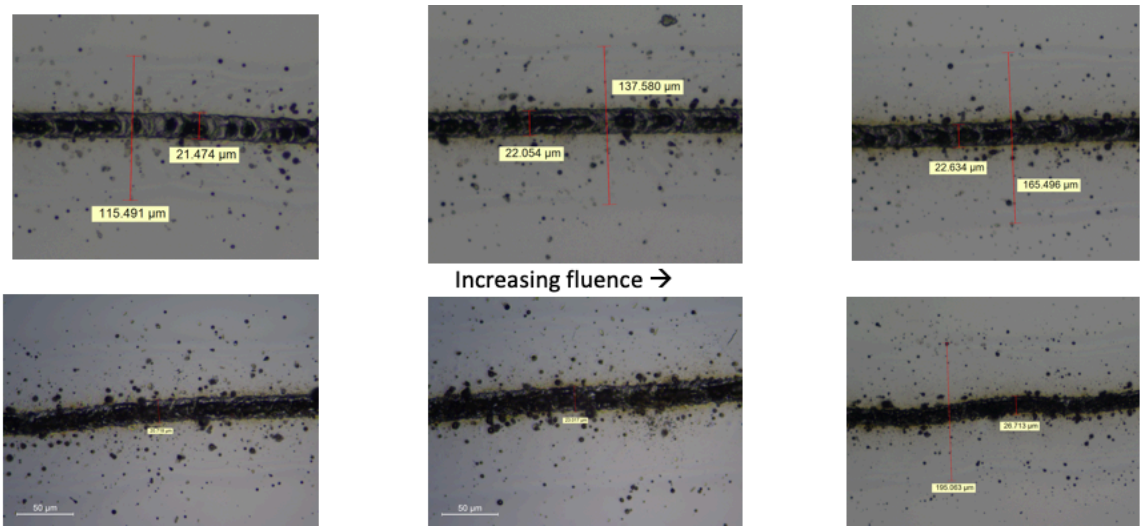

Figure 48: Lines ablated in Ge using the photon sieve (top row) and lens (bottom row). Near-field HAZ is again more intense in the lens case, similar to what was seen in stainless-steel.

Lastly, the same test was performed in Si, as the oxide layer of Si is much more stable and so the oxide layer will be easily visible with the optical microscope. Lines at three fluences were drawn: just above melting, circa ablation threshold, and well above the ablation threshold. The fluences from each lens at each of these regimes are by definition equivalent, as the melting and ablation thresholds are inherent material values. A comparison of lines at each of these fluences is shown in Fig. 49. Again, we see an increase in oxide thickness in the near field of the mark in the case of the refractive lens, which is perhaps most evident in the "circa ablation" images in Fig. 49, where the fluences are equivalent.

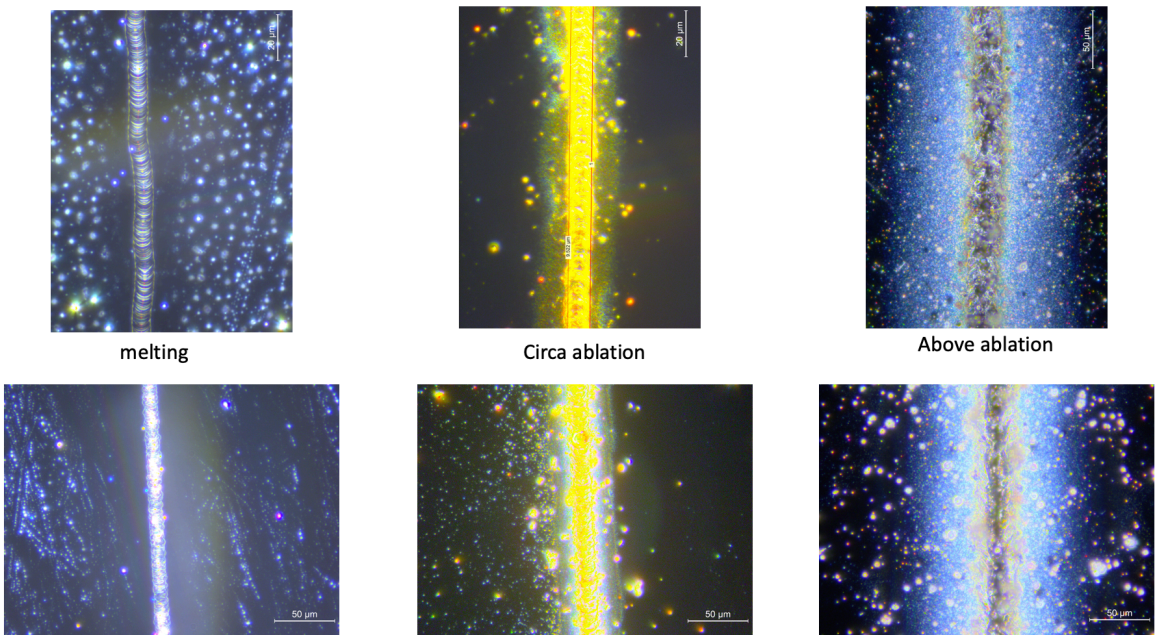

Figure 49: Comparison of lines drawn using the photon sieve (top) and lens (bottom) in Si at different fluence thresholds. The brightness in surface oxidation is indicative of the increased recast layer in the case of the lens.

A direct comparison of fluences above the ablation threshold (8.05 J/cm^2 in each case) is shown in Fig. 50, which again clearly shows the increased oxide width and thickness in the case of the lens. This is evidenced by the brighter coloration, as well as the sharper color gradient seen in the lens case. This coloration gradient is a result of the oxide thickness that forms on the Si surface. Increased temperatures at the Si surface (as a result of the HAZ) result in increased thicknesses of the oxide layer, which causes an interference effect, giving way to the different colors seen in the image [81-83]. Yellow colors correspond to thicker SiO_2 layers, while green and blue indicate thinner layers (in that order). Note that the thickness/color is cyclical due to the interference effect that generates the oxide color. However, the relative thickness between the colors is consistent.

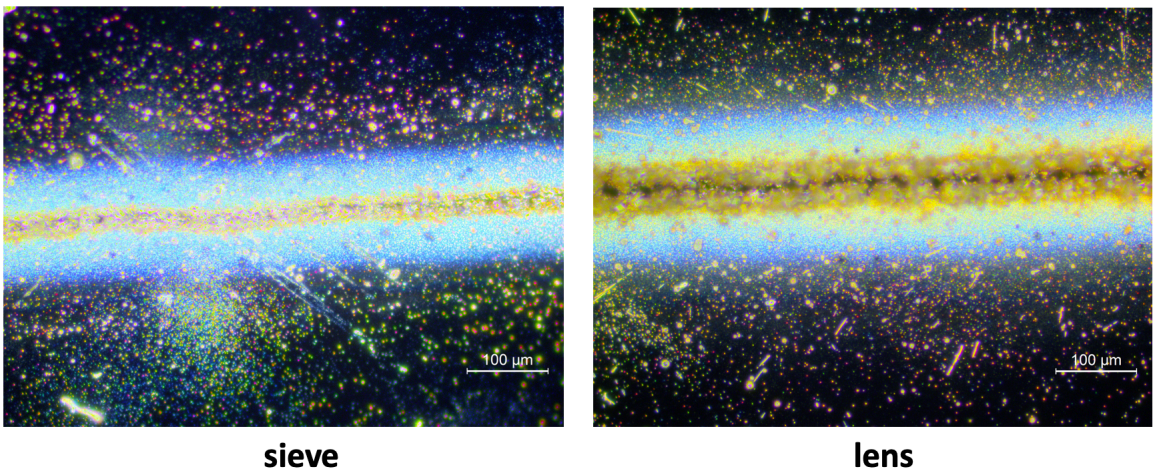

Figure 50: Lines ablated into Si using the sieve (left) and lens (right) at 8.05 J/cm^2. The more intense color gradient seen in the lens case is indicative of a larger oxide region in the near-region of the mark.

SEM images were also taken of the Si substrates in order to evaluate the difference in the surface quality of melted and ablated marks, as well as to analyze the spattered particles in terms of the lateral range of debris spread as a result of ablation. Based on the SEM data shown in Fig. 51, where each line is written at the same fluence, it can be clearly seen that the lens produces more spattered particles at greater distances than the sieve. Whereas the sieve ablated particles are primarily contained to within the oxide layer (shown in the image as the sharp white lines along either side of the ablated line), the lens generate a large number of particles outside of the oxide layer, thus causing greater contamination of the Si surface. Additionally, the relative widths of the oxides of the sieve and lens are measured to be 87.9% and 92.1%, respectively, which represents a ~5% reduction in oxide width in the case of the photon sieve. Melt lines written by the two optics looked essentially indistinguishable under SEM.

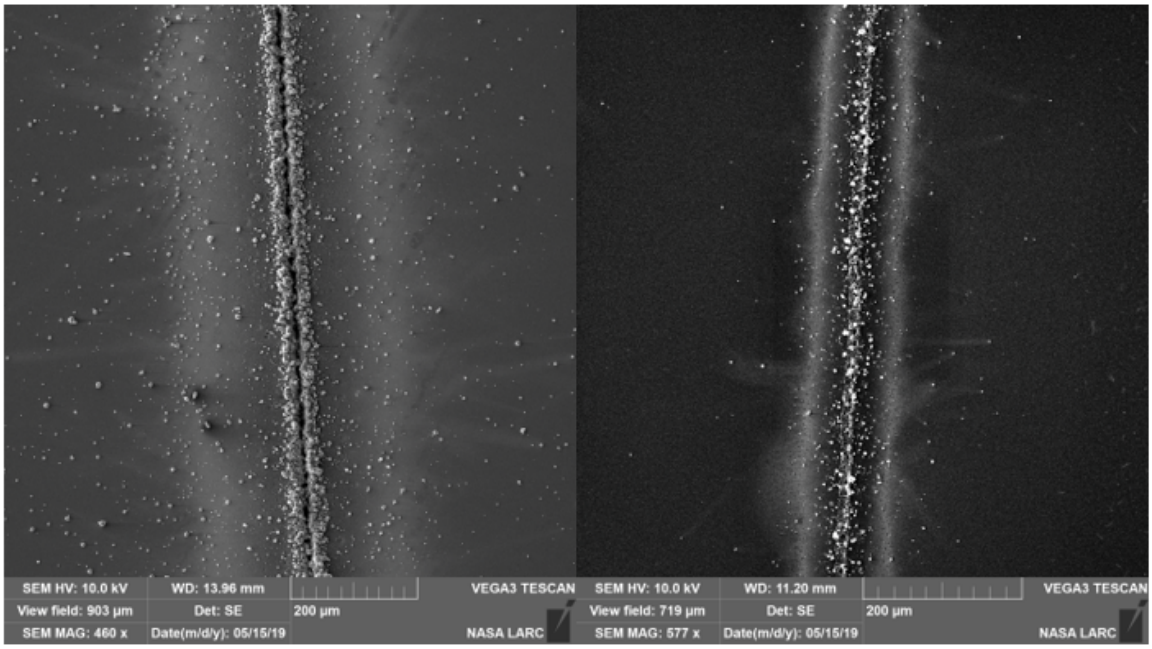

Figure 51: SEM images showing lines ablated in Si via lens (left) and photon sieve (right). The sieve shows a 5% reduction in oxide width as well as fewer ablated particles spattered outside of the oxide layer. The fluence in each case is 16.56 J/cm^2.

The ablative properties of the lens and photon sieve were also characterized in the few-laser pulse regime. At equal fluences above the ablation threshold, single spots of 100,000, 10,000, 1,000, 100, and 10 laser pulses were drilled into Si. At all pulse numbers, the lens showed an increased oxide thickness compared to the sieve, again as evidenced by the rainbowed coloration in the area very near to the mark. Micrographs of the 100 pulse and 10 pulse cases are shown in Fig. 52. As is seen in the figure, in the 100-pulse case, each optic shows a colorful oxide layer around the rim of the ablated crater. However, the photon sieve coloration is much more contained, despite cycling through the same colors (oxide thicknesses) as the lens. Whereas the yellow and green colored oxide layers (thicker layers) in the case of the sieve are contained to within ~25 µm of the crater edge before dissipating to the consistent blue color seen also in Fig. 50, the lens shows yellow and green coloration

up to ~40 μm from the crater edge. The 10-pulse case is similar, albeit with a reduced oxide thickness/width. The brown coloration around the craters is indicative of a low-thickness oxide layer resulting from a reduced oxide from the 100-pulse case, as expected. In the photon sieve crater, the brown color is much lighter than the lens crater, and there is less blue/purple coloration around the very edge of the ablation mark. The results from this single-spot test also point to the photon sieve showing a reduced surface oxidation compared to a lens. The uneven nature of the oxide colors in the case of the 100-pulse photon sieve crater is an optical effect as a result of the ablation rim. The rim of the ablated crater is spilling over onto the oxide, thus masking the coloration.

The formed oxide layer on silicon is likely not a result of the HAZ, as the heat dissipation for nanosecond laser pulse interaction with silicon occurs on too short a timescale to form such thick oxide layers. In order to confirm this, laser marking of silicon using a long-pulse laser (0.1-0.3 ms pulse width) at 1070 nm wavelength was performed. This longer pulse width will have a much more thermally-dominated interaction that will result in a large HAZ and reduced ablation. A clear oxide layer can be seen around the rim of the interaction site in these samples. The thickness of the oxide can clearly be seen increasing as the pulse width increases from 0.1 ms to 0.3 ms. Based on this, as well as the increased amount of vaporized/molten material redeposited around the ablation marks in Figs. 50, 51, and 52, we believe that the formed oxide layer is a result of the easily-oxidized molten/vapor phase silicon that is ejected from the ablated region. This recast layer is much more easily oxidized due to the non-solid phase of the material, and therefore is capable of forming much thicker oxides than purely thermal processes in nanosecond laser pulses. Additionally, a scotch tape delamination test was performed on the lines written in silicon

(Fig. 6, for example). The oxide layer was easily removed by the scotch tape, suggesting that the oxidized material was redeposited vaporized silicon particles (recast layer), as a purely thermally-grown oxide would not delaminate so easily. An SEM image and overlaid elemental spectroscopy images showing the redeposited oxide nanoparticles are shown in Fig. 53.

In order to investigate the origin of these differences, beam profiles from the photon sieve and galvo lens were measured using a commercial CCD profiler with 3 μm pixel pitch. Upon initial inspection, profiles seem very similar. Both are nicely Gaussian (as confirmed via least squares fitting of the profile data to a mathematical Gaussian), both are similar size and show uniform intensity distribution. However, when the plots are overlaid, it is seen that the photon sieve intensity drops off more rapidly than the lens intensity. Above the FWHM, each profile is essentially identical. Below the FWHM, the sieve beam is "sharper", that is the intensity drops off more rapidly and a narrower $1/e^2$ diameter is present. This is shown in the overlaid beam profiles in Fig. 54. Note that the photon sieve spot has been defocused slightly (such that the FWHM of each beam is equivalent) to more directly illustrate the differences between the two focused beams. Viewed another way, the ratio of FWHM and $1/e^2$ diameter is larger in the case of the photon sieve. Here, this ratio for lens and photon sieve were measured as 0.60 and 0.65, respectively. This is to say that the photon sieve focal point FWHM is more similar to the $1/e^2$ diameter than is the case for the lens focal point. Specifically, the difference in total deposited intensity (area under the curve) is ~5%, all of which is concentrated in the tails below the FWHMs of the beam profiles. Because the intensity below FWHM is lower for the photon sieve, there is less material removed from the substrate further from the center of the laser spot. As a result,

despite fluences being equivalent, the photon sieve will have a lower HAZ and reduced recast layer/surface oxidation. This reduction in $1/e^2$ intensity is known for photon sieves and was first explained by Kipp in 2001. It comes as a result of the pinhole distribution in photon sieves, which can increase or decrease resolution as desired based on their size and spatial distribution [25]. Therefore, these improvements are a natural consequence of the photon sieve. Additionally, the photon sieve will focus to a narrower/more vertical spot intensity compared to the lens for a given NA. The depth of focus in each case will be the same, as depth of focus is determined geometrically by the NA of the lens system, but the photon sieve will have a higher resolution. This combination is advantageous for many applications.

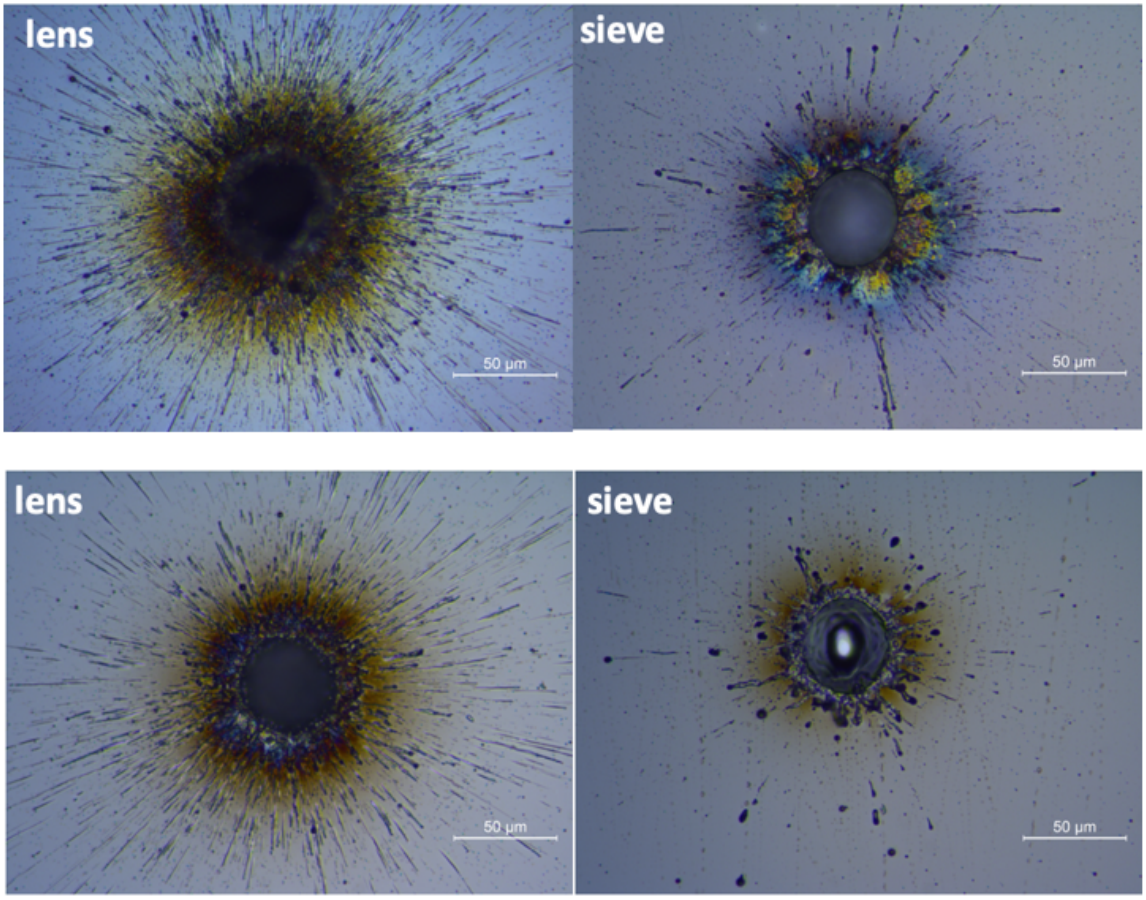

Figure 52: Optical microscope images of ablated craters using the photon sieve and lens. Craters were made using 100 (top) and 10 (bottom) pulses of equal fluences. The photon sieve again shows a thinner and/or more concentrated oxide layer around the crater. The fluence in each case is 8.05 J/cm^2.

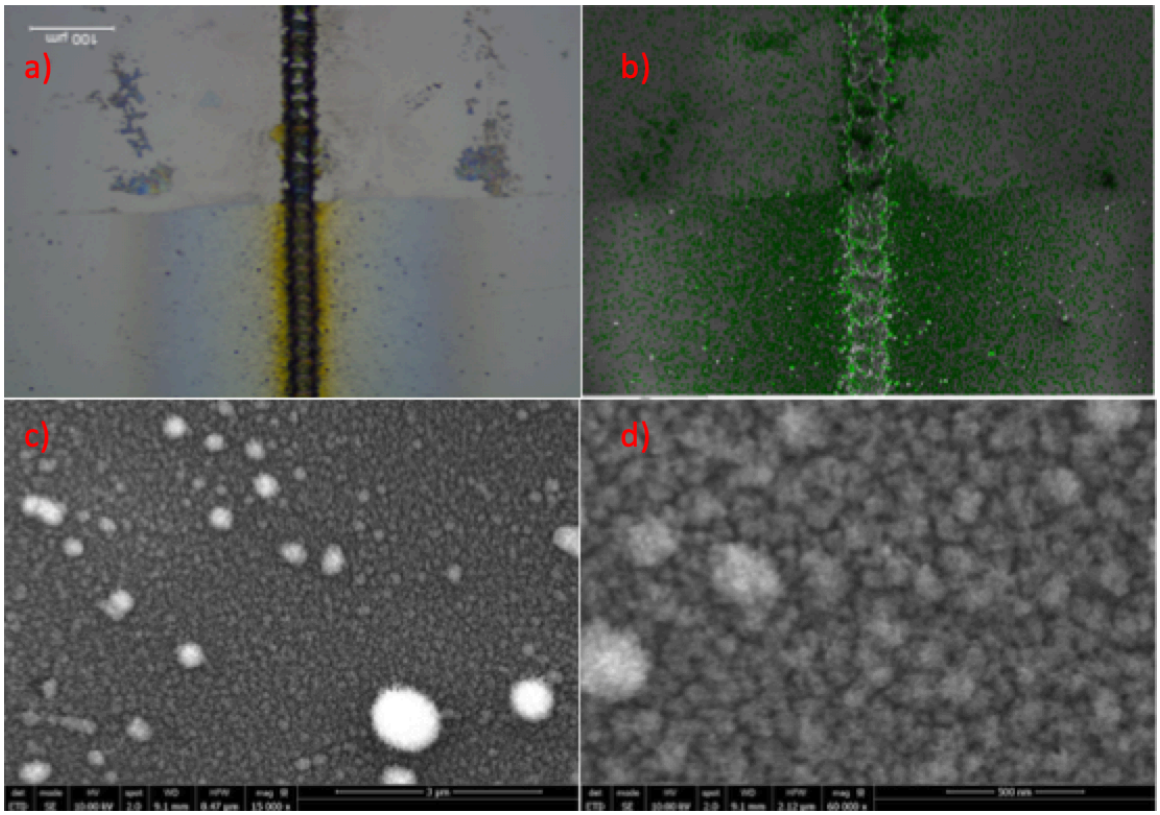

Figure 53: (a) Optical microscope image showing the boundary between scotch tape-delaminated oxide region and the undisturbed recast layer oxide. (b) SEM image of the same region depicted in (a) with energy-dispersive x-ray spectroscopy data overlaid to show the oxygen concentration on the surface (oxygen shown in green). (c) SEM image showing the recast layer oxide surface composed of nanoparticles that have re-agglomerated on the surface to form a thin film (scale bar is 3 microns). (d) Higher magnification view of (c) (scale bar is 500 nm).

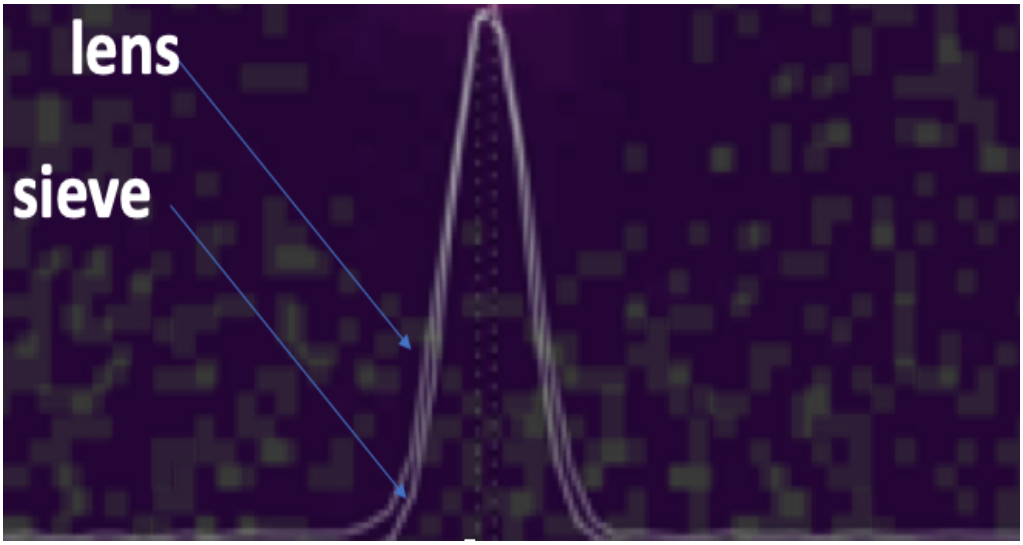

Figure 54: Overlaid beam profiles of the lens and photon sieve showing similar FWHMs, but a narrower $1/e^2$ diameter in the case of the photon sieve.

Based on the research presented in this chapter, it can be concluded that photon sieves offer unique advantages in the realm of laser processing of materials. We have shown a reduction in HAZ and recast layer oxide thickness and width, as well as clear surface morphology difference away from the ablated marks. These results suggest that photon sieves could be useful in laser processing of materials where the HAZ or surface oxidation must be carefully controlled, or small spot sizes are desirable, such as in optical surgery, welding, semiconductor processing, or applications that require high duty cycle / compact features [21-24]. The work presented here was enabled by previous work reported in chapter 7 of this dissertation, and thus represents a unique and important step forward in photon sieve technology as a result of the dissertation.

Chapter 10: Conclusions and Future Work

10.1 Conclusions

In this work, high-efficiency photon sieves were designed, simulated, fabricated, and demonstrated. First, a novel laser ablation fabrication technique was developed and demonstrated for use in photon sieve fabrication. Limitations of this technique were studied, and the effect of surface morphology on photon sieve performance was understood by comparing measured optical performance to simulated values.

Photon sieves were then demonstrated on flexible, transparent substrates using this same technique in order to demonstrate an increase in efficiency, as well as to show the robustness of the laser process. FDTD simulations were used to determine the focusing capabilities of the binary phase photon sieves, as well as to understand the effects of fabrication error on efficiency. Laser processing parameters were optimized and their effect on the photon sieve surface morphology were studied. Optimized photon sieves showed good agreement with theoretical results, which further allowed for an understanding of the laser process on photon sieve performance.

To increase the efficiency of these photon sieves, a multilevel phase approach was adopted from the Fresnel zone plate. First FDTD simulations were performed to understand the effect of phase step number of photon sieve efficiency, and an analytical efficiency limit of 70% was discovered. Experimentally, N = 4 and N = 8 photon sieves were demonstrated and showed efficiencies of 25% and 49.7%, respectively, which is nearly 5x higher than any photon sieve previously reported. Additionally, these photon sieves maintained their low side lobes as well as their focal spot size (i.e. an N = 8 photon sieve has the same spot size as an N = 2 photon sieve with the same diameter and focal length).

These discoveries are important for applications where photon sieve contrast and resolution are desired, but where the low efficiency had previously hindered their use. Additionally, these photon sieves were demonstrated at 10.6 microns wavelength in order to show their usefulness in the infrared spectral regime.

Several fundamental limitations of photon sieves were discovered throughout the course of this dissertation, specifically those related to operation light bandwidth, fabrication technique, and efficiency. The analytical limit of 70% was further studied, and a numerical model was developed based on the sinc^2 function used to predict efficiencies of MLFZPs. This model was compared with FDTD and experimental data and was found to agree well. The MLFZP formula need only be scaled by a simple fraction that varies with step number in order to successfully predict the efficiency of a MLPS.

In order to understand the effect of illumination bandwidth, the current state of the art was examined, and the widest bandwidth photon sieve design (HDWFCPS) was studied numerically and experimentally. It was found that this design can only be used over broad-spectrum illumination at low numerical apertures, as the geometry is overly reliant on depth of focus considerations. Additionally, it was found that HDWFCPS is not compatible with binary phase designs, as the increased space between adjacent rings allows for too much stray light, thus reducing the strength of the phase modulation across the aperture.

Additionally, it was shown that the laser ablation technique is comparable to traditional lithography techniques so long as the process is optimized, and thus suffers from no fundamental limitations in terms of fabricated photon sieve performance. Traditionally-fabricated sieves performed identically to laser-ablated sieves despite the difference in surface morphology.

Lastly, an application of the newly-developed high-efficiency photon sieves was demonstrated, and it was found that photon sieves reduce the HAZ in laser materials processing. This reduction is a result of the decrease in overall optical energy deposited onto the material surface. Despite a photon sieve and refractive lens having identical FWHM values, the photon sieve $1/e^2$ diameter was smaller than the refractive lens, which decreases the overall incident energy, and subsequently the HAZ of the material. This was shown in stainless steel, germanium, and silicon, thus demonstrating that the effect is independent of substrate material. This finding could have widespread use in laser materials processing applications.

10.2 Future Work

In order to fully realize optimal photon sieves, the following things should be addressed: achromatic behavior, actively-tunable devices, and additional applications. Photon sieves as diffractive lenses are unique in that they have improved contrast and resolution of other diffractive lenses, but they are limited by their low operation bandwidth when compared to other planar lenses (metasurfaces, microlenses, etc.). If photon sieves can be made widely achromatic with high efficiencies, their usefulness would be greatly increased, and their impact of the scientific community would be largely significant. These achromatic photon sieves would open up additional applications that can be explored. Additionally, an actively tunable photon sieve would be useful for a variety of applications such as LIDAR systems, space optics, 3D laser materials processing, and spectral imaging.

Summary of Publications, Conferences, Inventions, and Awards

List of publications

1. **M. N. Julian,** D. G. MacDonnell, and M. C. Gupta, "Fabrication of photon sieves by laser ablation and optical properties," Optics Express **25** (25), 31528-31538 (2017).
2. **M. N. Julian,** D. G. MacDonnell, and M. C. Gupta, "Flexible binary phase photon sieves on polyimide substrates by laser ablation," Optics Letters **43** (10) 2368-2371 (2018).
3. **M. N. Julian,** D. G. MacDonnell, and M. C. Gupta, "High efficiency flexible multilevel photon sieves by single-step laser-based fabrication and optical analysis," Applied Optics **58** (1) 109-114 (2019).
4. **M. N. Julian** and M. C. Gupta, "Photon sieves reduce heat affected zone in laser ablation processes," *(in preparation).*
5. **M. N. Julian,** C. Williams, and H. J. Kim, "Actively and passively tunable mid-wave infrared plasmonic metasurface filters based on phase change material Babinet inverted structures," *(in preparation).*

Conference Presentations

1. **M. N. Julian**, D. G. Macdonnell, and M. C. Gupta, "Diffractive lenses by laser direct writing," *6th SLIMS – International School on Lasers in Materials Science,* Venice, Italy, July 2018.

2. **M. N. Julian,** D. G. Macdonnell, and M. C. Gupta, "High efficiency multilevel phase photon sieves enabled by laser direct writing," *OSA Frontiers in Optics 2018,* Washington DC, September 2018.
3. **M. N. Julian,** C. Williams, and H. J. Kim, "Tunable mid-wave infrared plasmonic filters based on the phase-change material GeSbTe," *SPIE Photonics West 2019 – OPTO – Optical Components and Materials XVI,* San Francisco, California, February 2019.

Invention Disclosures

1. **M. N. Julian,** D. G. Macdonnell, and M. C. Gupta, "high efficiency multilevel photon sieves," U.S. Provisional patent application to be filed by NASA LaRC (2018).
2. **M. N. Julian,** C. Williams, and H. J. Kim, "Tunable mid-wave infrared filter based on exotic phase-change materials for multispectral imaging in science instruments," (2018).

Awards

1. National Institute of Aerospace Best Student Paper Award 2017, for **M. N. Julian,** D. G. MacDonnell, and M. C. Gupta, "Fabrication of photon sieves by laser ablation and optical properties," Optics Express **25** (2017).
2. Roger Kelly Award for Best Student/Post-doc Poster/Presentation, *6th Annual International School for Lasers in Materials Science* (2018).

Appendix A: Plasmonic Control of Chromatic Focal Shift in Photon Sieves

Plasmonics has been an interesting option in recent years for a variety of lensing applications, as they allow for tailored, fine-tuned control of light propagation at the nanoscale. For example, plasmonics has been shown in the form of Fresnel zone plates and zone plate-like structures for use in multispectral lensing devices [71-73]. Typically, this is accomplished by spatially multiplexing [71, 73] or monolithically integrating [72] nanostructured lenses designed for different wavelengths. These nanostructured lenses use metallic arrays to selectively filter or scatter light of a specific wavelength, with a certain bandwidth, generally tens of nanometers, while absorbing all light outside of this bandwidth. Thus, these structures act as a method of removing light away from the design wavelength in order to reduce the chromatic aberration of each lens. By adding multiple lenses, each with a unique design wavelength, multiple colors can be focused to the same point with minimal chromatic aberration.

In this work, we extend this concept to the field of photon sieves via FDTD simulations, where the "pinholes" will be made up of a nanostructured metal-insulator-metal (MIM) array that selectively filters the incident light and scatters it, thus acting like de facto apertures that allow for interference-based focusing as a normal photon sieve. These structures can then be coated with an insulating layer, such as photoresist, in order to build a multilayer structure to increase the overall device efficiency, and multiple designs can be spatially multiplexed to include more wavelengths. Images of the design concept and MIM structure are shown in Fig. 55. The MIM structure consists of an oxide layer, shown here as HfO_2, sandwiched between two Al layers, and is based on previously

published literature [74]. Upon irradiation with optical light, the bottom metallic layer will diffract the light. At the resonance wavelength, one of these orders will be parallel to the metal-insulator interface and will be supported as a plasmon resonance by the interface. This occurs when the phase matching condition for the MIM waveguide is satisfied. The guided plasmon mode can then be scattered by the second Al layer and propagate into the far field. By altering the period or refractive index of the insulator layer, the resonance passband can be tuned to different colors.

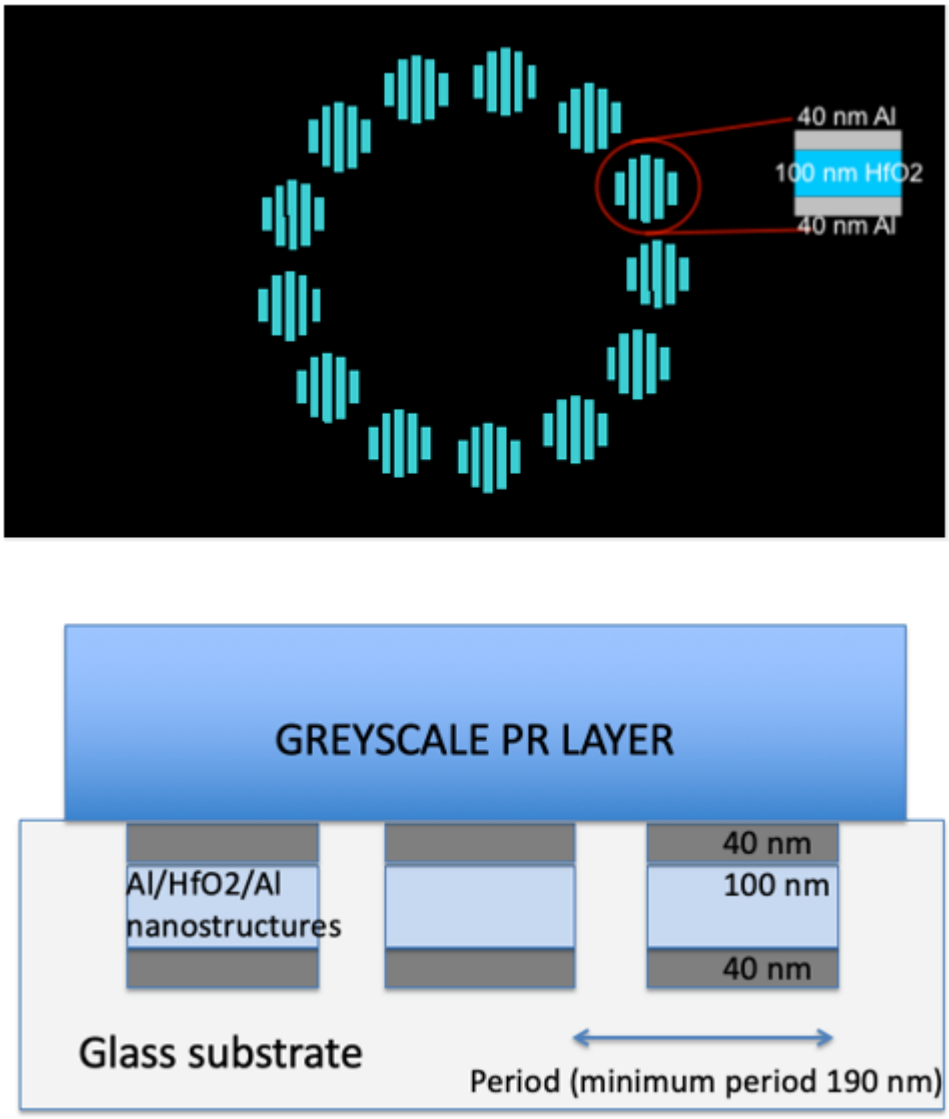

Figure 55: Example of inner ring of the proposed plasmonic MIM photon sieve (top), and a single array showing geometry and periodicity (bottom). The array can be buried into a glass substrate and covered with a photoresist layer in order to generate higher efficiencies.

Using FDTD simulations, transmission plots of the MIM array at different periodicities were obtained, as shown in Fig. 56. A transmission monitor was placed in the optical near field of the arrays, and the E and H fields were recorded. These transmitted fields were then arranged in a photon sieve pattern, where each field was positioned as a single, finite-width "pinhole". The fields were then propagated into the far field in order to simulate the

focusing of the photon sieve. E-field intensity distributions along the optical axis of the sieve are shown in Fig. 57 for wavelengths of 450 and 650 nm. As is seen in the figure, each wavelength focuses to the same designed focal length.

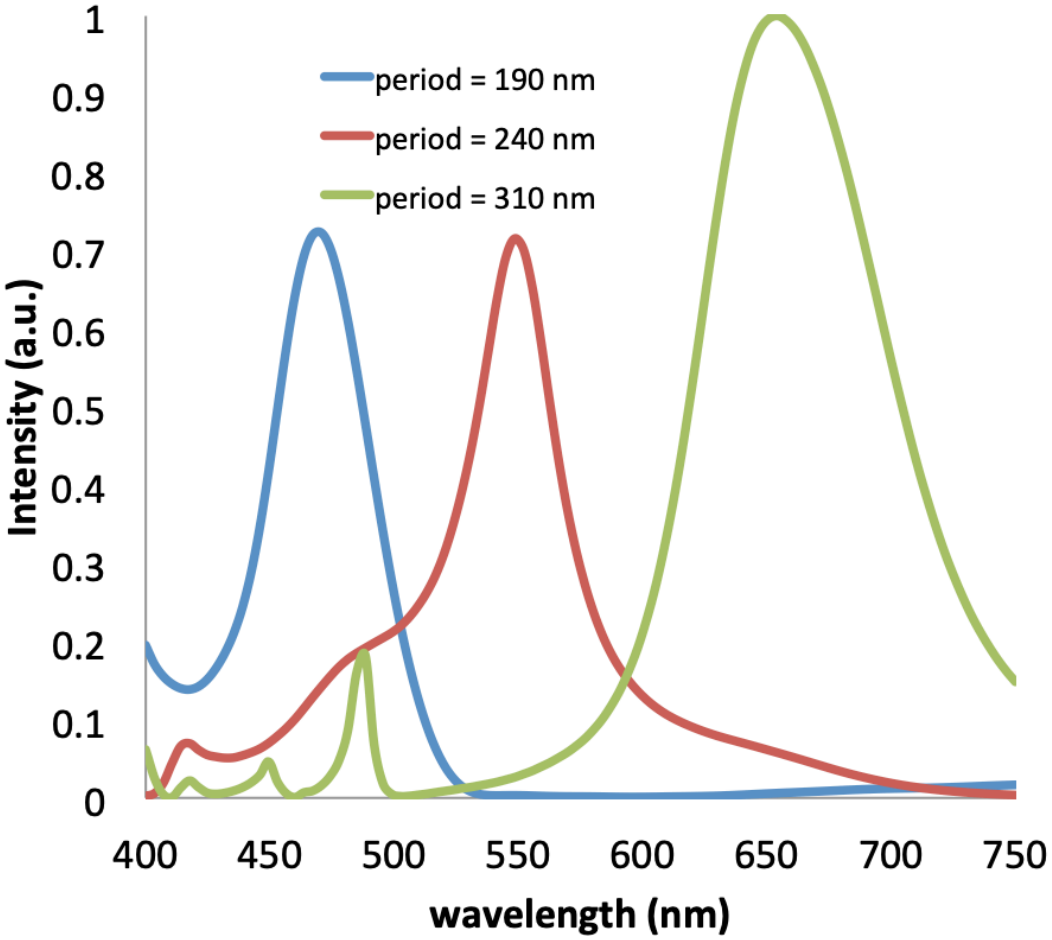

Figure 56: Plot of transmission vs. MIM array period for the proposed structure.

However, despite the relative success of this concept, which was expected based on past publications [69-71, 73], the design itself has several major limitations. In terms of spatial multiplexing, fabrication becomes very difficult as more wavelengths are added, which limits the achromaticity of the optic. Additionally, spatial multiplexing with a greyscale

layer adds an additional level of complexity, as overlapping layers would have to either be negated or a compromise in efficiency would be made. The MIM design itself does not easily lend itself to spatial multiplexing. Nanoantenna arrays can be easily multiplexed [71, 73, 75], but the number of possible wavelengths is still low, and antennae do not operate properly when coated with a dielectric layer such as a photoresist, or when they are buried in the substrate.

Additionally, the achromatic behavior of the optic itself is not perfect. Based on the transmission bandwidths shown in Fig. 56, a plot of focal length vs. wavelength can be generated and is shown in Fig. 58. As can be seen, the device is achromatic at the design wavelengths, but experiences slight blurring at wavelengths within the passband of the array. Based on these results, other avenues of achromatic photon sieves needed to be pursued, as the design limitations described above proved too costly to device performance.

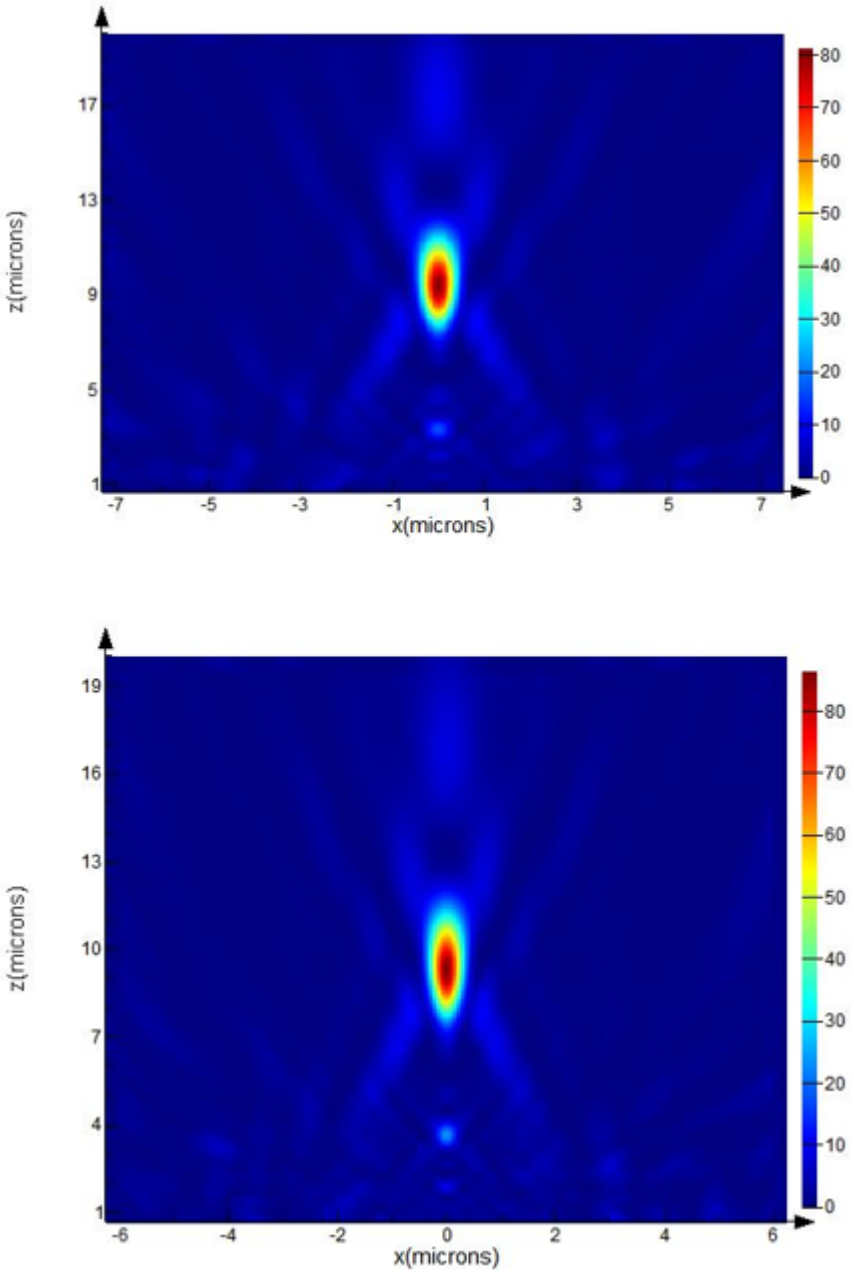

Figure 57: E-field distributions along the optical axis of the plasmonic photon sieve at 450 nm (top) and 650 nm (bottom) design wavelengths.

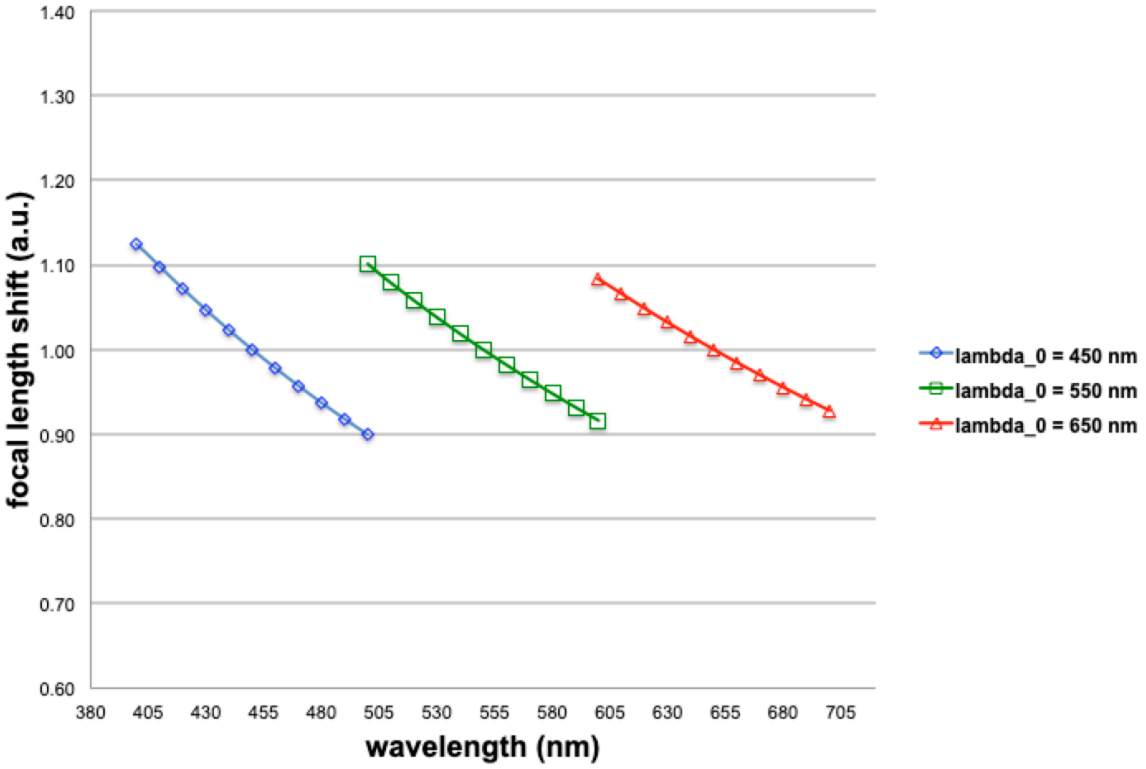

Figure 58: Calculated focal length shift across the visible spectrum for the proposed photon sieve. Design wavelengths were taken to be 450, 550, and 650 nm. The dispersion was calculated based on the standard photon sieve design equation given in chapter 1, rearranging the equation to solve for focal length and using wavelength as the independent variable.

The work presented in this appendix, along with section 8.3 of the dissertation, served to analyze the potential for demonstrating achromatic photon sieves. Two methods of controlling chromatic aberrations were proposed and investigated, and their efficacies evaluated. In each case, the designs had unique limitations that would affect the practicality of implementing such a design in practice. In the case of plasmonically-enhanced photon sieves, the chromatic aberrations were not truly eliminated, and multiple designs would need to be spatially multiplexed in order to further reduce the blurring of the focal point, which is not feasible from a fabrication standpoint. The HDWFCPSs are much simpler and easier to fabricate but suffer from drawbacks and limitations related to their numerical aperture, phasefront strength tradeoff, and efficiency. Overall, the results

of this chapter suggest that photon sieves are not appropriate optics for broad spectrum focusing applications in which chromatic aberrations must be eliminated. However, other options for achromatic diffractive optics do exist [80], and therefore it is postulated that the photon sieve geometry itself is inherently limiting in this area. Multispectral performance, on the other hand, is easily achievable via harmonic diffraction and/or wavefront coding.

Appendix B—Additional Research: Actively Tunable Mid-infrared Plasmonic Metasurface Filters Based on GeSbTe Phase-Change Materials

During the final year of the course of this Ph.D. study, additional research was undertaken at NASA Langley Research Center in collaboration with Dr. Hyun Jung Kim and Dr. Calum Williams of the University of Cambridge. This research is still in progress, but results obtained thus far will be presented in this chapter. As is indicated by the title of the following section, the research aimed at designing, fabricating, and demonstrating an actively tunable plasmonic metasurface based on phase change materials (PCMs) for the purpose of mid-infrared transmission filtering.

The mid-wave infrared (MWIR) spectrum contains a wealth of invaluable information: from the spectral 'fingerprint' of many chemical species, with applications in remote sensing, to radiant thermal signatures, utilized in astronomical and military imaging systems. Traditionally, filtering for the MWIR is achieved by means of passive multilayer interference (dichroic) filters, allowing for an extremely narrow filtering bandwidth. Image sensors in the MWIR typically utilize focal plane array (FPA) technology, which is similar to pixel arrays in the visible in that they consist of solid-state sensors with an overlaid filter mosaic in order to generate wavelength-encoded images. Depending on the wavelength range, detectors fabricated from a specific semiconductor material (e.g. InSb for MWIR applications), are covered by a mosaic baseplate to allow for detection of individual wavelength bands. Additionally, other, more advanced device types can be utilized, such as quantum well FPAs, however the fabrication complexity and cost rise significantly [85]. MWIR FPAs and filters are generally analogous to their visible spectrum counterparts, but

with much larger dimensions and more exotic materials/material stacks. Recently there have been developments toward 'smart' spectral imaging technologies; whereby the ability to provide electrically tunable narrowband filtering—spanning the entire MWIR—is highly desirable. Common technological approaches include Fabry-Perot-based micro-electro-mechanical systems [86] and liquid crystal tunable filters [87]. However, these approaches suffer from various limitations, such as: having moving parts, are complex to manufacture, have slow response times and limited spectral bandwidth / resolution.

In this work we numerically study the performance of a novel, narrow-bandwidth, actively tunable optical transmission filter operating in the MWIR. GeSbTe (GST) is a phase change material, exhibiting a large, reversible change in its refractive index upon phase transition (crystallization). This occurs when the GST film is heated above a critical temperature determined by its stoichiometry, generally near 80°C [88]. By combining thin (60 nm) GST films, we are able to tune the effective index of a sub-wavelength GST layer increasing the temperature (through an applied voltage or optical stimulus) across the GST layer. By integrating an Ag nanostructured array along with the GST film, surface plasmon resonance (SPR) can be excited at the Ag/GST interface. This results in high transmittance on resonance, with a < 200 nm full width half maximum (FWHM) band-stop within the 3-5 μm spectral range. Off resonance, the device shows near perfect reflection/absorption behavior. Additionally, the device can be passively tuned by altering the geometry of the nanostructure array. With passive and active tuning combined, this nanostructured device concept exhibits near perfect absorption beyond the 3-5 μm wavelength range.

B.1 Device Theory and Design

In 1998, it was discovered by Ebbesen et. al. that a periodic array of sub-wavelength nanoholes had an associated resonance at particular wavelengths, which gave rise to a phenomenon dubbed "extraordinary optical transmission" [47, 89]. At a particular wavelength, the transmission of light through the array is several orders of magnitude higher than what is predicted by classical aperture theory – in fact, the transmission is greater over 100% when normalized to the open area of apertures on the surface. Since the publication of that discovery, nanohole arrays (and other sub-wavelength array structures) have been of huge interest across various fields of optics and photonics, especially for color (wavelength) filtering applications [90]. Despite the popularity of hole arrays in research applications, there is some contention regarding the physical mechanism responsible for the phenomenon. However, most researchers agree that surface plasmons (SPs) play an important role in the process.

To provide a simplified explanation of the origin of the filtering phenomenon, consider a periodic array of sub-wavelength holes in a metallic film. This hole array is essentially a grating structure with a given periodicity. As such, the grating can diffract incident light at various angles, one of which will be parallel to the metal surface. This parallel diffracted order will couple to the free electrons in the metal, generating a SP wave. The SPs will travel through the hole along the boundary between the metal film and surrounding dielectric and will then re-radiate out the other side. At the resonance wavelength (dictated by the array periodicity and material properties, as explained below), these SP will form standing waves, which give rise to a large electric field intensity above each hole, thus generating a large increase in transmission at the resonance wavelength.

Alternatively, we can consider this phenomenon as a result of momentum matching between the incident light and the SPs of the metal film. If we consider the wave vector of a classical surface plasmon:

$$k_{sp} = \frac{\omega}{c}\sqrt{\frac{\epsilon_m \epsilon_d}{\epsilon_m + \epsilon_d}} \tag{15}$$

where ω is the electromagnetic field frequency, c is the speed of light in vacuum, and ε_m/ ε_d are the permittivity of the metal film and surrounding dielectric, respectively. We can plot this dispersion relation as a function of frequency, as shown in Fig. 59.

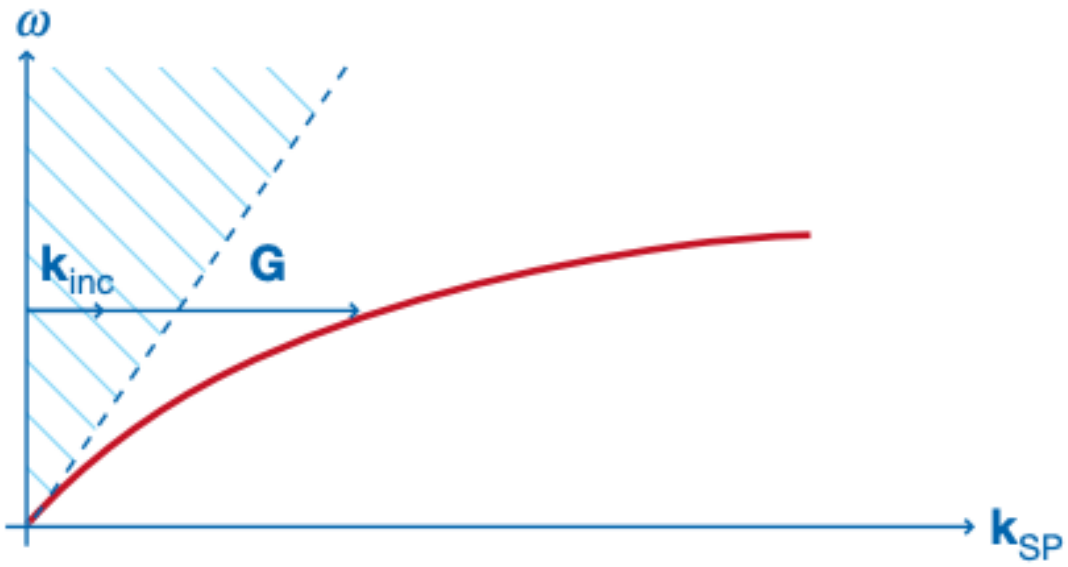

Figure 59: SP dispersion relation. The dotted line represents the light line, which separates free-space photons from evanescent photons. As is indicated by the arrow, the grating can provide additional momentum to the incident light, allowing for excitation of SP modes on the metal surface. Figure reproduced from [89].

As can be seen from the figure, the real part of the SP wave vector is always below the asymptote known as the "light line" which denotes free-space propagating photons from evanescently decaying ones – i.e. photons to the right of the light line decay exponentially as they propagate and cannot be excited directly by light alone due to their high momentum, as shown in the figure. However, the grating itself has a momentum, which can couple to the incident radiation and provides the necessary "kick" to excite SP waves on the metal surface. The momentum-matching condition required for this excitation is given as:

$$k_{sp} = k_0 \, sin(\theta) + \; l * \frac{2\pi}{a_0} \tag{12}$$

where G is the grating momentum and is well-known to be related to the lattice vector reciprocal $2\pi/a_0$, and l is an integer, When we consider this relation in the context of a square array of holes, we can obtain the position of the resonance wavelength given by the following equation:

$$\frac{\lambda_{res}}{\sqrt{l^2+j^2}} = a_0\sqrt{\frac{\epsilon_m\epsilon_d}{\epsilon_m+\epsilon_d}} \tag{13}$$

where l and j are integers. This equation changes very slightly depending on the array geometry, but the general form is the same. From here, we can see that by altering our choice of metal, dielectric, and array periodicity, one can fine-tune the resonance wavelength to be placed wherever they like.

A phase change material (PCM) is a material that undergoes a structural phase change (e.g. amorphous to crystalline) when exposed to a particular external stimulus. One example of a common PCM is GeSbTe (GST). It has been established for several years that GST undergoes a reversible phase change, from amorphous to crystalline and vice versa, when exposed to specific temperatures [88]. When GST crystallizes, it undergoes a linear increase in refractive index (with respect to crystallinity percentage) from ~3.0 to ~6.0. This huge increase in refractive index makes it attractive for various applications. However, it is particularly interesting for color filter array applications, as the large change in permittivity translates to a large change in resonance wavelength, as seen in the previous section.

Based on the above equation (13) for resonance wavelength, we can see that there are several degrees of freedom granted to the design of these hole array filters. Specifically,

the choice of metal, dielectric, and hole periodicity allow for the precise placement of the resonance wavelength. Therefore, for the mid-infrared (MWIR), one can see that for a given material and dielectric, the periodicity is quite simple to work out. For our purposes, Ag and Al were both tested numerically as metal materials, and GST was chosen as our dielectric, due to its phase change properties discussed in the previous section. Based on a target wavelength of 3.0 μm, a periodicity of 1800 nm was chosen. The hole diameter was further optimized to be 0.4-times the array periodicity, in this case 720 nm. Altering the hole diameter was shown to increase the width of the transmission peak to a point, before eventually eliminating any resonance behavior from the array altogether. Additionally, a hexagonal array geometry was chosen in order to allow for polarization insensitivity, as will be seen in the next section. This insensitivity arises from the rotational symmetry of a hexagonal array, in that the distance from one hole to all nearest neighbors in the unit cell is the same distance. A schematic of the design is shown below in Fig. 60. CaF_2 was chosen as a substrate due to its high transparency across the infrared.

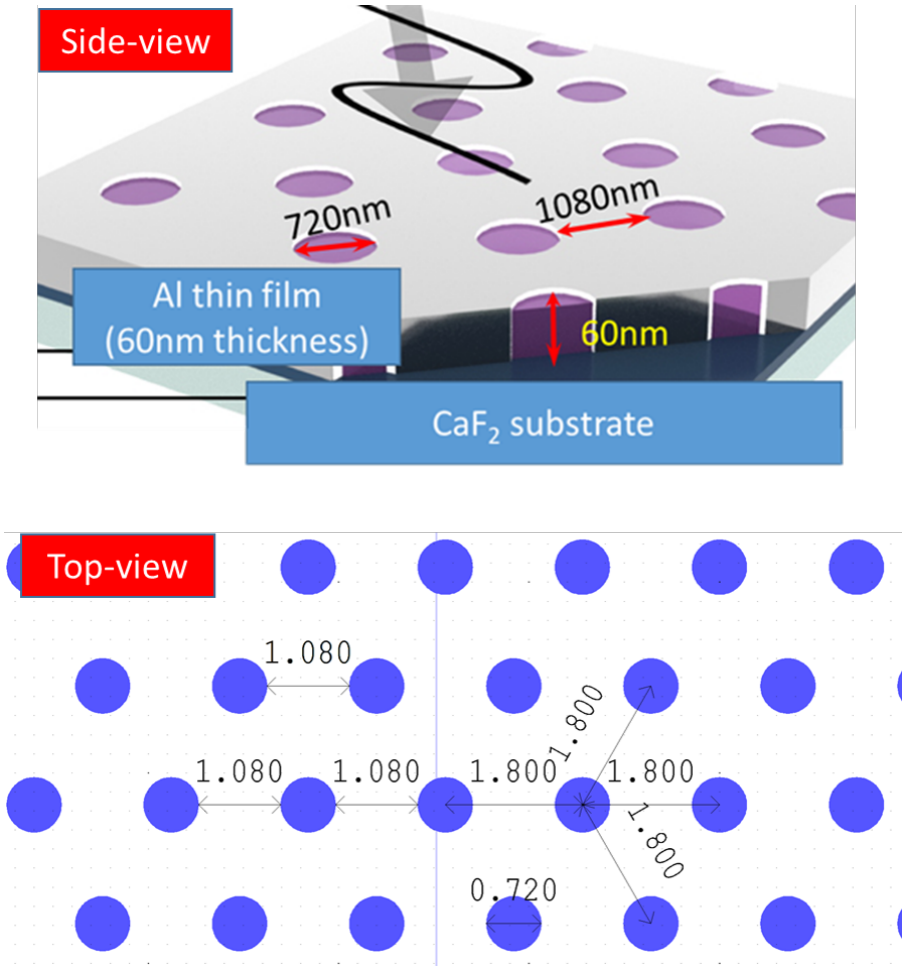

Figure 60: Schematic of the proposed device showing side view and top view. GST is shown in purple.

B.2 Results

Finite-difference time domain (FDTD) simulations were used to investigate the filtering behavior of the arrays. Fig. 61 shows tuning capabilities as a function of array periodicity and GST refractive index (crystallinity percentage). As is seen in the figure, each parameter can be used to independently tune the transmission peak. Therefore, by combining the two tuning modalities, passbands of < 200 nm can be tuned across huge wavelength ranges, with near-zero transmissivity outside of the passband. Additionally, polarization insensitivity is shown as well, as is expected from a hexagonal array geometry.

The effect of metal was also investigated, as is shown in Fig. 62. As can be seen in the figure, Al and Ag give very similar performances for a given array geometry, with Ag providing slightly higher transmission as a result of its lower extinction coefficient. The thickness of the GST/metal layer was also investigated, as GST is known to contract slightly when undergoing phase change. As is seen in Fig. 63, the thickness of GST film plays little role when contracting from 60 nm to 30 nm, with the transmission slightly higher at lower thicknesses. However, when the GST film is made much thicker (few hundreds of nanometers) the transmission drops slightly, due to the increased absorption in the thicker film. Fig. 62 shows the simulated behavior of crystalline and amorphous GST devices using measured refractive index values.

Once designs were optimized through numerical simulations, real devices were fabricated using direct write lithography. Fig. 60 shows the geometric parameters used in the fabricated device. 60 nm thick Ag films were patterned via lithography and subsequent chemical etching, and conformal deposition of 60 nm GST was performed via RF magnetron sputtering. The periodicity of the fabricated array is 1800 nm, and the hole diameter is 720 nm. An image of the fabricated device is shown in Fig. 65. Device dimensions matched well with designed values, and the fabrication error of the sample geometry was miniscule. Devices were characterized in terms of their optical transmission using FTIR spectroscopy. Samples were characterized in the amorphous phase before being heated on a hotplate to crystalline and characterized again. After the crystalline phase transmission was measured, samples were further heated in order to return the GST to the amorphous state and were re-measured for a comparison. Fig. 66 shows the FTIR results

of the three phases. Also shown is a plot of peak wavelength vs. number of heating/cooling cycles. The device shows consistent behavior across a number of phase change cycles.

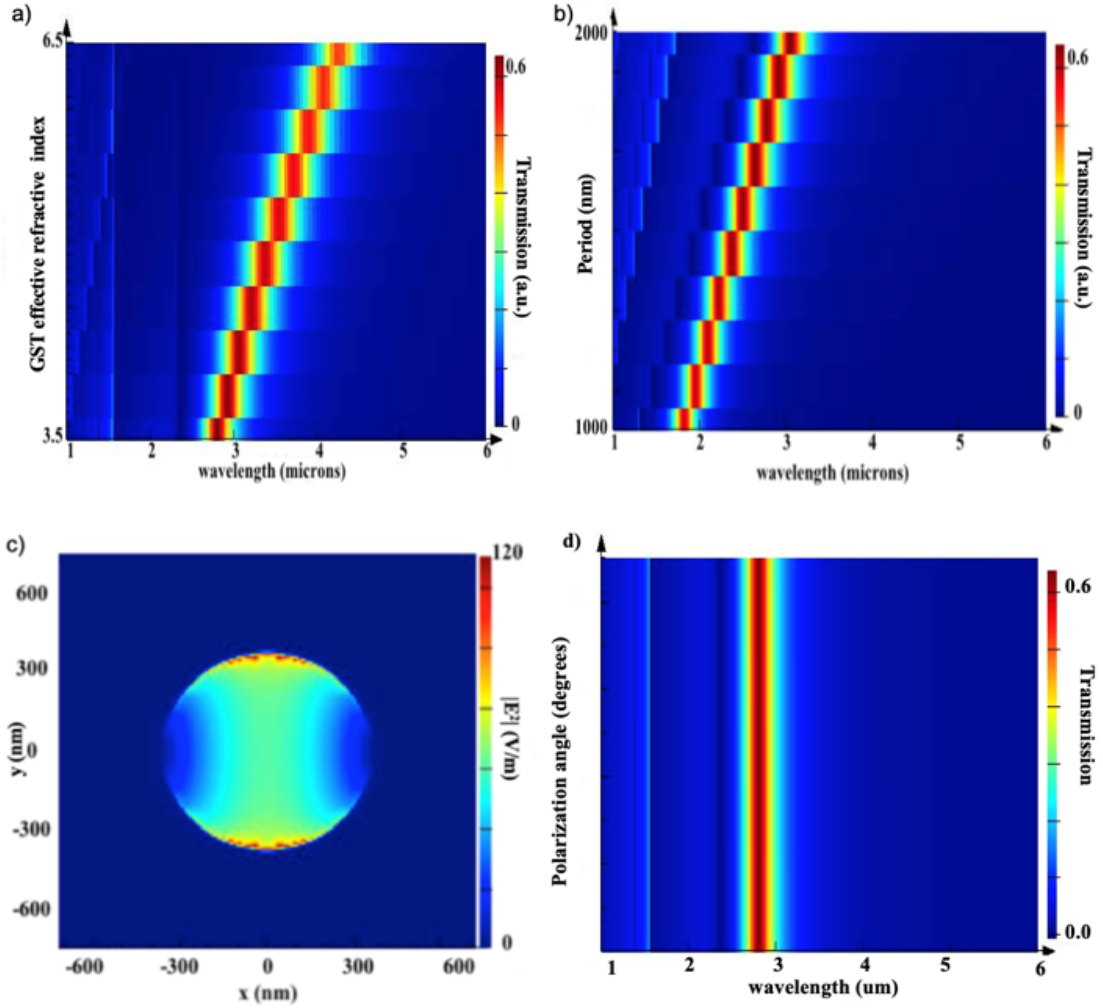

Figure 61: Simulated behavior of the GST nanohole array showing tuning capabilities via a) GST refractive index and b) array periodicity. By combining these two tuning methods, the full MWIR can be scanned. The passband in the above plots is 210 nm FWHM. c) E-field distribution inside a single hole at the resonance wavelength. Strong field confinement can be observed at the boundary between the GST-filled hole and Al film. The field intensity is nearly two orders of magnitude stronger at the resonance wavelength than away from resonance. d) Transmission vs. polarization angle showing polarization insensitivity.

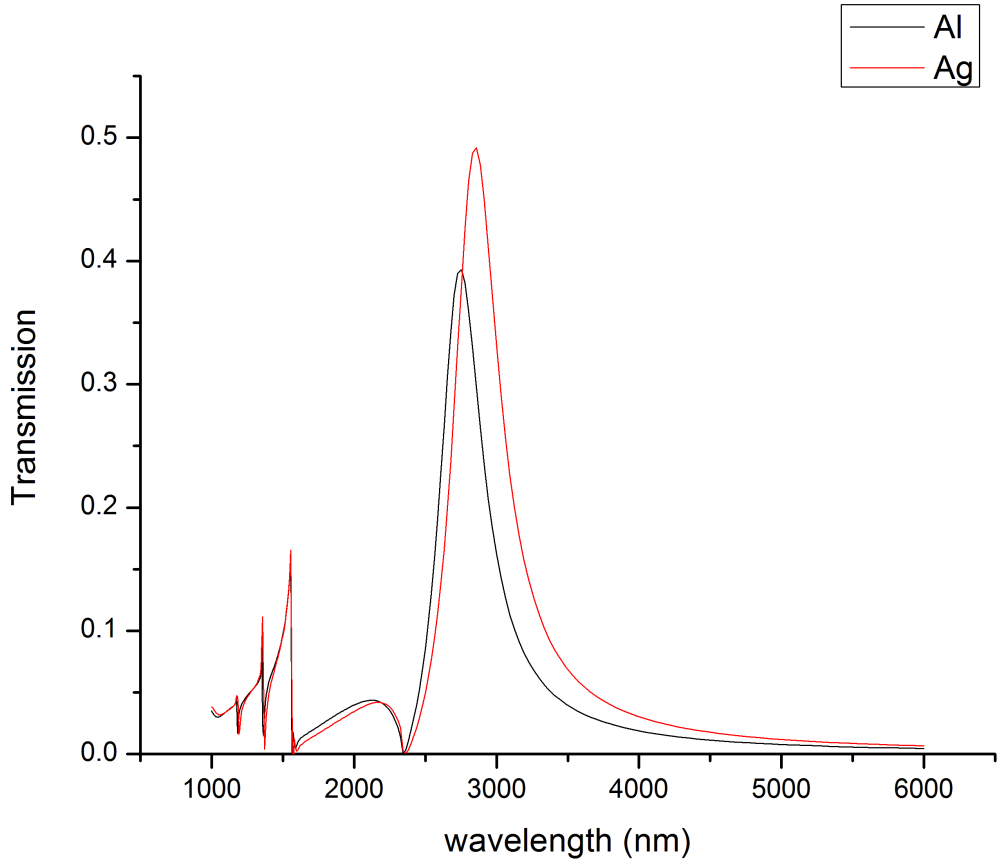

Figure 62: Transmission spectra for 60 nm Ag and Al metal films. The difference in transmission can be attributed to the difference in complex permittivity between Al and Ag. The real and complex index values for Al are significantly greater than those for Ag in the MWIR, resulting in a lower transmission efficiency due to the decrease in intensity of the SP field enhancement.

As is seen in Fig. 65, the measured data agrees well with the simulated values for the fabricated geometry. Upon re-entering the amorphous phase, the transmission spectrum is slightly shifted. This can possibly be attributed to a change in array geometry, as the heating could possibly lead to some slight expansion or deformation of the Al film. However, the performance is consistent across multiple heating/cooling cycles, which suggests that the design is robust and appropriate for switchable passband applications.

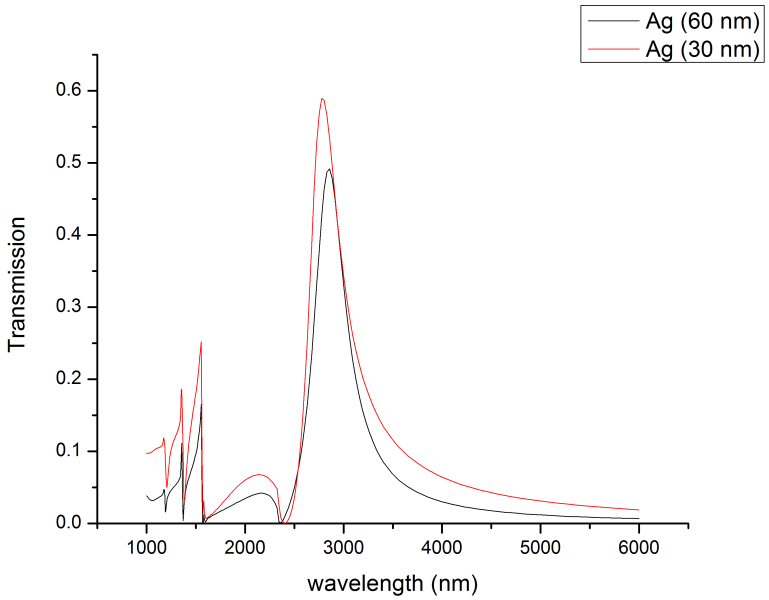

Figure 63: Transmission spectra for 60 nm and 30 nm of GST/Ag. The difference in transmission is attributed to the increased absorption in thicker films.

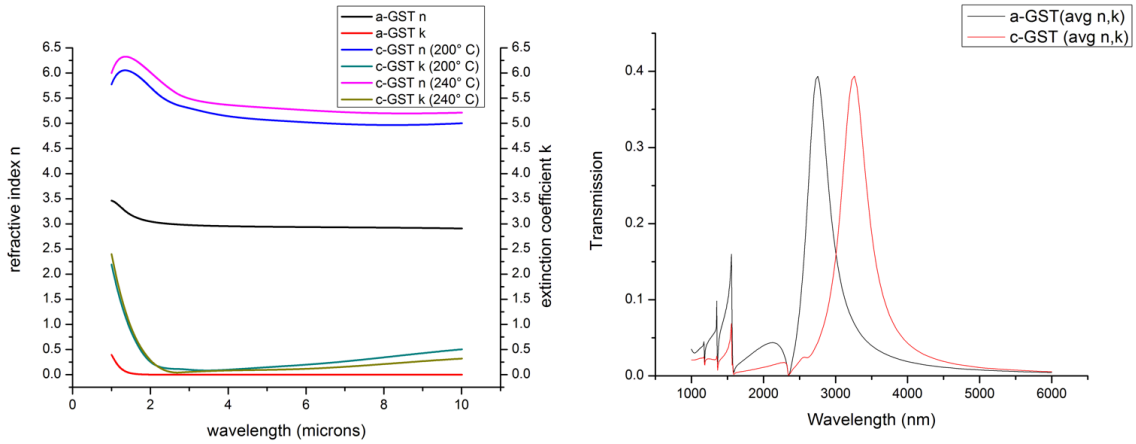

Figure 64: Measured complex refractive index data of the GST films deposited at NASA LaRC (left), and the corresponding transmission spectrum from a device based on the measured material dispersion for crystalline and amorphous GST (right).

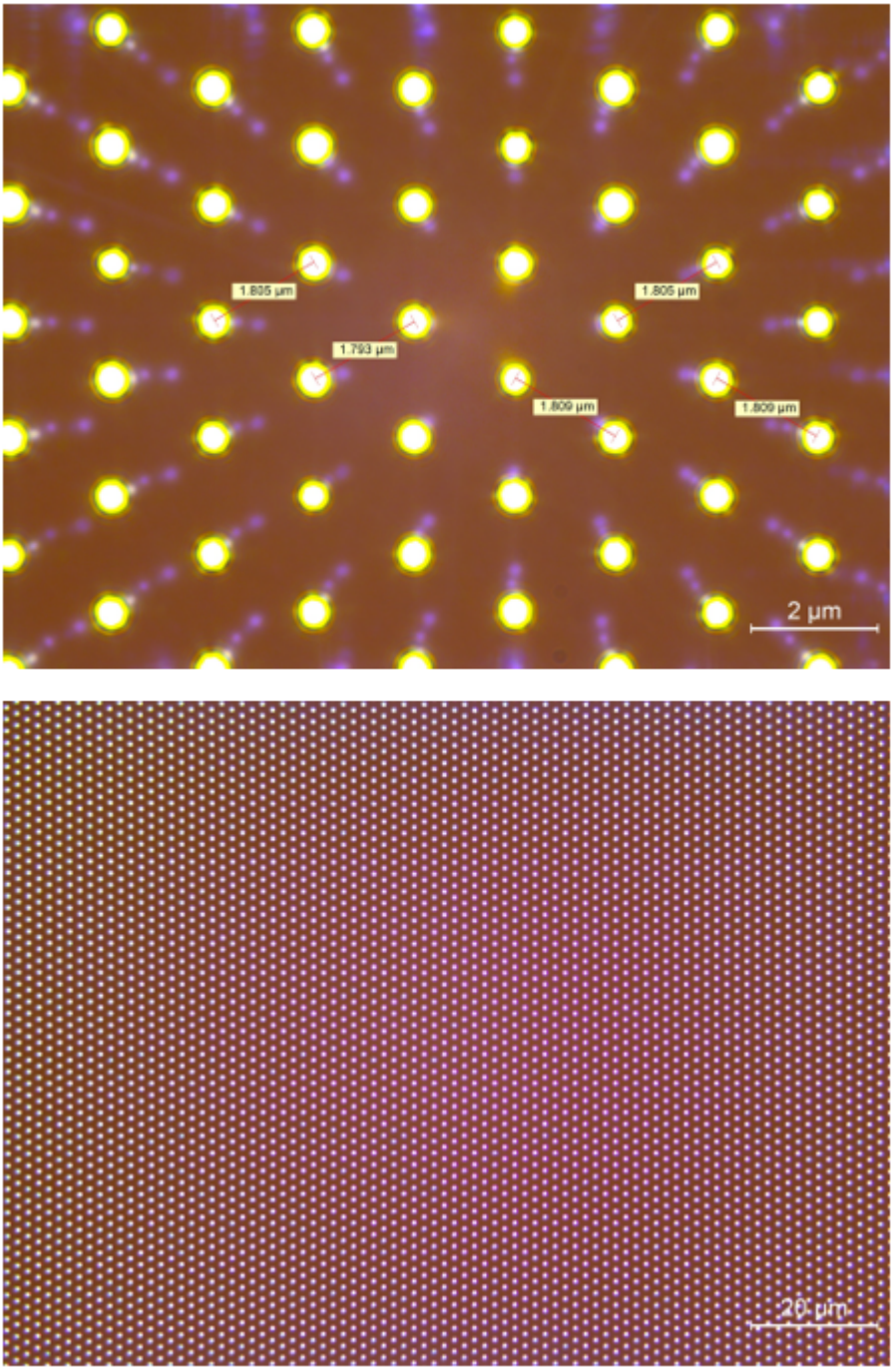

Figure 65: Microscope images of the fabricated device.

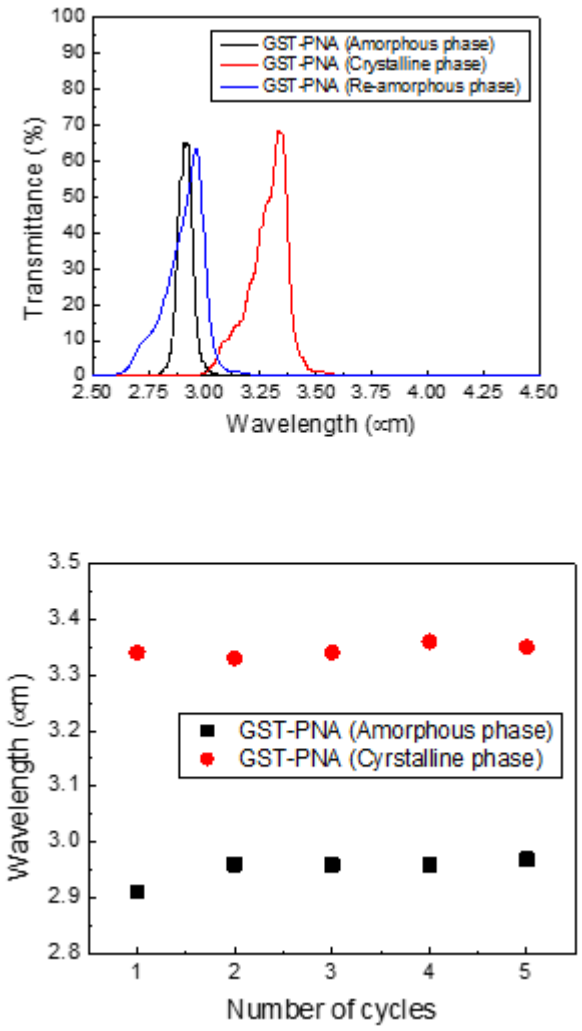

Figure 66: (top) FTIR data showing the temperature-tunable passbands of the nanohole array device. Results match reasonably well with simulated data. The widened passband in the case of re-amorphous samples is possibly due to material expansion (and thus a shift in array geometry) after heating. (bottom) Position of peak resonance wavelength as a function of the number of heating/cooling cycles showing consistent performance across multiple phase changes.

We have successfully designed, simulated, and experimentally demonstrated actively tunable MWIR transmission filters based on the phase change material GST incorporated into a plasmonic nanohole array in Al film. By altering the crystal phase of the GST film, active tuning of the plasmon resonance of the array can be achieved without

the use of any moving parts. Based on the results of this work, it can be concluded that plasmonic metasurfaces based on phase change materials are a promising method of achieving actively tunable optical filtering devices across the MWIR. Such a device can also be scale to other wavelength ranges so long as the phase change material is transparent to the wavelength of interest. Such a device would have far-reaching applications, such as thermal imaging, spectroscopy, tunable lenses, hyperspectral imaging, and so-forth.

References

1. J. Thieme, G. Schmahl, D. Rudolph, and E. Umbach, *X-Ray Microscopy and Spectroscopy* IV-3-IV-110 (Springer, Berlin, 1996).
2. D. Attwood, *Soft X-Rays and Extreme Ultraviolet Radiation* (Cambridge Univ. Press, Cambridge, 2000).
3. G. Schmahl, D. Rudolph, P. Guttmann, and O. Christ, in *Zone Plates for X-Ray Microscopy* (eds Schmahl, G. and Rudolph, D.) 63-74 (Springer Series in Optical Sciences, Academic, London, 1984).
4. Li, X., Wei, L., Poelma, R. H., Vollebregt, S., Wei, J., Urbach, H. P., Sarro, P.M., and Zhang, G. Q. "Stretchable Binary Fresnel Lens for Focus Tuning," Scientific Reports **6**, 25348 (2016).
5. S. Park, B. Park, S. Nam, S. Yun, S. K. Park, S. Mun, J. M. Lim, Y. Ryu, S. H. Song, and K.U. Kyung, "Electrically tunable binary phase Fresnel lens based on a dielectric elastomer actuator," Opt. Express **25**, 23801-23808 (2017).
6. G. Andersen, "Membrane photon sieve telescopes," Appl. Opt. **49**, 6391-6394 (2010).
7. Federal Aviation Administration - Office of Commercial Space Transportation. "FAA Semi-Annual Launch Report: Second Half of 2009," pp. end of document. Retrieved August 18, 2011.
8. G. Andersen, "Large optical photon sieve," Opt. Lett. **30**, 2976-2978 (2005).
9. G. Andersen and D. Tullson, "Broadband antihole photon sieve telescope," Appl. Opt. **46**, 3706-3708 (2007).

10. W. Sun, Y. Hu, D. G. MacDonnell, Hyun Jung Kim, Carl Weimer, and Rosemary R. Baize, "Fully transparent photon sieve," Opt. Express **25**, 17356-17363 (2017).

11. Wenbo Sun, Yongxiang Hu, D. G. MacDonnell, C. Weimer, and R. R. Baize, "Technique to separate lidar signal and sunlight," Opt. Express **24**, 12949-12954 (2016).

12. Lori Keesey, "NASA Team Begins Testing of a New-Fangled Optic," NASA Goddard Press Relsease (6 August 2017).

13. R. Menon, D. Gil, G. Barbastathis and H. I. Smith, "Photon-sieve lithography," J. Opt. Soc. Am. A **22** 342–345 (2005).

14. J. Jia, J. Jiang, C. Xie and M. Liu, "Photon sieve for reduction of the far-field diffraction spot size in the laser free-space communication system," Opt. Commun. **281** (17), 4536–4539 (2008).

15. R. Janeiro, R. Flores, P. Dahal and Jaime Viegas, "Fabrication of a phase photon sieve on an optical fiber tip by focused ion beam nanomachining for improved fiber to silicon photonics waveguide light coupling," Opt. Express **24**(11), 11611–11625 (2016).

16. J. M. Davila, "High-resolution solar imaging with a photon sieve," Proc. SPIE **8148** 81480O–81480O (2011).

17. F. S. Oktem, F. Kamalabadi, and J. M. Davila, "High-resolution computational spectral imaging with photon sieves," in Proc. of IEEE Int. Conf. on Image Processing (ICIP), 5122-5126 (2014).

18. A.Sabatyan, and S. A. Hosseini, "Diffractive performance of a photon-sieve-based axilens", Appl. Opt. **53** 7331-7336 (2014).

19. O. Asmolova, G. P. Andersen, M. A. Cumming, “Photon sieves for creating and identifying orbital angular momentum of light,” Proc. SPIE 10120, Complex Light and Optical Forces XI, 1012009 (27 February 2017).

20. Jie Ke and Junyong Zhang, "Generalized Fibonacci photon sieves," Appl. Opt. **54**, 7278-7283 (2015)

21. M. C. Gupta and D. Carlson, "Laser processing of materials for renewable energy applications," MRS Energy Sustainability, **2** (2015).

22. R Gattass and E. Mazur, “Femtosecond laser micromachining in transparent materials” Nature Photonics **2**, 219-225 (2008).

23. J. Ion, *Laser Processing of Engineering Materials: Principle, Procedure, and Industrial Application*, (Elsevier, Burlington, 2005).

24. M. Malinauskas, A. Zukauskas, S. Hasegawa, Y. Hayasaki, Y. Mizeikis, R. Buividas, and S. Juodkazis, “Ultrafast laser processing of materials: from science to industry,” Light: Science and Applications **5**, 16133 (2016).

25. L. Kipp and M. Skibowski, R. L. Johnson, R. Berndt, R. Adelung, S. Harm and R. Seemann, "Sharper images by focusing soft X-ray with photon sieves," Nature **414**, 184–188 (2001).

26. R. Liu, F. Li, M. J. Padgett, and D. B. Phillips, "Generalized photon sieves: fine control of complex fields with simple pinhole arrays," Optica **2**, 1028-1036 (2015)

27. A. F. Chrimes, I. Khodasevych, A. Mitchell, G. Rosengarten, and K. Kalantar-zadeh, “Dielectrophoretically controlled Fresnel zone plate,” Lab on a Chip **15,** 1092-1100 (2015).

28. Q. Cao and J. Jahns, “Focusing analysis of the pinhole photon sieve: individual far-field model,” J. Opt. Soc. Am. A **19**, 2387 (2002).

29. A. Sabatyan and S. Mirzaie, "Efficiency-enhanced photon sieve using Gaussian/overlapping distribution of pinholes," Appl. Opt. **50**, 1517-1522 (2011)

30. M. N. Julian, D. G. MacDonnell, and M. C. Gupta, “Flexible binary phase photon sieves on polyimide substrates by laser ablation,” Optics Letters 43, 2368-2371 (2018).

31. Andersen, G., Dearborn, M., and McHarg, G., “Photon Sieve Space Telescope,” 11th Annual AMOS (Advanced Maui Optical and Space Surveillance Technologies) Conference, Maui Economic Development Board, Inc., Wailea, HI, Sept. 2010.

32. F. Giménez, J. A. Monsoriu, W. D. Furlan, and A. Pons, "Fractal photon sieve," Opt. Express 14, 11958-11963 (2006).

33. H. Wach, E. Dowski, and W. T. Cathey, “Control of chromatic focal shift through wave-front coding,” Appl. Opt. 37, 5359-5367 (1998).

34. E. Dowski and W. T. Cathey, “Extended depth of field through wave-front coding,” Appl. Opt. 34, 1859-1866 (1995).

35. X. Zhao, F. Xu, J. Hu, and C. Wang, "Broadband photon sieves imaging with wavefront coding," Opt. Express **23**, 16812-16822 (2015).

36. X. Zhao, J. Hu, Y. Lin, F. Xu, X. Zhu, D. Pu, L. Chen, and C. Wang, “Ultra-broadband achromatic imaging with diffractive photon sieves,” Scientific Reports **6** (2016).

37. Y. Li, C. Wang, X. Zhao, F. Xu, and C. Wang, "Multispectral and large bandwidth achromatic imaging with a single diffractive photon sieve," Opt. Express 26, 21141-21152 (2018).

38. R. Vazquez, S. Eaton, R. Ramponi, G. Cerullo, and R. Osellame, "Fabrication of binary Fresnel lenses in PMMA by femtosecond laser surface ablation," Opt. Express 19, 11597-11604 (2011).

39. P. Srisungsitthisunti, O. Ersoy, and X. Xu, "Laser direct writing of modified Fresnel zone plates," J. Opt. Soc. Am. B, 24, 2090-2096 (2007).

40. G. Behrmann and M. Duignan, "Excimer laser micromachining for rapid fabrication of diffractive optical elements," Appl. Opt. 36, 4666-4674 (1997).

41. X. Wang, J. Leger, and R. Rediker, "Rapid fabrication of diffractive optical elements by use of image-based excimer laser ablation," Appl. Opt. 36, 4660-4665 (1997).

42. K. Sugioka, M. Meunier, and A. Pique, *Laser Precision Manufacturing*, Springer Series in Materials Science 135 (2010).

43. S. A. Maier, *Plasmonics: Fundamentals and Applications,* Springer (2007).

44. S. Pillai and M. A. Green, "Plasmonics for photovoltaic applications," Solar Energy Mat. And Solar Cells, 94, 1481-1486 (2010).

45. H. Atwater and A. Polman, "Plasmonics for improved photovoltaic devices," Nat. Materials 9, 205-213 (2010).

46. A. N. Grigorenko, M. Polini, and K. S. Novoselov, "Graphene plasmonics," Nat. Photonics 6, 749-758 (2012).

47. T. W. Ebbesen, H. J. Lezec, H. F. Ghaemi, T. Thio, and P. A. Wolff, “Extraordinary optical transmission through sub-wavelength hole arrays,” Nature 391, 667-669 (1998).

48. L. Martin-Moreno, F. J. Garcia-Vidal, H. J. Lezec, K. M. Pellerin, T. Thio, J. B. Pendry, and T. W. Ebbesen, “Theory of extraordinary optical transmission through subwavelength hole arrays,” Phys. Rev. Lett. 86, 1114 (2001).

49. F. J. Garcia-Vidal, L. Martin-Moreno, and J. B. Pendry, “Surfaces with holes in them: new plasmonic metamaterials,” Journal of Optics A 7, 97-101 (2005).

50. H. J. Lezec, A. Degiron, E. Devaux, R. A. Linke, L. Martin-Moreno, F. J. Garcia-Vidal, and T. W. Ebbesen, "Beaming light from a subwavelength aperture," Science **297**, 820-822 (2002).

51. C. Genet and T. W. Ebbesen, "Light in tiny holes," Nature (London) **445**, 39-46 (2007).

52. W. L. Barnes, A. Dereux, and T. W. Ebbesen, "Surface plasmon subwavelength optics," Nature (London) **424**, 824-830 (2003).

53. Y. Tang, S. Hu, Y. Yang and Y. He, "Focusing property of high numerical aperture photon sieves based on vector diffraction," Opt. Commun. **295** 1–4 (2013).

54. Goodman, Joseph W. *Introduction to Fourier Optics, 2nd Edition*. San Francisco: McGraw-Hill, 1996. Print.

55. Y. Tang, S. Hu, Y. Yang, and Y. He, “Focusing property of high numerical aperture photon sieves based on vector diffraction,” Opt. Commun. 295, 1–4 (2013).

56. M. N. Julian, D. G. MacDonnell, and M. C. Gupta, “Fabrication of photon sieves by laser ablation and optical properties,” Opt. Express **25** (25), 31528-31538

(2017).

57. P. P Pronko, S. K Dutta, J Squier, J. V Rudd, D Du and G Mourou, "Machining of sub-micron holes using a femtosecond laser at 800 nm," Opt. Commun. **114** (1), 106–110 (1995).

58. M. Castillejo, P. M. Ossi and L. Zhigilei, *Lasers in materials science*, (Springer 2014).

59. C. Zhou, X. Dong, L. Shi, C. Wang, and C. Du, "Experimental study of a multiwavelength photon sieve designed by random-area-divided approach," Appl. Opt. **48**, 1619-1623 (2009).

60. H. Chung, N. Bradman, M. Davidson, and P. Holloway, "Dual wavelength photon sieves," Optical Engineering **47**(11), (2008).

61. M. Finckenor and K. de Groh, *Space Environmental Effects*, NASA ISS Program Science Office (2015).

62. R. H. French, J. M. Rodriquez-Parada, M. K. Yang, R. A. Derryberry, R. H. French, M. J. Brown, C. R. Haeger, S. L. Samuels, E. C. Romano, and R. E. Richardson, "Optical properties of materials for concentrator photovoltaic systems," *Proc. IEEE Photovoltaic Specialists Conference (PVSEC),* 34th conference, 000394-000399 (2009).

63. Dupont, Kapton™ Summary of Properties, datasheet, (revised 2017).

64. G. Andersen, M. Dearborn, M. McHarg, and J. Harvey, "Membrane photon sieve telescope," Proc. SPIE **8167** (2011).

65. B. Pratap, C. B. Arnold, and A. Pique, "Depth and surface roughness control on laser micromachined polyimide for direct-write deposition," Proc. SPIE 4979, Micromachining and Microfabrication Process Technology VIII, (15 January 2003)

66. S. Metev and V. Veiko, *Laser Assisted Microtechnology*, Springer-Verlag, Berlin, 1994.

67. E. Di Fabrizio, F. Romanato, G. Gentili, S. Cabrini, B. Kaulich, J. Susini, and R. Barrett, "High-efficiency multilevel zone plates for keV X-rays," Nature **401** 895-898, (1999).

68. M. N. Julian, D. G. MacDonnell, and M. C. Gupta, "High-efficiency flexible multilevel photon sieves by single-step laser-based fabrication and optical analysis," Applied Optics **58** (1), 109-114 (2019).

69. Image modified from Paul Cherrer Insitut, blazed x-ray optics (https://www.psi.ch/lmn/blazed-x-ray-optics).

70. T. F. Johnston, "Beam propagation (M^2) measurement made as easy as it gets: the four-cuts method," Applied Optics **37** 4840-4850 (1998).

71. J. Hu, C. Liu, X. Ren, L. Lauhon, and T. Odom, "Plasmonic lattice lenses for multiwavelength achromatic focusing," ACS Nano 10, 10275-10282 (2016).

72. O. Avayu, E. Almeida, Y. Prior, and T. Ellenbogen, "Composite functional metasurfaces for multispectral achromatic optics," Nat. Comm. 8, 14992 (2017).

73. G. H. Yuan, E. Rodgers, N. I. Zheludev, "Achromatic super-oscillatory lenses with sub-wavelength focusing," Light: Science & Applications 6, 17036 (2017).

74. T. Xu, Y-K. Wu, X. Luo, and L. J. Guo, "Plasmonic nanoresonators for high-resolution colour filtering and spectral imaging," Nat. Comm 1, 59 (2010).

75. C. Williams, Y. Montelongo, and T. D. Wilkinson, "Plasmonic metalens for narrowband dual-focus imaging," Adv. Opt. Mat. 5 1700811 (2017).

76. M. Benk, K. Goldberg, I. Mochi, W. Chao, and E. Anderson, "Increased depth of field through wave-front coding: using an off-axis zone plate lens with cubic phase modulation in an EUV microscope," Proc. SPIE 8880, Photomask Technology 2013, 88801R (20 September 2013).

77. C. Pan, J. Chen, R. Zhang, and S. Zhuang, "Extension ratio of depth of field by wavefront coding method," Opt. Express 16, 13364 (2008).

78. D. W. Sweeney and G. E. Sommargren, "Harmonic diffractive lenses," Appl. Opt. 34, 2469-2475 (1995).

79. J. Yang, P. Twardowski, P. Gerard, W. Yu, and J. Fontaine, "Chromatic analysis of harmonic Fresnel lenses by FDTD and angular spectrum methods," Appl. Opt. 57, 5281-5287 (2018).

80. N. Mohammad, M. Meem, B. Shen, P. Wang, and R. Menon, "Broadband imaging with one planar diffractive lens," Sci. Rep. 8, 2799 (2018).

81. R. Beck, J. Parry, W. MacPherson, A. Waddie, N. Weston, J. Shephard, and D. Hand, "Applications of cooled spatial light modulator for high power nanosecond laser micromachining," Opt. Express 18, 17059-17065 (2010).

82. J. Henrie, S. Kellis, S. M. Schultz, and A. Hawkins, "Electronic color charts for dielectric films on silicon," Opt. Express 12, 1464 (2004).

83. "BYU Cleanroom – Electronic Color Charts," https://ece.byu.edu/cleanroom/color_chart.phtml.

84. "Silicon Dioxide Color Chart," Addison Engineering, Inc. (2019).

85. A. Rogalski, “Infrared detectors: an overview,” Infrared Physics & Technology 43, p. 187-210 (2002).

86. M. Ebermann, N. Neumann, K. Hiller, M. Seifert, M. Meinig, and S. Kurth, “Tunable MEMS Fabry-Perot filters for infrared microspectrometers: A review,” Proc. SPIE 9760, 97600H-1 (2016).

87. H. Zhang, A. Muhammad, J. Luo, Q. Tong, Y. Lei, Z. Zhang, H. Sang, and C. Xie, “Electrically tunable infrared filter based on the liquid crystal Fabry-Perot structure for spectral imaging detection,” Appl. Opt. 53, 5632-5639 (2014).

88. M. Wuttig, D. Lusebrink, D. Wamwangi, W. Welnic, M. Gilleben, and R. Dronskowski, “The role of vacancies and local distortions in the design of new phase-change materials,” Nature Materials, 6, 122-128 (2007).

89. C. Genet and T. W. Ebbesen, “Light in tiny holes,” Nature 445, 39-45 (2007).

90. M. K. Hedayati and M. Elbahri, “Review of metasurface plasmonic structural color,” Plasmonics 12, 1463-1479 (2017).

Summary of Published Works

Fabrication of photon sieves by laser ablation and optical properties

MATTHEW N. JULIAN,[1] DAVID G. MACDONNELL,[2] AND MOOL C. GUPTA[1*]

[1] *Charles L. Brown Department of Electrical and Computer Engineering, University of Virginia, Charlottesville, VA 22904, USA*
[2] *NASA Langley Research Center, Hampton, VA 23681, USA*
[*] *mgupta@virginia.edu*

Abstract: In this work, we demonstrate the feasibility and performance of photon sieve diffractive optical elements fabricated via a direct laser ablation process. Pulses of 50 ns width and wavelength 1064 nm from an ytterbium fiber laser were focused to a spot diameter of approximately 35 μm. Using a galvanometric scan head writing at 100 mm/s, a 30.22 mm^2 photon sieve operating at 633 nm wavelength with a focal length of 400 mm was fabricated. The optical performance of the sieve was characterized and is in strong agreement with numerical simulations, producing a focal spot size full-width at half-maximum (FWHM) of 45.12 ± 0.74 μm with a photon sieve minimum pinhole diameter of 62.2 μm. The total time to write the photon sieve pattern was 28 seconds as compared to many hours using photolithography methods. We also present, for the first time to our knowledge in the literature, thorough characterization of the influence of angle of incidence, temperature, and illumination wavelength on photon sieve performance. Thus, this work demonstrates the potential for a high speed, low cost fabrication method of photon sieves that is highly customizable and capable of producing sieves with low or high numerical apertures.

OCIS codes: (050.1970) Diffractive optics, (140.3390) Laser materials processing, (230.4000) Microstructure fabrication.

References and links

1. Roderick A. Hyde, "Eyeglass. 1. Very large aperture diffractive telescopes," Appl. Opt. **38** (19), 4198–4212 (1999).
2. L. Kipp, M. Skibowski, R. L. Johnson, R. Berndt, R. Adelung, S. Harm and R. Seemann, "Sharper images by focusing soft X-ray with photon sieves," Nature **414**, 184–188 (2001).
3. G. Andersen, "Membrane photon sieve telescopes," Appl. Opt. **49** 6391–6394 (2010).
4. G.Andersen, "Large optical photon sieve," Opt. Lett. **30** 2976–2978 (2005).
5. G. Andersen and D. Tullson, "Broadband antihole photon sieve telescope," Appl. Opt. **46** 3706–3708 (2007).
6. J. M. Davila, "High-resolution solar imaging with a photon sieve," Proc. SPIE **8148** 81480O–81480O (2011).
7. W. Sun, Y. Hu, D. G. MacDonnell, C. Weimer and R. R. Baize, "Technique to separate lidar signal and sunlight," Opt. Express **24** (12), 12949–12954 (2016).
8. R. Menon, D. Gil, G. Barbastathis and H. I. Smith, "Photon-sieve lithography," J. Opt. Soc. Am. A **22** 342–345 (2005).
9. J. Jia, J. Jiang, C. Xie and M. Liu, "Photon sieve for reduction of the far-field diffraction spot size in the laser free-space communication system," Opt. Commun. **281** (17), 4536–4539 (2008).
10. X. Zhao, F. Xu, J. Hu and C. Wang, "Broadband photon sieves imaging with wavefront coding," Opt. Express **23** (13), 16812–16822 (2015).
11. F. S. Oktem, F. Kamalabadi, and J. M. Davila, "High-resolution computational spectral imaging with photon sieves," in Proc. of IEEE Int. Conf. on Image Processing (ICIP), 5122-5126 (2014).
12. A.Sabatyan, and S. A. Hosseini, "Diffractive performance of a photon-sieve-based axilens," Appl. Opt. **53** 7331-7336 (2014).
13. R. Janeiro, R. Flores, P. Dahal and Jaime Viegas, "Fabrication of a phase photon sieve on an optical fiber tip by focused ion beam nanomachining for improved fiber to silicon photonics waveguide light coupling," Opt. Express **24** (11), 11611–11625 (2016).
14. A.Sabatyan, and P. Roshaninejad, "Super-resolving random-Gaussian apodized photon sieve," Appl. Opt. **51** 6315 - 6318 (2012).
15. W. N. Parker, A. D. Brodie and J. H. McCoy, "High-throughput NGL electron-beam direct-write lithography system," Proc. SPIE **3997** 713–720 (2000).
16. M. C. Gupta and D. Carlson, "Laser processing of materials for renewable energy applications," MRS Energy and Sustainability, **2** (2015).

17. B. K. Nayak and M. C. Gupta, "Self-organized micro/nano structures in metal surfaces by ultrafast laser irradiation," Optics and Lasers in Engineering, **48** (2010).
18. P. O. Caffrey, B. K. Nayak and M. C. Gupta, "Ultrafast laser-induced microstructure/nanostructure replication and optical properties," Appl. Opt. **51** (2012).
19. M. El-Bandrawy and M. C. Gupta, "Femtosecond laser micromachining of submicron features," in *Conference on Lasers and Electro-Optics/Quantum Electronics and Laser Science Conference,* OSA Technical Digest (Optical Society of America, 2003), paper CFF7.
20. M. Castillejo, P. M. Ossi and L. Zhigilei, "*Lasers in materials science,*" (Springer 2014).
21. P .P Pronko, S. K Dutta, J Squier, J. V Rudd, D Du and G Mourou, "Machining of sub-micron holes using a femtosecond laser at 800 nm," Opt. Commun. **114** (1), 106–110 (1995).
22. F. Brizuela, H. Bravo, G. Vaschenko, C. S. Menoni, J. J. Rocca, O. Hemberg, B. Frazer, S. Bloom, W. Chao, E. H. Anderson and D. T. Attwood, "Ablation of nanometer-scale features using a table-top soft x-ray laser," in *Frontiers in Optics,* OSA Technical Digest (CD) (Optical Society of America, 2006), paper JSuA21.
23. Y. Tang, S. Hu, Y. Yang and Y. He, "Focusing property of high numerical aperture photon sieves based on vector diffraction," Opt. Commun. **295** 1–4 (2013).
24. M. Domke, L. Nobile, S. Rapp, S. Eiselen, J. Sotrop, H. P. Huber and M. Schmidt, "Understanding thin film laser ablation: the role of the effective penetration depth and the film thickness," Physics Procedia, **56** 1007–1014 (2014).
25. Y. J. Liu, H. T. Dai, X. W. Sun and T. J. Huang, "Electrically switchable phase-type fractal zone plates and fractal photon sieves," Opt. Express **17** (15), 12418–12423 (2009).

1. Introduction

Diffractive optical elements (DOEs) offer a lightweight, planar alternative to traditional refractive lenses [1] due to their operating on the principles of optical diffraction and interference, unlike standard refractory optics. In 2001, Kipp et.al [2] developed a novel DOE based on the design of the Fresnel Zone Plate called the photon sieve, which consists of a large number of small pinholes arranged on the underlying Fresnel Zones. The diameter of the pinholes, d, can be equal to or greater than the width of the underlying Fresnel zones, w, and this quantity is typically given by the ratio $d/w = 1.5, 3.5, 5.5$, and so on in order to produce the maximum focal spot intensity, as explained in Kipp's seminal paper. It was shown that these photon sieves were capable of producing focus spots smaller than their minimum pinhole diameter due to the suppression of higher order diffraction maxima and larger numerical apertures. This property has made photon sieves attractive for applications such as space telescopes to study heliophysics and other astronomical phenomenon [3–6], improved signal-to-noise ratios in LIDAR systems [7], focusing elements in maskless photolithography [8], free-space laser communications systems [9], imaging systems [10, 11], increasing the focusing ability of axicons [12], and fiber-to-silicon photonics waveguide coupling [13]. A novel type of photon sieve employing overlapping pinholes has also recently been demonstrated and allows for an increase in the photon sieve resolution [14].

Typically, photon sieves are fabricated by UV or electron beam lithography. However, for large area devices, these writing processes can be extremely time consuming and costly. For example, based on electron beam exposure time equations given in [15], using typical beam current and dose parameters of 1 nA and 10^{-3} C/cm^2, respectively, a 30 mm^2 sample, such as the one presented in this work, should take approximately 3.5 days to expose. Laser-based UV lithography is much quicker, but still can take multiple hours to expose areas of several square-cm and requires chemical etching processes. Mask-based lithography is also very fast, but requires a new mask to be fabricated each time even a small change is made to the photon sieve design, and is therefore not ideal for applications with changing design parameters. In addition, the direct laser ablation system cost is less than $\$25,000$, while electron beam, direct laser lithography, and mask-based lithography system would cost many times more than the direct laser ablation system described in the manuscript. Secondly, lithography system requires coating of photoresist or e-bream resist, development of resist, and chemical or plasma etching of the metal film. This would add additional cost and time to fabricate the pattern. The proposed system also avoids the use of toxic chemicals and their costs.

The implementation of laser ablation to fabricate micro/nano features for photon sieves will

mitigate all of these issues, as no chemical processing is generally needed, and the pulsed beams can be scanned at speeds of greater than 1000 mm/s using commercial scan heads. High powered short and ultra-short pulsed lasers have shown great promise in the field of materials processing [16–18]. It has also been shown that by using ultra-short laser pulses, sub-micron features can be achieved [19]. This is because the effects of thermal diffusion are minimized in shorter pulses [20]. Few hundred nanometer diameter holes have been achieved using NIR lasers [21], and features as small as 82 nm have been reported using soft x-ray sources [22]. Thus, laser ablation techniques have the potential to produce both low and extremely high numerical aperture photon sieves without sacrificing device performance, as we will show, which is especially useful for applications where the photon sieve operating variables (focal length, numerical aperture, wavelength) are often changing, or multiple sieves are used. Currently, to write a 1 cm^2 pattern with a minimum feature size of 62.2 μm requires about 30 s. In order to achieve a higher NA value, the minimum pinhole diameter must decrease. However, the writing time will be relatively unchanged, as the primary factor affecting writing time is the total pattern area. Therefore, this method allows one to achieve high NA photon sieve with fast writing. However, it may be possible that feature roughness becomes more significant for extremely small feature sizes. In addition, the operation tolerances for photon sieves have not been thoroughly examined previous to this work, leaving a gap in understanding for actual integration of photon sieve devices into their applications.

2. Simulation of Photon Sieve Focal Point FWHM and Diffraction Efficiency

Numerical simulations of the photon sieve design were carried out using a custom numerical code adopted from the vector diffraction theory treatment of photon sieves. The specific mathematical derivations used to compute the focal plane intensity have previously been described elsewhere [23]. This code assumes that the electric field amplitude is a constant value (set to 1) of a user-chosen wavelength inside of the photon sieve pinholes, and is everywhere else zero. From this point, the code employs the angular spectrum representation of the vector diffraction field in the focal plane of the photon sieve. For each pinhole of the photon sieve, the vector diffraction field in computed at each specified point in the focal plane. The total focal plane intensity is the calculated by summing the contributions of each pinhole.

The photon sieve design used for both simulation and experiment was for operation at 633 nm wavelength, with a focal length of 400 mm and 19 rings. A d/w ratio of 1.53, and a total device diameter of 6.2 mm was used. A simulation was performed to obtain a line profile through the center of the photon sieve focus spot over a length of 150 μm. Data from the same simulation was also used to predict the diffraction efficiency of the photon sieve. In order to model the diffraction efficiency, an integration of the square modulus of the total three-dimensional complex electric field at the focal point was performed to obtain the total optical intensity inside a sphere with radius equal to the $1/e^2$ radius of the focal point. The value of the electric field incident on the sieve was taken to have a magnitude of 1. The code was also used to model the illumination wavelength tolerances of the focal point intensity and size, which was done by changing the illumination wavelength of the simulated 633 nm sieve design. The simulated sieve was shown to have a focal point FWHM of 44.59 μm when illuminated with 633 nm wavelength light. The simulated diffraction efficiency was 1.275%.

3. Photon Sieve Fabrication via Laser Ablation

Fabrication of the photon sieve was carried out on soda lime glass substrate coated with 50 nm of silver film via electron beam evaporation. The total optical transmission through the silver layer is approximately 2% of the incident light at 633 nm wavelength. Photon sieve pinholes were formed using a commercial 1064 nm wavelength ytterbium fiber laser (IPG Photonics, model YLP-RA-1-50-30-30) with a pulse width of 50 ns, pulse repetition rate of 20 kHz, and

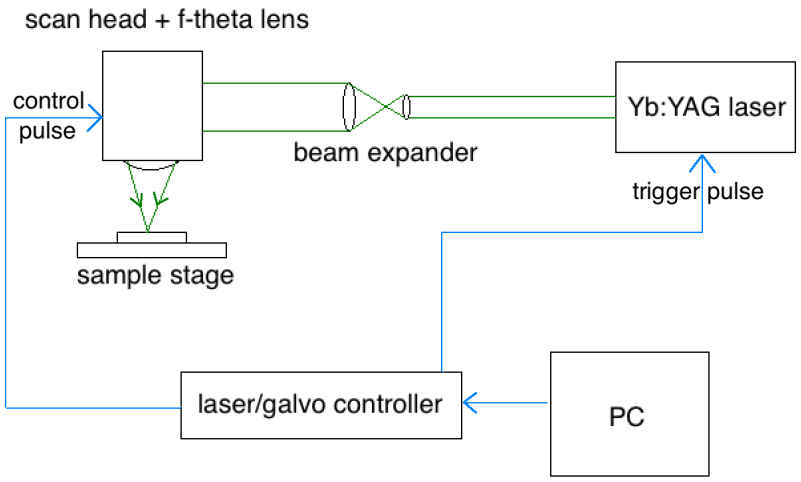

Fig. 1. Schematic of the laser direct writing setup used in this study.

an average output power of 9 W. A schematic of the full experimental setup is shown in Fig. 1. The laser beam was directed through a beam expander and into a commercial galvanometric scan head (Sino-Galvo, model JD2206) fitted with an f-theta lens, producing a focus spot of approximately 35 μm. The laser and scan head were controlled simultaneously by an external controller (Lanmark Controls, Winlase LAN software and Maestro3000 controller) which reads the design as a vector graphic or image file and scans the beam across the desired substrate areas one line at a time to produce the desired features. The software is not limited to photon sieve designs; any image or vector file can be uploaded and fabricated. The line spacing can be selected by the user in the software GUI, and was set to 10 μm for this work. The beam was scanned at 100 mm/s, resulting in one laser shot per micron. A small vacuum nozzle was used above the substrate in order to remove the ablation plume to prevent silver from re-depositing on the photon sieve surface.

4. Results and Discussion

4.1. Photon Sieve Pinhole Morphology

An image of the fabricated photon sieve is shown in Fig. 2. Because the laser beam intensity distribution at the focus of the f-theta lens is a Gaussian distribution, and due to line-scanning of the laser beam across the substrate to create features, the inner edges of the presented photon sieve pinholes are not perfectly clean circles. The line-by-line scan, coupled with the Gaussian laser intensity seems to cause the edges of the filled features to not fully ablate, due to the edge of the feature receiving ablation energy from beam minimum rather that the center maximum. The effects of this uneven irradiance are shown in Fig. 3.

When the laser beam is scanned across the substrate, the control software assumes that the incident laser beam focus is a mathematical point positioned on the center of the physical laser spot. This is because beam-scanning software does not account for the size of the beam being scanned; it can only control the scan head mirrors. For example, for a 20 μm laser spot with its center being scanned over a distance of 50 μm, the actual laser spot will irradiate the 50 μm line, plus an additional distance at the beginning and end of a scan line equal to the laser spot radius. Thus, in the above example, a distance of 70 μm is irradiated and therefore subject to larger ablation area. However, the additional spot radius on either side of the mark is only exposed to a

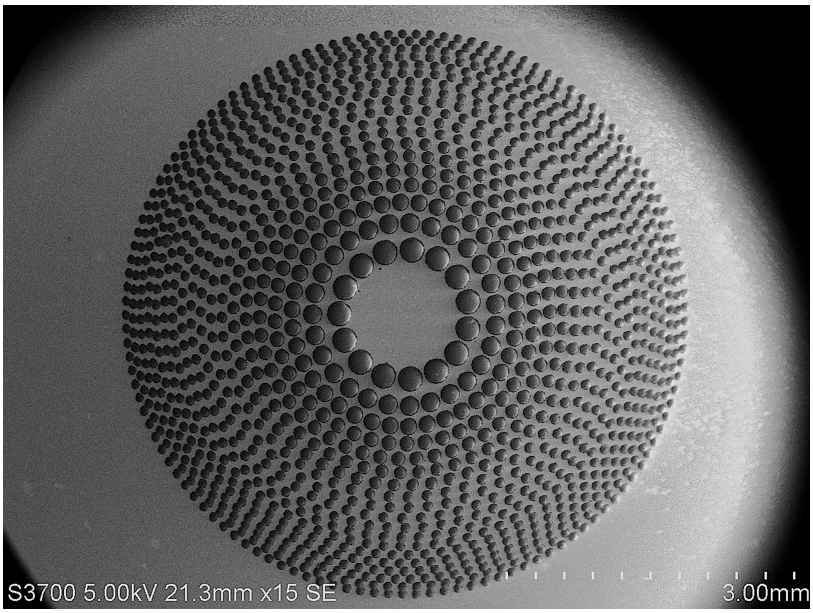

Fig. 2. SEM image of the laser fabricated photon sieve.

fraction of the maximum laser intensity seen by the rest of the scan line, as it is being irradiated by an off-center portion of the laser spot. This discrepancy in irradiance (and therefore optical energy) of the substrate can cause less material to be ablated from the edges of a scan line or feature, resulting in the marks shown in Fig. 3. This effect can be managed by shrinking the size of desired features in software in order to account for the size of the beam. If the focused laser spot size is known, the user can define the line spacing when creating a filled object such as a pinhole.

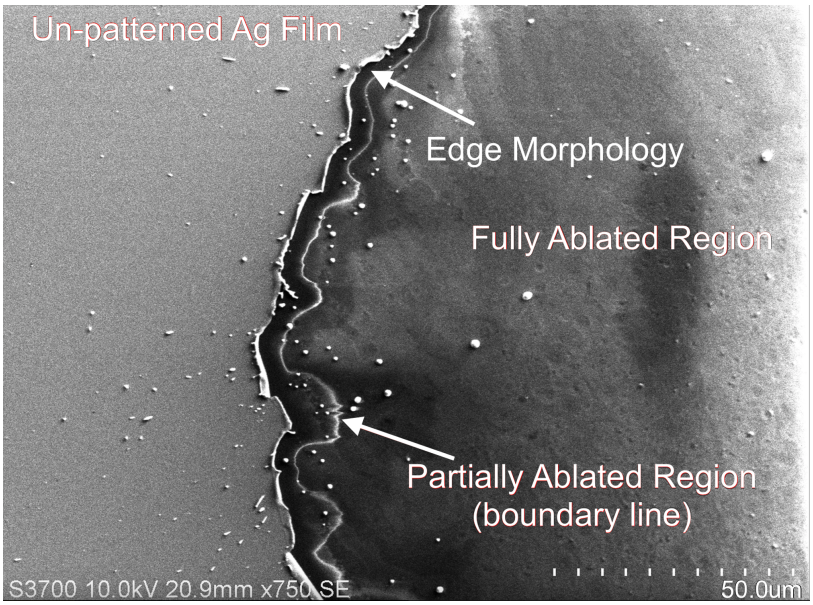

Fig. 3. SEM image of photon sieve pinhole edge morphology. Characterization results suggest that the imperfections as explained above do not affect device performance.

This effect, however, does not appear to impact photon sieve performance, as indicated by the good agreement between numerical simulations and measured data for the focus spot. Beam shaping optics can be used to produce a flat-top laser intensity profile at the focus of the f-theta lens, which would result in the entire laser mark seeing a constant irradiation intensity, and therefore ablate more uniformly. The use of ultrafast laser pulses such as pico or femtosecond sources could potentially also mitigate the issue without the need for beam shaping optics, as the shorter pulse time can prevent melt formation at the edge of a mark, as explained by Domke et. al [24].

4.2. Characterization of Photon Sieve Focal Spot Size and Efficiency

The fabricated photon sieves were characterized using a Helium-Neon laser illumination wavelength of 632.8 nm and a scanning slit beam profiler (Thorlabs model BP109-VIS) with 1.20 μm resolution placed at the focal point. The collimated testing laser beam was expanded via a Keplerian telescope setup to cover the full area of the photon sieve. A 200 μm aperture was placed between the sieve and beam profiler in order to block out the zero order diffracted light, which resulted in a more simple beam profile measurement. A schematic of the optical characterization setup is shown in Fig. 4.

In order to account for the slightly transmissive nature of the Ag thin film, a background measurement was taken by shining the laser light onto the unpatterned silver film and recording the intensity data with the beam profiler. This was done so that this background signal could be accounted for when analyzing the photon sieve performance. In practice, this issue can be avoided by using a slightly thicker Ag film. By using 75 nm thick Ag, the transmission would be less than 1%, and the film thickness would be well within the range for laser ablation. A plot of the measured photon sieve focus intensity distribution with background signal subtraction is shown in Fig. 5 and is compared with the numerical simulation result. The measurement is in very strong agreement with simulation, with measured FWHM values of (45.12 ± 0.74) μm. In the un-subtracted data, we see a baseline power of approximately 4.5% of the peak value, whereas the subtracted background noise gives essentially zero intensity surrounding the focus

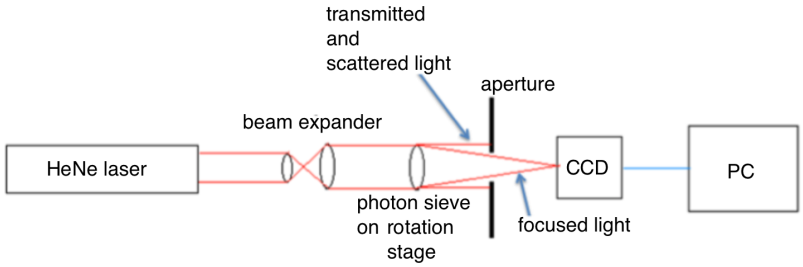

Fig. 4. Schematic of the photon sieve characterization setup.

spot (less than 1% of the maximum intensity value). Both of these results are consistent with data published in other works, such as Liu et. al [25].

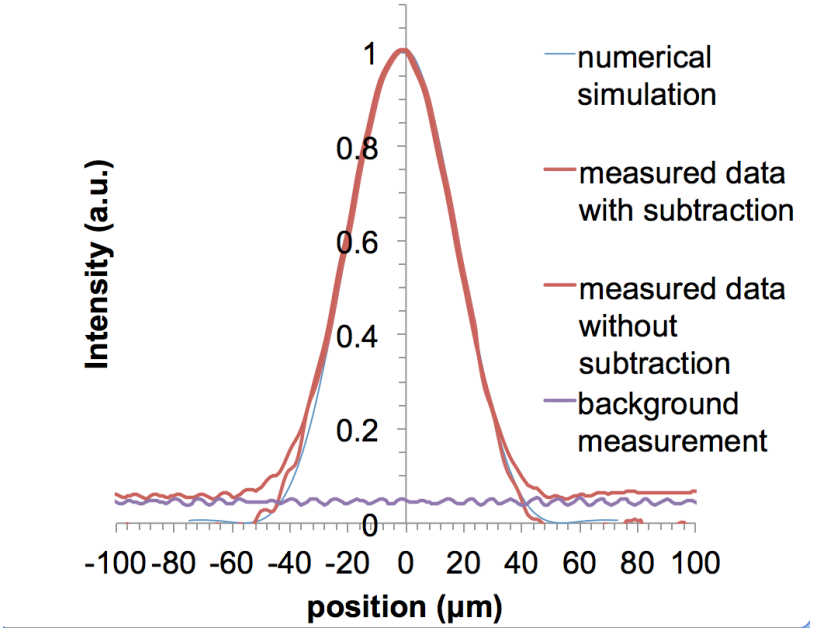

Fig. 5. Simulated and measured photon sieve focal point x-axis intensity profiles (normalized). Both subtracted and un-subtracted data are shown, as well as the background measurement.

Diffraction efficiency of the photon sieve was also investigated, and is here defined as the ratio of the total power in the focal spot to the total power incident upon the photon sieve. In order to measure this, the beam profiler in the setup described above was replaced by a photodiode and optical power meter. A 200 μm aperture was then placed onto the face of the detector and aligned with the photon sieve focus spot in order to block any light outside of the focal spot, such as the zero order diffracted light, which would otherwise result in an artificially inflated efficiency value. The diffraction efficiency was measured multiple times for consistency, and found to be (1.1995 ± 0.0025)%, which is in strong agreement with simulated values.

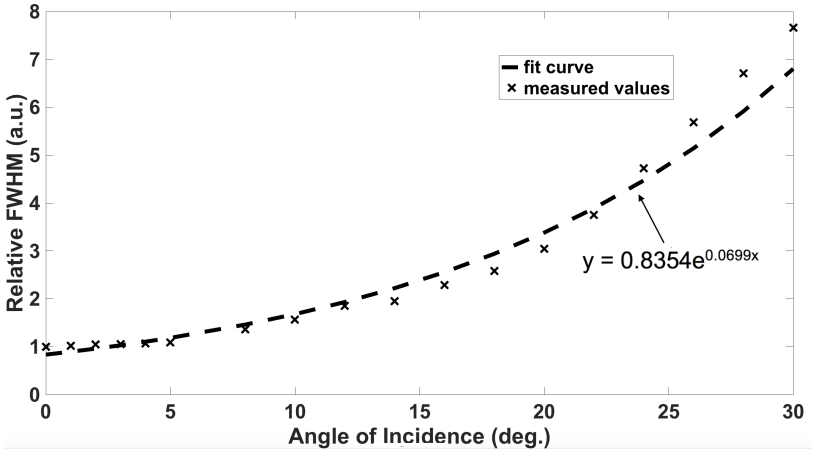

Fig. 6. Plot of the relative change in x-axis FWHM vs. angle of incidence.

4.3. Dependence of Focal Point Characteristics on Angle of Incidence, Illumination Wavelength, and Temperature

It is known that the behavior of diffractive optical elements is strongly tied to angle of incidence. However, the actual influence of incident angle on photon sieve focusing capabilities, to the best of our knowledge, has not been reported. Therefore it is useful to characterize the angular dependence of photon sieve focal spot size and diffraction efficiency, as it gives insight to alignment tolerances for any potential applications.

In order to characterize the focal point at various angles of incidence, the photon sieve was mounted on a rotational stage and aligned at the different incident angles. Beam profile data was taken at each angle, with the angle being increased by one degree from 0°to 6°, and two degrees from 6°to 30°. This was done to thoroughly characterize the small angle behavior of the photon sieve, as these smaller angular misalignments are more likely to occur than large misalignments in potential applications. The incident laser beam was made to cover the entire photon sieve pattern at every angle, and the sieve was rotated about the y-axis. Data was taken to understand the relative change in FWHM at various incidence angles, as well as the change in relative intensity of the focal point. As is shown in Fig. 6, the focal point FWHM along the x-axis is fairly constant until 4°, with the focal point expanding approximately one micron per degree. At incident angles greater than 5°, the focal spot quickly and exponentially increases in size with increasing angle. At approximately 13°, the focal point had doubled in size, and by 20°had tripled and was no longer Gaussian in shape. The expansion of x-axis FWHM at increasing angles of incidence follows an exponential dependence, as shown in Fig. 6. The deviations from the fit curve at larger incidence angles can be attributed to the focal point instability at these large angles. The y-axis FWHM remained fairly unchanged, expanding by only 3 microns at an incidence angle of 20 degrees. As a result, rotation of the photon sieve about the y-axis resulted in a stretched focal point along the x-axis.

Focal point intensity along the x-axis was also greatly affected by increasing angle of incidence. A plot of the relative focal point intensities is given in Fig. 7. Again, the photon sieve is fairly tolerant with angular misalignment up to 4°, but performance is quickly diminished at larger angles, with focal point intensity dropping to 80% of the normal incidence value at 10°, and to roughly 50% at 15°. This drop in intensity can easily be explained, since when the sieve pinholes are rotated about the y-axis the effective area of the pinhole is reduced by the cosine of the angle of incidence, resulting in a lower photon flux through each pinhole. More interesting is the slight

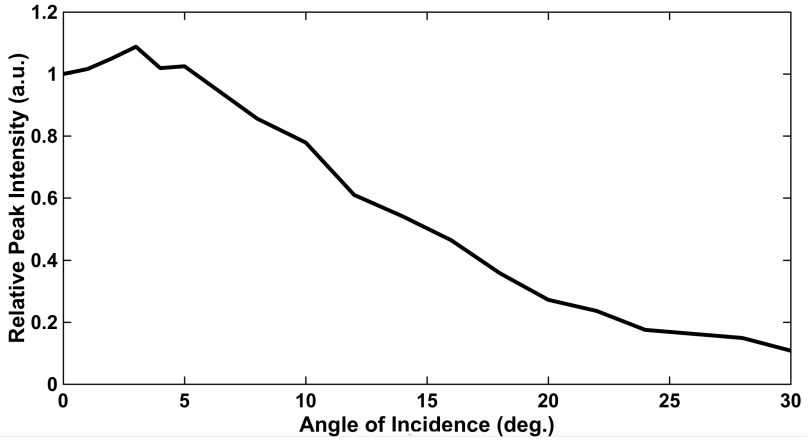

Fig. 7. Plot of the relative change in focal point intensity vs. angle of incidence.

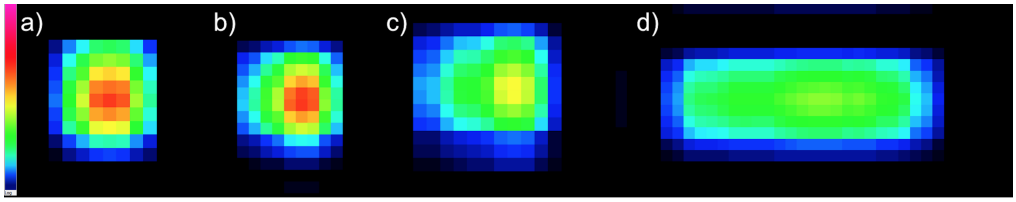

Fig. 8. Images of focal point showing 2D intensity profile at different angles of incidence (a) 0°, (b) 4°, (c) 10°, and (d) 25°(Intensity scale at far left of image).

increase in intensity at small angles (less than 5°). To corroborate the validity of this result, these measurements were taken on the presented sieve several times. Measurements were also taken on a 150 mm focal length photon sieve fabricated using the same system. The results were consistent across all measurements of both devices, and all showed an intensity increase at small angles of incidence. Raw images of the beam profile at various angles of incidence are shown in Fig. 8.

As with FWHM measurements, the y-axis intensity profile was largely unchanged with sieve rotation about the y-axis. From this we can ascertain that sieve rotation about an axis results in a change in focal point characteristics along the opposite axis. It has been shown here that photon sieves are relatively stable under small angular misalignment, but performance rapidly degrades at incident angles greater than 4°.

Simulations and measurements were also carried out to evaluate the photon sieve performance as a function of illumination wavelength in order to better understand the photon sieve effective bandwidth. Findings regarding FWHM and peak intensity are summarized in Fig. 9, and measured values in the table are denoted as such. Data was simulated for wavelengths of 633, 636.57, 638.37, 640, 646, and 653 nanometers. Measured values for off-design wavelength FWHM and intensity were taken using laser diodes operating at 636.57 nm and 638.37 nm, as measured by a spectrometer. It is known that photon sieves with $d/w < 2.4$ do not possess strict tolerances to illumination source linewidth [2], so the slightly larger linewidth of the laser diode compared to the 632.8 nm Helium-Neon laser source should not affect sieve performance for this measurement. The elliptical diode output beam was collimated using an aspheric lens and made circular by an anamorphic prism pair. It was then passed through a spatial filter and re-collimated prior to illuminating the photon sieve. As is seen in Fig. 8, focal point intensity quickly degrades with

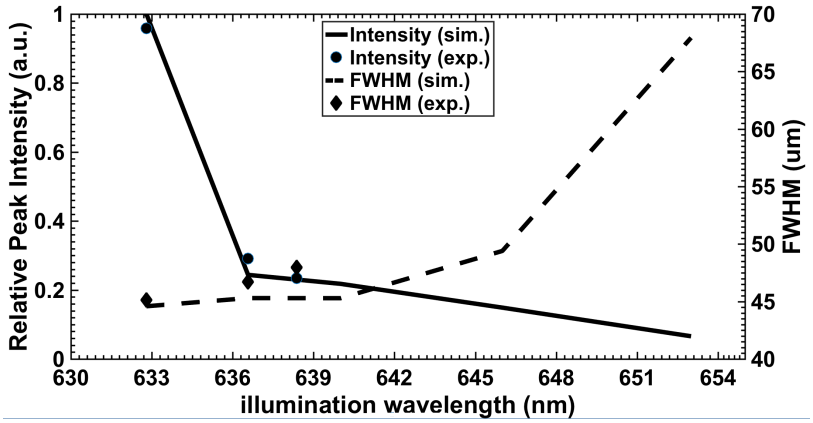

Fig. 9. Effect of illumination wavelength on focal point properties.

deviation from the design wavelength. FWHM is more tolerant to small deviations, but increases quickly at $\Delta\lambda > 7nm$. Simulated values agree well with experimental data.

Lastly, data was gathered to understand the temperature dependence of focal point characteristics to asses the normal operating temperatures that are encountered in different real applications. In order to do so, the photon sieve was placed in a mount that allowed for free expansion of the substrate in the x and y directions. This was done so as to not force the photon sieve into maintaining its structural shape as well as to prevent cracking of the substrate. The photon sieve was heated from the glass side using a heat gun, and the temperature was monitored using a thermocouple attached to the silver film side of the photon sieve near the pattern, and was fixed to the silver with aluminum tape to ensure good thermal contact. Measurements were taken from room temperature (24 °C) to 100 °C in 10 °C increments. The photon sieve was heated to the desired temperature and maintained at that temperature while beam profile measurements were collected, in order to guarantee stability of the temperature. A summary of FWHM and peak intensity characteristics are shown in Fig. 10. There was little to no variation seen in focal point characteristics of the photon sieve at elevated temperatures, with 3.2% maximum variation in FWHM values (1.5 μm variation) and 10.5% maximum variation in focal point intensity. This demonstrates the consistency of rigid-substrate photon sieve performance at elevated temperatures.

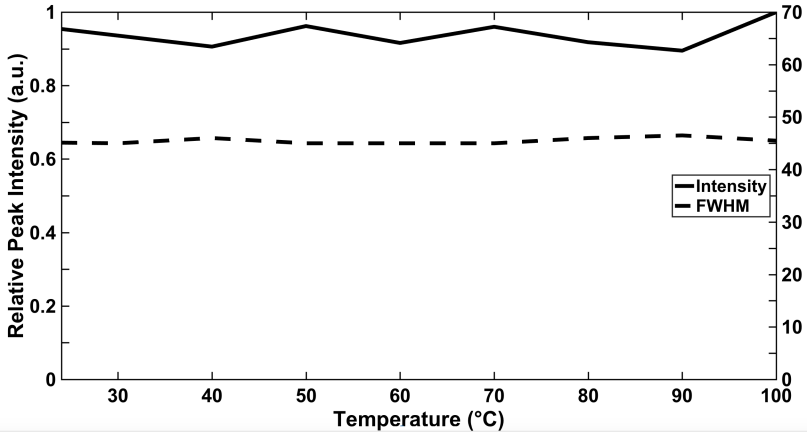

Fig. 10. Photon sieve performance at various temperatures.

5. Conclusion

We have successfully demonstrated the fabrication of photon sieve lenses via laser ablation process. A photon sieve of 400 mm focal length and area of 30.22 mm^2 was fabricated by means of a nanosecond-pulsed ytterbium fiber laser. The total time to pattern the photon sieve lens was 28 seconds only, and the use of high power and/or shorter pulse lasers would decrease this time even further. Photon sieve performance has a fair tolerance for pinhole morphology. Despite imperfections in the partially ablated regions near pinhole edges, photon sieves performed very similarly to the simulated values. The differences between measured and simulated FWHM and diffraction efficiency were 1.18% and 5.96%, respectively. The performance of photon sieves under various angles of incidence was characterized and small angle tolerances exist for most purposes, with limited change in FWHM and focal point intensity at angles less than 4°. Illumination wavelength tolerance was also simulated, measured, and presented. FWHM values are fairly stable when the photon sieve is illuminated by light within a few nanometers of the design wavelength, but increases rapidly at greater than 7 nm $\Delta\lambda$. However, the intensity of the focal point drops by a factor of 4.5 within this same 7 nm range, with greater reduction in intensity seen at larger $\Delta\lambda$ values. Based on the work presented here, we conclude that high quality, high performance photon sieves with large or small numerical apertures can be rapidly and reliably fabricated via laser direct writing, resulting in a reduced fabrication time and cost of photon sieves for various research and industrial applications.

Funding

This work is supported by the Lab Demo (Photon Sieve) IRAD project of NASA Langley Research Center, the NASA Langley Professor Program and the NSF I/UCRC Laser and Plasma for Advanced Manufacturing program.

Acknowledgments

The authors thank Dr. Wenbo Sun and Mr. Harold Haldren for useful discussions regarding the simulation code.

Flexible Binary Phase Photon Sieves on Polyimide Substrates by Laser Ablation

MATTHEW N. JULIAN,[1] DAVID G. MACDONNELL,[2] MOOL C. GUPTA[1,*]

[1]*Charles L. Brown Department of Electrical and Computer Engineering, University of Virginia, Charlottesville, VA 22904*
[2]*NASA Langley Research Center, Hampton, VA 23681*

**Corresponding author: mgupta@virginia.edu*

Received XX Month XXXX; revised XX Month, XXXX; accepted XX Month XXXX; posted XX Month XXXX (Doc. ID XXXXX); published XX Month XXXX

Binary phase diffractive optical element photon sieve is fabricated by direct laser ablation of a thin, flexible polyimide substrate with a nanosecond-pulsed ultraviolet (UV) laser. The binary phase photon sieve operates at 633 nm and was designed with 19 rings and a focal length of 400 mm. The total time to fabricate the photon sieves were tens of seconds. Surface properties of the laser-processed areas are examined, and optical performance of the photon sieve is characterized and compared to FDTD simulations. By optimizing the laser fluence and travel distance between laser pulses, features with sub-wavelength surface roughness were achieved. The photon sieve showed good focusing ability with suppressed side-lobes. When the fractional area of photon sieve pinholes was made to approach 50%, the binary sieve diffraction efficiency approached 11%; matching the highest value reported in the literature for a photon sieve. Thus, this work demonstrates both high efficiency, lightweight diffractive optics suitable for space satellite and other applications, with capabilities for low cost and high throughput fabrication. © 2017 Optical Society of America

OCIS codes: *(140.3390) Laser materials processing; (050.1970) Diffractive optics; (120.4610) Optical fabrication.*

http://dx.doi.org/10.1364/OL.99.099999

Photon sieves are diffractive optical elements consisting of a large number of pinholes positioned on top of the underlying zones of the corresponding Fresnel zone plate. By properly positioning the pinholes, the side-lobes of the focal point can be adequately suppressed [1], and the transmitted wavefront can be shaped into a chosen intensity distribution [2]. In addition, the pinholes can be made larger than the underlying Fresnel zones without sacrificing resolution, relaxing fabrication tolerances [3]. Due to these properties, photon sieves have been investigated for applications such as space telescopes [4, 5], optical communication [6], generation and identification of optical orbital angular momentum [7], and nano-lithography [8], axicon lens systems [9], and imaging [10, 11]. However, traditional amplitude photon sieves suffer from inherently low diffraction efficiencies (~1-4%). In order to increase the viability of photon sieves in various applications, transparent phase-type devices have been investigated and show increased diffraction efficiency due to increased optical throughput [12]. For applications such as space telescopes, it is also important to have a photon sieve that is lightweight, and deployable. In order to address these needs, temperature-stable polyimide substrates have been investigated, and maximum efficiencies of 10% were obtained [4, 13].

Traditionally, photon sieves are fabricated by optical or electron beam lithography. However, these methods are often slow, costly, and lack process robustness. Pulsed lasers have been shown to be promising candidates in the field of materials processing owing to their robustness, customizability, low cost, and high throughput [14-18]. By carefully choosing the correct focusing optics and controlling the parameters of the laser pulse such as wavelength, pulse energy, pulse width, and the travel distance between laser pulses, virtually any pattern can be written, surface morphology and etch depth can be carefully controlled, and sub-micron resolution can be attained [19, 20]. UV laser processing of polyimide substrates has also been widely investigated for applications in flexible microelectronics [21] due to the high UV absorption of the polymer. In addition, due to the long (~μs) heat diffusion time in many polyimides, nanosecond pulsed lasers are able to directly vaporize the laser-exposed areas primarily by photolytic decomposition processes, as opposed to the thermally dominated pyrolytic processes typically present in nanosecond laser processing [22]. This leads to very limited heat affected zones (HAZ), and therefore very clean features similar to those typically seen in ultrafast laser processing of metals and semiconductors. In this work, we will further demonstrate the robustness of UV laser processing of polymers, and demonstrate its usefulness in the field of optical element fabrication.

In order to model the diffraction efficiency of the binary phase photon sieves, finite difference time domain (FDTD) simulations were carried out using a commercial-grade simulator (Lumerical FDTD). For an N-level phase device, the optimal etch depth for

each step should be such that the phase difference between each step is an odd integer multiple of λ/N. The exact equation for etch depth *d* for a photon sieve operating in air is given as:

$$d = (2m+1)\frac{\lambda}{N(n_{film}-1)}, \quad \textbf{(1)}$$

where *m* is an integer, λ is the photon sieve design wavelength, and n_{film} is the refractive index of the film at the sieve design wavelength. The refractive index of the Kapton™ film substrate used in this study was taken to be 1.70 [23]. This gives a depth of 0.452 μm (m = 0) for a binary phase device operating at 633 nm wavelength.

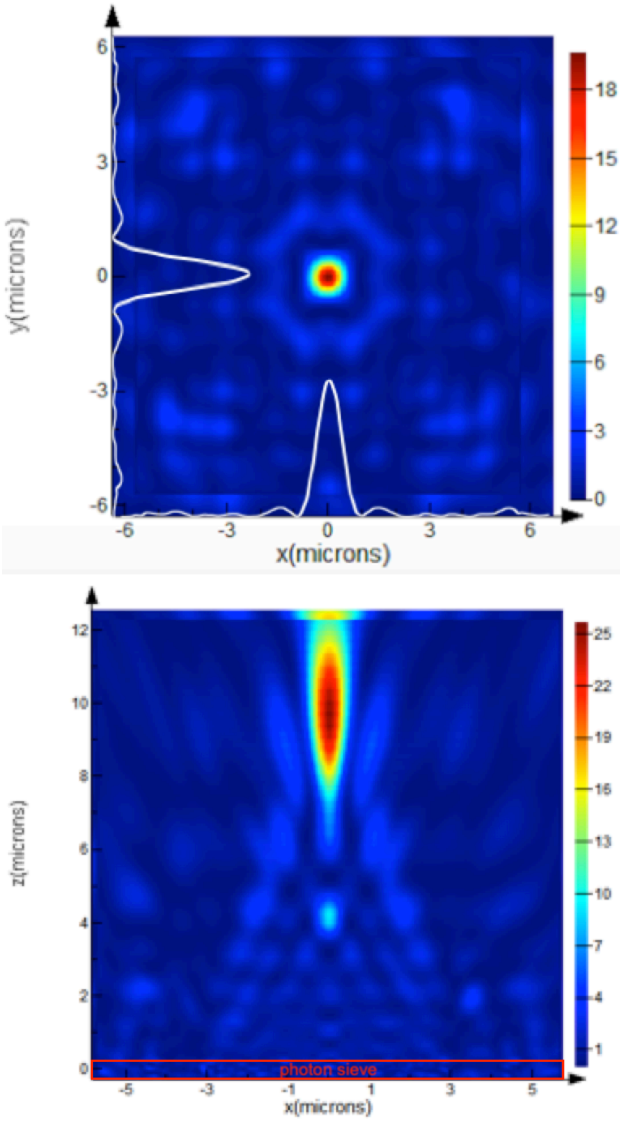

Fig. 1. FDTD simulation result showing the binary phase photon sieve E-field distribution in the focal plane (top) and axis of propagation (bottom).

The simulations were carried out for a miniaturized version of the experimental device in order to reduce the computational memory requirements. Altering the dimensions of the optics should have no effect on their efficiencies, so long as all of the incident light used in the efficiency calculation is collected by the optics (i.e. the light source is the same diameter as the optics). The photon sieve parameters used in the simulation were as follows: two rings, focal length of 10 μm, design wavelength of 633 nm, etch depth of 0.452 μm into the substrate. The substrate was a dielectric with refractive index 1.7 and extinction coefficient of 0. The photon sieves were designed such that 48% of the total photon sieve area was patterned with pinholes (filling fraction) in order to maximize performance. Images of the simulated focal plane intensity and z-axis electric field evolution are shown in Fig. 1. The simulated diffraction efficiency for the photon sieve was 11.45%. Analysis of the corresponding binary phase Fresnel zone plate was also performed for comparison and gave an efficiency of 34.31%.

For this experiment, commercial polyimide substrates (DuPont Kapton™-type HN, 12.5 μm thick) were irradiated by a 355 nm DPSS laser (Coherent MATRIX) providing pulses of 25 ns duration at 0.64 J/cm² pulse energy at the substrate and 20 kHz repetition rate. The laser beam was expanded and steered across the substrate by a galvanometric scan head and focused by an F-Theta scan lens to a spot of approximately 15 μm in diameter. In order to sufficiently reduce the laser pulse energy for this study, the laser output was passed through a neutral density filter of OD = 0.3 prior to impinging the sample. Polyimide substrates were cleaned with acetone and DI water prior to exposure, and were placed on glass substrates during laser irradiation. All processing was carried out under ambient conditions. Various scan speeds, and thus laser shot-to-shot distances, were tested and examined to obtain the optimum etch depth and surface roughness for photon sieve applications.

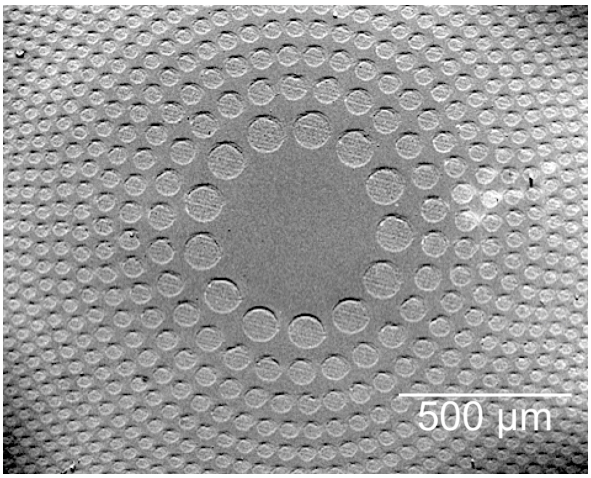

Fig. 2. SEM image showing the inner rings of the laser-fabricated binary phase photon sieve.

In this study, photon sieve pinholes were fabricated by raster scanning the laser beam across a selected area in order to produce a filled circle. An SEM image of the fabricated photon sieve is shown in Fig. 2. The control software utilized in this study allows for the manipulation of the raster line spacing when marking a filled object. In order to understand the dependence of etch depth on fill line spacing, photon sieves were fabricated using 7.5 and 10

μm line spacing, resulting in a 50% and 33% overlap between adjacent lines, respectively. Here, line spacing is the distance between adjacent laser scan lines used to create the filled features. Controlling the line spacing and scanning speed allows to control the overlap between subsequent laser shots in the same line as well as adjacent laser line scans, respectively.

Photon sieves were fabricated with various laser scan speeds at each of the line spacing in order to fully understand the effect of shot-to-shot travel distance on etch depth. The filling fraction of these photon sieves was approximately 23%. Photon sieves with filling fractions of 48% were also fabricated and tested. Etch depth was measured via white light interference profilometry, and the results are shown in Fig. 3. As is shown, for a given photon sieve filling fraction, the etch depth has little dependence on the line spacing within a fill. This is likely due to the high degree of thermal confinement experienced by the laser pulse when the pulse duration is significantly less than the substrate thermalization time. In addition, the laser fluence is sufficiently low that the tails of the Gaussian beam are below the ablation threshold, hence the lack of change in etch depth between the spacing used here. Higher fluence or larger difference in line spacing would show an effect on etch depth. The fit line in Fig. 3 follows the relation between etch depth and shot-to-shot travel distance:

$$d = \frac{A}{\Delta}, \qquad (2)$$

where Δ is the travel distance and A is a fitting parameter [24]. However, the laser-processed areas show an increased surface roughness compared to the un-processed film, suggesting the presence of some thermal effects in the ablation process, similar to those commonly seen in ns laser ablation of metals. We attribute these to the laser photon energy, $E = hf$, being slightly too low to directly break each of the various different chemical bonds of the polymer. This leads to the presence of a small number of pyrolytic ablation processes, as opposed to purely photolytic ones, during laser irradiation. Profilometer images showing the morphology of individual pinholes are shown in Fig. 4.

Photon sieves were then characterized in terms of focal point FWHM and diffraction efficiency using a CCD laser beam profiler and an optical power meter, respectively. For characterization, the photon sieve of each filling factor with an etch depth closest to the ideal value was selected. The FWHM of the 23% and 48% filling factor photon sieves were 75.4 μm and 65.9 μm, respectively. The diameter of the input Gaussian beam incident on the photon sieve was 6.2 mm. An image of the 48% filling factor photon sieve focal points is shown in Fig. 5. The diffraction efficiency of a phase type photon sieve should approach a maximum value as the filling fraction of pinholes approaches 50% due to the more efficient suppression of the zero-order diffracted light. In this study, photon sieves of filling fraction 23% showed diffraction efficiencies of 7%, while sieves with 48% filling fractions showed diffraction efficiencies of 9.5% on Kapton™ films. The total reflection loss from the two polyimide surfaces is 13.44%. Therefore, by employing an anti-reflection coating, device efficiencies should rise to 8.09% and 10.97%, respectively. Diffraction efficiencies can be further improved by employing a multi-level phase structure and further reduction in pinhole surface roughness via a shorter wavelength or shorter pulse width laser.

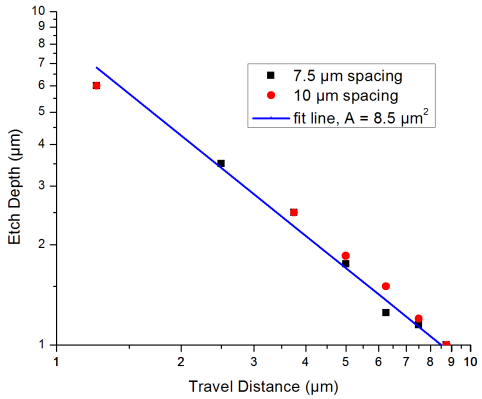

Fig. 3. Plot of polyimide etch depth vs. shot-to-shot travel distance for various photon sieve line spacing. Measured data is in good agreement with expected behavior.

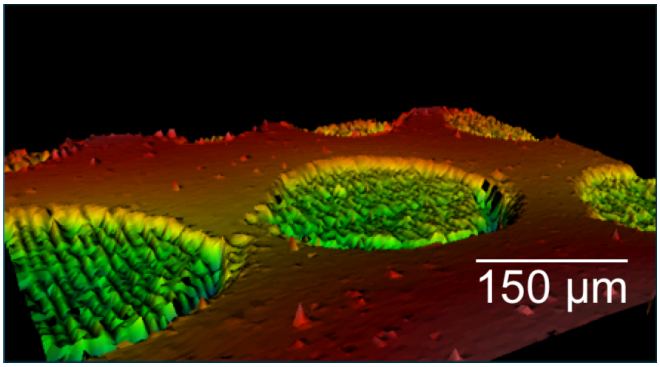

Fig. 4. 3D profilometry scan showing binary photon sieve pinhole morphology in the innermost ring. Measured depth and RMS roughness in patterned area = 1.35 μm and 469 nm, respectively.

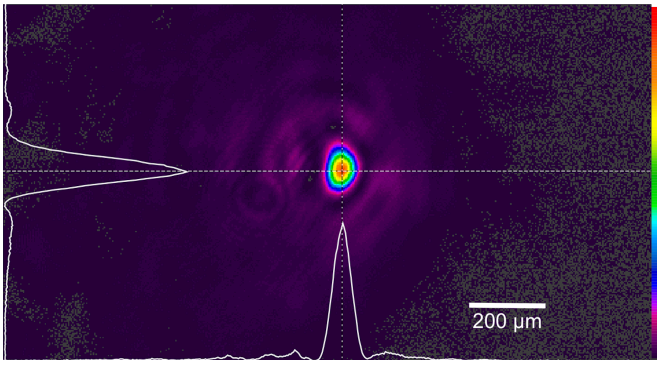

Fig. 5. Beam profile image of the binary photon sieve focal point. Photon sieve parameters used are: f = 400 mm, n = 19, λ = 633 nm, 48% fill factor.

As a phase type device, proper phase separation is necessary in order for the light to properly focus. In order to understand the effects of improper phase separation on sieve performance,

various sieves with etch depths diverging from the ideal value were characterized by their diffraction efficiencies. The results are shown in Fig. 6. As etch depths diverged from their nearest ideal value, diffraction efficiency decreased linearly from the maximum efficiency value. Binary phase Fresnel zone plates were also fabricated by the laser ablation method. An image of the fabricated zone plate is shown in Fig. 7. The measured diffraction efficiency of the zone plate was 33.7%, which is in good agreement with the simulated value. It should also be noted that the Kapton™ sieves are largely insensitive to temperature variation due to the low CTE value of the polyimide [23]. Additionally, folding cycle tests were performed, and sieve focal point properties were largely unaffected by folding cycles so long as firm creases were not formed in the film.

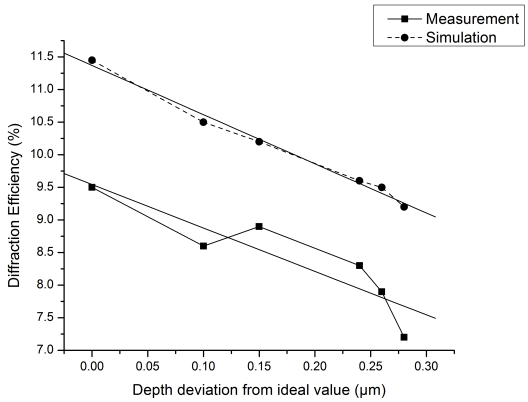

Fig. 6. Data showing the effect of etch depth on photon sieve diffraction efficiency obtained experimentally (solid) and via FDTD simulations (dashed). Linear fits for each data set are shown as solid, unmarked lines.

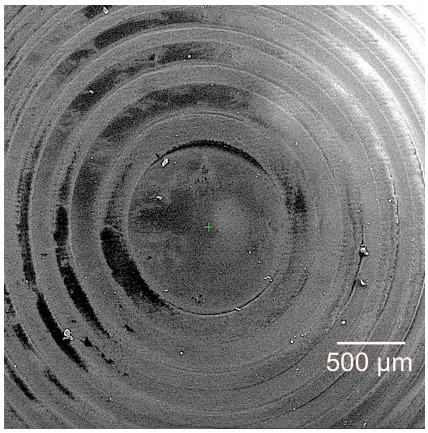

Fig. 7. SEM image of the laser fabricated binary phase Fresnel zone plate. Shadowing effects are attributed to slight charging of the sample.

In conclusion, we have successfully demonstrated flexible binary photon sieve via UV pulsed laser processing of polyimides. The laser direct writing process allows for precise control of polyimide etch depths and surface roughness by simply altering laser parameters and shot-to-shot travel distances. The fabricated photon sieves performed well and demonstrated the highest diffraction efficiencies yet reported for a photon sieve at 11%. By employing multilevel phase structures and antireflection coatings, diffraction efficiencies can be further improved. Such highly efficient photon sieves fabricated with low cost and high throughput laser processing method could find use in a variety of applications, in particular space-based deployable satellites for telescopes and optical communication systems. This study also demonstrates the usefulness of pulsed laser processing in the field of flexible polymer diffractive optics.

Funding. This work is supported by the Lab Demo (Photon Sieve) IRAD project of NASA Langley Research Center, the NASA Langley Professor Program and the NSF I/UCRC Laser and Plasma for Advanced Manufacturing program.

Acknowledgment. The authors thank George Wilkes for assistance with optical profilometry measurements.

References

1. L. Kipp, M. Skibowski, R. L. Johnson, R. Berndt, R. Adelung, S. Harm and R. Seemann, Nature **414**, 184 (2001).
2. R. Liu, F. Li, M. J. Padgett, and D. B. Phillips, Optica **2** (12), (2015).
3. G. Andersen, Opt. Lett. **30** (22), (2005).
4. G. Andersen, Appl. Opt. **49** (33), (2010).
5. G. Andersen and D. Tullson, Appl. Opt. **46** (18), (2007).
6. J. Jia, J. Jiang, C. Xie and M. Liu, Opt. Comm. **281** (17), (2008).
7. O. Asmolova, G. P. Anderson and M. A. Cumming, Proc. SPIE 10120, 1012009 (2017).
8. R. Menon, D. Gil, G. Barbastathis and H. I. Smith, J. Opt. Soc. Am. **22** (2), (2005).
9. A.Sabatyan, and S. A. Hosseini, Appl. Opt. **53** (31), (2014).
10. F. S. Oktem, F. Kamalabadi, and J. M. Davila, in Proc. of IEEE Int. Conf. on Image Processing (ICIP) (2014).
11. J. M. Davila, Proc. SPIE 8148, (2011).
12. Jia Jia and Xie Chang-Qing, Chinese Phys. B **18** (1), 183, (2009).
13. Andersen, G., Dearborn, M., and McHarg, G., 11th Annual AMOS Conference, Maui Economic Development Board, Inc., (2010).
14. B. K. Nayak and M. C. Gupta, Optics and Lasers in Engineering, **48** (10), (2010).
15. M. C. Gupta and D. Carlson, MRS Energy & Sustainability **2**, (2015).
16. R. R. Gattass and E. Mazur, Nature Photonics **2**, (2008)
17. J. Serbin, A. Egbert, A. Ostendorf, B. N. Chichkov, R. Houbertz, G. Domann, J. Schulz, C. Cronauer, L. Fröhlich, and M. Popall, Opt. Lett. **28** (5), (2003).
18. M. Julian, D. MacDonnell, and M. Gupta, Opt. Express **25** (25), (2017).
19. P. P. Pronko, S. K. Dutta, J. Squier, J. V. Rudd, D. Du and G. Mourou, Opt. Comm. **114** (1), (1995).
20. P.R. Herman, R.S. Marjoribanks, A. Oettl, K. Chen, I. Konovalov and S. Ness, Appl. Surf. Sci., **154-155** (2000).
21. B. Pratap, C. B. Arnold and A. Pique, Proc. SPIE 4979, Micromachining and Microfabrication Process Technology VIII, (2003).
22. K. Sugioka, M. Meunier, and A. Pique, Laser Precision Manufacturing, Springer Series in Materials Science 135 (Springer, 2010).
23. Dupont, KaptonTM Summary of Properties, datasheet, (revised 2016).
24. S. Metev and V. Veiko, Laser Assisted Microtechnology, Springer-Verlag, (Springer-Verlag, 1994).

HIGH-EFFICIENCY FLEXIBLE MULTILEVEL PHOTON SIEVES BY SINGLE-STEP LASER-BASED FABRICATION AND OPTICAL ANALYSIS

MATTHEW N. JULIAN,[1] DAVID G. MACDONNELL,[2,*] AND MOOL C. GUPTA[1,*]

[1]*Charles L. Brown Department of Electrical and Computer Engineering, University of Virginia, Charlottesville, VA 22904, USA*
[2]*NASA Langley Research Center, Hampton, VA 23666, USA*
**mgupta@virginia.edu*

Abstract: Over the past several decades, the need for high-resolution, high-efficiency, lightweight, high contrast focusing optics has continued to increase due to their applications in fields such as astronomy, spectroscopy, free-space optical communications, defense, and remote sensing. In recent years, photon sieve planar diffractive optics, which are essentially Fresnel zone plates with the rings broken into individual "pinhole" apertures, have been developed on flexible, lightweight polyimide substrates. However, transmission efficiencies have continuously been very low (~1-11%) until this work, thus impeding the widespread use of photon sieves in practical applications. Here, we present flexible, lightweight, 4 and 8-level level phase photon sieves with 25.7% and 49.7% transmission efficiency, respectively – up to 5x greater than that of any other photon sieve reported thus far. Additionally, these sieves were fabricated via a single step pulsed laser ablation method. The total time to fabricate a ~3 cm^2 photon sieve via the single-step fabrication was tens of seconds, giving the technique a significant advantage over traditional photolithography used to generate multilevel structures. Analytical analysis of the photon sieve was carried out via finite-difference time domain (FDTD) method, and was in very good agreement with experimental results. We have also calculated via FDTD modeling the behavior of higher level photon sieves for further enhanced efficiencies, and analytically show an estimated upper bound on photon sieve efficiency of 70% within the first focal plane null in the limit of increasing step number, and the data presented herein provides a relationship between efficiency and step number. Additionally, this process of multilevel diffractive lens fabrication can be extended to multilevel Fresnel zone plates, which have not previously been demonstrated by this process. The results presented in this work represent a new step in high-resolution diffractive optics, showing efficiencies suitable for widespread applications in addition to drastically reducing the cost and complexity of fabricating multilevel focusing elements.

1. Introduction

Diffractive optical focusing elements have long been studied for applications in telescope objectives, spectroscopy, orbital angular momentum sensing, THz, deep ultraviolet (DUV), and electron beam optics, and nanolithography as alternatives to conventional refractive lenses which have higher weight and are difficult to fabricate for these applications. In recent years, photon sieves have been investigated to perform several of these applications [1-5].

Even more recently, they have been fabricated on flexible polymer substrates [6, 7]. Photon sieves are essentially Fresnel zone plates in which the Fresnel zones are divided into a large number of circular pinholes. The geometry and behavior of the optics are essentially the same, however photon sieves offer a distinct advantage in several fields due to their suppression of side-lobes in the focal plane, leading to higher resolution and contrast [1]. However, until this work, photon sieves have always suffered a drawback in that their efficiency is inherently much lower than their corresponding zone plate. Attempts have been made to increase photon sieve efficiency dramatically, such as fully transparent photon sieves, although these require physical holes in a material substrate, and are still limited in efficiency [8]. It is well known from diffractive optics that by employing a multilevel phase structure, the focusing efficiency of diffractive lenses is increased to much higher values compared to binary structures. However, the complexity of lithographic fabrication on flexible substrates has previously hindered the development of high-efficiency, lightweight photon sieves. Typically, using photolithography, an L level phase element requires 2^L exposure/etch steps. Here, we design and present results for a high-efficiency, multilevel phase photon sieve that employs a single-step multilevel laser ablation technique for fast, simple, and low-cost fabrication. Two-photon polymerization via direct laser writing has been demonstrated for multilevel Fresnel zone plates, and devices performed well [9]. However, this technique is limited in that only specific polymers can be used, which limits the device operation wavelength range. Previous work by our group has led to the development of laser ablation techniques for photon sieve fabrication [7, 10]. However, these works were limited to single level or binary phase structures, and had not been explored for single-step fabrication of multilevel phase structures. Additionally, the process presented in this work can be extended to Fresnel zone plate lenses, as multilevel devices by laser ablation have not been demonstrated to the best of our knowledge. Reaching an experimental maximum focusing efficiency of 49.7% for an eight-level device, these sieves demonstrate a nearly five-fold increase in focusing efficiency compared to reported phase type photon sieves. Furthermore,

higher orders of multilevel photon sieves were simulated, and an estimated upper limit on photon sieve efficiency was revealed. Efficiency approaches 70% (within the first null) and 91% (across the entire focal plane) for phase type photon sieves, placing a previously unknown estimated bound of photon sieve efficiency values. In addition, the laser ablation fabrication technique employed here is very robust and suitable for low cost, large area device fabrication [7, 10, 11].

2. Design and Numerical Analysis of Multilevel Photon Sieves

Because photon sieves are directly derived from the Fresnel zone plate, very similar governing equations are used in their design. In the case of a multilevel photon sieve, each bright/dark zone pair is divided into L levels, where L is the number of steps in the phase structure. The basis of the zone plate/photon sieve design principle is that each Fresnel zone is positioned at a radius such that the diffracted light all constructively interferes at the focal point. As a result, subsequent bright zones are separated by integer multiples of n half wavelengths. In the case of a phase type device, the dark zones, which would typically be blocked from transmitting light, are phase-shifted in order to provide the proper constructive phase at the focal point. In the case of a binary phase device, this corresponds to a half-wavelength phase shift. However, because the design equations specify the radius of the outer edge of the Fresnel zone, and the zone has a physical width, it is clear that the phase of light passing near the outer zone edge is different than that of light passing near the inner zone edge. To combat this, multilevel phase structures divide the wavelength-wide bright and dark zone pair into a gradient of phase shifts, such that a nearly continuous phase shift is applied from 0 to λ. The specific phase height d of each zone is given by

$$d = (2m+1)\frac{(l-1)\lambda}{L(n_{sub} - n_{env})} \qquad (1)$$

and the sub-zone radius is given by

$$r(n,L)=\sqrt{\lambda f(\frac{2l}{L}+n-2)} \tag{2}$$

as adopted from the multilevel zone plate publication [12]. A schematic of the multilevel structure is shown in Fig. 1. In the above equations, n_{sub} and n_{env} are the refractive indices of the substrate and surrounding environment, respectively; f is the design focal length, l is the subzone index ranging from 1 to L, n is the zone number, m is an integer, and λ is the design wavelength. The photon sieve pinhole diameter was set equal to the corresponding Fresnel zone width in these studies. In order to maximize the phase shifted area of the photon sieves, each sieve was designed such that the maximum number of pinholes occupied each zone.

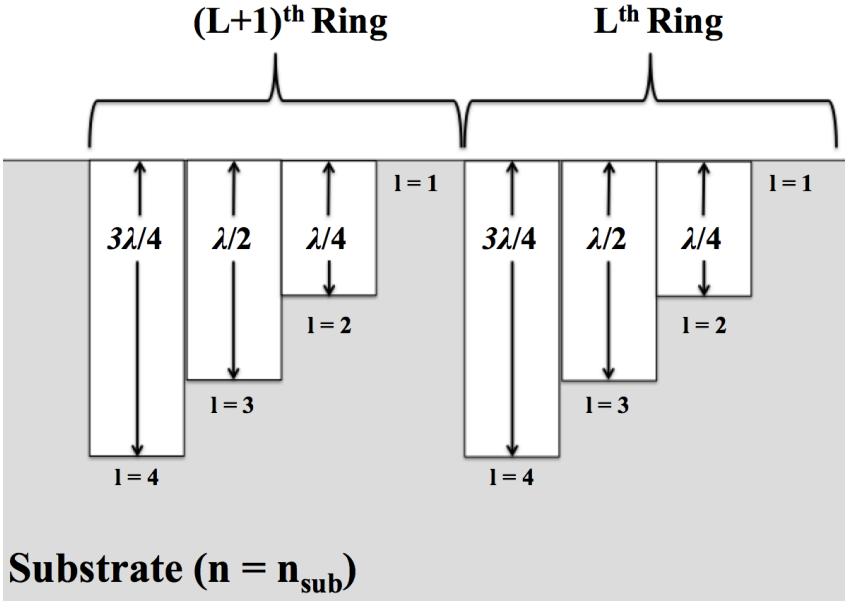

Fig. 1. Design schematic showing two rings of an L = 4 photon sieve cross section. Each ring is divided into L sub-zones, which are patterned to a depth given by equation 1. The first sub-zone is the unpatterned substrate [12].

The focusing efficiency of each photon sieve was simulated using a commercial finite-difference time domain solver (Lumerical FDTD). It should be noted that FDTD was chosen for convenience, but other methods such as Fresnel integral evaluation can be used as well, and both are expected to give identical results. The simulated photon sieve design parameters differed from the fabricated samples due to the large computational time required for FDTD simulations with large dimensions. The photon sieves used in the simulations operated at 633 nm wavelength and had a diameter of 11 μm. A full 3D vectorial simulation was performed with 20 nm mesh size across the full simulation environment. However, this should have no effect on the focusing efficiency, as it is independent of the device dimensions. Furthermore, because the focal length is well beyond the optical near field ($d >> \lambda$), there should be no near field effects such as dielectric scattering that would artificially inflate the efficiency values [8]. Additionally, as will be discussed in the next section, experimentally obtained efficiencies are in good agreement with FDTD values. The electric field amplitude after the L = 4 photon sieve along the optical axis and focal plane are shown in Fig. 2.

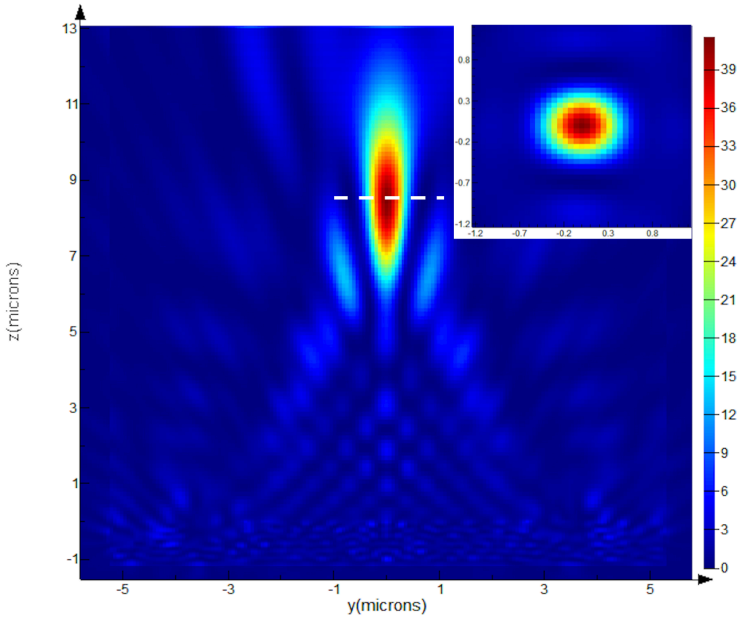

Fig 2. FDTD results showing the L = 4 photon sieve E-field distribution along the optical axis and focal plane (inset).

Multilevel sieves of L = 8, 16, and 32 were also simulated, as well as the corresponding Fresnel zone plates for comparison. The resulting focusing efficiencies are shown in Fig. 3. In this work, focusing efficiency is defined as the ratio of the power inside of the first null of the focal point to the total power incident on the sieve. The source is made to be the same area as the sieve. Note that these efficiencies differ from the mathematically calculated value for zone plate efficiency due to our restriction that only power inside of the first null is counted. When power in all nulls is counted, the zone plate efficiency approaches 100%, while the photon sieve efficiency approaches 91% [13].

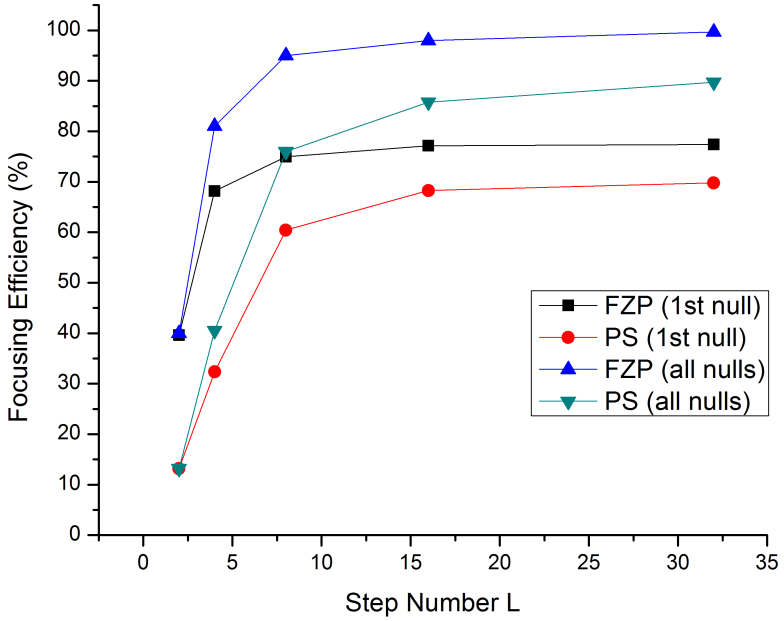

Fig. 3. Summary of FDTD simulated zone plate (FZP) and photon sieve (PS) efficiencies η for various step numbers both in the first null and all nulls of the focal plane. The photon sieve efficiency (across all focal plane nulls) asymptotically approaches ~91% of the zone plate value for a photon sieve with 50% fill factor as the number of steps approaches infinity. For a reflectionless substrate, the photon sieve focusing efficiency (within the first null of the focal plane) approaches 70%.

It can be seen in Fig. 3 that the photon sieve efficiency is always lower than the corresponding zone plate. The authors attribute this to the ratio of the patterned sieve area to the zone plate area. As described for an opaque photon sieve (such as metal on glass), the photon sieve first order diffraction efficiency (here referred to as focusing efficiency) is reduced by the square of the transmissive area relative to a zone plate [1]. Based on the results of the simulations presented here, we propose that this relationship approximately holds true for phase type photon sieves as well, with the adjustment that "transmissive area" is replaced with "phase shifted area". In this work, the total patterned area of the photon sieve rings is calculated to be ~95.6% (i.e. the pinhole area divided by the total zone area). If we consider this to be the "transmissive" area, we see that by squaring this number, we arrive at 91.4% focusing efficiency, which is in very good agreement with FDTD simulations when accounting for all focal plane nulls. When restricted to only the first null (i.e. the primary focal spot only), the focusing efficiency approaches 70% as seen in Fig. 3. Therefore, we propose an estimated efficiency limit of a photon sieve is ~70% within the first null, and ~91% when all nulls are accounted for.

3. Experimental Results

In order to fabricate multilevel phase structures in a single processing step, a laser ablation technique was employed whereby the phase depth is precisely controlled by laser power and scanning speed. Photon sieves were fabricated on 12.5 μm thick commercial polyimide substrates (DuPont Kapton^{TM}) via pulsed laser ablation using a 25 ns pulse width, 355 nm wavelength source (Coherent MATRIX) delivering 0.64 J/cm^2 pulses, and operating at 20 kHz repetition rate. The beam was expanded and focused to a spot size of ~15 μm (1/e^2 diameter). Schematics of the fabrication and characterization setups are shown in Fig. 4. In order to write individual features, the beam is raster scanned across the substrate as described in detail in our previous work [10]. In short, the beam is raster scanned across the location of each feature in order to produce a filled feature. The beam is then blanked while the Galvo

positions itself to mark the next feature location. The minimum feature size of L = 4 and L = 8 photon sieves were each ~60 μm due to resolution limits of the employed laser system. Laser scanning speed, which can be tuned on-the-fly, was used to precisely control etch depth, allowing for single-step fabrication of multilevel phase elements [7]. Substrates were cleaned with acetone and de-ionized water prior to exposure. L = 4 and L = 8 photon sieves operating at 633 nm wavelength were designed with a 1 m (NA = 0.005) and 2 m (NA = 0.0025) focal lengths, respectively. The diameters of both photon sieves is 10 mm. L = 4 sieves were designed with 19 rings and m = 2, while L = 8 sieves were designed with one ring and m = 3 due to feature size constraints. These parameters were chosen for ease of fabrication, although much smaller features and focal lengths are possible via the same fabrication technique with a different system [14]. The total fabrication time is ~30 s for each sieve. A scanning electron microscope (SEM) image and optical profilometer scan of the fabricated L = 4 photon sieve are shown in Fig. 5.

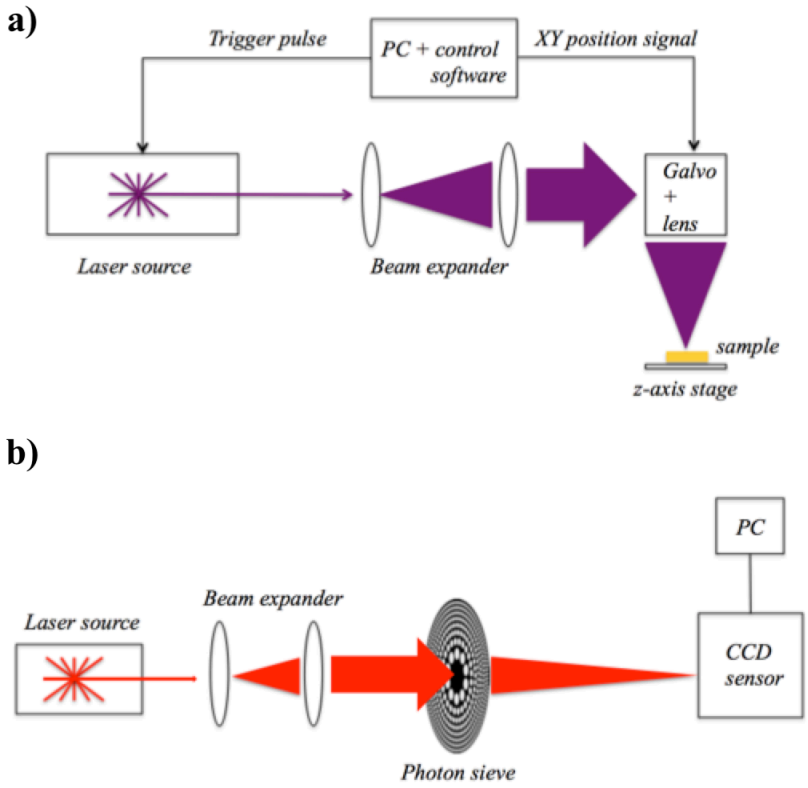

Fig. 4 Diagram of the (a) fabrication setup and (b) characterization setup used in the experiment.

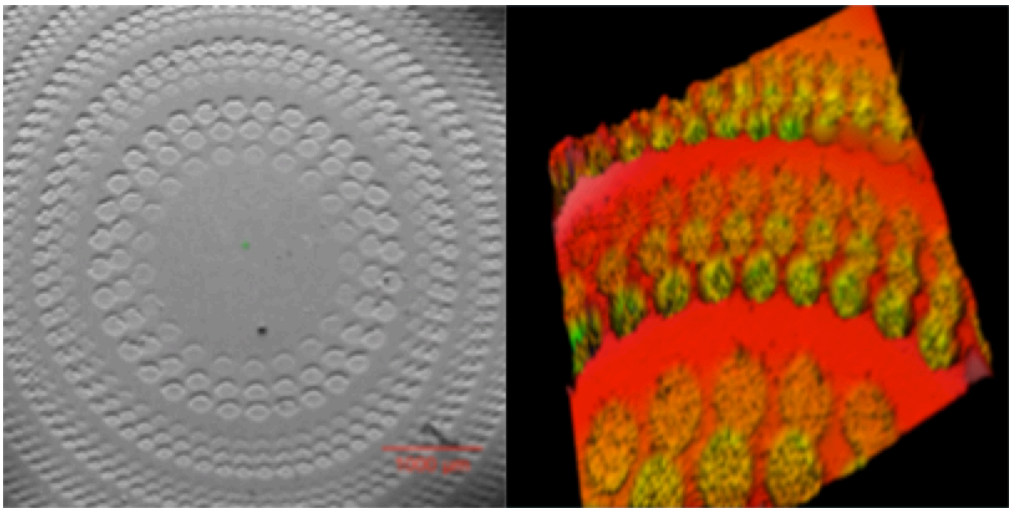

Fig. 5. (left) SEM image of the fabricated L = 4 photon sieve and its corresponding optical profilometer scan across several zones (right). Average surface roughness in the processed area was measured as 469 nm.

It can be seen in the profilometer scan that the laser processing imparts a small surface roughness onto the substrate, as the patterned area is slightly rougher than the unpatterned surface. This can be attributed to a combination of the laser wavelength and pulse width. In polyimide laser ablation, the polymer bonds can be directly broken in a photolytic ablation process if the laser wavelength is sufficiently short [15]. This, coupled with the relatively long heat diffusion time in polyimides, generally provides for a very small heat affected zone and leads to smoother structures. Therefore, it can be deduced that the surface roughness results from a small amount of melting and re-solidification from the laser irradiation. Using an even shorter wavelength and/or pulse width source can mitigate this effect, reducing surface roughness significantly. Post-treatment using chemical etching and other similar techniques can also be employed. Additionally, by using a high numerical aperture scan lens in the fabrication setup, features as small as sub-micron dimension can be achieved [16]. Such a system would make low surface roughness, high L designs easily realizable for high numerical aperture applications. Furthermore, as discussed in our previous work, common fabrication errors from laser ablation are related to etch depth into the substrate, which must be carefully optimized by controlling laser pulse energy, scanning speed, and number of shots, and negatively impact focusing efficiency [7]. With respect to multilevel elements specifically, careful theoretical analysis of similar fabrication errors has been presented elsewhere in the context of zone plates [17].

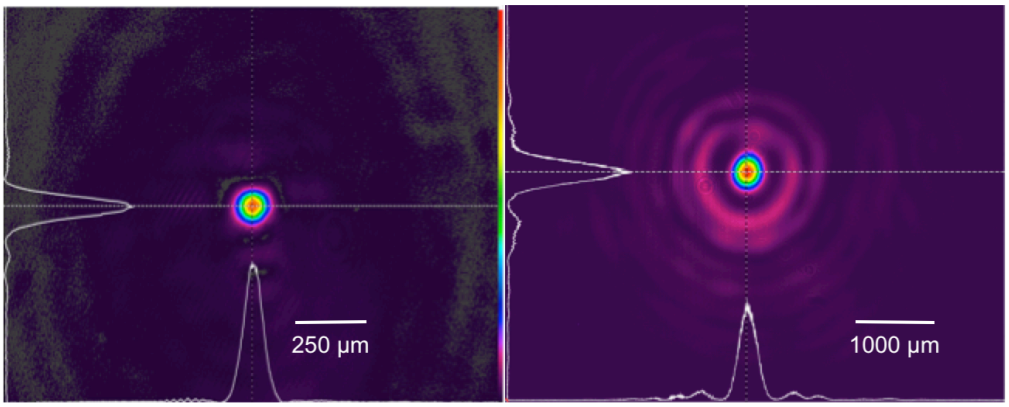

Fig. 6. CCD beam profiler image of the L = 4 (left) and L = 8 (right) photon sieve focal point. The measured focusing efficiencies were 25.7% and 49.7%, and the focal point FWHMs were 102 µm and 295 µm, respectively. Focal lengths are 1 m (left) and 2 m (right).

In order to evaluate the photon sieve performance, a CCD beam profiler and optical power meter were used. The CCD image of the fabricated L = 4 device focal point is shown in Fig. 6. A comparison between simulated and measured efficiency values are shown in Fig. 7. The measured focal lengths of the fabricated devices were 1.01 m and 2.01 m, respectively. The resulting FWHM and focusing efficiency were 102 µm and 25.7%, respectively. This is in very close agreement with the simulated efficiency value of 28% for the L = 4 device. For the L = 8 device, the measured efficiency was 49.7%, which is in good agreement with the simulated value of 52.3%. The focal point FWHM of the L = 8 sieve was 295 µm. This increase in FWHM from the L = 4 device is due to the much lower numerical aperture of the L = 8 device, which was reduced due to fabrication constraints in our laser system. Additionally, focal point FWHMs were simulated for the L = 4 and L = 8 devices using scalar theory for amplitude type photon sieves as a general comparison [10]. The simulated FWHMs for the L = 4 and L = 8 sieves were 91.3 µm and 283 µm, respectively, which are in good agreement with experimentally obtained values. This agreement shows that, like amplitude-type photon sieves, multilevel phase photon sieve focal point diameters are limited by the width of the outermost Fresnel zone. Focal point ellipticity was also measured for both

samples, and values of 0.96 and 0.93 were obtained for the L = 4 and L = 8 sieves, respectively.

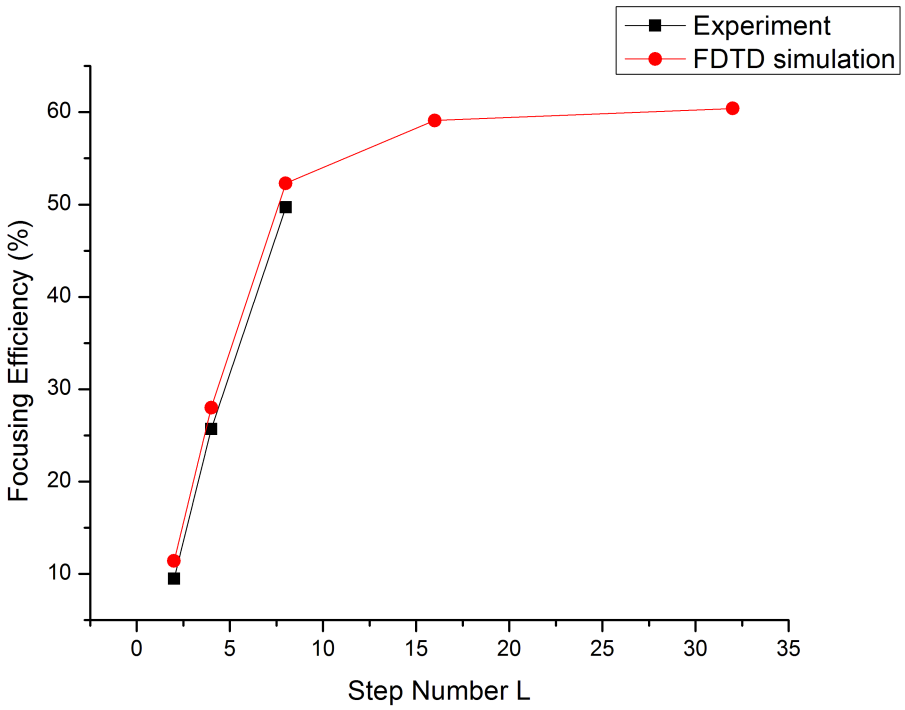

Fig. 7. Comparison of measured and simulated photon sieve efficiencies (within the first null of the focal plane) on polyimide substrates (n = 1.7).

4. Conclusion

We have successfully demonstrated multilevel phase photon sieve diffractive optical elements fabricated by single-step laser ablation process, whereby the phase depth is controlled by laser power and modulating the laser scanning speed. The multilevel phase elements displayed significantly enhanced efficiencies, as expected, with efficiencies of 25.7% and 49.7% for L = 4 and L = 8 step sieves. These sieve efficiencies are three and five times higher than any previously reported value, respectively, and their optical performance agreed well with FDTD

simulations. In addition, based on FDTD simulation results, we propose an estimated maximum efficiency limit of 70% (within the first null) for a multilevel photon sieve with 50% fill factor as the step number L approaches infinity. When all nulls are accounted for, the focusing efficiency approaches ~91%. Furthermore, based on the simulation results, we propose that the maximum possible efficiency of the photon sieve is approximately limited by the square of the ratio of the phase shifted photon sieve area to the phase shifted area of a kinoform zone plate. Additionally, we have shown that multilevel photon sieve focal point FWHM are still limited by the width of the underlying (undivided) Fresnel zone, just as in a binary or amplitude type device. It again should be noted that the low NA lenses demonstrated here serve only as proof of concept due to the fabrication limits of our laboratory system and do not represent a fundamental limitation of the photon sieve lens or the laser ablation fabrication technique. In general, high NA multilevel photon sieves are possible via this technique using a higher resolution fabrication system. However, applications for large focal length devices do exist, for example large telephoto lenses and large depth of field imaging. The results in this paper suggest that photon sieves are suitable for various imaging and sensing applications, where previously efficiencies hindered their applicability, and that they can be fabricated at a significantly reduced cost and time consumption compared to photolithographic techniques.

Funding

This work was supported by Lab Demo (Photon Sieve) IRAD project of NASA Langley Research Center; NASA Langley Professor Program; National Science Foundation (NSF) I/UCRC Laser and Plasma for Advanced Manufacturing program.

Acknowledgements

The authors thank George Wilkes for assistance with optical profilometry measurements.

References

1. L. Kipp, M. Skibowski, R. L. Johnson, R. Berndt, R. Adelung, S. Harm and R. Seemann, "Sharper images by focusing soft X-ray with photon sieves," Nature 414, 184--188 (2001).
2. G.Andersen, "Large optical photon sieve," Optics Letters 30, 2976--2978 (2005).
3. R. Menon, D. Gil, G. Barbastathis and H. I. Smith, "Photon-sieve lithography," Journal of the Optical Society of America 22, 342--345 (2005).
4. O. Asmolova, G. P. Andersen, M. A. Cumming, "Photon sieves for creating and identifying orbital angular momentum of light," Proc. SPIE 10120, Complex Light and Optical Forces XI, 1012009 (27 February 2017).
5. S. Wang and X. Zhang, "Terahertz tomographic imaging with a Fresnel lens," Opt. Photonics News 13 (59), (2002).
6. Geoff Andersen, "Membrane photon sieve telescopes," Appl. Opt. 49, 6391-6394 (2010).
7. M. N. Julian, D. G. MacDonnell, and M. C. Gupta, "Binary phase photon sieves on flexible polyimide substrates by laser ablation," Optics Letters **43** (10), 2368-2371 (2018).
8. W. Sun, Y. Hu, D. G. MacDonnell, H. J. Kim, C. Weimer, and R. R. Baize, "Fully transparent photon sieve," Optics Express **25** (15), 17356-17363 (2017).
9. D. We, L.G. Niu, Q. D. Chen, R. Wang, and H. B. Sun, "High efficiency multilevel phase-type fractal zone plates," Optics Letters **33** (24), 2913 (2008).
10. M. N. Julian, D. G. MacDonnell, and M. C. Gupta, "Fabrication of photon sieves by laser ablation and optical properties," Optics Express 25, 31528-31538 (2017).
11. O. A. Araromi, S. Rosset, and H. R. Shea, "High-resolution, large-area fabrication of compliant electrodes via laser ablation for robust, stretchable dielectric elastomer actuators and sensors," ACS Applied Materials & Interfaces 7 (32), 18046-18053 (2015).
12. E. Di Fabrizio, F. Romanato, G. Gentili, S. Cabrini, B. Kaulich, J. Susini, and R. Barrett, "High-efficiency multilevel zone plates for keV X-rays," Nature 401, 895-898, (1999).
13. D. Attwood, A. Sakdinawat, *X-Rays and Extreme Ultraviolet Radiation: Principles and Applications,* 2nd ed., Cambridge University Press, Cambridge, UK (2017).
14. R.Martínez Vázquez, S. M. Eaton, R. Ramponi, G. Cerullo, and R.Osellame, "Fabrication of binary Fresnel lenses in PMMA by femtosecond laser surface ablation," Opt. Express 19, 11597-11604 (2011).
15. K. Sugioka M. Meunier, and A. Pique (eds.), *Laser Precision Microfabrication*, Springer Series in Materials Science 135, (2010).
16. P. Pronko, S. Dutta, J. Rudd, D. Du, and G. Mourou, "Machining of sub-micron holes using a femtosecond laser at 800 nm," Optics Communication **114** (1), 106-110 (1995).
17. M. Ferstl, B. Kuhlow, and E. Pawlowski, "Effect of fabrication errors on multilevel Fresnel zone lenses," Optical Engineering **33** (4), (1994).

Laser processing of materials using a photon sieve lens

M. N. Julian[1,†] and M. C. Gupta[1,*]

[1]Charles L. Brown Department of Electrical and Computer Engineering, University of Virginia, Charlottesville, Virginia 22904, USA

[†]mnj3db@virginia.edu
[*]mgupta@virginia.edu

Abstract

A laser ablation study was carried out by focusing optical energy via a photon sieve planar diffractive lens and the results are compared with traditional refractive lenses. It was found that the materials processed by the photon sieve show a significant reduction in the lateral spread and thickness of the oxidized surface when compared to the refractive lens. This oxide layer is primarily attributed to the heat affected zone and recast layer in the silicon substrate. This difference is attributed to the pinhole diffraction of the photon sieve, which produces a reduced $1/e^2$ diameter compared to the f-theta lens for a given full-width at half-maximum value. This reduced spot size compared to a refractive lens, for a given numerical aperture, translates to less material removal/redeposition and a narrower ablation region in the case of the photon sieve, without any sacrifice in depth of focus. The numerical apertures achievable with photon sieves are comparable to those of commercial microscope objectives, but with a sub-Airy disk focal spot size. This increased resolution, combined with a longer depth of focus for a given spot size, reduced material redeposition, and a narrower ablation region show a significant improvement over the current state of the art. The results of this study could have a large impact on laser materials processing in the aerospace, medical, semiconductor, and automotive industries, among others.

Laser processing of materials is a large area of both academic and industrial research across many fields including surgery, semiconductor processing, marking, cutting, drilling, annealing, welding, and so forth [1-6]. In order to create precise features, the heat spread in the material, or the heat affected zone (HAZ) must be carefully controlled so as to only affect the areas that are to be modified by the laser. For example, in optical surgery, a small HAZ is necessary so that the surrounding area is not damaged by the laser. The HAZ of a laser

mark is dependent on parameters such as the incident laser fluence, pulse width, the incident laser beam profile, and the material thermal conductivity. The HAZ describes the region that is mechanically or chemically altered as a direct result of thermal processes following absorption of the incident laser energy [7].

Additionally, a recast layer is present in short pulse laser ablation of materials and greatly affects the surface properties and chemical makeup of the affected area. This recast layer consists of molten material that is vaporized and re-solidified around the mark edge, as well as vaporized material that redeposits as a film around the ablation mark. Because this layer is initially in a liquid/vapor phase before re-solidification, it is also more readily oxidized by the surrounding atmosphere. The amount of recast material is also dependent on laser fluence, number of shots, and the total amount of removed material (i.e. laser spot size). For many applications, fluence and material are fixed, leaving the laser beam profile as the sole variable. Additionally, a Gaussian profile is often desired and is commonly used. Therefore, it is important to be able to control the HAZ and recast layer formed from a Gaussian beam incident on a material. To that end, we demonstrate the use of planar diffractive lenses known as photon sieves for the reduction of these unwanted effects.

A photon sieve is essentially a Fresnel zone plate with each ring segmented into circular pinholes [8]. This difference in design allows photon sieves to have sub-Airy disk focal point diameters, as well as essentially zero side lobes in the focal plane, which makes them preferable to zone plates and refractive lenses for applications such as imaging. Previously, photon sieves have been investigated for uses such as space telescopes, lithography optics, beam shapers, holography optics, and fiber-to-chip-coupling elements [8-13]. However, until recently their focusing efficiency limited their applicability in many other applications. Our group has previously demonstrated a multilevel phase design that allows for up to 70% focusing efficiency using a photon sieve (compared to 1-10% with past designs), without sacrificing the high-contrast or high-resolution performance of the sieve [14]. By utilizing this high-efficiency design, laser processing of materials using a photon sieve is made possible and is investigated in this study. The results show that the photon sieve lens provides several advantages in laser processing of materials compared to refractive lenses such as smaller HAZ, less redeposited material, the formation of smaller mark size, lighter-weight optics, and large area processing.

In order to study the differences in laser materials processing, experiments were carried out using a traditional f-theta lens and a photon sieve. For these experiments, a 4-level phase step (N = 4) photon sieve with 20 mm focal length and ~4 mm diameter (NA ~ 0.1) was fabricated using direct-write laser lithography. Full details of the photon sieve fabrication process can be found in the Supporting Information. An image of the fabricated device used in the experiments is shown in Fig. 1. As demonstrated in [14], the focusing efficiency of the N = 4 device was approximately 25%.

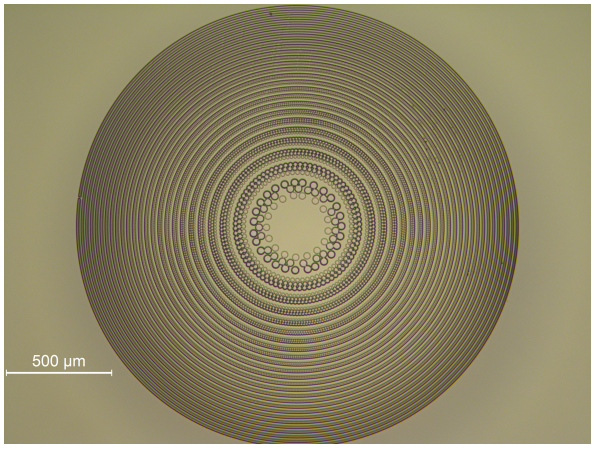

Fig. 1. Image of the fabricated N = 4 photon sieve used in the study.

For all laser processing experiments, a 1064 nm wavelength, 50 ns pulse width (IPG Photonics YLP-1/50/30/30/) was used. The photon sieve was compared to an f-theta lens in a commercial galvo system (Sino-Galvo). The focal spot sizes from the lens and photon sieve were slightly different; however, the laser fluences for each experiment were the same in each case. The laser pulse repetition rate was held constant at 30 kHz for all experiments, and scanning speeds were adjusted such that the shot overlap was the same in each experiment. Experiments were conducted by drawing lines at various fluences near the melting threshold, ablation threshold, and above the ablation threshold. All substrates were cleaned using isopropanol prior to laser exposure. Additional details regarding the experimental setup can be found in the Supporting Information.

Ablation lines were written into Si wafers due to the stability of the oxide layers, which makes the examination of the recast layers and HAZ much more reliable and therefore will be easily visible under an optical microscope. A direct comparison of fluences of 2.06 J/cm^2 is shown in Fig. 2, which shows the increased oxide width and thickness in the case of the lens. Note that the spot size in each case is slightly different (larger in the lens case), which causes more ablated material in the case of the lens. However, energy densities in each case are equal. This increased oxidized area is evidenced by the difference in colors seen in the images. Whereas the photon sieve shows a more consistent blue color from edge to edge, the lens clearly has a large gradient from yellow to green to blue. These colors are indicative of the oxide thickness formed on the Si surface. The yellow, metallic blue, and royal blue colors likely correspond to oxide thicknesses of 200, 150, and 120 nm, respectively, based on commonly accepted SiO_2 color charts [15-17].

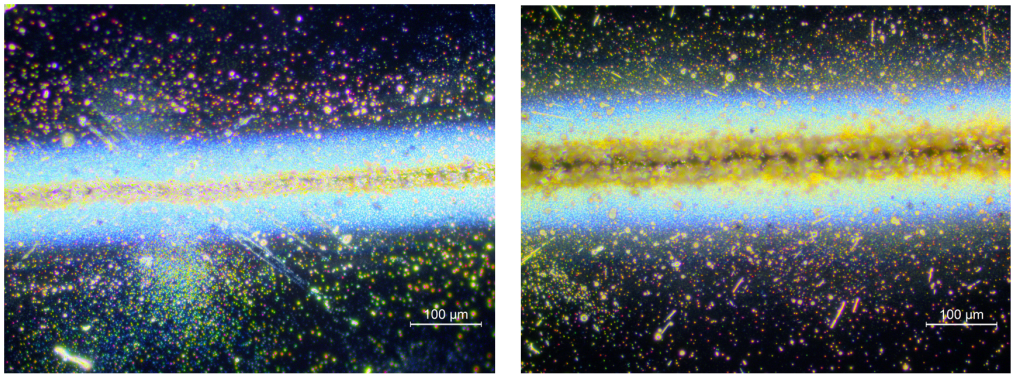

Fig. 2. Lines ablated into Si using the sieve (left) and lens (right) at 2.06 J/cm^2. The more intense color gradient seen in the lens case is indicative of a larger recast layer and formed oxide. Yellow colored oxides are ~200 nm thick, metallic blues are ~150 nm thick, and royal blues are ~120 nm thick [16].

In order to objectively compare the lateral extent of the HAZ/redeposition, we have used the quantity herein referred to as “relative width”. Here, we define the relative width as:

Relative width = oxide width / (oxide width + mark width)

This definition allows us to account for the difference in spot size between the sieve and refractive lens. As measured in the microscope images, the relative widths of the oxide layers of the sieve and lens are measured to be 87.9% and 92.1%, respectively, which represents a ~5% reduction in oxide layer width,

and about 50 nm reduction in oxide thickness in the case of the photon sieve. SEM images of the lines shown in Fig. 2 are provided in the Supporting Information, along with ablated craters formed in silicon via 10 and 100 laser pulses. The results of these tests are identical to those seen in Fig. 2. The same experiments were also performed in stainless-steel. These experiments are also summarized in the Supporting Information, as the results are identical to silicon tests.

The formed oxide layer on silicon is likely not a result of the HAZ, as the heat dissipation for nanosecond laser pulse interaction with silicon occurs on too short a timescale to form such thick oxide layers, and oxygen diffusion into the oxide layers will be much less. In order to confirm this, laser marking of silicon using a millisecond-pulse laser at 1070 nm wavelength was performed. This longer pulse width will have a much more thermally-dominated interaction that will result in a large HAZ and reduced ablation. Images and specific details of this experiment are provided in the Supporting Information, where a clear HAZ can be seen around the mark, but no ablated/redeposited particles are present. Based on this, we believe that the formed oxide layers seen in Fig. 2 are a result of the easily-oxidized molten/vapor phase silicon that is ejected from the ablated region and is redeposited. This recast layer is much more easily oxidized due to the non-solid phase of the material, and therefore is capable of forming much thicker oxides than purely from thermal processes (i.e. HAZ alone) in nanosecond laser pulses. Additionally, the oxide layer was easily removed by the scotch tape, suggesting that the oxidized material was redeposited vaporized silicon particles (recast layer), as a purely thermally-grown oxide would not delaminate so easily. Images of this delaminated boundary, energy dispersive x-ray spectroscopy (EDX) images showing oxide concentration on the surface, and SEM images of the recast layer nanoparticles are shown in Fig. 3.

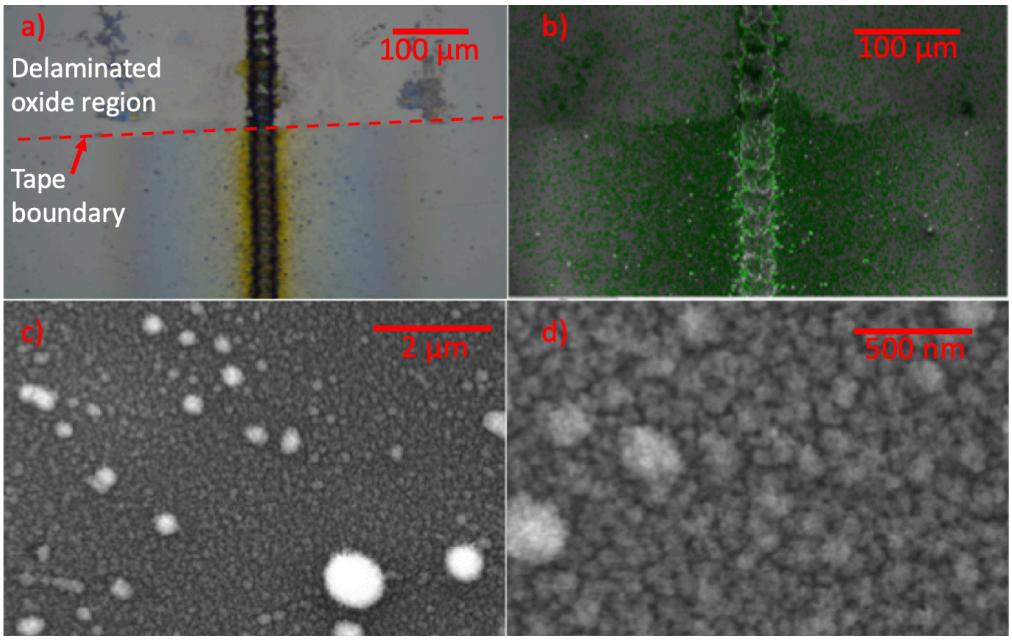

Fig. 3. (a) Optical microscope image showing the boundary between scotch tape-delaminated oxide region and the undisturbed recast layer oxide. (b) SEM image of the same region depicted in (a) with EDX data overlaid to show the oxygen concentration on the surface (oxygen is shown in green). (c) SEM image showing the recast layer oxide surface composed of nanoparticles that have re-agglomerated on the surface to form a thin film. (d) Higher magnification view of (c).

In order to investigate the origin of these differences, beam profiles from the photon sieve and galvo lens were measured using a commercial CCD profiler with 3 µm pixel pitch (Newport LBP-2-HR-VIS). The beam profile was measured at the focus, and the intensity distribution in the focal plane was recorded. Below the FWHM, the sieve beam is "sharper", that is the intensity drops off more rapidly and a narrower $1/e^2$ diameter is present. This is shown in the overlaid beam profiles in Fig. 4. Note that the photon sieve spot has been defocused slightly (such that the FWHM of each beam is equivalent) to more clearly illustrate this point. Viewed another way, the ratio of FWHM to $1/e^2$ diameter is larger in the case of the photon sieve. Here, this ratio for lens and photon sieve were measured as 0.60 and 0.65, respectively, as measured at their respective focal planes. This is to say that the photon sieve focal point FWHM is more similar to the $1/e^2$ diameter than is the case for the lens focal point.

Because the intensity below FWHM is lower for the photon sieve, the energy imparted on the material surface is more concentrated near the center of the focal spot rather than in the tails of the Gaussian profile. As a result, despite fluences being equivalent, the photon sieve will have a lower HAZ/redeposition, especially in the immediate vicinity of the mark. Additionally, less material will be removed in the case of the photon sieve

compared to the refractive lens at a given numerical aperture and equal energy densities. This results in a reduced recast layer, and thus a reduced surface oxide as illustrated in Figs. 2 and 3.

This reduction in $1/e^2$ intensity was explained by Kipp et. al. in 2001 as a result of the pinhole distribution in photon sieves, which can increase or decrease resolution as desired based on their size and spatial distribution [8]. The photon sieve is able to focus to a tighter spot at a given NA while the depth of focus remains the same (as the depth of focus is determined geometrically by the NA of the focusing optic). Therefore, this reduction in HAZ and recast layer oxide formation is a natural consequence of the photon sieve.

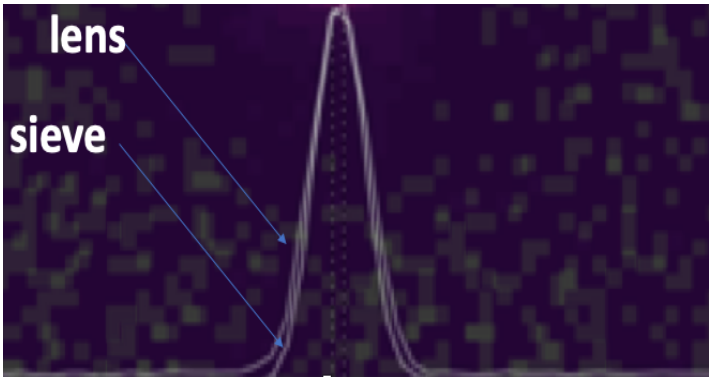

Fig. 4. Overlaid beam profiles of the lens and photon sieve showing similar FWHMs, but a narrower $1/e^2$ in the photon sieve focal point. The difference in the area under each intensity curve is ~5%, which is a result of the lack of "tails" in the photon sieve profile. The photon sieve profile is defocused slightly in order to show each profile at the same FWHM in order to illustrate the difference more clearly.

We have experimentally studied the differences in laser materials processing when using a traditional refractive lens versus a planar diffractive photon sieve. Differences in processing behavior were analyzed in terms of the HAZ and redeposited film thickness of the marked/ablated area. It was found that at equal fluences, the photon sieve produces a reduced HAZ and oxide layer in terms of relative width and oxide thickness compared to the lens. These results were consistent across multiple substrates. The oxide formation in the experiments presented here was as thick as ~200 nm. As such, the oxidation of the recast layer is likely the physical mechanism behind such thick layer formations. Upon examination of the focused beam profiles, it was found that the photon sieve has reduced tails in the focal plane compared to the lens (i.e. a narrower $1/e^2$ diameter) despite having the same FWHM as the lens. This is attributed to the pinhole diffraction phenomenon of the photon sieve and follows the theme of photon sieves for improved resolution and contrast in imaging applications. Therefore, for a given NA, the photon sieve will have a narrower and sharper

spot size with the same depth of focus. Therefore, less material will be removed further from the center of the focused beam, which results in both a reduced HAZ and recast layer oxide thickness. Based on the results in this study, photon sieves are an advantageous option for laser materials processing applications due to their increased resolution and reduced relative HAZ and recast layer/oxide thickness at a constant fluence value. Additionally, the light weight and ease of fabrication of the photon sieve makes high NA systems and/or large-area marking more practical than traditional galvos or microscope objectives. These findings could have an important impact on laser materials processing in various fields such as optical surgery, semiconductor processing, material welding, ablation, pump/probe thermal spectroscopy, or other applications that require high confinement of thermal and optical energy.

The authors acknowledge support from the NASA Langley Professor program (3776-UVA) and the NSF I/UCRC for Laser and Plasma Advanced Manufacturing (IIP-1338917).

The authors thank Elisa Pantoja-Rodriguez for providing the long-pulse laser sample and George Wilkes for providing the SEM in Fig. 3.

References

1. J. C. Ion, Laser Processing in Engineering Materials: Principles, Procedure, and Industrial Application (Butterworth-Heinemann, Oxford, 2005).
2. K. Sugioka and Y. Cheng, “Ultrafast lasers – reliable tools for advanced materials processing,” Light: Science & Applications 3 (149) (2014).
3. R. Gattass and E. Mazur, “Femtosecond laser micromachining in transparent materials,” Nature Photonics 2, 219-225 (2008).
4. J. Walsh, T. Flotte, and T. Deutsch, “Er:YAG laser ablation of tissue: Effect of pulse duration and tissue type on thermal damage,” Lasers in Surgery and Medicine 9 (4), 314-326 (1989).
5. S. L. Trokel, R. Srinivasan, and B. Baren, “Excimer laser surgery of the cornea,” American Journal of Ophthalmology 96 (6), 710-715 (1983).
6. K. Sugioka, M. Meunier, and A. Pique, eds., Laser Precision Microfabrication, Vol. 135 of Springer Series in Materials Science (Springer, 2010).
7. M. G. Gupta and D. Carlson, “Laser processing of materials for renewable energy applications,” MRS Energy Sustainability, 2 (2015).
8. L. Kipp, M. Skibowski, R. L. Johnson, R. Berndt, R. Adelung, S. Harm, and R. Seemann, “Sharper images by focusing soft x-rays with photon sieves,” Nature 414, 184-188 (2001).

9. G. Andersen, “Membrane photon sieve telescopes,” Applied Optics 49 6391-6394 (2010).
10. R. Menon, D. Gil, G. Barbastathis, and H. I. Smith, “Photon-sieve lithography,” Journal of the Optical Society of America A 22, 342-345 (2005).
11. O. Asmolova, G. P. Andersen, and M. A. Cumming, “Photon sieves for creating and identifying orbital angular momentum of light,” Proc. SPIE 10120, 1012009 (2017).
12. R. Janeiro, R. Flores, P. Dahal, and J. Viegas, “Fabrication of phase photon sieve on an optical fiber tip by focused ion beam nanomachining for improved fiber to silicon photonics waveguide light coupling,” Optics Express 24 (11), 11611-11625 (2016).
13. J. Park, K. Lee, and Y. Park, “Ultrathin wide-angle large-area digital 3D holographic display using a non-period photon sieve,” Nature Communications 10 (1304) (2019).
14. M. N. Julian, D. G. MacDonnell, and M. C. Gupta, “High-efficiency flexible multilevel photon sieves by single-step laser-based fabrication and optical analysis,” Applied Optics 58 (1) 109-114 (2019).
15. J. Henrie, S. Kellis, S. M. Schultz, and A. Hawkind, “Electronic color charts for dielectric films on silicon,” Optics Express 12, 1464 (2004).
16. “BYU Cleanroom – Electronic Color Charts,” https://ece.byu.edu/cleanroom/color_chart.phtml.
17. “Silicon dioxide color chart,” Addison Engineering, Inc. (2019).